Advanced Near-Field Microscopic Studies of Nanophotonic and Complex Biological Samples

Thorsten Nicolas Gölz

Munich, 2024

Advanced Near-Field Microscopic Studies of Nanophotonic and Complex Biological Samples

Thorsten Nicolas Gölz

Dissertation
to obtain the doctoral degree of natural sciences (Dr. rer. nat.)
at the Faculty of Physics
of the Ludwig-Maximilians-Universität München

submitted by
Thorsten Nicolas Gölz
from Karlsruhe

München, 10/12/2024

First referee: Prof. Dr. Andreas Tittl
Second referee: Prof. Dr. Achim Hartschuh
Date of oral examination: 06.02.2025

Fortgeschrittene Nahfeldmikroskopische Untersuchungen von Nanophotonischen und Komplexen Biologischen Proben

Thorsten Nicolas Gölz

Dissertation
zur Erlangung des Doktorgrades der Naturwissenschaften (Dr. rer. nat.)
an der Fakultät fur Physik
der Ludwig–Maximilians–Universität
München

vorgelegt von
Thorsten Nicolas Gölz
aus Karlsruhe

München, den 10.12.2024

Erstgutachter: Prof. Dr. Andreas Tittl
Zweitgutachter: Prof. Dr. Achim Hartschuh
Tag der mündlichen Prüfung: 06.02.2025

Contents

List of Figures

List of Abbreviations

AFM	Atomic Force Microscope
ATR	Attenuated Total Reflection
AZO-PC	Azobenzene-Phosphatidylcholine
BIC	Bound-State in the Continuum
BS	Beamsplitter
CL	Cathodoluminescence
DAQ	Data Acquisition
DFG	Difference Frequency Generation
DOPC	1,2-dioleoyl-sn-glycero-3-phosphocholine
EC-QCL	External Cavity-Quantum Cascade Laser
EELS	Electron Energy Loss Spectroscopy
FDTD	Finite Difference Time Domain
FPA	Focal Plane Array
FOM	Figure of Merit
FOV	Field of View
FTIR	Fourier-Transformed Infrared (Spectroscopy)
FWHM	Full Width at Half Maximum
LNP	Lipid Nanoparticles
MCT	Mercury Cadmium Telluride
MIR	Mid Infrared
NA	Numerical Aperture
PDM	Point Dipole Model
PECVD	Plasma Enhanced Chemical Vapor Deposition
PMMA	Poly(methyl methacrylate)
PS-Het	Pseudo-Heterodyne
PSS	Photostationary State
OPD	Optical Path Difference
ORMOCER	Organically Modified Ceramics
Q factor	Quality Factor
RBC	Resin-Based Composites
RIE	Reactive Ion Etching
RM	Reference Mirror
ROI	Region of Interest
a-SNOM	Aperture-Scanning Near-Field Optical Microscope
SEM	Scanning Electron Microscopy
s-SNOM	Scattering-Scanning Near-Field Optical Microscope
SiN	Silicon Nitride
SNR	Signal-to-Noise Ratio
TEM	Transmission Electron Microscopy
THz	Terahertz
TIR	Total Internal Reflection
MIR	Mid Infrared
WLP	White Light Position

Zusammenfassung

Infrarrotmikroskopie wird allgemein auch als chemische Mikroskopie bezeichnet, da sie die chemische Struktur der untersuchten Materialien anhand der intrinsischen, materialspezifischen Infrarotabsorption entschlüsseln kann. Die Infrarotabsorption dient dabei als spektroskopischer Fingerabdruck, der spezifisch für die chemische Natur der Materialien ist. Die optische Rasternahfeldmikroskopie (*s-SNOM*, englisch: *Scattering scanning near-field microscopy*) ist eine Mikroskopiemethode, die Infrarotmikroskopie und -spektroskopie von Materialien auf der Nanometerebene weit unterhalb des Beugungslimits von Licht ermöglicht. Sie macht damit die Nanowelt für chemische Mikroskopie zugänglich, die bisher aufgrund des Beugungslimits auf mehrere Mikrometer beschränkt war. Diese Arbeit dient dazu, den Wirkbereich von s-SNOM in Kombination mit klassischen beugungslimitierten Fernfeld-Infrarotmikroskopiemethoden auf verschiedenen Gebieten zu erweitern.

In dem ersten Abschnitt dieser Arbeit wird s-SNOM auf optische dielektrische Metaoberflächen angewendet, deren ultrascharfe Resonanzen auf der Physik von gebundenen Zuständen im Kontinuum (*BICs*, englisch: *Bound states in the continuum*) basieren. Es wird gezeigt, dass s-SNOM die optischen Nahfelder der einzelnen Metaoberflächenresonatoren auflösen kann. Zudem wird mithilfe eines neu eingeführten Bilderverarbeitungsverfahrens für s-SNOM Bildern gezeigt, dass der endliche Feldeffekt (englisch: finite array effect), die gerichtete Kopplung der Resonatoren, Defekte und Randeffekte in den optischen Metaoberflächen im Nahfeld entschlüsselt werden kann. Die gewonnen Erkenntnisse können unter anderem genutzt werden, um die geometrische Grundfläche von Metaoberflächen für Anwendungen in der Katalyse oder der Biosensorik zu verkleinern.

Der zweite Teil dieser Arbeit stellt eine auf eine biomedizinische Anwendung ausgerichtete Studie vor, in der eine Zahnfüllung mit verschiedenen Infrarotmikroskopietechniken charakterisiert wird. Dabei wird gezeigt, dass anhand der Infrarotbilder und Spektren die chemische Natur der Füllung und des Dentalharzes unterschieden werden kann. Darüber hinaus können einige der Infrarrotbilder genutzt werden, um die Porosität von Zahnfüllung zu bestimmen. Schließlich wurde mit s-SNOM der Kompositwerkstoff der Dentalfüllung auf Nanoebene untersucht und die chemische Heterogenität aufgezeigt. Die aufgezeigte infrarotmikroskopische Charakterisierung von Dentalfüllungen hat großes Potenzial, die immer komplexer werdenden Kompositwerkstoffe durch ein besseres Verständnis ihrer chemischen Zusammensetzung zu optimieren.

Der letzte Teil der Arbeit erweitert den Funktionsbereich von s-SNOM, der bisher fast ausschließlich trockene Proben umfasst hat, auf wässrige Lösungen. Hierfür wird eine Methode vorgestellt, die ultradünne Siliziumnitrid-Membranen nutzt, um die delikate s-SNOM Spitze vor der wässrigen Lösung zu schützen. Als spannendes Modelsystem wird mit der Methode photoschaltbare Lipidvesikel in deren native Lösung untersucht, die als potenzielle lichtgesteuerte Medikamentenwirkstoffbereitstellungssysteme gelten. In dem Kapitel wird gezeigt, dass man die Lipidvesikel weit unter dem Beugungslimit von Infrarotlicht mikroskopisch und spektroskopisch charakterisieren kann. Darüber hinaus zeigen wir ein transientes Infrarotspektroskopischesverfahren basierenden auf s-SNOM, dass die Milisekundenschaltdynamik der Lipidvesikel entschlüsseln kann. Das vorgestellte Konzept von s-SNOM Messungen in Flüssigkeiten wird in der Zukunft viele weitere Studien von zum Beispiel der Degradierung von Katalysatoren oder von neurotoxischen Proteinfibrillen ermöglichen.

Die in dieser Arbeit vorgestellten Studien zeigen die vielseitige Einsetzbarkeit von s-SNOM auf, die von optischen Metaoberfläche über Dentalfüllungen bis hin zu photoschaltbaren Lipiden in wässrigen Lösungen reicht. Dies wird die weitere Optimierung der verschiedenen Materialsysteme auf Basis der infrarotmikroskopischen und spektroskopischen Ergebnisse und Methodiken ermöglichen.

Abstract

Infrared microscopy is commonly referred to as chemical microscopy, as it enables the deciphering of the chemical structure of examined materials based on their intrinsic, material-specific infrared absorption. The detected infrared absorption serves as a spectroscopic fingerprint that is unique to the chemical nature of the material. *Scattering scanning near-field optical microscopy* (*s-SNOM*) is a technique that extends infrared microscopy and spectroscopy to the nanometer level, far below the diffraction limit of light, making the nanoworld accessible to chemical microscopy, previously restricted to several micrometers due to the diffraction limit. This work serves as a milestone in expanding the application range of s-SNOM across multiple fields, in combination with classical diffraction-limited far-field infrared microscopy methods.

In the first section of this work, s-SNOM is applied to optical all-dielectric metasurfaces whose ultra-sharp resonances are based on the physics of *bound-states in the continuum* (*BIC*). It is shown that s-SNOM can resolve the optical near-fields of the individual metasurface resonators. Furthermore, using a newly introduced image-processing method for s-SNOM images, it is demonstrated that the finite array size effect, directional coupling of the resonators, defects, and edge effects in optical metasurfaces can be decoded within the near field. The insights gained trough this method can be used, among other things, to reduce the geometric footprint of metasurfaces for applications in catalysis or biosensor technology.

In the second part of this work, a study oriented towards a biomedical application is presented in which a dental filling is characterized using various infrared microscopy techniques. It is shown that the infrared images and spectra can distinguish the chemical nature of the composite filling and the dental resin. In addition, the infrared images can be used to determine the porosity of dental fillings. Finally, s-SNOM is employed to examine the composite material of the dental filling at the nanoscale, revealing its chemical heterogeneities. The demonstrated infrared microscopy-driven characterization of the dental filling has great potential to optimize the increasingly complex composite materials through a better understanding of their chemical composition down to the nanoscale.

In the final part of this work, the functional range of s-SNOM, which has so far been almost exclusively applied to dry samples, is extended to aqueous solutions. For this purpose, a method is presented that uses ultra-thin silicon nitride membranes to protect the delicate s-SNOM tip from the aqueous solution. As a highly relevant model system, the method is applied to investigate photoswitchable lipid vesicles in aqueous solution, which are potential light-driven drug delivery systems. The study demonstrates that lipid vesicles can be characterized by near-field microscopy and spectroscopy far below the diffraction limit of infrared light. In addition, a transient infrared spectroscopic method based on s-SNOM is introduced that resolves the millisecond switching dynamics of single lipid vesicles. The presented concept of s-SNOM measurements in liquids holds great potential for future studies on e.g. the degradation of catalysts or the assembly of neurotoxic protein fibrils.

The studies presented in this thesis demonstrate the versatility of s-SNOM with investigations ranging from photonic metasurfaces and dental fillings to photoswitchable lipids in aqueous solution. The findings and concepts will allow further optimization of different material systems based on the attained near-field microscopic and spectroscopic results.

1 Introduction

The advent of modern microbiology can be closely linked to the life and work of Antonie van Leeuwenhoek, who crafted some of the first single-lens microscopes in the 17th century[1]. His craftsmanship and innate curiosity led him to study local pond water with his microscopes, resulting in the first observation of bacteria, which he famously called "animalcules"[1]. Despite this groundbreaking discovery, it took another 200 years for Louis Pasteur and Robert Koch to link these microorganisms to diseases through the germ theory of disease[2]. Similarly, Joseph von Fraunhofer made a significant impact on the world by developing the first modern spectroscope, which he used to study the absorption lines in the solar spectrum, now known as Fraunhofer lines[3]. His work laid the foundation for the field of astronomical spectroscopy and greatly deepened our understanding of the universe. These historic examples demonstrate that advancements in scientific instrumentation, especially those based on the interaction of light with matter, can drive significant societal progress by providing new insights into the natural world around us. Today, the new frontier of imaging and spectroscopy lies in the study of materials and organisms at the nanoscale, where breakthroughs in computation, energy materials, and medicine increasingly depend on understanding and manipulating these materials at the nanoscale.

The major physical limitation arising from the wave nature of light that hinders microscopy and spectroscopy on the nanoscale is the diffraction limit of light. The universal principle, stemming from the Heisenberg uncertainty principle, is formulated for microscopy as the Abbe limit, expressed in equation 1.1[4]. The principle states that the distance d at which two point sources can be resolved depends on the wavelength λ of the light source and the numerical aperture NA of the microscope objective.

$$d = \frac{\lambda}{2NA} \tag{1.1}$$

In practical experiments, this limits the resolution of visible light microscopes to several hundred nanometers and that of infrared microscopes to several micrometers. Nanoscale investigation of matter can be achieved by addressing the Abbe limit, such as by reducing the wavelength λ, as demonstrated in electron microscopy. However, this approach requires high-energy radiation, often causing sample damage through ionization. It also necessitates a vacuum environment, is incompatible with liquid samples, and requires expensive

setups[5]. Alternatively, superresolution fluorescence microscopy has been employed to investigate nanoscale biomolecules in living cells[6–8]. Despite its advantages, this technique is constrained by the need for fluorescently labeled molecules, which can photobleach or induce phototoxicity[9], perturb the system under investigation[10], and require labor-intensive preparation for specific samples.

A fundamentally different approach to achieving nanoscale optical microscopy and spectroscopy, spanning from the UV-VIS to the THz range, is the use of scattering scanning near-field optical microscopy (s-SNOM)[11]. The key principle in this field of microscopy involves using ultra-sharp tips as antennas that interact with light and generate evanescent waves (known as near-fields) bound to the apex of the tip. These near-fields enhance and concentrate the incoming light via the lightning rod effect of the tip, enabling microscopy at a scale far below the diffraction limit. This technique, particularly in the infrared range, offers numerous advantages over the aforementioned state-of-the-art nanoscopy techniques. As infrared light is low in energy, it generally does not cause damage to the sample and does not require operation in vacuum. Furthermore, with infrared light and spectroscopy, the inherent chemical nature of a sample can be visualized based on its specific infrared absorption pattern[12] and does not require any advanced labeling technique.

Yet, infrared near-field microscopy is still perceived as a niche technique due to its relatively recent introduction in the field of microscopy. This thesis aims to address this perception by demonstrating the significant utility of the technique for investigating optical metasurfaces and dental samples. Furthermore, the thesis demonstrates that the method can be straightforwardly applied to studying soft matter in liquid samples, a task traditionally considered highly challenging.

Chapter 2 lays the theoretical foundation of infrared spectroscopy and microscopy by explaining the unique characteristics of infrared light and its technical application in common far-field microscopy and spectroscopy setups for investigating the chemical content of materials. Building on this foundation, the thesis details the complex physical concepts that enable subdiffraction near-field infrared microscopy and spectroscopy.

Chapter 3 discusses the technical details of the optical infrared microscopy setups employed in this thesis. First, the different far-field microscopy setups are introduced. Then, the near-field microscope will be explained in the detail with its different measurement modes. In addition, the liquid near-field microscopy method will be introduced. Finally, the different sample preparation techniques will be discussed.

Chapter 4 presents a concept based on transmission s-SNOM measurements to decipher mode formation in optical metasurfaces, utilizing the physics of quasi-bound states in the continuum. The concept overcomes the current constraints, which limit the investigation of metasurfaces primarily to the diffraction-limited far-field spectroscopy response and numerical simulations. It sheds light on phenomena such as the finite array size effect, directional coupling of resonators, and the impact of edge states and defects on mode formation in metasurfaces. This study has the potential for shrinking the foot print of metasurfaces for application such as biosensing and catalysis.

Chapter 5 highlights a proof-of-principle study that compares and exemplifies the usefulness of classic far-field infrared microspectroscopy techniques and advanced nanoscopy techniques for the investigation of dental materials from the micro- to the nanoscale. The results demonstrate that it is possible to differentiate between different areas of a dental filling based on their intrinsic infrared response and present an algorithmic method that uses infrared images to asses the porosity of different dental materials. Finally, we show that near-field

microscopy can be used to decipher the nanoscale material composition of dental composites. The insights attained can be used in the future to optimize the properties of complex nanoscale dental materials through a better understanding of their chemical composition.

Chapter 6 present near-field nanoscopy of a complex liquid sample, specifically photoswitchable lipid vesicles in their aqueous environment. These lipids are a significant topic of current research, as they have the potential to enable light-mediated drug delivery in biological systems. The chapter demonstrates the spectroscopy and imaging of different switching states of the photoisomeric lipid vesicle system on a scale impossible to achieve with standard far-field microscopes. Moreover, a nanoscopy based measuring technique is introduced that can resolve the millisecond switching dynamics at the single vesicle level. The study presents a significant advancement in the state-of-the-art of near-field microscopy, as the method has long been believed not to be able to investigate liquid samples.

Overall, this thesis provides a wide ranging overview of the strength of infrared near-field microscopy by studying diverse samples, ranging from optical metasurfaces to dental materials and photoswitchable lipid vesicles. The spectroscopic and microscopy insights gained can be employed to better understand and optimize these widely different sample categories, potentially leading to future improvements on the application level, in the spirit of Fraunhofer and van Leeuwenhoek.

2 Fundamentals

2.1 Infrared radiation

This thesis is focused on the use of mid-infrared (MIR) microscopy for the investigation of matter. In general, this section of the electromagnetic spectrum is defined to range from $\lambda = 2.5$ to 25 μm as displayed in Fig. 2.1. This range corresponds to 4000 to 400 cm^{-1} wavenumbers[12]. The unit of wavenumbers relates to the spatial frequency ($\tilde{\nu}$) and is typically used for infrared radiation. It provides a more convenient scale for the typical frequencies encountered in infrared imaging and spectroscopy and is defined according to the following equation 2.1 with E being the energy, c the speed of light and h the Planck constant.

$$\tilde{\nu} = \frac{1}{\lambda} = \frac{E}{hc} \tag{2.1}$$

Importantly, the angular wavenumber $k = |\vec{k}|$ is defined by equation 2.2 with the angular frequency ω.

$$k = |\vec{k}| = \frac{2\pi}{\lambda} = \frac{\omega}{c} \tag{2.2}$$

A comprehensive way to describe the interaction of light with matter is the wavelength dependent material specific complex refractive index $\tilde{n}(\omega)$ as defined in equation 2.3 with $n(\omega)$ being the real part of the refractive index and $\kappa(\omega)$ being the imaginary part of the refractive index often also called absorption index. The real part relates to the amount of light that is reflected from the interface of the material, whereas the imaginary part provides information about the amount of light that is absorbed by the material and helps to determine the attenuation of light as it propagates through the material.

$$\tilde{n}(\omega) = n(\omega) + i\kappa(\omega) \tag{2.3}$$

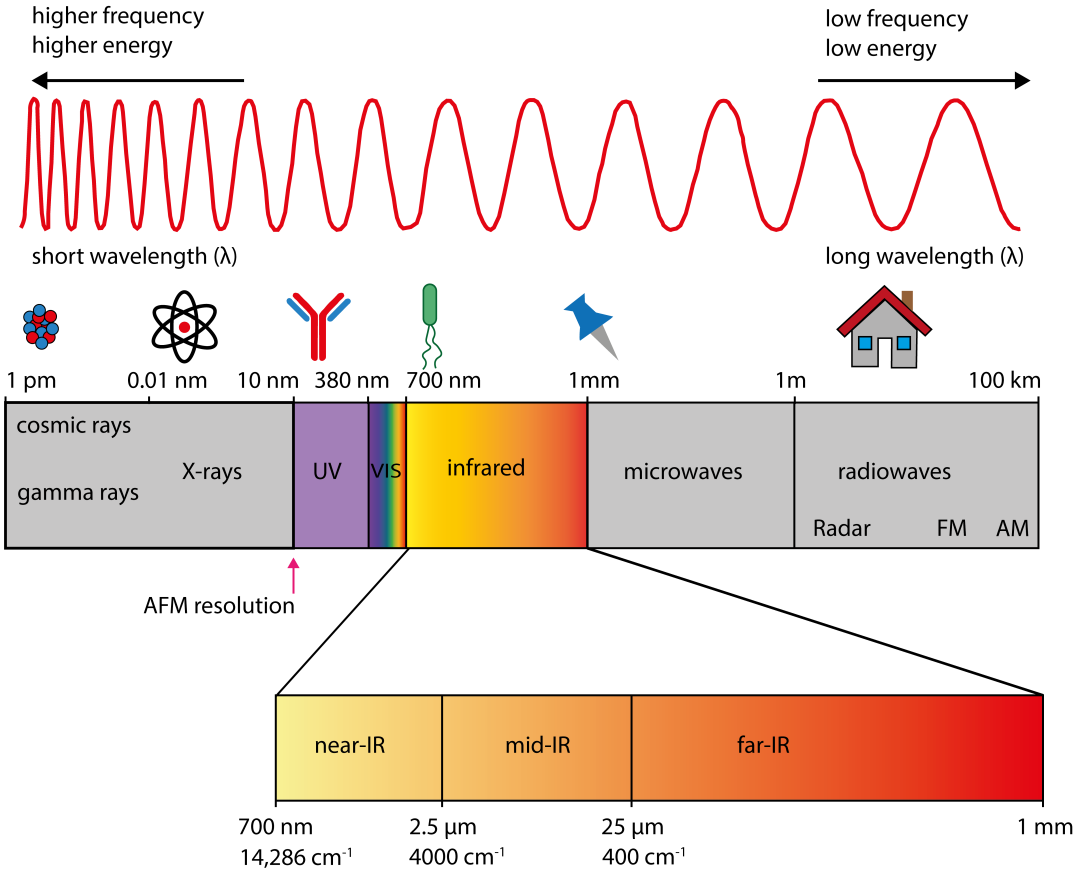

Figure 2.1: Infrared radiation in the context of the electromagnetic spectrum. The infrared radiation ranging from approx. 700 nm to 1 mm is located on the longer wavelength side of the UV-VIS radiation resulting in a lower energy content of the IR radiation. The wavelength of the IR radiation compares to the scale of a single bacterium in the near-IR range and to the scale of a pinhole in the far-IR range. Importantly, the AFM resolution is highlighted by the red arrow relating to the wavelength of extreme UV radiation of around 5 to 20 nm underlining the extreme magnification possible with AFM-based infrared imaging.

Through the refractive index of the material the *reflectance* R at the interface of the material can be calculated. It is defined as the fraction of incident light that is reflected from the incoming light and can be calculated using the following form of Fresnel equation 2.4, if the incident angle of the light to the interface is perpendicular[4]. Using the refractive index of the medium surrounding the material n_1 and the refractive index of the material itself n_2. This equation shows that the greater the difference in refractive indices $(n_1 - n_2)$, the higher the reflectance.

$$R = \left| \frac{\tilde{n}_1 - \tilde{n}_2}{\tilde{n}_1 + \tilde{n}_2} \right|^2 \tag{2.4}$$

Fig. 2.2 shows the complex refractive index of the polymer PMMA in the MIR-range with both the real and imaginary part of the spectra displaying clear and distinct spectral signatures. The peak positions of the spectrum allow for assigning the frequency of the vibrational resonance, while the height of the peaks relate to the strength of the resonances. In the case of PMMA, the main resonance is located at around 5.8 μm (1735 cm^{-1}) and is connected to the carbonyl bond vibration of the organic polymer[12]. The PMMA spectrum exemplifies the inherent advantage of the MIR section of the electromagnetic spectrum for imaging and spectroscopy as it allows to probe the chemical composition of the investigated material sample due to the material specific absorption of the infrared radiation. This specific absorption is based on the fact that infrared light excites vibrational modes at different frequencies in each chemical bond and functional group of an organic or inorganic material. This excitation leads to a

characteristic and often highly complex absorption pattern of infrared radiation for every material, also termed its spectroscopic fingerprint[12]. In turn, this spectroscopic fingerprint can be used to identify unknown materials and decipher the interaction of molecules with their environment. For example, MIR spectroscopy can be used to study isomerization of molecules[13], the intermolecular interaction of different compounds[14], secondary structures in biomolecules[15] and polymerization states in macromolecules[16]. Furthermore, infrared radiation can also excite free charge carriers[17] and lattice vibrations (optical phonons)[18] and for some materials even interband transitions, which is the basis of current state-of-the-art infrared detectors based on $Hg_{1-x}Cd_xTe$ (MCT) semiconductors[19].

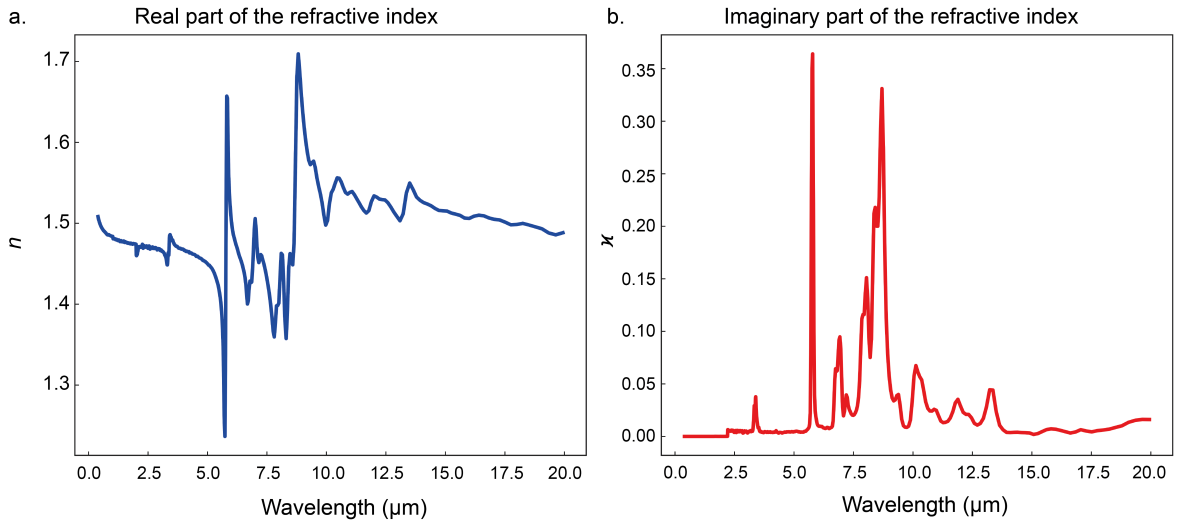

Figure 2.2: Complex refractive index of PMMA. (a) Real part n and **(b)** imaginary part κ of the refractive index of the polymer PMMA showing characteristic IR resonance of organic compounds with data taken from https://refractiveindex.info.

The underlying principles for resolving wavelength-specific absorption and extracting the material's spectroscopic fingerprint are detailed in the following sections.

2.2 Infrared spectroscopy

Spectroscopy in the visible range is based on the diffraction of light on gratings at different angles to divide the different wavelengths of a broadband spectrum and then detect the wavelength at defined position usually on a photodetector chip. However, this highly refined technology, which profited from the fast developing consumer market for camera technology, cannot be used in the MIR spectral range. The reasons are manifold and can be summarized mainly by the fact that the wavelength range of the camera chips and signal-to-noise ratio (SNR) characteristics are not good enough for broadband MIR spectroscopy spanning several micrometers of the low energy spectral range. Therefore, MIR spectroscopy is based on recording interferograms, which has its own inherent advantages. One of the advantages is the so-called Fellgett's advantages or multiplex advantage[12], which states that the SNR attained with multiplex measurements such as the measurements in FTIR is higher compared to a single direct measurement obtained through a scanning monochromator from a grating. This advantage is especially important for measurements in which the dominant noise source is the detector as is the case in MIR. Another advantage of interferometer based spectroscopy methods is the Jacquinot advantage[12] or through put advantage, which describes the fact that

more light reaches the detector element as no exit slit is employed in comparison to grating monochromator leading to higher SNR for low intensity sources.

2.2.1 Interferometry for infrared spectroscopy and imaging

Nowadays, the most established infrared technique is Fourier-Transformed infrared (FTIR) spectroscopy. The core of this technique is the Michelson interferometer as shown in Fig. 2.3a. A slightly more complex interferometer scheme is the Mach-Zehnder interferometer displayed in Fig. 2.3b, which has the advantage of a more flexible and complex optical beam path enabling more advanced optical setups such as a transmission near-field microscope. Both interferometer schemes function in a very similar way with the MIR light source being either a thermal light source or a MIR-laser. In the interferometer the emitted light is split into two beams by a beamsplitter (BS). One part of the beam is backreflected by a fixed mirror, while the second part of the beam called reference beam is modulated by a moving reference mirror (RM). Both beams are recombined at the beamsplitter and the intensity of the resulting interference is detected by a MIR-detector. Through the movement of the RM, in relation to the unmodulated beam path, a path difference Δd is introduced between the two arms of the interferometer.

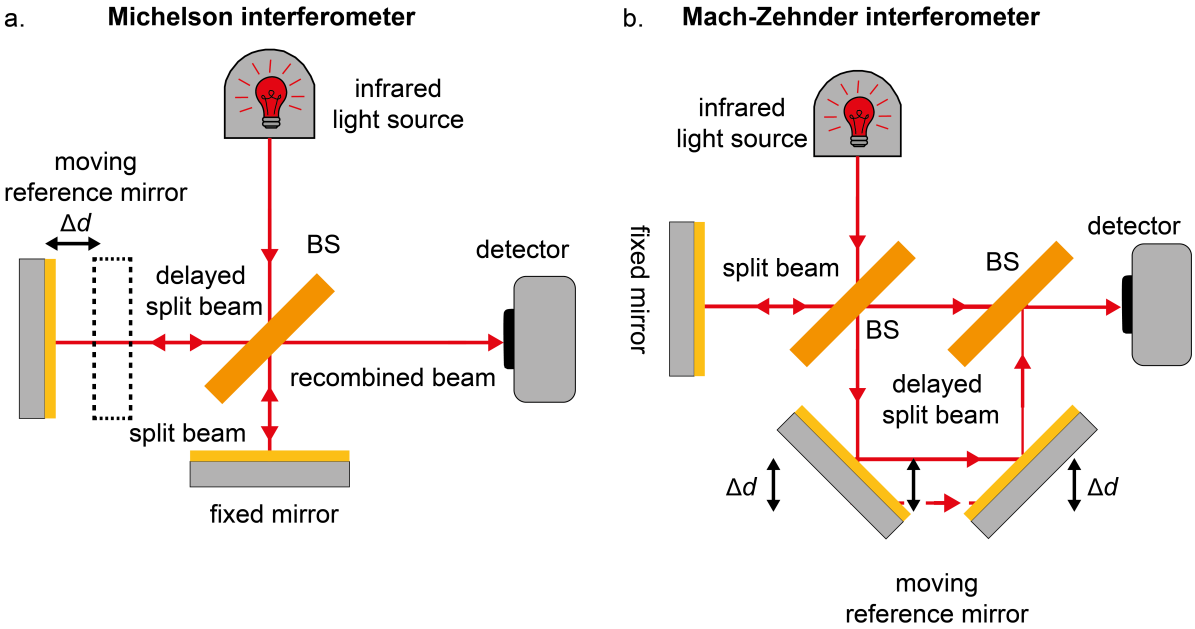

Figure 2.3: Michelson and Mach-Zehnder interferometer setup. Optical setup of a Michelson interferometer (**a**) and a Mach-Zehnder interferometer (**b**) with a light source emitting a beam (red), which is split in two parts by a beamsplitter (BS). One part is reflected by a fixed mirror, while the other is reflected by a moving reference mirror, creating an optical path difference (OPD). The two beams then recombine at the beamsplitter and are directed towards the detector. Notably, the Mach-Zehnder interferometer contains two BS making the setup more flexible but also more complex regarding the beam path.

The overall optical path difference (OPD) between the two beams is given by $\delta = 2\Delta d$ and is called retardation δ. As a consequence of changing the RM position a change in retardation takes place. This leads to a change in the interference of the two beams due to the optical phase delay $\Delta\varphi$ between the two beams and results in a different intensity value recorded by the detector. The recorded intensity as a function of the retardation δ is called interferogram, which can be used to obtain the output spectrum of the light source or with a further modification of the setup the absorption spectrum of a sample via Fourier

transformation.
In order to understand the basis of this transformation this discussion starts with a infinitely narrow monochromatic laser source with a wavelength λ_0 and a spacial frequency ω_0 as displayed in Fig. 2.5. The electric field of the laser source with a intensity of I_0 can be described by the following equation 2.5.

$$E_{\text{source}} = |E_{\text{source}}|e^{i\omega_0 t} \tag{2.5}$$

Now, considering the optical phase delay $\Delta\varphi$ induced through the retardation of the reference beam $\varphi = 2\pi\omega_0\delta$. Both beams need to be described before recombining at the BS by equation 2.6.

$$E_{\text{A}} = |E_{\text{A}}|e^{i\omega_0 t} \quad \text{and} \quad E_{\text{B}} = |E_{\text{B}}|e^{i\omega_0 t+\Delta\varphi} = |E_{\text{B}}|e^{i\omega_0 t+2\pi\omega_0\delta} \tag{2.6}$$

The detector records the intensity signal $I_{\text{det}}$and not the electric field of the recombined beam, which results in the detected signal to be a complex convolution of the two beams described by equation 2.7.

$$I_{\text{det}}(\delta) = \left|E_{\text{det}}E^*_{\text{det}}\right| = |E_{\text{A}}|^2 + |E_{\text{B}}|^2 + 2|E_{\text{A}}||E_{\text{B}}|\cos 2\pi\omega_0\delta \tag{2.7}$$

This equation can be transformed under the assumption that a perfect BS with 50% transmittance and reflectance is employed in the interferometer system.

$$I_{\text{det}}(\delta) = 0.5I_0(\omega)(1 + \cos(2\pi\omega_0\delta)) \tag{2.8}$$

If the two beams are perfectly in-phase both beams interfere constructively yielding $I_{\text{det}} = I_0$, while if there is a mirror displacement of $\Delta d = 1/4\lambda_0$ there is a optical phase difference of 180° leading to destructive interference of both beams and $I_{\text{det}} = 0$. Importantly, the measured detector signal is influenced by several factors such as atmospheric absorption, unequal emission properties and responsitivity of the laser source and detector over the whole spectral range. These influences can be seen in a not normalized FTIR-spectrum as the one shown in Fig. 2.4. The influences are constant over short time spans and have a reproducible effect over all subsequent measurements and can be taken into account by a wavenumber dependent instrumental correction factor R_0 as described in equation 2.9[20].

$$I_{\text{det}}(\delta) = 0.5R_0(\omega)I_0(\omega)(1 + \cos(2\pi\omega_0\delta)) \tag{2.9}$$

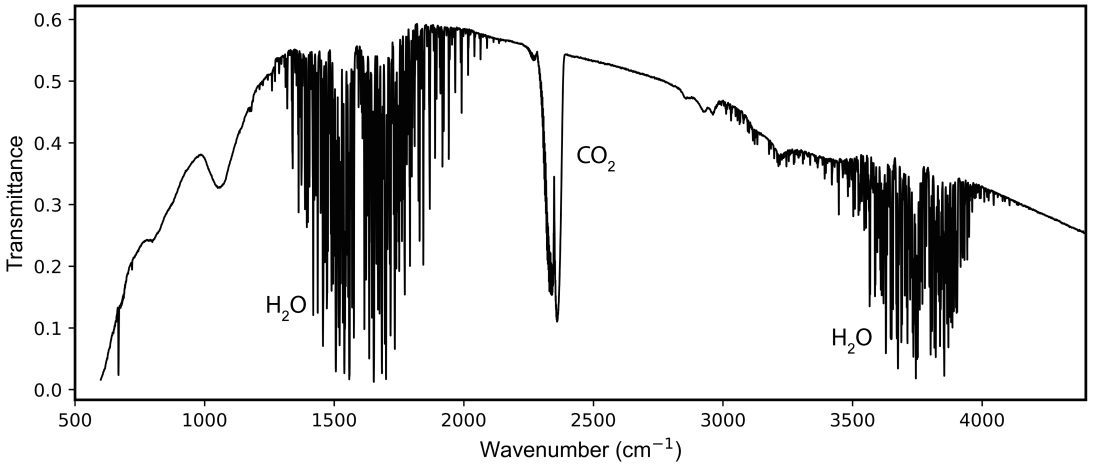

Figure 2.4: Background spectrum of a FTIR-spectrometer. FTIR-spectrum recorded with a commercial FTIR-microscope (see chapter 3) measured in absence of a sample on a gold mirror. The spectrum includes contributions from elements of the instrumental response function R_0 as can be seen from the characteristic atmospheric absorption pattern originating from water vapor and carbon dioxide. Furthermore, the curve like nature of the background signal is due to the difference in blackbody radiation intensity over the MIR spectrum and the detector responsivity at different wavelengths.

The interferogram signal $I(\delta)$ is now defined as the modulated component (in the detector case the AC signal) of the signal neglecting the constant offset DC value, while moving the reference mirror at a constant velocity. For a monochromatic source this results in a sinusoidal signal[20]. By simplifying equation 2.9 through $S(\omega_0) = 0.5 R_0 I_0$ and excluding the constant term which relates to the DC-term of the detector signal, the interferogram equation 2.10 is attained.

$$I(\delta) = S(\omega_0) \cos(2\pi\omega_0\delta) \tag{2.10}$$

The equation enables the direct determination of the wavelength of the monochromatic laser source from the sinusoidal interferogram. Moreover, the amplitude of the interferogram relates to the intensity of the source I_0 modified by the instrumental response function R_0[20].

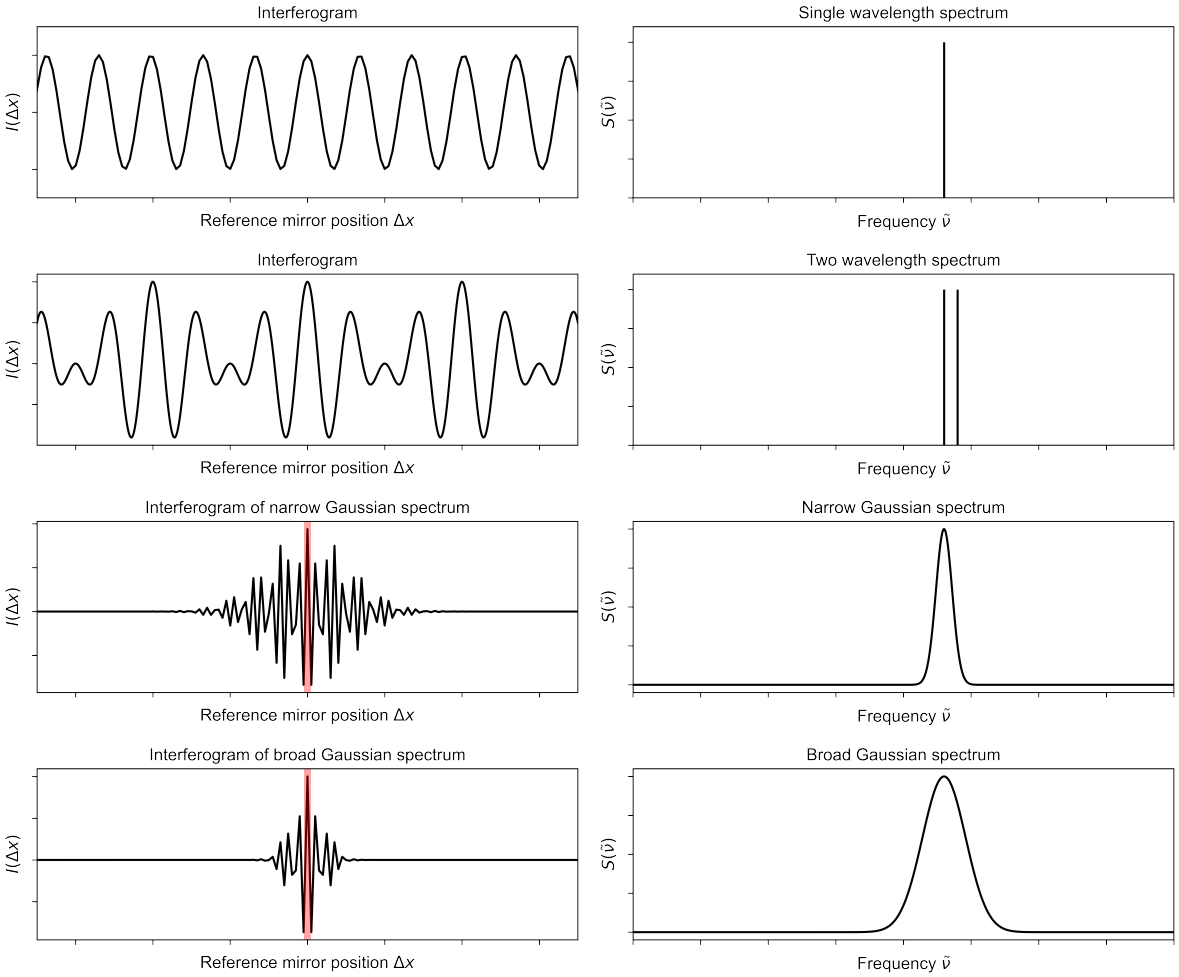

Figure 2.5: Calculated interferograms and associated frequency spectrum of the possible laser source. Different interferograms (left side) are displayed ranging from a simple sinusoidal interferogram associated with a monochromatic source in the frequency spectrum (right side) to a complex interferogram associated with a Gaussian spectrum. The white light position of the complex interferograms is highlighted in red. All plots have the same x-axis.

2.2.2 FTIR spectroscopy with a broadband source

In order to identify a material based on its spectroscopic fingerprint it is important to attain an infrared spectrum over a broad wavelength range. Therefore, FTIR spectroscopy with broadband sources is discussed in the following, which is much closer to the experimental

implementation of FTIR compared to the monochromatic case introduced above. The broadband continuum spectrum of a common MIR source can be expressed by an integral over the whole spectral range of the source, which leads to the modification of the interferogram equation 2.10 resulting in equation 2.11.

$$I(\delta) = \int_{-\infty}^{+\infty} S(\omega) e^{i2\pi\omega\delta}\, d\omega \int_{-\infty}^{+\infty} S(\omega)\cos(2\pi\omega\delta)\, d\omega \tag{2.11}$$

The intensity spectrum of the broadband source can be attained from the recorded interferogram $I(\delta)$ through the use of the Fourier inversion theorem[12,20] given by equation 2.12.

$$S(\omega) = \int_{-\infty}^{+\infty} I(\delta) e^{-i2\pi\omega\delta}\, d\delta = \int_{-\infty}^{+\infty} I(\delta)\cos(2\pi\omega\delta)\, d\delta \tag{2.12}$$

However, the acquired spectrum $S(\omega)$ is still affected by the instrumental response function and does not equal the "real" laser source intensity spectrum $I(\omega)$. For the use of Michelson interferometer scheme for FTIR-spectroscopy the instrumental response is removed through the normalization to a reference spectrum, which will be discussed in the section on transmission FTIR-spectroscopy. An important position of the broadband source interferograms, is the location at which the distance of the reference mirror is equal to the fixed mirror location in the interferogram $\Delta d = 0$. This position is called *white light position* (WLP) of the interferogram[12] and displayed in Fig. 2.5. At this defined position, all frequencies interfere constructively, resulting in the maximal intensity recorded at the detector. Finally, the equation represents the ideal case but is in fact affected by several technical limitations with important effects on the FTIR-spectrum.

2.2.3 Spectral properties in FTIR spectroscopy

In a practically implemented Michelson interferometer for FTIR-spectroscopy, the reference mirror is restricted in its operational movement range, due to the physical limit of the delay stage, which constrains the total retardation δ_t. This limit in turn has effects on the recorded spectral resolution $\Delta\omega$ as both variables are connected by equation 2.13.

$$\Delta\omega = \frac{1}{\delta_t} \tag{2.13}$$

As an example a piezo driven mirror with a range of 300 μm results in a total retardation of $\delta_t = 600$ μm and a spectral resolution limit of $\Delta\omega = 1/0.6$ cm $= 1.666$ cm^{-1}.
A further consequence of the finite distance of the interferometer stage is a sharp cut-off of the recorded interferogram. To illustrate this cut-off effect on the attained spectra a truncation function[21], also called *boxcar truncation function* $D(\delta)$ as defined by equation 2.14 is multiplied onto the spectral function E2.12.

$$D(\delta) = \begin{cases} 1 & \text{if } -\delta_t \leq \delta \leq +\delta_t \\ 0 & \text{if } |\delta| > \delta_t \end{cases} \tag{2.14}$$

This results in the following spectrum:

$$S(\omega) = \int_{-\infty}^{+\infty} D(\delta) I(\delta)\cos(2\pi\omega\delta)\, \mathrm{d}\delta \tag{2.15}$$

The Fourier transform of the product of two functions is the convolution of the Fourier transform of each function[21]. Therefore, the limited retardation δ_t simulated as the truncation

function, leads to a convoluted spectrum of an infinitely long interferogram with a boxcar function. In practice, this causes a broadening of the spectrum and the occurrence of satellite oscillations[21] on both sides of the main peak caused by the sudden stop of the interferogram at the maximum and minimum position as displayed in Fig. 2.6.

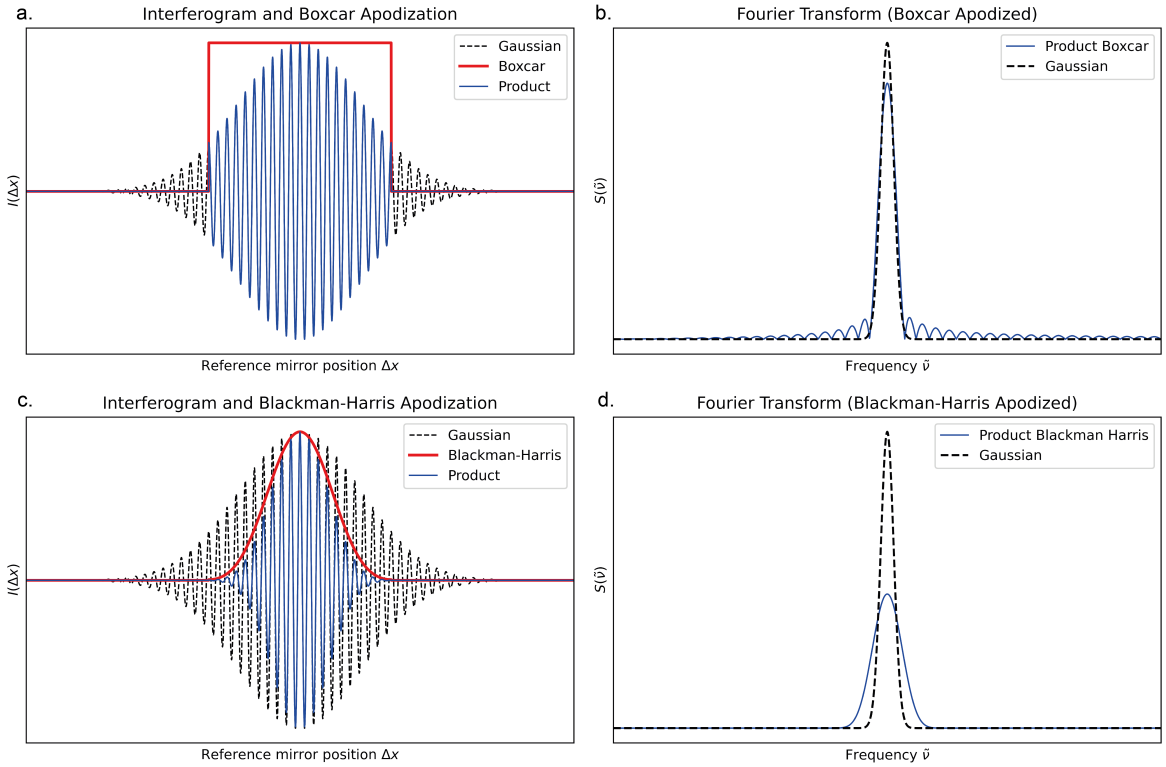

Figure 2.6: Finite interferogram artefacts in FTIR spectroscopy. (a, c) Plot of the interferogram of a Gaussian spectrum (black), the truncation function of either a boxcar car function or the Blackman-Harris 3 term apodization function (red) and the product of both functions (blue). **(b, d)** FT of the Gaussian interferogram (black) and FT of the product of both functions (blue). Note, the oscillatory artefacts at the side of the Gaussian function, which are due to the sudden truncation of the interferogram in **(a)**.

The oscillatory artefacts can be reduced through *apodization* of the measured interferogram[21]. This is conducted through the multiplication of the interferogram by an apodization function $A(\delta)$, which is a smoothing function that can be in principle any monotonically decreasing function with a value of unity at the central position of the interferogram and a symmetric decrease of the values to zero at the edges of the interferogram. As an example, the application of a common apodization function used in FTIR-spectroscopy called *"blackman harris 3-term"*[22,23] is shown in Fig. 2.6. The application leads to a significant reduction in the oscillatory artefacts. Importantly, the apodization of the interferogram leads to suppression of information on the end points of the interferogram, which results in broadening and attenuation of the spectral peaks.

An additional data processing step used in many modern FTIR spectrometers is zero filling or padding[22]. As discussed above the resolution is limited by $\Delta\omega = 1/\delta_t$. However, the total retardation δ_t can be artificially extended by adding zero data points to both ends of the interferogram. This process increases the number of data points per wavenumber resulting in a smoother spectrum leading to a better rendering of the spectral peaks and easier interpretation of complex spectra. Importantly, this process does not increase the overall spectral resolution and original data points are not distorted.

Another variable, which is dependent on the technical implementation of the Michelson

interferometer is the spectral bandwidth, corresponding to the maximum frequency ω_{max} that can be recorded. As the detector signal is recorded with a discrete sampling rate $\Delta\delta$, the recorded interferogram is composed of a finite number of discrete data points. The sampling rates is inversely correlated to the maximum frequency that can be detected as described by equation 2.16.

$$\omega_{max} = \frac{1}{\Delta\delta} \tag{2.16}$$

Finally, there are experimental decisions that can affect the SNR of the recorded spectrum and should be taken in account, when planning experiments. The SNR of a average spectrum increases with the number of co-added scans n with a $n^{1/2}$ relation. However, it needs to be considered that the total measurement time scales with n[22]. Furthermore, the SNR decreases as the spectral resolution of the recorded FTIR spectrum is increased by choosing a longer total retardation distance[22].

2.2.4 Transmission-FTIR spectroscopy

When the Michelson-interferometer setup shown in Fig. 2.3 is extended through the placement of a sample after the recombined beam path a transmission-FTIR-spectrometer is obtained as shown in Fig. 2.7. The incident light can be either reflected, transmitted or absorbed by the sample. Experimentally, the reflected portion of light is often negligible and therefore the absorption of the sample can be measured as the difference in intensity with the sample in the beam path and without the sample. This value is the *transmittance* $T(\omega)$ and is effectively the difference of the intensity of the incident beam $I_i(\omega)$ and the intensity of the transmitted light through the sample $I_t(\omega)$:

$$T(\omega) = \frac{I_t(\omega)}{I_i(\omega)} \tag{2.17}$$

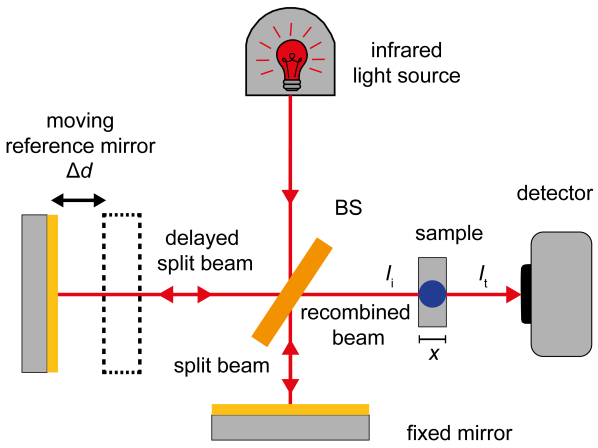

Figure 2.7: Optical setup of a transmission-FTIR spectrometer. The Michelson-interferometer shown in Fig. 2.3 is extended with a sample holder, which is placed in the beam path after both beams are recombined leading to a incidence intensity of I_i. The transmitted intensity I_t after the light passes through the sample is recorded by the detector. The sample FTIR spectrum is attained from the recorded interferogram and the subsequent normalization of the spectrum to a reference spectrum.

As mentioned above to eliminate the instrumental response function $R_0(\omega)$ and to obtain the transmittance $T(\omega)$ of the sample, two separate spectra are recorded. A reference spectra without the sample in the FTIR-spectrometer $B_0(\omega)$ and a the sample spectrum with the

sample inside $B_S(\omega)$. The normalization procedure leads to the following equation E2.18:

$$T(\omega) = \frac{B_s(\omega)}{B_0(\omega)} = \frac{I_t(\omega)R_0(\omega)}{I_i(\omega)R_0(\omega)} = \frac{I_t(\omega)}{I_i(\omega)} \tag{2.18}$$

Next, the relationship between the complex refractive index $\tilde{n}(\omega)$ of the material and the transmittance is established in order to relate the transmittance to the material absorption to attain a the spectroscopic information of the sample. Starting from the electric field of the plane wave MIR radiation that travels in x direction through the material, which can be described by the following equation 2.19.

$$E(x,t) = E_0 \mathrm{Re}\left[e^{i\left(\frac{2\pi\tilde{n}}{\lambda}x-\omega t\right)}\right] = E_0 e^{-\frac{2\pi\kappa x}{\lambda}} \mathrm{Re}\left[e^{i\left(\frac{2\pi n}{\lambda}x-\omega t\right)}\right] \tag{2.19}$$

When the electromagnetic wave travels through a medium with an given absorption index κ, the electromagnetic wave will be exponentially attenuated with the distance x as described in Beer–Lambert law and in equation 2.20[12]. As noted earlier the observable measured on the FTIR detector is the intensity I. Therefore, the absorption is described by considering the recorded intensity with the wavenumber dependent linear absorption coefficient $\alpha(\omega) = \frac{4\pi}{\lambda}\kappa(\omega)$.

$$I(\mathrm{x}) = E_0^2 e^{-\frac{4\pi\kappa(\omega)x}{\lambda}} = I_0 e^{-\alpha(\omega)\mathrm{x}} \tag{2.20}$$

Through the combination of equation 2.18 and 2.20 we attain equation 2.21.

$$T(\omega) = \frac{I_t(\omega)}{I_i(\omega)} = \frac{I_0 e^{-\alpha(\omega)x}}{I_0} = e^{-\alpha(\omega)x} \tag{2.21}$$

In order to define a better quantity for the absorption, which is linearly dependent on the absorption index $\kappa(\omega)$ the *absorbance* $A_t(\omega)$ is introduced as defined by equation 2.22.

$$A_t(\omega) = \log_{10}\frac{1}{T(\omega)} = \frac{1}{\ln 10}\alpha(\omega)x \tag{2.22}$$

2.2.5 Attenuated-total-reflection-FTIR spectroscopy

A second very common FTIR-spectroscopic technique is attenuated total reflection-FTIR (ATR-FTIR), which resembles near-field spectroscopy more closely in its fundamental working principle. As depicted in Fig. 2.8, instead of measuring the transmitted intensity of the sample under investigation as in transmittance-FTIR, the sample is placed onto a high refractive index crystal. Then, the MIR light beam is coupled into the ATR-crystal at such an incidence angle that the beam undergoes total internal reflection (TIR) due to the refractive index difference between the sample and the crystal. The TIR leads to an evanescent wave at the boundary between the ATR-crystal and the sample. The penetration depth d_p of the evanescent wave into the sample is dependent on probing wavelength λ, the relation between the refractive index of the crystal n_1 and the sample n_2 as well as the angle of incidence Θ as described by equation 2.23.

$$d_p = \frac{\lambda}{2\pi n_1\sqrt{\sin^2(\Theta) - \left(\frac{n_2}{n_1}\right)^2}} \tag{2.23}$$

The evanescent field penetrates only a few hundred nanometers to a few micrometers into the sample. Moreover, the beam usually experiences multiple TIR events until it leaves the

ATR-crystal. These characteristics make the method highly surface-sensitive and enables the investigation of a tiny amount of sample substance with high SNR.

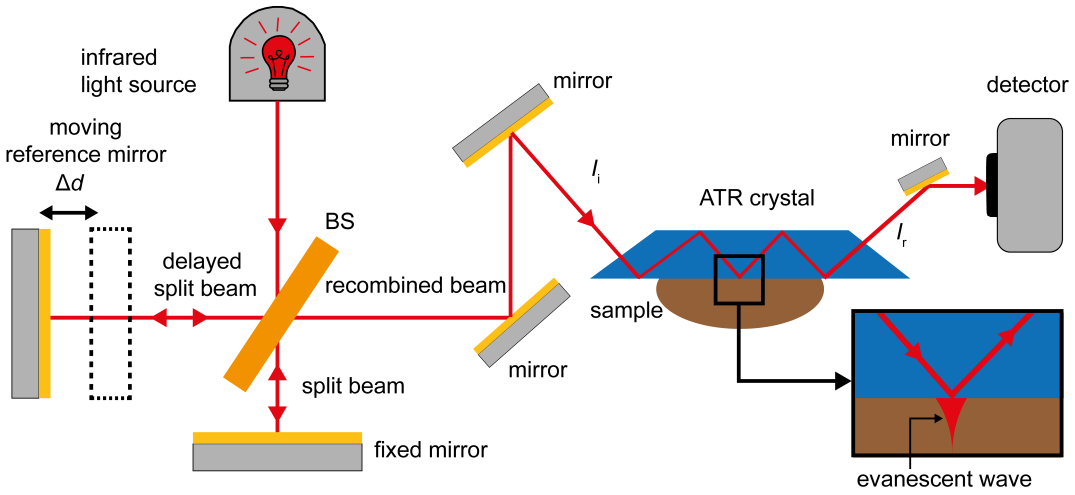

Figure 2.8: Optical setup of an ATR-FTIR spectrometer. The ATR-FTIR is an alteration of the transmission-FTIR spectrometer shown above. It replaces the classic transmission sample holder with a high refractive index crystal prism on which the sample is placed. The incoming beam with an intensity I_i undergoes TIR and is reflected several times at the boundary between the crystal and the sample creating an evanescent field at the boundary that gets attenuated through the characteristic absorption of the sample material. The resulting attenuated beam with a intensity of I_r leaves the prism and is recorded at the detector. The methods enables FTIR-spectroscopy with significantly smaller sample sizes.

As with transmittance FTIR, part of the MIR radiation is absorbed by the sample in contact with the crystal and the detected beam is altered by the absorption characteristics of the sample. In ATR-FTIR the main observable is the *reflectance* R_{ATR}, defined in the following equation 2.24 with $I_i(\omega)$ being the incident beam and $I_r(\omega)$ the detected beam after exiting the ATR-crystal.

$$R_{ATR}(\omega) = \frac{I_r(\omega)}{I_i(\omega)} \tag{2.24}$$

Again, a reference spectrum is measured from a clean crystal with no sample in contact and used to normalize the recorded sample spectrum. In order to acquire the absorbance of the sample $A_{ATR}(\omega)$ the reflectance is transformed in the following way:

$$A_{ATR}(\omega) = \log_{10}\left(\frac{1}{R_{ATR}(\omega)}\right) \tag{2.25}$$

2.3 Infrared microscopy

A major advancement in FTIR-spectroscopy was the combination of microscopy optics with a FTIR-spectrometer, which leads to a FTIR-microscope often also called a chemical microscope[12]. It extends the MIR-spectroscopic investigation to micrometer sized sample regions in contrast to normal FTIR-spectroscopy, which records an average spectrum of the whole bulk sample. Moreover, it enables chemical mapping to characterize chemical inhomogeneities by recording hyperspectral images as displayed in Fig. 2.9. A hyperspectral image is a 3D data cube of the spatial coordinates of the microscopy image and the associated FTIR-spectra, which connect the coordinates with the chemical information and is often also connected to an optical microscopy image of the same area. This data recording method

is enabled by so-called focal plan array (FPA) detectors, which is a pixelated MIR-detector that enables the correlation of spatial information to the infrared response of single pixels. Importantly, transmission FTIR-imaging of absorbing samples is only possible for ultra-thin samples in the range of 5 to 10 μm with a size of around 25 μm to minimize the diffraction of light[24]. Samples with such requirements are often produced by microtomming, rolling and flattening of samples or squeezing the samples between salt plates. Due to the simpler sample preparation, FTIR-imaging through reflectance measurements is often preferred. However, unlike optical microscopy, which uses diffractive lenses for focusing and collecting light, infrared microscopy predominantly employs reflective objectives. The requirement to use reflective optics is due to the fact that the quality and availability of refractive infrared lenses across the entire MIR-spectrum is limited. The recording of the reflectance of the sample can lead to spectral distortion in relation to the known absorption spectra due to several factors such as the angle of incidence of the reflective objective, the complex refractive index of the sample, and the sample's surface morphology[24]. FTIR-imaging in reflectance is best suited for smooth, highly reflective samples, such as thin films on a mirror. Reflectance spectra often differ from standard transmission-FTIR reference spectra, displaying derivative-like shapes that require correction via a Kramers-Kronig transformation to obtain absorbance-like spectra for better comparability[24]. A more in depth discussion of specific MIR-imaging microscopes will be given in the method part of the thesis.

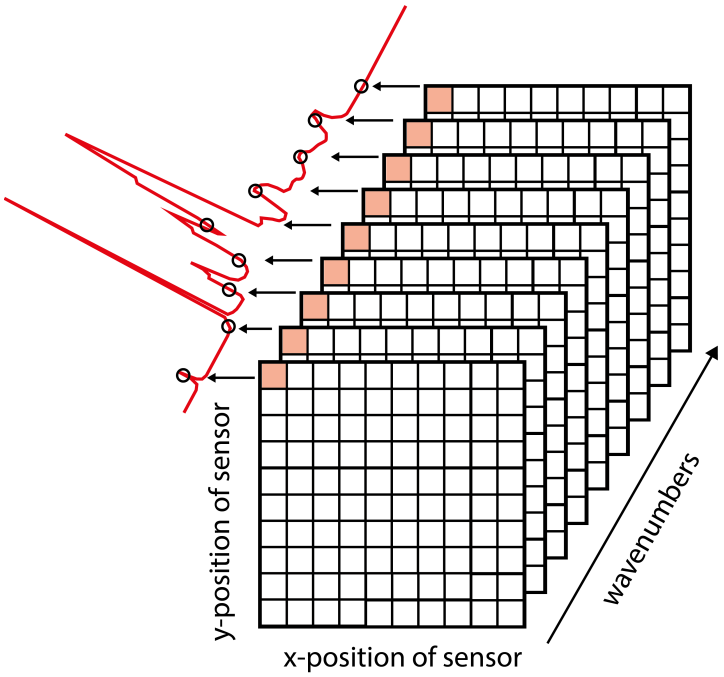

Figure 2.9: Concept of hyperspectral imaging. Sketch of a hyperspectral image datacube with the detected signal of a defined pixel on a focal plane array detector (FPA) corresponding to the spatial encoded MIR-response of the sample.

2.4 Near-field microscopy

The above mentioned microscopy techniques are standard far-field microscopy techniques and, as a consequence, are limited by the diffraction limit of MIR-light to several micrometers making the investigation of nanoscale heterogeneities impossible. In contrast, near-field microscopes enable the nanoscale subdiffraction scale analysis of materials in the infrared

regime. In the following the physical and technical fundamentals will be discussed on how the diffraction limit can be circumvented and how the near-field signal can be isolated from the far-field background.

2.4.1 Circumventing the diffraction limit with near-field optics

The diffraction limit presented in the introduction of this thesis in form of the Abbe limit is a manifestation of the Heisenberg uncertainty principle[25]:

$$\Delta x \Delta p_x \geq \frac{\hbar}{2} \tag{2.26}$$

The relation expresses that the uncertainty in the spatial position in a specific direction (here given by Δx) and the uncertainty in the momentum in the same direction (here given by k_x) cannot be smaller than $\hbar/2$. For photons utilized in microscopy with a momentum of $\Delta p_x = \Delta k_x \hbar$ and a refractive index $n = 1$ in vacuum the relation transforms to the following[25]:

$$\Delta x \geq \frac{1}{2\Delta k_x} \tag{2.27}$$

$$\Delta x \geq \frac{\lambda}{4\pi} \tag{2.28}$$

The consequence of this consideration is that the magnitude of the components of the wavevector $\boldsymbol{k}$ need to fulfill the below equation and are fixed by the wavelength of light and the refractive index.

$$|\boldsymbol{k}| = \sqrt{k_x^2 + k_y^2 + k_z^2} = \frac{2\pi n}{\lambda} \tag{2.29}$$

A simple example of the imaging of a subdiffraction object in x-z plane in vacuum displayed in Fig. 2.10 showcases the outcome of the cut-off limit for the spatial wavevector k_x. The electric field $\boldsymbol{E}$ originating from the nanoscale object at $z = 0$ recorded at the detector plane z is expressed with the angular spectrum representation as the superposition of harmonic waves of the form $\exp(\mathrm{i}\mathbf{kr} - \mathrm{i}\omega t)$ with amplitudes of $\bar{\boldsymbol{E}}(k_x, k_y, z = 0)$ resulting from the two-dimensional Fourier-transformation of $\boldsymbol{E}$ in the following equation[26]:

$$\boldsymbol{E}(x, y, z) = \iint_{-\infty}^{\infty} \bar{\boldsymbol{E}}(k_x, k_y, z = 0) \mathrm{e}^{\mathrm{i}(k_x x + k_y y)} \mathrm{e}^{\pm \mathrm{i} k_z z} \, \mathrm{d}k_x \, \mathrm{d}k_y \tag{2.30}$$

The term $\exp(\pm \mathrm{i} k_z z)$ expresses the propagation of the associated wave. Importantly, for $k_x \leq \frac{2\pi}{\lambda}$ the component k_z is real and thus the associated wave propagates in z-direction into the far-field with amplitude $\bar{\boldsymbol{E}}(k_x, z = 0)$ and an oscillation of $\exp(-\mathrm{i} k_x z)$[26]. On the other hand, if $k_x > \frac{2\pi}{\lambda}$ the wavevector k_z needs to become complex to satisfy $|k_z| = \sqrt{\frac{2\pi^2}{\lambda^2} - k_x^2}$ relating to equation 2.29 resulting in a exponential decaying wave of the form $\exp(-|k_z|z)$[26]. This exponentially decaying wave is the aforementioned evanescent wave, which represents the basis of near-field optics. The subdiffraction object has an initial electromagnetic field distribution of $\boldsymbol{E}(x, z = 0)$ and the associated angular spectrum $\left|\bar{\boldsymbol{E}}(k_x, z = 0)\right|$ at the sample plane. The spectrum contains both propagating and evanescent components resulting in a broad spread of wavevector components in x direction and thus a high confinement in real-space[26] as shown in Fig. 2.10. However, when the spatial wavevectors propagate to

the detector plane the high spatial frequencies ($k_x \geq 2\pi/\lambda$) get lost resulting in a spatial broadening of the real-space location information. The broadening results in a blurring of the spatial location of the object at the detector. The above discussion leads to the conclusion that the loss of the high frequency in-plane spatial wavevectors ($k_{||} = k_x^2 + k_y^2$), which cannot propagate to the far-field restricts the sharp real space location originating from subdiffraction objects.

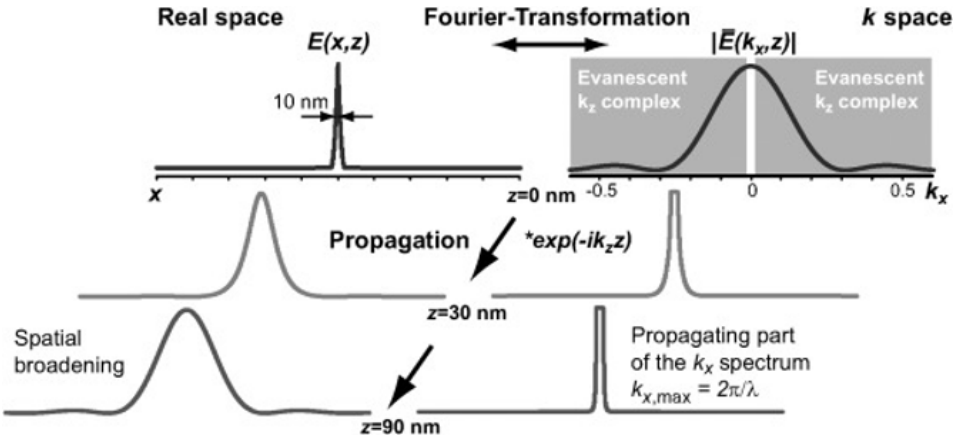

Figure 2.10: Schematic representation of the electromagnetic field propagation from a subdiffraction object. At the position of the sample (z = 0) the source with the associated electromagnetic field distribution $\boldsymbol{E}(x, z = 0)$ and the corresponding angular spectrum representation $\left|\bar{\boldsymbol{E}}(k_y, z = 0)\right|$ contains both propagating and evanescent components. However, the propagation of the electromagnetic fields leads to a loss of high frequency wavevector components resulting at a spatial broadening of the real space information at the detector plane in the far-field. The figure was taken from [26].

Near-field microscopy enables the detection of high spatial frequencies in-plane wavevector with magnitudes beyond the total wavevector length. This statement seems to contradict the above requirement expressed in equation 2.29 at first glance. However, the detection of an in-plane wavevector higher than the magnitude of the wavevector can be achieved, if an imaginary perpendicular wavevector k_z is utilized. As described above evanescent waves do not radiate into the far-field and thus cannot be manipulated by diffractive far-field optics. Therefore, a near-field probe with an associated evanescent field needs to be placed in close proximity to the sample of interest to enable the interaction. Importantly, the methodology is restricted to the surface of a sample and a small subsurface area as the probe cannot be moved inside the sample to image the inside with the rapidly decaying near-fields. The interaction between the different near-field components of the sample and the probe will be discussed in the following in general and qualitative terms in order to attain a better understanding on how the normally non-propagating high frequency in-plane wavevectors of the sample travel to the far-field detector and achieve subdiffraction resolution. A three plane system is considered as displayed in Fig. 2.11 with a near-field light source in the plane $z = -z_0$, the sample plane at $z = 0$ and the far-field detector plane at $z = z_\infty$. The planes are infinite in x and y-direction and the near-field probe is in close proximity to the sample $z_0 \ll \lambda$. Again, the near-field source is expressed through the angular spectrum representation in the following representation:

$$\boldsymbol{E}_{\text{source}}(x, y, -z_0) = \iint_{-\infty}^{\infty} \bar{\boldsymbol{E}}_{\text{source}}(k_x, k_y; -z_0)\, e^{i(k_x x + k_y y)}\, dk_x\, dk_y \tag{2.31}$$

The source field just before it interacts with the sample surface is given by:

$$\boldsymbol{E}_{\text{source}}(x, y, 0) = \iint_{-\infty}^{\infty} \bar{\boldsymbol{E}}_{\text{source}}(k_x, k_y; -z_0)\, e^{i(k_x x + k_y y + k_z z_0)}\, dk_x\, dk_y \tag{2.32}$$

The near-field probe field at the sample due to the close proximity of the probe is a superposition of propagating plane waves and evanescent waves as shown in Fig. 2.11. Notably, the evanescent waves decay in magnitude over the distance. The interaction with the sample is defined by the transmission function $T(x, y)$, which does not take into account topographic effects and assumes a very thin sample. The source field after transmitting the sample translates to:

$$\boldsymbol{E}_{\text{sample}}(x, y, 0) = T(x, y)\boldsymbol{E}_{\text{source}} \tag{2.33}$$

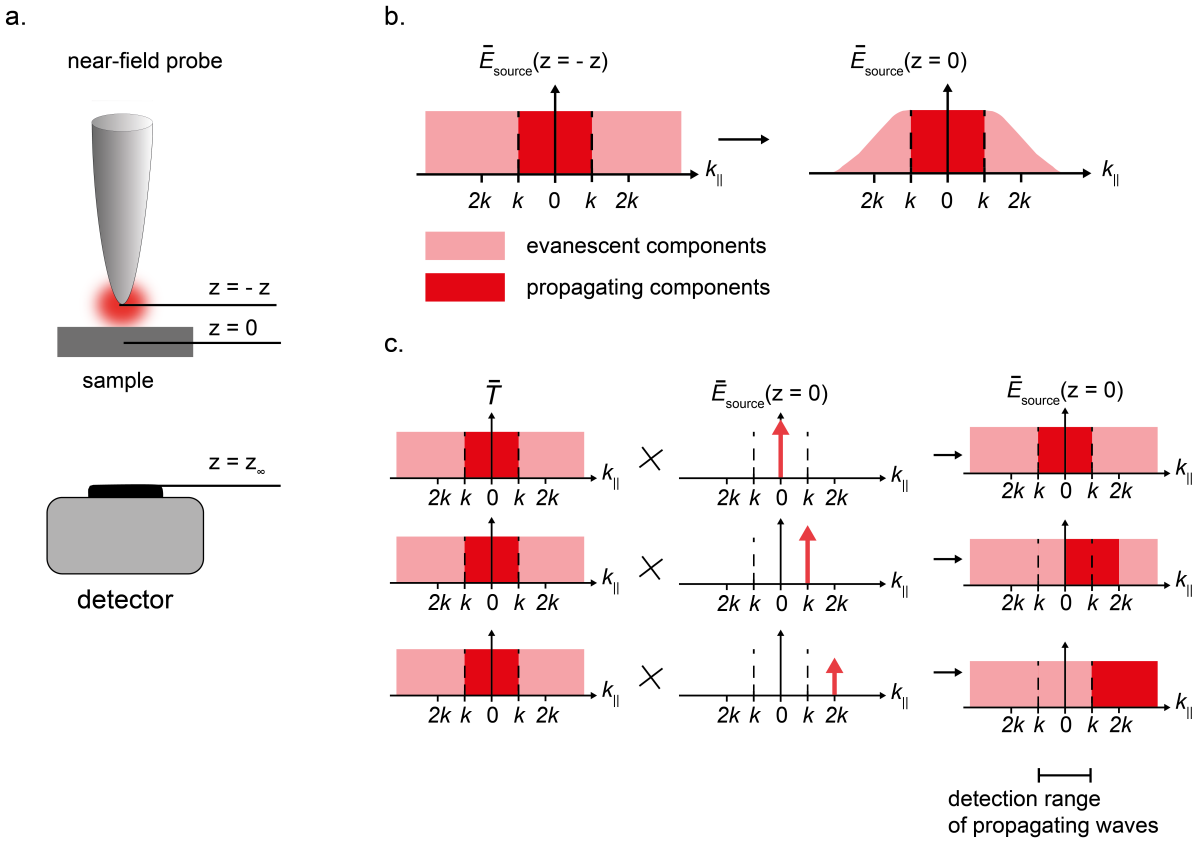

Figure 2.11: Wave propagation in near-field microscopy. **(a)** Different planes in the imaging setup of a near-field microscopy. The detector is in the far-field with $z = z_\infty \gg \lambda$. **(b)** Conceptional sketch of the frequency spectrum of the near-field imaging source $\bar{\boldsymbol{E}}_{\text{source}}$ propagating from the tip $z = -z$ to the sample surface $z = 0$ causing the attenuation of non-propagating high frequency parts of the spectrum. **(c)** Concept of the far-field propagation of the frequency spectrum of the sample response function $\bar{\text{T}}$ through the interaction with the near-field source spectrum at the sample surface $\bar{\boldsymbol{E}}_{\text{source}}$. The interaction leads to the shifting of high frequency components $k_{||} \gg k$ to a frequency range in which they can propagate to the far-field and can be recorded by the detector. The figure was adapted from [25].

In Fourier space the multiplication of the transmission function with the source field becomes a convolution[25] with $\bar{T}(k'_{\text{x}}, k'_{\text{y}})$ being the Fourier transform of T and $k'_{\text{x,y}} = \kappa_{\text{x,y}} - k_{\text{x,y}}$.

$$\begin{aligned}\bar{\boldsymbol{E}}_{\text{sample}}(\kappa_{\text{x}}, \kappa_{\text{y}}, 0) &= \iint_{-\infty}^{\infty} \bar{T}(\kappa_{\text{x}} - k_{\text{x}}, \kappa_{\text{y}} - k_{\text{y}})\bar{\boldsymbol{E}}_{\text{source}}(k_{\text{x}}, k_{\text{y}}; 0)\,\mathrm{d}k_{\text{x}}\,\mathrm{d}k_{\text{y}}, \\ &= \iint_{-\infty}^{\infty} \bar{T}(\kappa_{\text{x}} - k_{\text{x}}, \kappa_{\text{y}} - k_{\text{y}})\bar{\boldsymbol{E}}_{\text{source}}(k_{\text{x}}, k_{\text{y}}; -z_0)\,\mathrm{e}^{\mathrm{i}k_{z1}z_0}\,\mathrm{d}k_{\text{x}}\,\mathrm{d}k_{\text{y}}\end{aligned} \tag{2.34}$$

To further simplify the interaction between the sample and the source field. The interaction is described as an infinite number of interactions between the discrete spatial frequencies

δ of the source field and the sample and the resulting far-field detector signal as shown for three different spatial frequencies $\delta(k_{\parallel})$, $\delta(k_{\parallel} - k)$ and $\delta(k_{\parallel} - 2k)$ in Fig. 2.11.

$$\bar{\boldsymbol{E}}_{\text{source}}(k_{\text{x}}, k_{\text{y}}, 0) = \iint_{-\infty}^{\infty} \bar{\boldsymbol{E}}_{\text{source}}(\tilde{k}_{\text{x}}, \tilde{k}_{\text{y}}; 0)\, \delta(\tilde{k}_{\text{x}} - k_{\text{x}})\, \delta(\tilde{k}_{\text{y}} - k_{\text{y}})\, \mathrm{d}\tilde{k}_{\text{x}}\, \mathrm{d}\tilde{k}_{\text{y}} \tag{2.35}$$

Each interaction of the discrete frequencies with the sample and the ensuing detector signal can be understood in a separate event[25]. A discrete source with a single spatial frequency $\boldsymbol{k}_{\parallel} = (k_{\text{x}}, k_{\text{y}})$ will displace the transverse wavevector of the sample $\boldsymbol{k}'_{\parallel}$ by

$$\boldsymbol{\kappa}_{\parallel} = \boldsymbol{k}_{\parallel} + \boldsymbol{k}'_{\parallel} \tag{2.36}$$

meaning that it translates the spectrum $\bar{T}$ by $\boldsymbol{k}_{\parallel}$. The frequency $\delta(k_{\parallel})$ displayed in Fig. 2.11c represents the case of a plane wave in normal incidence on the sample and does not shift the original spectrum[25]. The case of $\delta(k_{\parallel} - k)$ manifests a plane wave with the largest transverse wavenumber resulting in a plane wave parallel to the sample surface. The original sample function gets shifted by k resulting in a detectable frequency range of $k'_{\parallel} = [k \ldots 2k]$. Again, this is just a conceptional discussion as a plane wave parallel to the incidence must have a zero amplitude value[25]. The case of an evanescent wave is described by $\delta(k_{\parallel} - 2k)$ resulting in a shift of $\bar{T}$ by $2k$ resulting in the spatial frequency range of $k'_{\parallel} = [2k \ldots 3k]$ being detectable in the far-field. Ultimately, high spatial frequencies from the source plane are combined with high spatial frequencies of the sample to attain a difference wavevector that is small enough to propagate in the far-field and can be detected[25]. Thus, by employing a near-field probe with an evanescent field that contains a large bandwidth of spatial frequencies the normally non-propagating near-fields of the sample become detectable. Moreover, the better the near-field confinement and as a result the higher the spread of the spatial frequencies the higher the attained spatial resolution of the sample. The above discussion can be employed to assess the attainable resolution by a near-field probe by the following equation[25].

$$\left| \boldsymbol{k}'_{\parallel,\text{max}} + \boldsymbol{k}_{\parallel,\text{max}} \right| = \frac{2\pi NA}{\lambda} \tag{2.37}$$

The wavevector spread of the near-field probe is mainly defined by the lateral dimension L of either an aperture or the tip apex resulting in the highest spatial wavevectors being around $k_{\parallel,\text{max}} \approx \frac{\pi}{L}$[25], which results in the following maximal wavevector:

$$\boldsymbol{k}'_{\parallel,\text{max}} \approx \left| \frac{\pi}{L} \mp \frac{2\pi NA}{\lambda} \right| \tag{2.38}$$

Especially in the infrared range the last term of the equation can be neglected as $L \ll \lambda$. Therefore, the confinement of the near-field by the diameter of the probe is the main factor that restricts the detection bandwidth and thus the attainable resolution. On the other hand, by achieving intense near-field confinement the evanescent waves decay more rapidly leading to a smaller probing volume restricting subsurface investigations[25]. At the same time, it is important to remember that the detection range is restricted to [-k...k], resulting in an mix of high and low spatial frequencies making image construction difficult. After this general discussion the question arises how these high frequency wavevectors can be utilized in a practical microscope.

2.4.2 Practical implementation of near-field microscopes

The two most common experimental implementations of near-field microscopes are aperture scanning near-field optical microscopy (a-SNOM) and scattering-type scanning near-field

optical microscopy (s-SNOM)[25]. A key commonality between these microscopy techniques, which is at the same time also the basis for their superresolution microscopy mechanism, is the use of nanoscale scanning probes on the basis of tapping mode atomic force microscopy (AFM) as displayed in Fig. 2.12. In this technique a cantilever with a nanoscale probe is driven near its mechanical resonance frequency through a piezo element.

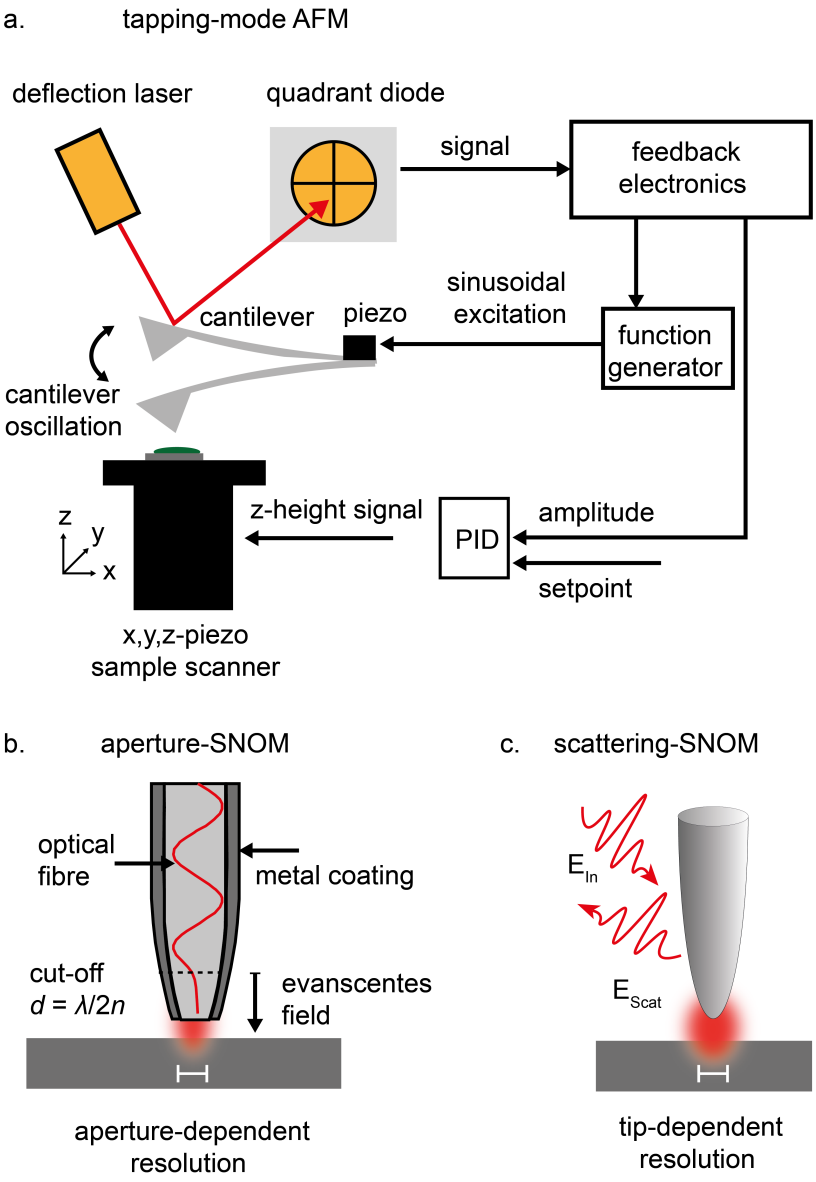

Figure 2.12: Sketch of a tapping mode AFM and comparison of a-SNOM and s-SNOM. (a) Sketch of the working principle of a tapping mode AFM with the oscillating cantilever the deflection laser and the diode detector and the feedback electronics, which control the z-movement of the sample table and lead to a recording of the topography. The a-SNOM principle **(b)** is based on a tapered dielectric fiber with a subwavelength aperture on the end. The subwavelength aperture creates an evanescent wave, which enables the investigation of the sample surface with a resolution of the aperture size below the diffraction limit. The fiber is coated with a reflective metal on the sides to minimize the loss of intensity. **(c)** S-SNOM is based on the detecting the backscattering E_{Scat} of a incoming focused laser beam E_{In}, which carries the material specific information of the sample beneath the apex of the tip with deep subdiffraction resolution limited by the tip radius.

The tip periodically and intermittently touches the surface of the sample through the driving motion. A laser is focused onto the back of the reflective cantilever, and its reflection is

captured by a quadrant photodiode. The photodiode detects positional changes in the laser beam, generating a signal that corresponds to the oscillation amplitude of the cantilever. The feedback electronics in combination with a PID-controller continuously monitors the detected amplitude of the cantilever oscillation and compares it to a defined setpoint value, which controls the force applied to the sample. The PID-controller regulates the z-height of the sample scanner to maintain a constant tapping amplitude and stable tip-sample-interaction. The recorded variations in z-height are used to construct a high-resolution topographical map of the sample.
In near-field microscopy, the AFM feedback mechanism enables a correlative measurement of the surface topography in combination with the optical contrast and ultra-fine control of the tip sample distance crucial for optical near-field measurements. In general, both methods are inherently surface-sensitive, as they probe the sample area located in the optical near-field region. In a-SNOM a tapered, dielectric fiber is used as a scanning probe with additional metal coating to reduce the leakage of light. At its apex the fiber is tapered to a size smaller than the probing wavelength. This confinement results in the propagating modes to become imaginary. The light passes through a subwavelength aperture in the metal coating of radius r, which defines the optical resolution of the microscope. Importantly, this principle leads to a background free near-field optical image as the imaging is purely based on the evanescent field from the fiber aperture[25]. However, at the same time the aperture results in a strong cut-off effect of the transmission intensity of $I \propto (r/\lambda)^4$ resulting in a very strong decrease in transmission power for small apertures and long wavelength[27,28]. This cut-off effect leads to limited use of the a-SNOM technique in the MIR-regime as very high laser intensities are necessary for imaging, which are not compatible with the structural integrity of the fiber. Moreover, fiber technology in the MIR-range is still not as mature as in the VIS-range. Nevertheless, a-SNOM is regularly employed in the UV-VIS and NIR-regimes achieving resolutions of around $\lambda/10$[29].
In contrast, to the high transmission intensity loss in a-SNOM in the MIR-regime the s-SNOM technique can be flexibly applied over a wide wavelength range from UV-VIS to the THz-regime and does not suffer from a strong wavelength dependent intensity loss as the near-field imaging mechanism is based on the elastic scattering of light on the tip as shown in Fig. 2.12b. For this method, the resolution is exclusively defined by the radius of the apex of the tip. S-SNOM commonly achieves 20 nm resolution with commercially available tips[27]. However, in comparison to a-SNOM the near-field signal of s-SNOM is convoluted with a much higher background signal and the great engineering challenge lies in the extraction of the "true" near-field signal from the much stronger background signal originating from the far-field laser illumination of the tip. Overall, s-SNOM is the superior method for the MIR- and THz-regime due to a much better signal-to-noise-ratio of the technique. For the UV-VIS and NIR ranges a-SNOM and s-SNOM are wieldy used in research. Therefore, we employ s-SNOM as our method of choice in this thesis to conduct nanoscale MIR-imaging and spectroscopy and will focus in the following on the intricate details of how to extract the desired near-field signal from the always present background signal.

2.4.3 Fundamentals of near-field imaging in s-SNOM

In s-SNOM, the metallic tip is polarized through the incoming homogeneous p-polarized electromagnetic field E_{in} and acts as an optical antenna concentrating the light at the apex of the tip. This antenna focusing effect is wavelength independent and mainly based on the geometric lightning rod effect of the sharp tip, which leads to a charge accumulation at the apex of the tip with an associated intense field enhancement. This effect enables even

nanoscale near-field microscopy using a wavelength of 118 μm (2.54 THz)[29] as displayed in the numerical simulation in Fig. 2.13a. In the MIR to UV-VIS range plasmonic enhancement[30] and antenna mode effects[31] can further increase field confinement at the apex of the tip leading to an even stronger enhancement of the near-field signal of the sample. The polarized tip scatters the incoming light E_{in} as shown in Fig. 2.13b, which can be described by a complex valued scattering coefficient σ with $E_{\text{in}} = e^{i(kx-\omega t)}$ and $E_{\text{scat}} = se^{i(kx-\omega t+\varphi)}$:

$$\sigma = se^{i\varphi} = \frac{E_{\text{scat}}}{E_{\text{in}}} \tag{2.39}$$

When the tip is in sufficiently close proximity to the sample ($z \ll \lambda$), such that the tip's near-field interacts with it the backscattered field E_{scat} is modified by a sample induced near-field scattering term σ_{nf} that contains the material information of the sample as shown in Fig. 2.13c.

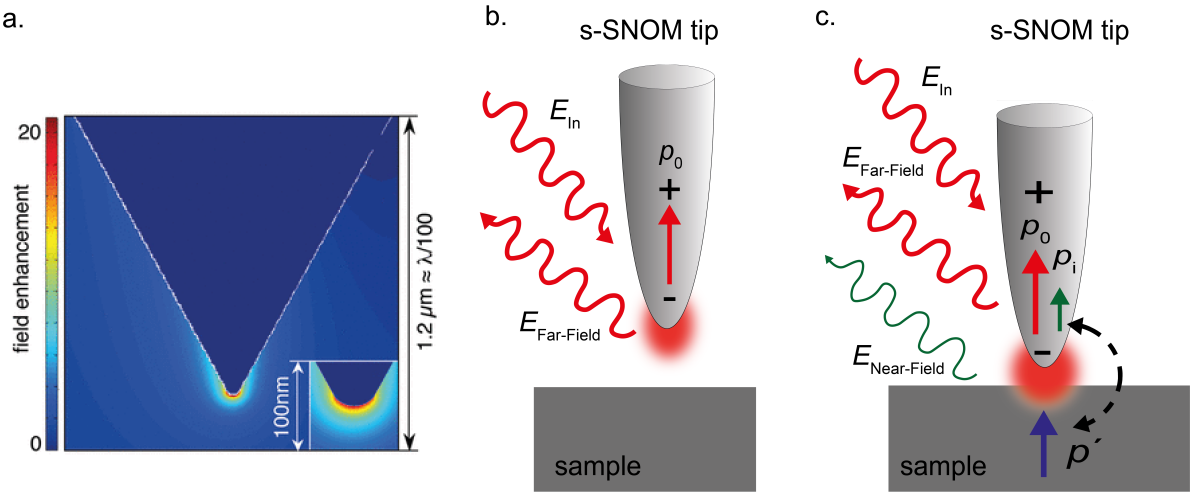

Figure 2.13: Far-field and near-field scattering behavior of a s-SNOM tip. **(a)** Numerical calculated field distribution at the apex of a s-SNOM tip being illuminated with 2.54 THz (118 μm) p-polarized laser radiation. The simulation shows a 25-fold field enhancement and a confinement of the light by several orders of magnitude. **(b)** Conceptional sketch of the scattering process of light at the s-SNOM tip being out of contact from the sample. The incoming p-polarized laser light E_{in} induces a dipole p_0 in the tip, which scatters light back to the detector in the far-field $E_{\text{far-field}}$. **(c)** Displays the case, when the tip comes in close proximity to the sample. In this situation the distance between the tip and the sample is much smaller than the wavelength of light and usually on the scale of several tens of nanometers. At this distance the far-field induced dipoles interacts with the sample and induces a mirror dipole in the sample p', which in turn interacts with the tip creating a sample induced dipole p_i in the tip. Crucially, this sample induced dipole modifies the scattering behavior of the tip with the response of the sample below the apex of the tip. In s-SNOM the extraction of the sample induced backscatttering $E_{\text{Near-field}}$ from the background scattering $E_{\text{far-field}}$ gives the nanoscale sample response. Fig. 2.13a is adapted with permission from ref. [29]. Copyright 2008 American Chemical Society.

In this case, the backscattering term is a convolution of the background scattering E_{bg} from the diffraction limited far-field laser spot and the desired near-field scattering term E_{nf}.

$$E_{\text{scat}} = E_{\text{nf}} + E_{\text{bg}} = (\sigma_{\text{nf}} + \sigma_{\text{bg}})E_{\text{in}} \tag{2.40}$$

The crucial near-field interaction with the sample, which enables the nanoscale MIR-imaging and spectroscopy of the sample, can be understood in the framework of the simple analytical

point dipole model (PDM), which is displayed in Fig. 2.14a[11]. The backscattered light E_{scat} is influenced by the effective polarizability α_{eff} of the tip, which is the key variable that accounts for the near-field interaction between the tip and the sample. In combination with the Fresnel reflection factor of the surface reflectivity r the dependence between the incoming and scattering field can be described as follows[32]:

$$E_{\text{scat}} \propto \alpha_{\text{eff}}(1 + r)^2 E_{\text{in}} \tag{2.41}$$

In the model the tip is approximated as a sphere with an radius a equal to the apex radius. This sphere becomes polarized through the incoming electromagnetic field E_{in}, which can be expressed through the following equation 2.42.

$$p_0 = \alpha E_{\text{in}} \tag{2.42}$$

The polarizability α of the sphere in air is defined by the following equation 2.43 with the dielectric function of the metal tip ϵ_{t}[33].

$$\alpha = 4\pi a^3 \frac{\epsilon_{\text{t}} - 1}{\epsilon_{\text{t}} + 2} \tag{2.43}$$

This induced dipole and associated bound evanescent wave at the apex of the tip scatters the light. When the tip comes in close enough proximity to the sample surface the tip dipole p_0 induces an image dipole p' in the sample[32], which can be described with equation 2.44.

$$p' = \beta p_0 \tag{2.44}$$

The sample polarization can be described by the sample response function β relating the strength of the mirror dipole to the quasi-electrostatic reflection coefficient of the sample with the sample permittivity ϵ_{s} by the following relation[32]:

$$\beta = \frac{\epsilon_{\text{s}} - 1}{\epsilon_{\text{s}} + 1} \tag{2.45}$$

In return, the mirror dipole in the sample acts back on the probe inducing an additional polarization p_{i} in the tip and modifying the light scattered by the tip. This increased polarization acts back and strengthens the sample's mirror dipole, which in return increases the polarizability of the tip resulting in a coupled tip-sample system as shown in Fig. 2.14. The effective polarizability of the near-field coupled dipoles with a tip-sample distance of z in the electrostatic limit is given by[32,33]:

$$\alpha_{\text{eff}} = \frac{\alpha}{1 - \frac{\alpha\beta}{16\pi(a+z)^3}} \tag{2.46}$$

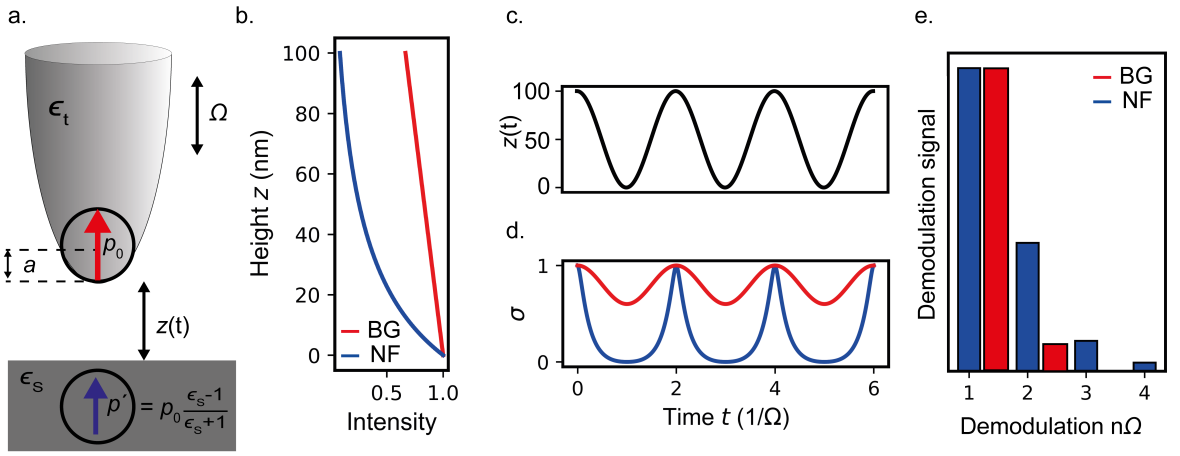

Figure 2.14: Tip modulation of the background and near-field signal. (a) Sketch of the point dipole model system with the modulated tip-sample distance z and a tip radius of a. The far-field induced tip dipole p_0 and the mirror dipole p' are shown in red and blue respectively. For the analytical calculations a tip diameter of a = 60 nm and a tapping amplitude A = 100 nm is used. **(b)** Approach curve of the tip to the sample surface displaying the different decay behaviors of near-field (NF) in blue and far-field background signal (BG) in red. **(c)** Periodic modulation of the tip distance z through the tapping movement of the tip at the tapping frequency Ω. **(d)** Corresponding modulation of the near-field and far-field scattering coefficient σ through the tip motion. **(e)** Near-field and far-field signal demodulated at higher harmonics of the tapping frequency nΩ.

The closer the near-field probe is located to the sample, the stronger the near-field interacts with the sample and in turn the strength of the induced mirror dipole. In general, the accuracy can be improved by extending the approach to the finite dipole model, which describes the tip as an elongated spheroid[32].
Nevertheless, this discussion underlines the fact that for near-field microscopy only the near-field induced mirror dipole scattering E_{nf} is of interest and needs to be isolated from the far-field induced tip scattering E_{bg}. Importantly, in an experiment the detector measures the intensity of the backscattered signal I_{det} and not the electric field E_{scat} resulting in the following convolution of near-field and far-field backscattering at the detector consisting of additive background contribution $|E_{\mathrm{bg}}|^2$ and a multiplicative background contribution $E_{\mathrm{nf}}E_{\mathrm{bg}}^* + E_{\mathrm{nf}}^* E_{\mathrm{bg}}$[34].

$$I_{\mathrm{det}} \propto I_{\mathrm{scat}} \propto |E_{\mathrm{scat}}|^2 = |E_{\mathrm{nf}} + E_{\mathrm{bg}}|^2 = |E_{\mathrm{nf}}|^2 + |E_{\mathrm{bg}}|^2 + E_{\mathrm{nf}}E_{\mathrm{bg}}^* + E_{\mathrm{nf}}^* E_{\mathrm{bg}} \tag{2.47}$$

The AFM is operated in tapping mode with an oscillation frequency of $\Omega \approx 250$ kHz in order to separate near-field from background signal. The harmonic tapping movement can be expressed in the following form $z(\mathrm{t}) = z_0 + A(1 + \cos(\Omega \mathrm{t}))$ with A being the tapping amplitude of the AFM and z_0 being the minimum tip sample distance as displayed in Fig. 2.14c. Equation 2.46 shows that α_{eff} and as a result the near-field scattering depends non-linearly on the tip distance. In contrast, the background scattering changes due to the spatial variation of the incoming electromagnetic field E_{in}, which is on the length scale of the wavelength of the incoming light. Because the tapping amplitude is of only about 80 nm the background signal can be approximated to change linearly with tip-sample distance. This signal behavior can also be seen from approach curves as the one displayed in Fig. 2.14b. The modulation of the background scattering is sinusoidal and has the same form as the tip oscillation $z(\mathrm{t})$, whereas the near-field scattering is anharmonic as shown in Fig. 2.14d. This difference in modulation behavior of far-field and near-field is one of the keys of separating near-field from far-field scattering. The near-field and background scattering coefficients can be expressed as a n^{th}

order complex-valued Fourier series:

$$I_{\mathrm{det}} \propto \left| \sum_{\mathrm{n}=-\infty}^{\infty} (\sigma_{\mathrm{nf,n}} + \sigma_{\mathrm{bg,n}}) \mathrm{e}^{\mathrm{in}\Omega \mathrm{t}} \right|^2 \tag{2.48}$$

The non-linearity of the near-field scattering signal results in stronger signal contributions in the higher harmonics of the tip oscillation $\mathrm{n}\Omega$, whereas the far-field background scattering mainly contributes to the oscillation frequency Ω with weak signal contributions in the higher harmonics as shown in Fig. 2.14e. Through the use of a lock-in amplifier card and the demodulation of the detector signal at a higher harmonic ($\mathrm{n} \geq 2$ for the MIR wavelength) the additive background scattering term $|E_{\mathrm{bg}}|^2$ in equation 2.47 can be eliminated. However, due to the fact that the intensity is measured at the detector the demodulated intensity signal I_{n} still contains background signal contributions mixed with the pure near-field signal $E_{\mathrm{nf,n}}$ through the multiplicative background term as expressed with the following equation 2.49.

$$I_{\mathrm{n}} \propto |E_{\mathrm{nf,n}}|^2 + E_{\mathrm{nf,n}} E^*_{\mathrm{bg,0}} + E^*_{\mathrm{nf,n}} E_{\mathrm{bg,0}} \tag{2.49}$$

As the properties of the background scattering are unknown a reference field E_{ref} in combination with the demodulation procedure needs to be introduced to extract the pure near-field scattering term, which comes with the added benefit of being able to detect the decoupled optical near-field amplitude s_{n} and phase φ_{n}. In the following the interferometric detection scheme will be introduced that allows the background free MIR near-field imaging with a narrow-band laser source.

2.4.4 Pseudo-heterodyne near-field detection

The pseudo-heterodyne (Ps-Het) interferometric detection method is the basis for background free near-field imaging with a narrow band laser source. The term describes an interferometer technique, which is based on a frequency shifted reference beam with known properties[11]. The method eliminates the multiplicative background term that still exists even after the demodulation of the detector signal. It also reconstructs the optical phase φ_{n} and amplitude s_{n} from the detected optical signal as well as increases the SNR through interferometric enhancement[35,36]. This detection scheme is based on a modified asymmetric Michelson-interferometer as shown in Fig. 2.15, which consists of a reference arm with a mirror modulated at a frequency $\mathrm{M} \ll \Omega$ and a second interferometer arm housing the tip.

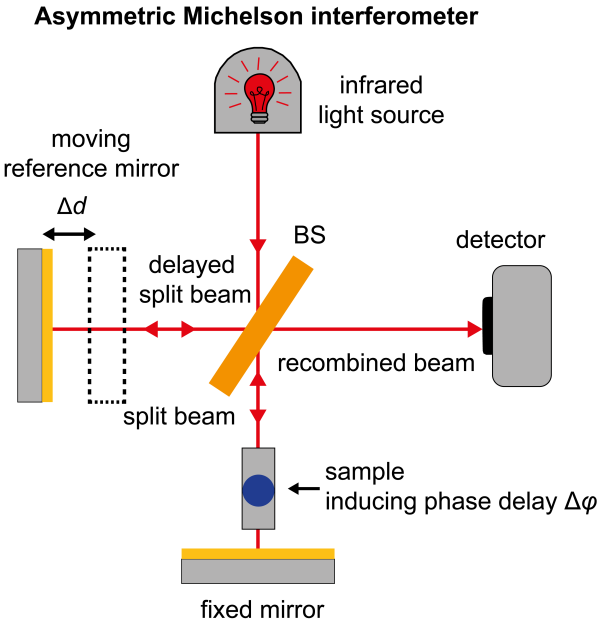

Figure 2.15: Asymmetric Michelson interferometer setup. The asymmetric Michelson-interferometer is a modification of the standard Michelson-interferometer that is displayed in Fig. 2.3 with the sample placed in one of the interferometer arms. This modification enables the detection of an optical phase delay $\Delta\varphi$ induced by the sample.

The backscattered light from the tip and the modulated reference beam is recombined at the beamsplitter and the intensity of the beam is registered. The intensity signal of the detector can be defined by the following equation 2.50, which is a modification of equation 2.47 with the addition of the term of the reference wave E_{ref}.

$$I \propto \left| E_{\mathrm{nf}} + E_{\mathrm{bg}} + E_{\mathrm{ref}} \right|^2 = \left(E_{\mathrm{nf}} + E_{\mathrm{bg}} + E_{\mathrm{ref}} \right) \left(E_{\mathrm{nf}} + E_{\mathrm{bg}} + E_{\mathrm{ref}} \right)^* \tag{2.50}$$

The electromagnetic field of the reference beam, which is displaced through the mirror movement in the following form $d(\mathrm{t}) = d_{\mathrm{ref}} + \Delta d \sin(\mathrm{Mt})$ can be expressed by the following equation 2.51[36]:

$$E_{\mathrm{ref}} = A_{\mathrm{ref}} \mathrm{e}^{\mathrm{i}(\gamma \sin(\mathrm{mM})\mathrm{t} + \Phi_{\mathrm{ref}})} \tag{2.51}$$

A_{ref} is the amplitude of the reference field E_{ref}, M is the modulation frequency of the piezo mirror vibration, Φ_{ref} is the average optical path difference between the tip signal and the reference beam and γ is the phase-modulation depth through the mirror displacement given by the following expression[36]:

$$\gamma = 4\pi \cdot \Delta d / \lambda \tag{2.52}$$

Notably, the phase-modulation depth γ is dependent on the wavelength of the laser source λ and needs to be recalibrated for every new laser frequency employed in near-field imaging experiments. Furthermore, this fact also hinders the use of the Ps-Het detection for broadband spectroscopy with many laser lines. To simplify the reference field expression equation 2.51 is expanded in terms of plane-wave components by the Jacobi-Anger expansion with a oscillatory term that is linear in time and the Bessel functions $\mathcal{J}_{\mathrm{m}}$[36]:

$$E_{\mathrm{ref}} = A_{\mathrm{ref}} \sum_{\mathrm{m}=-\infty}^{\infty} \mathcal{J}_{\mathrm{m}}(\gamma) \mathrm{e}^{\mathrm{im}(\mathrm{Mt})} \tag{2.53}$$

The resulting detector signal I_{Det} of the demodulated tip signal in combination with the modulated reference beam results in a complex frequency spectrum as displayed in Fig. 2.16

and can be described by the following Fourier coefficients[36]:

$$I_{\mathrm{Det}} \propto A_{\mathrm{ref}} \sum_{n=-\infty}^{\infty} \sum_{m=-\infty}^{\infty} I_{n,m} e^{i(n\Omega+mM)t} \tag{2.54}$$

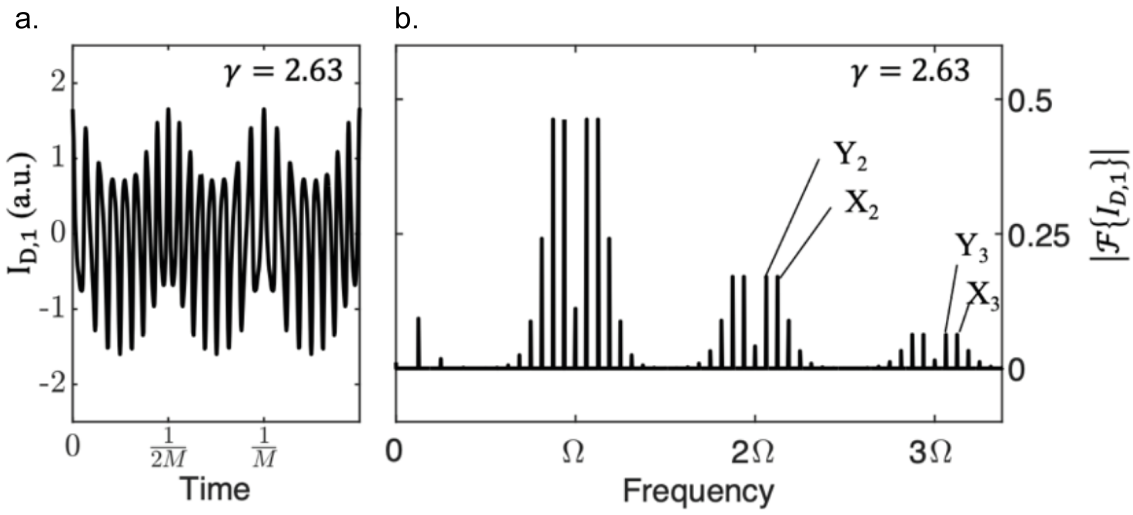

Figure 2.16: Simulation of a time and frequency spectrum of the pseudo-heterodyne modulated detector signal. The time **(a)** and frequency spectrum **(b)** was simulated with a phase modulation depth of $\gamma = 2.63$. The frequency spectrum displays the splitting of the tip frequency demodulated signal $n\Omega$ into several side bands Y_n and X_n, which can be utilized for the extraction of the background free optical near-field amplitude and phase. The Figure is taken from [36].

In this complex spectrum the multiplicative background term $\sigma_{nf,n}\sigma_{bg,0}$ is entirely contained in $I_{n,0}$ and suppressed. In contrast, the sidebands of the following frequency $f_{n,m} = n\Omega + mM$ are chosen as demodulation frequencies of the detector signal I_{Det}. The first sideband (e.g. $Y_2 \rightarrow 2\Omega + 1M$) relates to the imaginary part and the second sideband (e.g. $X_2 \rightarrow 2\Omega + 2M$) to the real part of $\sigma_{nf,n}$ with the following relations[36].

$$Y_n = -2iA_{\mathrm{ref}} \,\mathrm{Im}\left\{E_{nf,n}\right\} \mathcal{J}_1(\gamma) \tag{2.55}$$

$$X_n = 2A_{\mathrm{ref}} \,\mathrm{Re}\left\{E_{nf,n}\right\} \mathcal{J}_2(\gamma) \tag{2.56}$$

In order to determine the Bessel functions that scale the sideband signal the microscope is operated at a defined phase modulation depth $y = 2.63$, where the two Bessel functions are equal $\mathcal{J}_1(\gamma) = \mathcal{J}_2(\gamma)$ as this leads to the best SNR characteristics of the detection scheme the so-called optimal performance setting[36]. When inserting this requirement in equation 2.52 the following laser wavelength dependent reference mirror displacement relation is obtained:

$$\Delta d \approx 0.21 \cdot \lambda \tag{2.57}$$

The pure demodulated near-field amplitude $s_{nf,n}$ and phase $\varphi_{nf,n}$ with a correctly calibrated interferometer are then attain by the following relations with $A_{R,1}$ being a proportionality constant[36]:

$$s_{nf,n} = \frac{1}{2A_{R,1} \cdot \mathcal{J}_1(\gamma_0)} \cdot \sqrt{|X_n|^2 + |Y_n|^2} \tag{2.58}$$

$$\varphi_{nf,n} = \mathrm{atan2}(Y_n, X_n) \tag{2.59}$$

This powerful detection scheme is perfectly suited for near-field imaging of chemically specific resonances of materials by using monochromatic or narrow-band laser sources and is discussed in its practical implementation in the method section of this thesis. However, the detection method breaks down when using broadband MIR-Laser sources. In this case an interferometer scheme oriented on the classical FTIR-spectrometer is employed and is commonly known as nano-FTIR, as it enables the nanoscale acquisition of FTIR-spectra.

2.4.5 Nano-FTIR spectroscopy

The optical setup for nano-FTIR spectroscopy is similar to the Ps-Het detection scheme. However, whereas the reference beam in the asym. Michelson-interferometer is modulated through a vibrating piezo mirror at a high frequency M, the reference beam in the nano-FTIR setup is displaced in discrete steps to attain an interferogram in analogy to classic FTIR-spectroscopy. The asym. FTIR setup has two major advantages, for one a strong signal enhancement can be achieved through interferometric gain, which also applies to the Ps-Het detection mode. As the multiplicative term of the near-field scattering and reference signal is detected amounting to $I \propto \sqrt{I_{\mathrm{ref}} I_{\mathrm{Scat}}}$ and not only the weak tip signal I_{Scat}, which leads to an enhancement of the total detected power of several orders of magnitude[37]. Furthermore, it enables to decouple optical amplitude s_{n} and the optical phase shift $\Delta\varphi$ induced through interaction with the sample[38]. The phase shift $\Delta\varphi$ is normally lost in the classical interferometer scheme as both the reference beam and the sample beam interact with the sample and thus would cancel out the phase shift $\Delta\varphi$. Another crucial difference to a classic symmetric FTIR-setup is the fact that the interferograms attained by nano-FTIR are asymmetric around the zero point of the OPD and only one half of the interferogram contains information about the sample[39]. Thus, spectral acquisition time can be saved when only the left half of the interferogram is recorded. The detector signal can be described in analogy to the detector signal for the Ps-Het detection method by the following equation with *c.c.* indicating the complex conjugates of the three terms in parenthesis.

$$I \propto |E_{\mathrm{nf}}|^2 + |E_{\mathrm{bg}}|^2 + |E_{\mathrm{ref}}|^2 + \left(E_{\mathrm{nf}} E_{\mathrm{bg}}^* + E_{\mathrm{nf}} \mathrm{E}_{\mathrm{ref}}^* + E_{\mathrm{bg}} E_{\mathrm{ref}}^*\right) + \mathrm{c.c.} \tag{2.60}$$

In parallel, higher order signal demodulation is employed to eliminate the additive background leading to the following demodulated detector signal.

$$I_{\mathrm{n}} \propto |E_{\mathrm{nf,n}}|^2 + \left(E_{\mathrm{nf,n}} E_{\mathrm{bg,n}}^* + E_{\mathrm{nf,n}} E_{\mathrm{ref}}^*\right) + \mathrm{c.c.} \tag{2.61}$$

The multiplicative background term is eliminated by considering that the Fourier-Transform in relation to the mirror displacement position x and the limit of the reference mirror $\pm d_0$ is calculated as shown in the following equation.

$$s_{\mathrm{n}} \propto \int_{-\mathrm{d}_0}^{\mathrm{d}_0} \mathrm{d}x\, \mathrm{e}^{\mathrm{i}\omega x} \left[|E_{\mathrm{nf,n}}|^2 + \left(E_{\mathrm{nf,n}} \mathrm{E}_{\mathrm{bg,n}}^* + E_{\mathrm{nf,n}} E_{\mathrm{ref}}(x)^*\right) + \mathrm{c.c.}\right] \tag{2.62}$$

The relation shows that the mirror position dependency only appears in the pure near-field term $E_{\mathrm{nf,n}} E_{\mathrm{ref}}(x)^*$. In contrast, the expressions $|E_{\mathrm{nf,n}}|^2$ and $E_{\mathrm{nf,n}} E_{\mathrm{bg,n}}^*$ do not have a mirror position dependency, which leads to the elimination of these multiplicative background terms during the computation of the spectrum as they do not contribute to the spectral components. Therefore, a background free interferometric enhanced signal is attained after the Fourier-Transformation of the higher order demodulated detector signal. Equivalent to

classic FTIR-spectroscopy the recorded nano-FTIR spectrum needs to be normalized to a background spectrum to eliminate the instrumental response function and attain the complex valued scattering coefficient of the near-field signal $\sigma_{nf}(\omega) = s_{nf}(\omega) \cdot e^{i\varphi_{nf}(\omega)}$. For this process a near-field spectrum is recorded on a spectrally flat substrate like a gold mirror or a piece of silicon with the equivalent operation parameters like same tip, tapping amplitude and laser source settings. The normalized near-field amplitude is given as $s_{n,Sample}/s_{n,ref}$ and $\varphi_{n,Sample} - \varphi_{n,ref}$. In literature[38], it is well accepted that for weak oscillators such as polymers or biomolecules the optical amplitude s_n relates to the reflectivity of the sample and the optical phase φ_n relates to the absorption of the sample. The infrared absorption can be calculated through the following relation.

$$\alpha_n(\omega) = \mathrm{Im}[\eta_n(\omega)] = \mathrm{Im}\left[\frac{\sigma_n(\omega)}{\sigma_{n,ref}(\omega)}\right] = \frac{S_n(\omega)}{S_{n,ref}(\omega)} \sin\left(\varphi_n(\omega) - \varphi_{n,ref}(\omega)\right) \tag{2.63}$$

2.4.6 Near-field tomography

The s-SNOM technique is not only applicable to the surface investigation of thin samples but can be used to decipher sample sections buried up to around 100 nm underneath the sample surface[40,41]. Furthermore, research has demonstrated that depth resolved sample information can be extracted by using different demodulation orders of the tip signal, which differ in their probing depth as shown in the sketch in Fig. 2.17. This behavior of the demodulated signal orders has the potential to enable a 3D reconstruction of the samples dielectric function[42]. Importantly, it was observed that the near-field MIR peak positions shift to lower wavenumbers with increasing probing depth with the effect being stronger for higher demodulation orders[40]. This effect has been measured on quasi-infinite layered systems and is expected to be less pronounced for systems, which have a smaller lateral expansion than the illumination wavelength. The spectral shift is dependent on the oscillator strength of the bond vibration and can result in negligibly small shifts ($\omega_{shift} < 1\mathrm{cm}^{-1}$) for weak molecular vibrations to several wavenumbers for strong molecular vibrations such as a carbonyl-vibration in PMMA[40]. In addition, the subsurface probing of buried structures is connected with a loss in resolution and SNR due to the exponential decay of the near-field, which results in less material probed due to lower near-field interaction. This effect is again stronger for higher demodulation orders as the field is stronger confined to the tip at higher demodulation orders. Interestingly, analytical modeling has shown that for subsurface spectroscopy the apex-near part of the tip shaft is important for the tip-sample interaction, which provides longer reaching evanes-

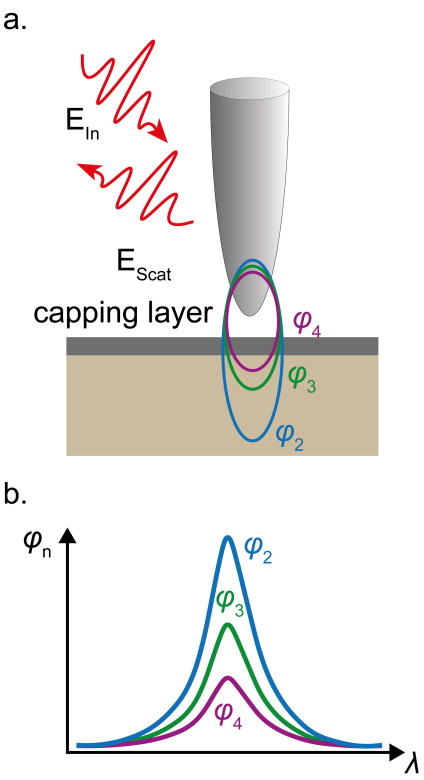

Figure 2.17: Near-field signal behavior for subsurface tomography. (a) Sketch of different demodulated near-field orders (φ_n) penetrating a capping layer for subsurface near-field investigation. **(b)** Idealistic signal behavior of the different demodulation order with regards to a subsurface MIR-sample absorption.

cent waves, highlighting the choice of s-SNOM tip as an important factor for subsurface s-SNOM[40,43]. Finally, especially important for capping layer based liquid s-SNOM methods, as the one introduced in chapter 6, the probing depth, spectral peak height and spectral shifts reduce with increasing permittivity and thickness of the capping layer[40]. Overall, this introduction to the fundamentals of FTIR-spectroscopy and s-SNOM provides an overview of the capabilities of infrared based microscopy. Next, the question will be addressed, how these systems a technically implemented in this thesis.

3 Methodology

3.1 Far-field infrared spectroscopy

This thesis utilizes two far-field infrared microscopes for hyperspectral imaging of samples. One of them is a FTIR microscope with a broad spectral range, albeit with a low SNR due to a weak thermal blackbody radiation source. The other is a quantum cascade laser (QCL-IR) microscope, which operates with a more restricted spectral range because it is based on a tunable laser system. However, the laser based source increases the SNR of the acquired hyperspectral images and leads to a much faster acquisition time. In the following section both microscopes are discussed in their technical details.

3.1.1 FTIR imaging microscopy

The FTIR-microscope used in this thesis consists of a FTIR spectrometer (Vertex 80v, *Bruker optics*, Ettlingen, Germany) coupled to an MIR-microscope (Hyperion 3000, *Bruker optics*, Ettlingen, Germany). The complete setup, comprising the spectrometer and the microscope, is illustrated in Fig. 3.1a. The light source is a blackbody radiation thermal emitter, based on a u-shaped silicon carbide rod, producing a broad band MIR emission spectrum as shown in Fig. 2.4. The light is polarized through a polarizer in the beam path and then focused on the sample with a reflective 15x Cassegrain objective (NA = 0.4) as shown in Fig. 3.1b. This objective enables achromatic focusing across a wide range of wavelengths. Notably, the objective illuminates the sample with an angular spread ranging from about 12° to 23.6°[44]. The reflected IR light from the sample is detected by a liquid nitrogen cooled FPA detector with 64 × 64 pixels, covering a FOV (Field of view) of 170 μm × 170 μm. To attain a larger FOV, 3 × 3 or 4 × 4 image arrays were stitched together, resulting in an expanded FOV of 510 × 510 μm^2 and 680 × 680 μm^2, respectively. Each pixel represents an area of 2.7 μm^2 on the sample. However, the lateral imaging resolution is further diminished due to a 2 × 2 binning (four pixels are averaged into one larger pixel) applied in this thesis to increase the SNR of the recorded hyperspectral data cube. The hyperspectral data cubes were recorded at a spectral resolution of 4 cm^{-1} and are made of 4096 single spectra arranged in a 2D array and

relating to the pixels of the FPA detector. In addition to binning, an averaging of 256 scans was performed to further improve the SNR of the recorded spectra. Overall, the recording of the hyperspectral data cubes presented in chapter 5 required approximately three hours acquisition time with the aforementioned settings. To minimize atmospheric absorption, the sample was placed in an acrylic glass box and purged with dry nitrogen. The sample spectra are normalized to a reference hyperspectral datacube recorded on a gold mirror inside the acrylic box.

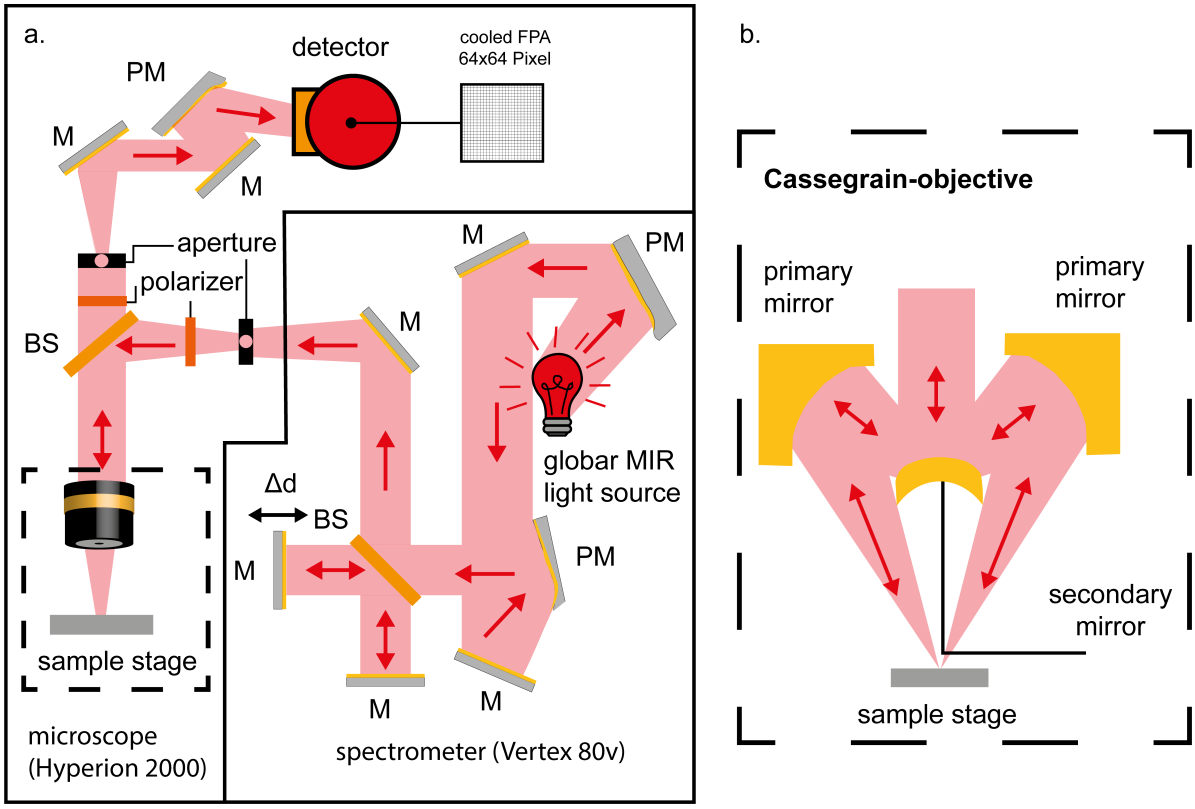

Figure 3.1: FTIR microscope setup. (a) The microscopy setup consists of a microscope coupled to an IR spectrometer with a Michelson-interferometer and a thermal MIR light source. For hyperspectral imaging, a liquid nitrogen-cooled FPA detector with 64 x 64 pixels is employed alongside a parabolic mirror (PM) serving as a collimator positioned before the detector and light source. The MIR light is focused onto the sample using a reflective Cassegrain-objective (*NA* = 0.4) **(b)**, resulting in angled illumination of the sample.

3.2 Quantum cascade laser-based infrared (QCL-IR) microscopy

The second far-field IR microscope employed in this thesis is an external cavity QCL-based wide-field spectro-imaging microscope (Spero, *DRS Daylight Solutions Inc.*, San Diego, USA) as illustrated in Fig. 3.2. Its laser module is based on four different QCLs covering a wavenumber range from 950 to 1800 cm^{-1} (5.56 to 10.55 µm), emitting laser light with a spectroscopic linewidth of 1 cm^{-1}, controlled via frequency-selective external diffraction gratings. The physics of a QCL is based on inter-subband electron transitions in a repeated stack of semiconductor quantum well heterostructures resulting in the emission of narrowband MIR radiation[45]. The laser light is focused using one of two different refractive objectives, with *NA* of either 0.7 (high-magnification objective) or 0.3 (low-magnification objective), and working distances of > 8 mm and > 25 mm, respectively. The corresponding image pixel sizes

are 1.3 μm and 4.3 μm. The objectives can achieve spatial resolutions of up to < 5μm (high magnification) and < 12μm (low magnification) for a wavelength of 5.5μm, with a FOV of 650 × 650 μm and 2 mm x 2 mm, respectively. The sample reflectance is recorded at video rate using an uncooled FPA detector based on µ-bolometer technology with 480 x 480 pixels. A full spectral data cube, consisting of a 2D array of 480 x 480 spectra (resulting in 230,400 individual spectra), can be acquired across the full spectroscopic range with a resolution of 2 cm^{-1} in under 1 min. During spectral acquisition, the sample chamber is purged with dry nitrogen gas, and the data is normalized to a clean flat gold mirror to eliminate atmospheric and instrumental contributions to the sample spectra.

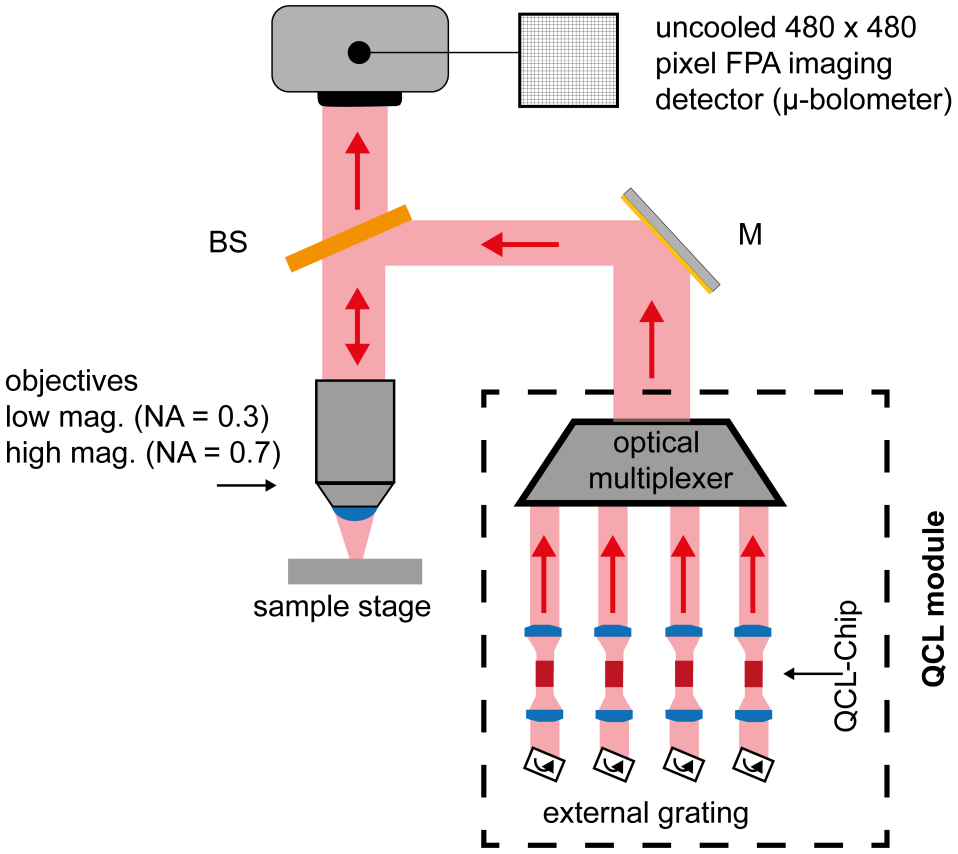

Figure 3.2: QCL-IR microscope setup. The microscope setup consists of a laser module, a beam path with a either high-*NA* (0.7) or low-*NA* (0.3) focusing objective, a sample stage and an uncooled FPA detector. The laser module contains four QCL-chips, which can be rapidly tuned between different emission wavelengths using external gratings that adjust the QCL chip's emission. The uncooled FPA detector has 480 x 480 pixels allowing rapid acquisition of a spectral datacube.

3.3 Scattering-scanning near-field microscopy

In this section, the technical details of conducting s-SNOM measurements are explained. First, the laser sources are introduced, which have been employed in combination with the s-SNOM to conduct the optical measurements. Second, the measurement modes of reflection and transmission s-SNOM are described. Then, the liquid s-SNOM method is introduced, which forms the basis for chapter 6. Finally, the last subsection provides an in-depth discussion of the sample preparation techniques.

3.3.1 Laser light sources

The different spectral ranges of the MIR lasers are shown in Fig. 3.3. For s-SNOM imaging, a laser power of around 4 to 6 mW is commonly accepted as the optimal power level. Therefore, all of the lasers employed for s-SNOM imaging are attenuated by an infrared grid attenuator (*Lasnix*, Berg, Germany), which functions based on the diffraction of MIR light. The attenuators also protect the laser source from back reflections that can damage the laser resonator.

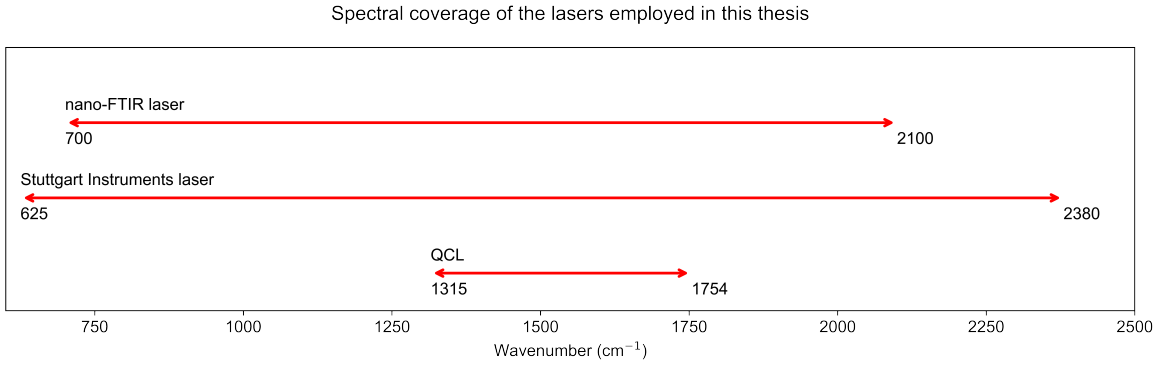

Figure 3.3: Spectral range of MIR lasers utilized for s-SNOM measurements. Three different MIR lasers are employed in this thesis, each with a substantially different spectral range. The QCL has the narrowest spectral coverage, ranging from 1315 to 1754 cm^{-1}, with single-wavenumber spectral emission. The nano-FTIR laser has a spectral range from 700 to 2100 cm^{-1}. However, its emission spectrum covers only 800 cm^{-1} at a time, and the laser must be retuned to change the spectral position. The broadest coverage is provided by the Stuttgart Instruments laser, which offers a spectral range from 625 to 2380 cm^{-1} in the MIR region, with a possible extension into the NIR range.

Quantum cascade laser:
The QCL (MIRcat, *DRS Daylight Solutions Inc.*, San Diego, USA) employed in this thesis is very similar to the laser source in the QCL-IR microscope. The laser is due to the narrowband emission utilized for Ps-Het imaging of chemically specific resonances. The laser range covers most of the fingerprint region of the MIR spectrum, ranging from 1315 to 1754 cm^{-1}. Importantly, the emission is based on two QCL chips with emission ranges from 1315 to 1457 cm^{-1} and 1465 to 1754 cm^{-1}. The emission power, normally around 100 mW, drops off significantly toward the edges of the chip emission range, and laser operation can become unstable, making it difficult to conduct s-SNOM imaging at edge of the spectral range. Furthermore, due to the narrowband nature of the emission spectrum of 1 cm^{-1}, s-SNOM imaging can be unstable, if an atmospheric resonance of water vapor interferes with the QCL emission signal. Often, changing the wavenumber by 1 to 2 cm^{-1} is sufficient to regain a stable s-SNOM signal.
Stuttgart instrument optical parametric oscillator:
The laser is an ultrawide tunable low-noise MIR laser, which is based on a Yb solid state oscillator. The pump laser, pumps a fiber-feedback optical parametric oscillator (FFOPO) and a optical parametric amplifier (OPA) as displayed in Fig. 3.4[46,47]. The OPO output of the signal and idler are focused on a nonlinear $AgGaSe_2$-crystal, which creates through a difference frequency generation (DFG) process a 100 cm^{-1} broad spectral output, which can be gaplessly tuned from 4.2 to 16 μm[46,47]. For chemically specific Ps-Het imaging the output is limited to 10 cm^{-1} spectral width by a grating monochromator as shown in Fig. 3.4b. The low-noise and highly stable output is crucial for conducting the transient MIR-time traces

displayed in chapter 6, which could not be reliably conducted with the above introduced QCL.

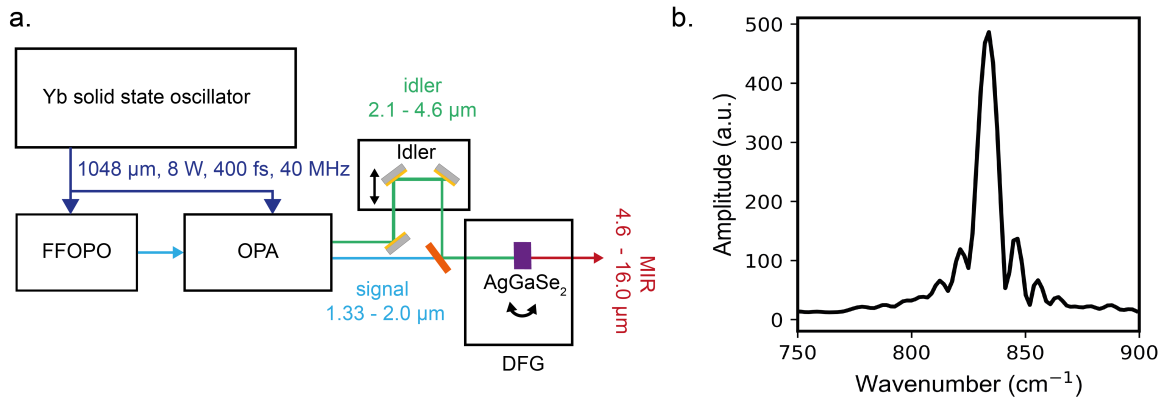

Figure 3.4: Setup and output spectrum of the Stuttgart Instruments laser. (a) Sketch of the optical setup of the Stuttgart instrument laser. A Yb solid-state laser is used as a pump source with central wavelength of 1048 μm from which part of the output power is used to pump a fiber-feedback optical parametric oscillator (FFOPO) and the other part to pump a optical parametric amplifier (OPA). The signal and idler are combined on a $AgGaSe_2$ crystal to generate a DFG signal. **(b)** FTIR spectrum of the spectral output of the MIR stage of the Stuttgart instruments laser after going through the monochromator. The FWHM is approx. 10 cm^{-1} with a central tuning wavelength at 835 cm^{-1}. Note that the oscillations besides the central peak of the laser are artefacts caused due to the finite length of the FTIR stage.

nano-FTIR laser (broadband difference frequency generation source):
In contrast to the narrowband MIR-lasers discussed above the nano-FTIR laser (FFdichro-midIR-NEA 31002, *Toptica Photonics*, Martinsried, Germany) is used because of its broad spectral range. The laser is based on difference frequency generation (DFG) in a GaSe crystal by two Er fiber amplifiers[18] with an emission wavelength of 1.55 μm as shown in Fig. 3.5. One of the two beams passes through a nonlinear fiber to attain a supercontinuum spectrum, which can be tuned between 1.7 to 2.23 μm[18]. The beams are superimposed on a dichroic reflector and focused on the GaSe crystal to generate the DFG emission. The MIR beam is filtered by a low-pass filter to prevent heating of the s-SNOM tip from high frequency spectral components. A total output power of approx. 400 μW can be measured with an overall spectral range of around 800 cm^{-1} with a maximum output power wavelength depending on the chosen emission mode as shown in Fig. 3.5b. Depending on the desired infrared resonance the laser needs to be tuned to the correct mode, whereby the retuning process of the laser takes about 1 to 2 min.

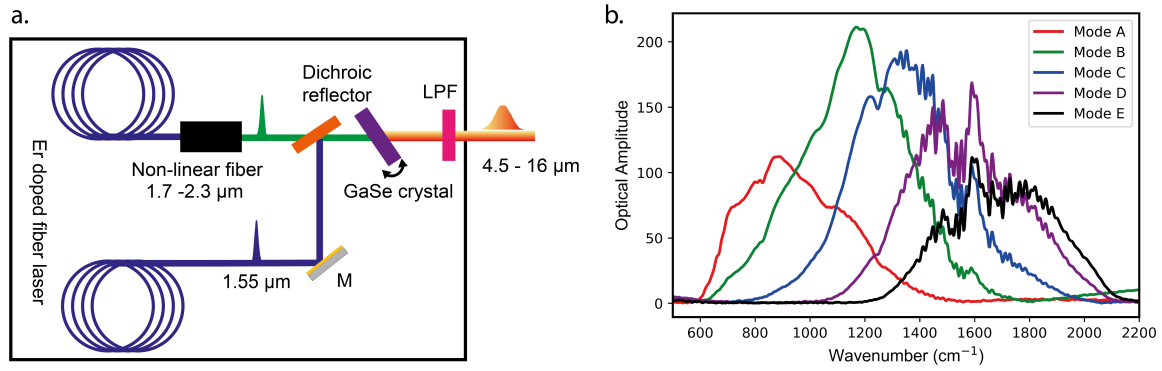

Figure 3.5: Setup and output spectra of the nano-FTIR laser. (a) Layout of the nano-FTIR laser based on the difference frequency generation of two superimposed light pulses emitted from Er-doped fiber lasers at a GaSe-crystal leading to a broadband coherent MIR-radiation. **(b)** FTIR spectra of the operating modes of the nano-FTIR laser with different spectral positions.

HeNe laser:
In general, the alignment of MIR-lasers in the s-SNOM setup can be challenging due to the fact that the MIR beams cannot be seen with the naked eye and that liquid crystal detector cards commonly only function with a power of > 10 mW. Therefore, a HeNe-laser (Modell 1125P, *Lumentum*, Milipitas, United States of America) with a emission wavelength of 632.8 nm and an output power of 5 mW is utilized as an alignment laser on which the MIR lasers can be superimposed. This simplifies and accelerates the alignment process of the MIR-lasers on the s-SNOM tip as most of the rough alignment can be performed with the visible laser.

3.3.2 Reflection-mode scattering-scanning near-field microscopy

The near-field microscopy studies in this thesis are conducted on a commercial s-SNOM system (neaSCOPE, *attocube systems AG*, Haar, Germany), which is operated in reflection mode for nano-FTIR and Ps-Het measurements in chapter 5 and 6. In all imaging modes, the microscope simultaneously acquires AFM tapping-mode images containing the topography (z), mechanical amplitude (A_{Mech}), and mechanical phase (φ_{Mech}) correlated with concurrently recorded optical near-field microscopy images. The tapping amplitude is regulated by a feedback mechanism that uses a laser beam reflected off the cantilever's backside and detected by a four-quadrant photodiode. In this thesis, all experiments were conducted with PtIr-coated AFM tips (nanoFTIR-tips, *attocube systems*, Haar, Germany) with a tip apex of approx. 50 - 60 nm and a mechanical resonance frequency of $\Omega \approx 250$ kHz. The images were recorded with a tapping amplitude of around 80 nm and a mechanical set point of 80%. PID-parameters were chosen such that the maximal mechanical SNR was attained on a flat Si-reference sample achieving values of SNR $\approx$ 6000. In both Ps-Het and nano-FITR operation an asymmetric Michelson-interferometer detection scheme is employed. The whole optical setup with light sources and the different interferometer schemes are shown in Fig. 3.7. In both the nano-FTIR and Ps-Het detection schemes, the asymmetric interferometer is composed of two arms. In one of the interferometer arms, a modulated reference mirror is positioned, while the other arm contains the AFM with the parabolic mirror focusing optic. In the tip arm, p-polarized laser light is focused onto the scattering tip with a parabolic mirror (NA = 0.42) at an angle of incident of $\theta = 60^{\circ}$ as shown in Fig. 3.6. The backscattering of the tip is collected with the same parabolic mirror and recombined with the modulated reference beam at a beamsplitter made of zinc selenide (ZnSe). The recombined beam is focused with a second parabolic mirror on an one-pixel liquid nitrogen cooled MCT-detector (IR-20-00103, *Infrared Associates Inc.*, Stuart, USA) and the detector signal is demodulated at higher harmonics of the AFM-tapping frequency nΩ with n > 1. The detector has a bandwidth of > 1 MHz to enable the signal demodulation at frequencies of around 250 kHz.

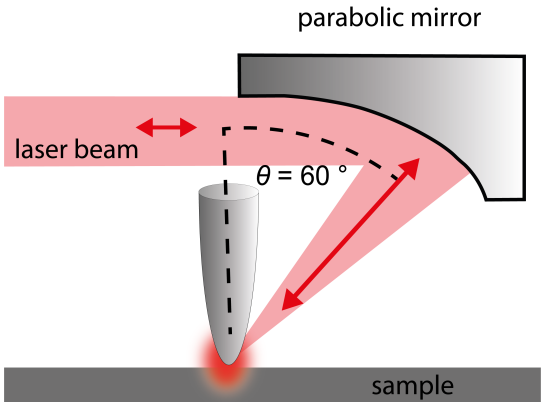

Figure 3.6: Angle of illumination of reflection-mode s-SNOM. The upper parabolic mirror focuses the laser with a angle of incident to the surface normal of $\theta = 60^{\circ}$ on the tip.

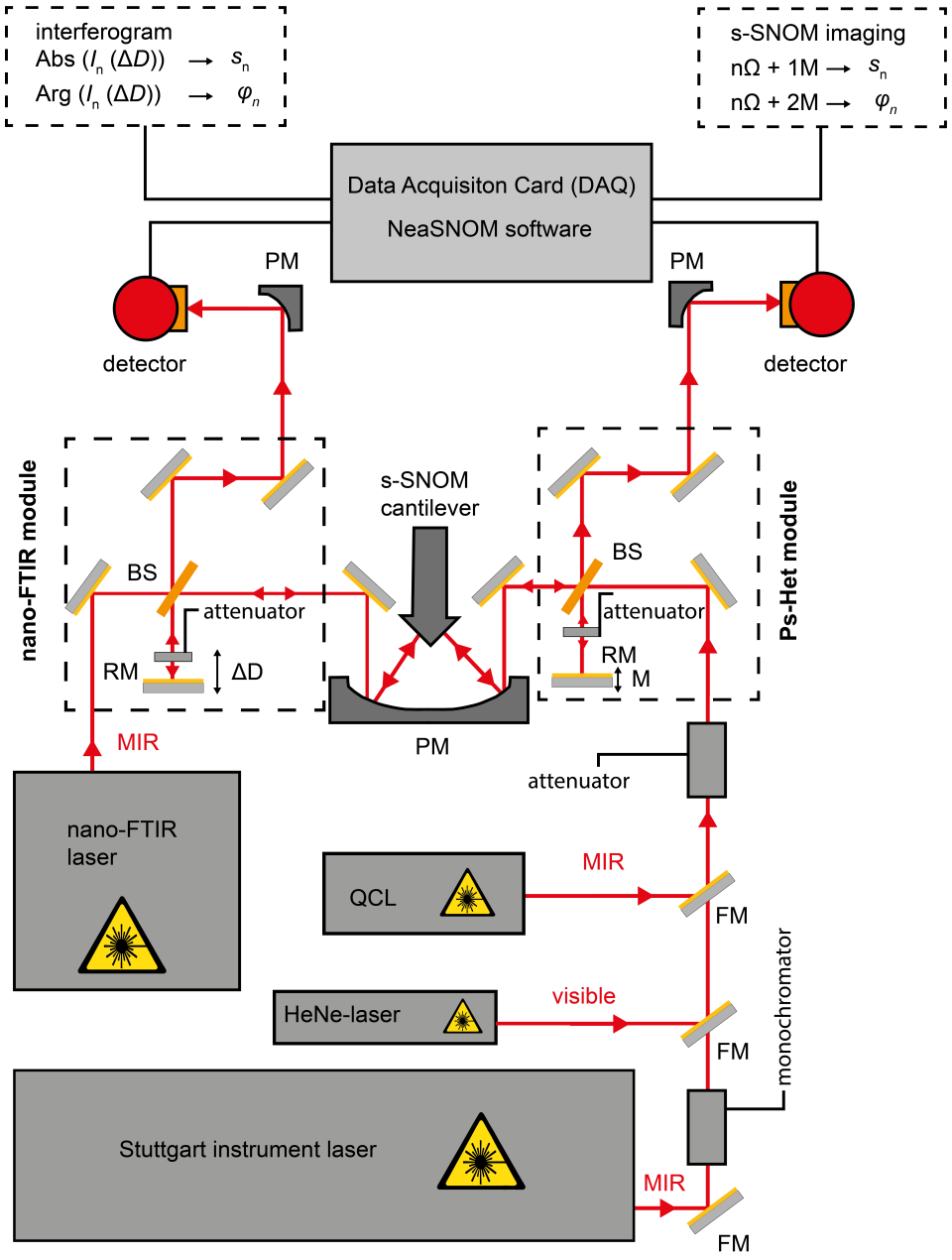

Figure 3.7: Sketch of the experimental s-SNOM setup. The setup consists of the s-SNOM setup, the data acquisition card (DAQ) electronics and three different MIR-lasers and a visible HeNe-laser for alignment purposes. The lasers can be coupled into the system by different flip mirrors (FM). All incoming laser beams can be attenuated by a series of grid attenuators placed before the entry to the microscope. In addition, single grid attenuators are placed before the reference mirrors (RM) of the interferometer arms of the nano-FTIR and Ps-Het modules to enable high power illumination of the tip without over saturating the detector with the reference beam power. The laser beam is focused onto the tip and the respective detectors with a parabolic mirror (PM). Importantly, nano-FTIR and Ps-Het can not be operated at the same time as the DAQ card and the parabolic tip focusing is limited in this setup to a single operation mode. The lock-in detection is performed by the DAQ and the NeaScan software package.

Pseudo-Heterodyne detection: For Ps-Het imaging either the QCL or the Stuttgart Instrument lasers have been employed with p-polarized output. For the Ps-Het demodulation the reference mirror is modulated with a frequency $M = 300$ Hz. If both the tip- and reference-beam are correctly spatially and temporally recombined the detector signal shows a interferogram like signal, when changing the spatial overlap position through moving the RM. When the Ps-Het modulation is activated the optical amplitude signal and SNR increases significantly

due to the interferometric gain as discussed in the chapter 2. To identify the correct vibration amplitude Δd, a so-called offset sweep is performed, which is based on a small and slow linear displacement of the reference mirror in the Ps-Het interferometer. This displacement results in a phase variation $\Delta\varphi$ and allows for the determination of Δd by observing and reducing the measured variation in the near-field amplitude s_n by adjusting Δd[36]. After this procedure a decoupled optical near-field amplitude s_n and phase φ_n image can be recorded. Importantly, the vibration amplitude Δd needs to be readjusted, if the imaging wavelength is changed.
Nano-FTIR detection: Both nano-FTIR spectra and the associated white light images were acquired with the nano-FTIR laser. For the modulation of the OPD a piezo-driven linear stage with a mirror is employed in one arm of the asymmetric Michelson interferometer and operated in closed-loop operation with a total operation distance of 800 μm. For white-light images, used to identify suitable sample regions for nano-FTIR spectroscopy, the reference mirror position is fixed at $d \approx 0$ resulting in no OPD. At this mirror position the simultaneous interference of all spectral components is maximal and the highest optical amplitude s_n can be detected. The detected signal is the integrated signal $I_n = \int_0^\infty |\mathrm{Re}\,(\sigma_n(\omega))\,\mathrm{d}\omega|$ of the complex scattering signal at a given frequency ω over the whole spectroscopic range weighted by the spectral responsivity of the whole setup and laser source[37]. As discussed in chapter 2 and in analogy to classic FTIR-spectroscopy, the recorded nano-FTIR spectrum of a sample is normalized to a reference spectrum recorded on clean Si- or Au-surface. The constant response of the reference sample yields the spectral characteristics of the setup including the responsivity of the detector, emission properties of the laser source and transmission characteristics of the beamsplitter as well as atmospheric absorption of the air and can be used to eliminate these contributions from the sample spectrum. The normalization procedure is shown explanatory for a nano-FTIR spectrum recorded on a PMMA thin film normalized to a Si-reference spectrum displayed in Fig. 3.8. The normalized PMMA spectra clearly show that the normalized optical phase $\varphi_{2,\mathrm{norm}}$ is analogous to a recorded ATR-FTIR spectrum of PMMA and relates to the MIR absorption of the sample under the tip. On the other hand, the optical amplitude $s_{2,\mathrm{norm}}$ relates to the reflectivity of the sample.

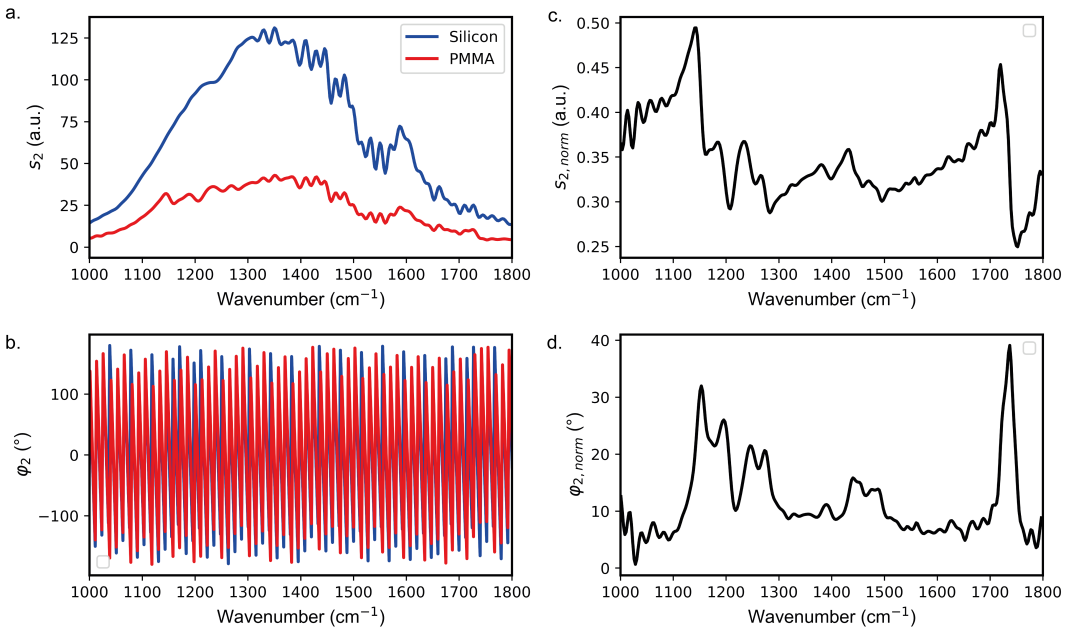

Figure 3.8: Normalization of nano-FTIR spectra. (a, b) Optical amplitude (s_2) and phase (φ_2) of a nano-FTIR spectrum recorded on a clean piece of Si (blue) and on a 200 nm thick film of PMMA (red). **(c, d)** Normalized amplitude ($s_{2,\mathrm{norm}}$) and phase ($\varphi_{2,\mathrm{norm}}$) spectrum of the PMMA spectrum to the Si spectrum showing distinct MIR molecular resonance of PMMA in the optical phase.

3.3.3 Transmission-mode scattering scanning near-field microscopy

Transmission-mode s-SNOM was employed only for Ps-Het imaging. The detection scheme is based on a Mach-Zehnder interferometer as shown in Fig. 3.9 providing better flexibility for the beampath in transmission mode. In the detection scheme, the incoming laser beam is split in two parts by the first beamsplitter. One part of the beam is guided through the Mach-Zehnder interferometer and gets modulated by a vibrating mirror system with frequency M. The second part of the beam gets focused by a lower parabolic mirror ($NA \approx 0.42$) on to the sample and the s-SNOM tip. In contrast to reflection-mode, the transmission-mode beam is normal on the sample and has in-plane polarization. The polarization causes the light to primarily polarize nanostructures on the investigated sample with a high in-plane polarizability and not the s-SNOM tip. However, in the next step the tip becomes polarized by the near-field of the excited nanostructures and the backscattered near-field from the tip contains primarily information on the out of plane near-field component E_z above the sample.

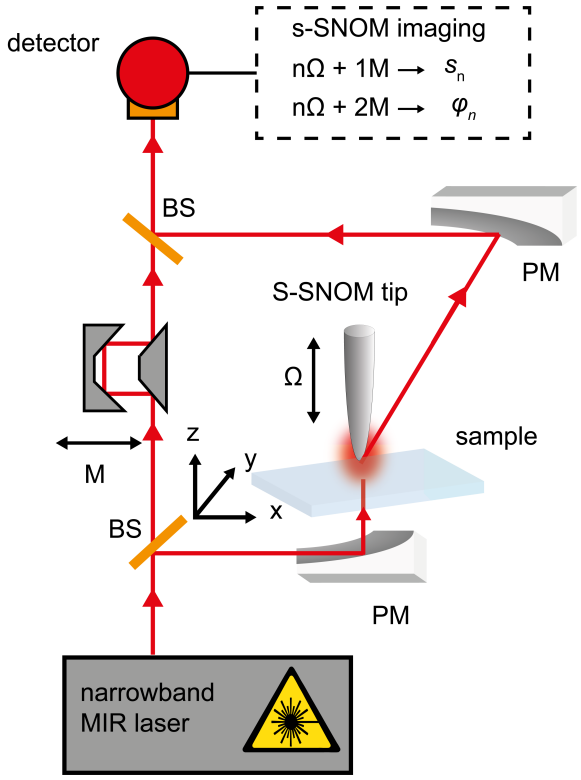

Figure 3.9: Transmission s-SNOM setup. The setup is based on two parabolic mirrors (PM) with the bottom PM illuminating first the sample and then the tip with a focused beam. The second parabolic mirror collimates the backscattering of the s-SNOM tip as in reflection s-SNOM. The interferometer scheme follows a Mach-Zehnder-interferometer scheme with two beamsplitter (BS), which enables a flexible guiding of the reference and tip beam in order to achieve a transmission illumination. As in classical reflection-mode Ps-Het the reference beam is modulated by a vibrating mirror system with a frequency M.

The backscattered tip field from the polarized tip is collimated by the upper parabolic mirror and superimposed with the reference beam on the second beamsplitter of the Mach-Zehnder interferometer and detected by a MCT-detector. In general, transmission-mode s-SNOM can be even more challenging to align than reflection-mode s-SNOM. Therefore, it is advantageous to first align the upper parabolic mirror to attain a high near-field signal and then fix the upper parabolic mirror to ensure optimal placement of the upper optics. Subsequently, the optical setup is switched to transmission-mode illumination and the HeNe-laser is utilized for the first rough alignment. The VIS laser is aligned with the lower parabolic mirror to achieve

a tightly focused symmetrically expanding laser spot when the z-position of the mirror is displaced. Finally, the setup can be switched to a MIR-laser and the final fine alignment of the lower parabolic mirror and the Ps-Het detection scheme can be performed.

3.3.4 Scattering scanning near-field microscopy of liquid samples

Liquid s-SNOM measurements in the context of this work are based on a recently introduced ultra-thin membrane separation layer method[48]. The central idea of the method is to separate the AFM-tip from the liquid compartment by the SiN membrane layer ensuring that the delicate AFM and infrared optic do not get contaminated and damaged by the liquid sample. In the experiments, a 250 μm x 250 μm size and 10 nm thin SiN membrane (NX5025Z, *Norcada*, Edmonton, Canada) suspended in the middle of a Si-chip is employed as displayed in Fig. 3.11a. For increased wettability of the hydrophobic SiN surface a 45 min UV-Ozone cleaning procedure is conducted by irradiating the cavity side of the SiN membrane with UV radiation with a commercial UV-Ozone cleaner (UV/Ozone ProCleaner, *BioForce Nanosciences*, Ames, United States). Directly after the procedure the membrane is mounted onto an aluminum holder by using two sided scotch tape as shown in the assembly sketch in Fig. 3.10. Next, the sample is deposited on the membrane cavity side by drop casting around 20 μl of liquid sample into the sample holder cavity and turning the holder upside down. The sample is incubated for 30 min and the sample deposition on the membrane can be checked depending on the sample by the overview microscope of the s-SNOM. Finally, the unsealed bottom side used for drop casting the liquid sample is closed and sealed by a glass cover slide with a tiny amount of grease. Then the sample can be placed in the microscope and used for hour long measurements without the danger of water evaporating and destroying the sample or the tip.

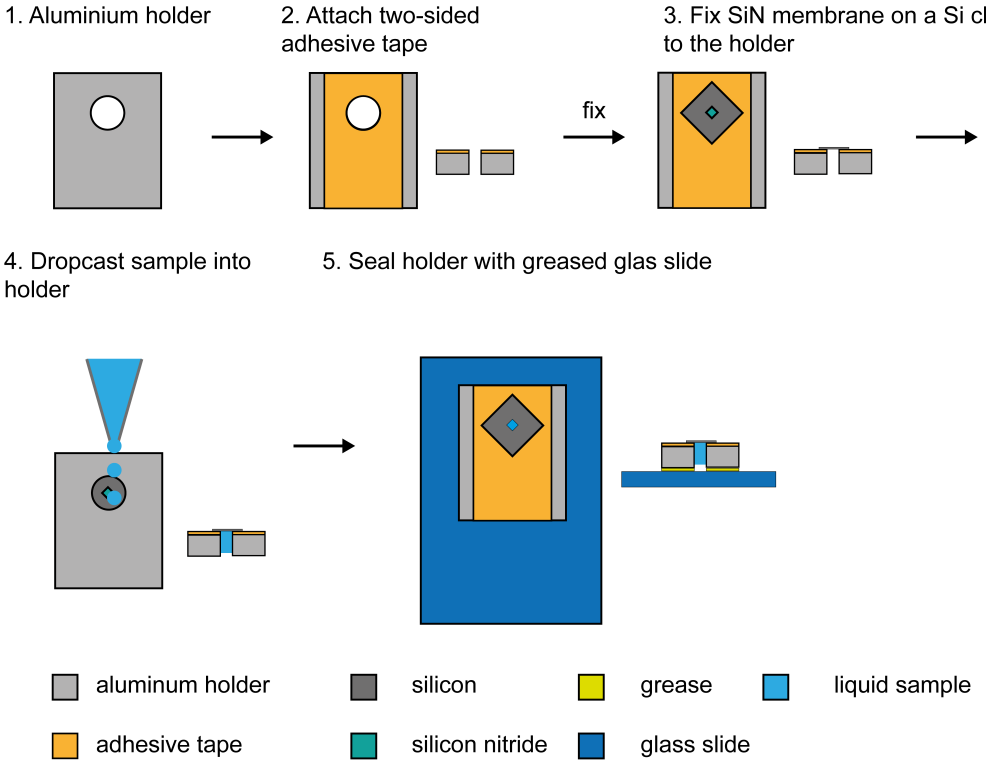

Figure 3.10: Assembly of the drop casting liquid cell. The materials are highlighted by different colors and assigned by labels below the assembly guide. In the end of the process the liquid cell is filled with a sample and sealed such that the liquid does not evaporate and hour long stable measurements are possible.

For conducting near-field microscopy measurements on the membrane it is recommended to first proceed with a scan encompassing both Si chip and SiN membrane as shown in Fig. 3.11b. If the water and sample adhesion was successful, a typical ratio between the silicon edge signal and the water signal below the SiN membrane of 4:1 should be detected as displayed in Fig. 3.11c. As the next step, a big overview scan of 40 x 40 μm should be conducted to identify suitable samples for a high resolution close up scan. Mechanical instabilities and artefacts in the AFM measurements on the liquid sample can be overcome by tuning the PID-parameters of the AFM and the tapping amplitude[49].

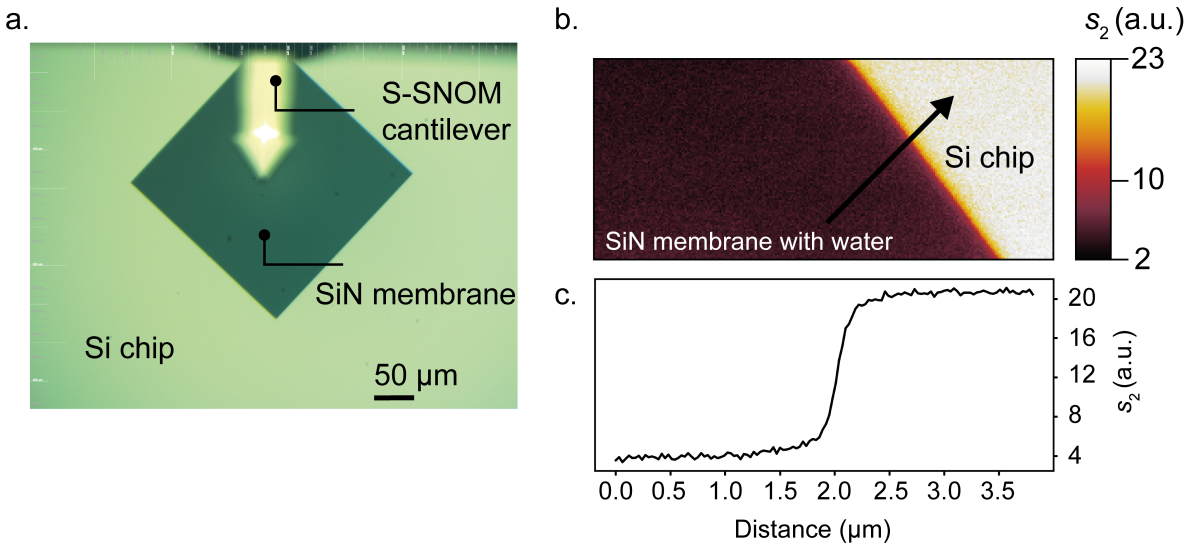

Figure 3.11: Liquid s-SNOM membrane measurement technique. (a) Optical microscopy image of the s-SNOM cantilever on top of the SiN membrane suspended on the Si frame and filled with water underneath. **(b)** White light s-SNOM image (s_2) showing the wetted SiN membrane and the Si edge. **(c)** Optical amplitude (s_2) contrast recorded on a line comprising the wetted SiN membrane and the Si edge highlighted by the black arrow in **(b)** equivalent to a 1:4 signal contrast between the membrane and the Si edge.

3.4 Sample preparation

3.4.1 Metasurface fabrication

The metasurfaces were fabricated with standard nanofabrication techniques as illustrated in Fig. 3.12. In short, on a calcium fluoride (CaF_2) substrate a 750 nm thick amorphous silicon (a-Si) was deposited at 180°C by plasma-enhanced chemical vapor deposition (PlasmaPro 100 PECVD, *Oxford Instruments*, Oxford, United Kingdom). Subsequently, the sample was spin coated with a positive photoresist consisting of poly(methyl methacrylate) (PMMA) with a molecular weight of 950k and baked at 170°C for 2 min. Additionally, to prevent charging effects during electron beam lithography processing a second layer of conductive polymer (Espacer 300Z) was spin coated on the baked resist. The patterning was performed by electron beam lithography (eLINE Plus, *Raith GmbH*, Germany) with an acceleration voltage of 20 kV and an aperture of 15 μm. The patterned samples were developed in a solution of isopropanol alcohol (IPA) and ultrapure water with a ratio of 7:3 for 60 s. Then, a hardmask made out of 20 nm SiO_2 and 40 nm Cr was deposited with electron beam evaporation. In the next step, the lift off was performed with a remover (Microsposit remover 1165). The hard mask pattern was etched into the silicon film with reactive ion etching (PlasmaPro 100 Cobra, *Oxford Instruments*, Oxford, United Kingdom). Finally, the remaining sections of the hard

mask were removed with a Cr etch (Cr etch 210, *NB Technologies GmbH*) for the Cr layer of the hard mask and another reactive ion etching step for the SiO_2 layer resulting in pure silicon nanostrucutres on CaF_2.

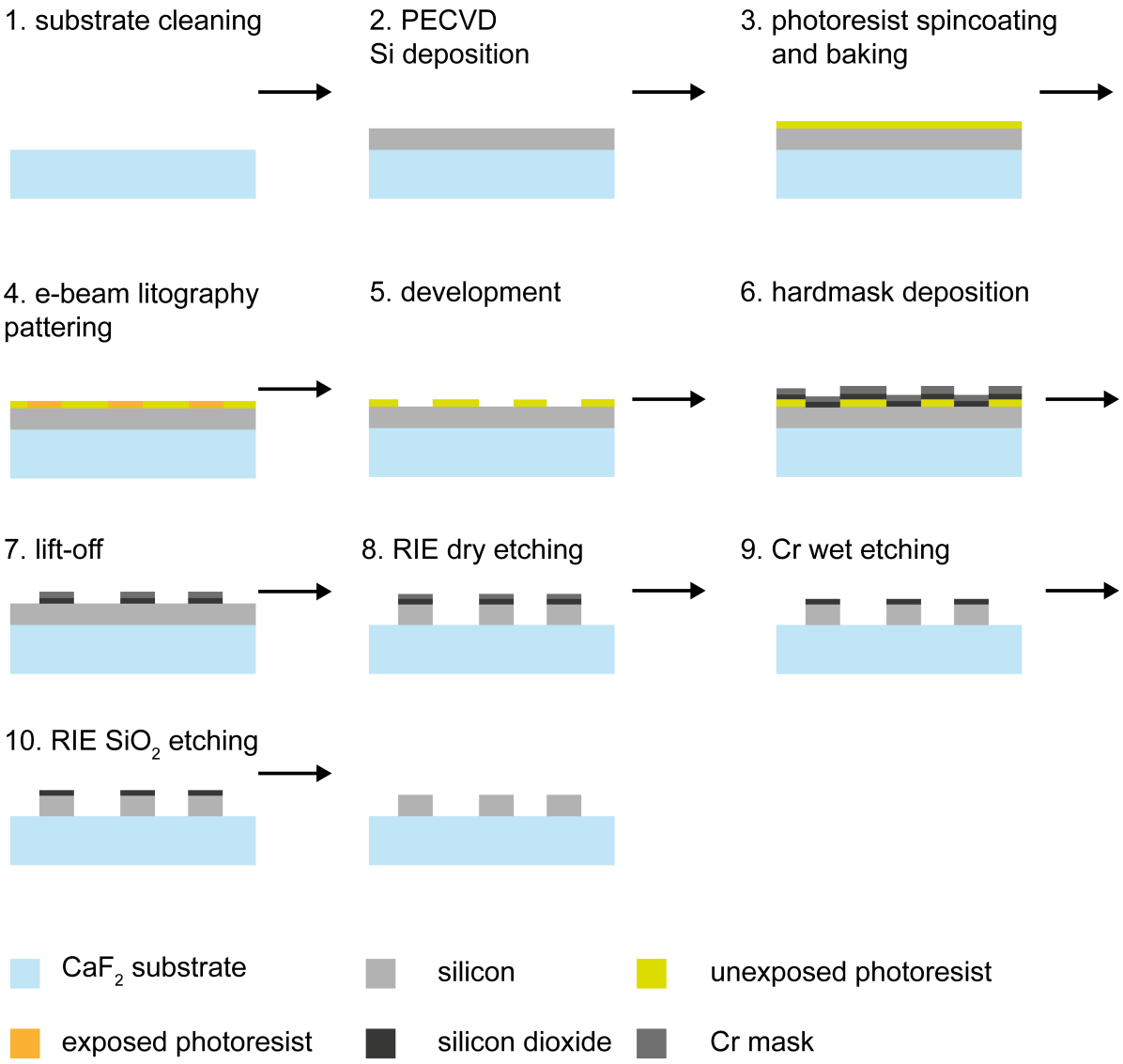

Figure 3.12: Nanofabrication process scheme. Starting of from a clean CaF_2 substrate silicon is deposited with a plasma enhanced chemical vapor deposition (PECVD) process. Next, the design is patterned in the photoresist using e-beam lithography. After the development, hard mask deposition and lift-off the pattern is etched into the silicon layer by reactive ion etching (RIE). Finally, the hard mask is removed through chromium etching and another RIE step to obtain the functional silicon metasurface.

3.4.2 Dental sample preparation

The dental sample shown in Fig. 3.13 has been prepared in the group of Prof. Ille at the Poliklinik für Zahnerhaltung und Parodontologie of the Ludwig-Maximilians Universität München. The protocol is as following and was published in the context of the work[50] detailed in chapter 5. A freshly extracted human third molar, preserved in a 0.4 % sodium azide solution at a temperature of 4°C, was selected and cleaned from adherent tissue and debris. The tooth was collected according to the routine at the dental clinic, which involves a network of dentists who collect teeth for research purposes after obtaining their patients' consent to do so and with approval of the ethics committee (No. 19-418KB). Two geometrically

similar Class I cavities, 3.5 mm x 3.5 mm x 3.5 mm, encompassing both enamel and dentin areas, were prepared in the mesial and distal aspects of the tooth, using a dental bur.
One of the two Class I cavities was then treated with a mild two-step, self-etching commercial adhesive, which will from now on be referred to as the adhesive A (Clearfill SE BOND 2, *Kuraray Co. Ltd.*, Kurashiki, Japan) consisting of a self-etching primer and a light-curing bonding agent. The primer was applied to the cavity surfaces with a disposable microbrush and left for 20 s, followed by air drying for 5 s. The adhesive was then applied while using a gentle stream of air to create an even and thin layer of adhesive. The adhesive surface was then light-cured for 20 s using an LED light-curing unit (LCU) (*Bluephase Style*, Ivoclar-Vivadent, Shaan, Lichtenstein). Finally, the cavity was filled in one increment with a low-shrinkage resin-based bulk-fill composite, hereafter referred to as composite (ORMOCER, *Admira Fusion X-tra*, Voco GmbH, Cuxhaven, Germany), and which was light-cured for 20 s with the LCU described above. The second Class I cavity was bonded with an experimental one-step self-etch adhesive, from now on referred to as the adhesive B. The adhesive was applied into the cavity for 20 s with a disposable microbrush and air dried for 5 s. The light curing of the adhesive and the restoration with the resin composite were similar to the above.
Details of the chemical composition of the adhesive A and B have been described in detail elsewhere[51]. Briefly, the commercially available adhesive consists of an acidic primer based on 10-methacryloyloxydecyl dihydrogen phosphate (MDP) and an adhesive encompassing MDP in addition to 2-hydroxyethylmethacrylate (HEMA) and dimethacrylate. There is no explicit reference to the presence of inorganic fillers in the commercial material. In contrast, the organic matrix of the experimental adhesives was a mixture of monomers, in which an experimental bisphenol A-glycidyl methacrylate (bis-GMA) monomer was used as a base monomer and triethylene glycol dimethacrylate (TEGDMA) and HEMA were used as dilution monomers. Polyacrylic acid (PAA) was added to create an acidic pH, while the inorganic filler was 7% per weight and consisted of a mixture of 6.8% zircon-hydroxyapatite and 0.2% graphene oxide – zircon oxide particles. The composite material is denominated as Ormocer (organically modified ceramic) and consists of large monomers of modified urethane dimethacrylates (UDMA)[52] with few crosslinks[53] aiming to reduce polymerization shrinkage. Therefore inorganic Si-O-Si networks based on polysiloxanes were produced using a sol-gel process and then cross-linked with polyfunctional urethane and thioether (meth) acrylate[54].
The restored tooth was kept in distilled water at a temperature of 37°C for 24 hours. The tooth and implicitly the restored cavities were subsequently cut in half, parallel to the long axis of the teeth and in mesial-distal direction, using a water-cooled, low speed diamond saw (Isomet, *Buehler*, Lake Bluff, IL, USA). The specimen, exposing the interface between tooth structure, adhesive and composite, was wet finished with a series of silicon carbide abrasive papers (1200 grit, 1500 grit, 2000 grit, 2400 grit, *LECO*, St. Joseph, MI, USA) and then polished with diamond spray (6 µm, 3 µm, 1 µm; DP-Spray, Struers GmbH, *Puch*, Austria) and textile polishing cloths (DP-Pan 200 mm, *Struers GmbH*). The sample was cleaned ultrasonically (RK 31, *Badelin Electronic*, Berlin, Germany) for 5 min after each polishing step (see Fig. 3.13 for a picture of the sample). The tooth sample was kept in distilled water until measurement to avoid dehydration and associated artifacts (microcracks, shrinkage). Before the measurements, the sample was placed in a desiccator with silica gel and evacuated to evaporate any remaining water, which could interfere with the measurements. The drying process was performed gently over several hours and no drying artefacts as such as microcracks could be observed in any of the microscopes.

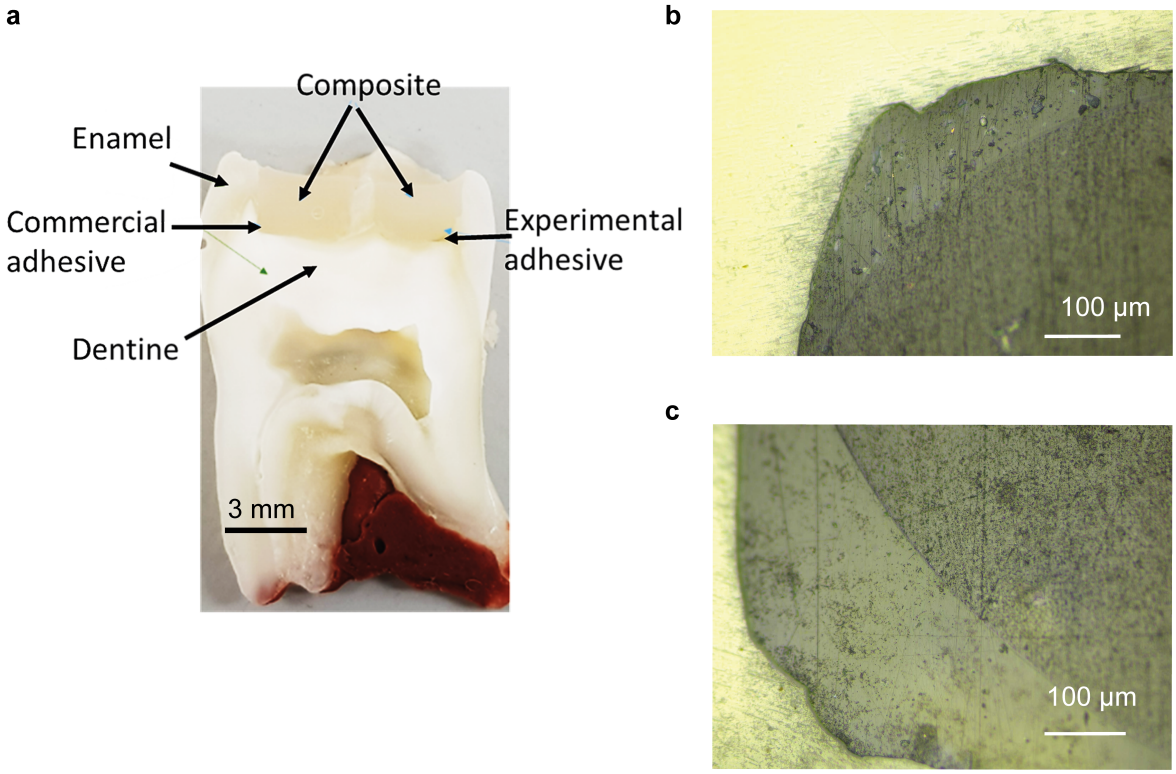

Figure 3.13: Photo and microscopy images of the investigated dental sample. (a) Image of the investigated tooth cross section with different sections labeled. Optical microscopy of **(b)** the experimental adhesive and **(c)** the commercial adhesive. Figure taken from [50]

3.4.3 Photoswitchable liposomes preparation

The photoswitchable azo-PC liposomes of a heterogeneous range from around 100 nm to several micrometers of diameters were prepared according to a published protocol[55,56]. The liposomes were made by a gentle hydration of a lipid film and a subsequent liposome electroformation facilitated by an alternating electric field process[57] using a commercial vesicle prep pro device (*Nanion Technologies*, Munich, Germany). The process is based on the swelling of rehydrated lipid films due to the alternating electric field on the indium tin oxide (ITO) substrate surface and the resulting detachment of the lipid bilayer from the surface in liposomes[57] as shown in schematically in Fig. 3.14. The method has been employed due to its ease and high yield of liposomes with photoswitchable lipids. In the device two conductive glass substrates, which are coated by an conductive ITO layer, were separated by an O-ring making a sandwich-constructed chamber. The lipids composing the liposomes (50% DOPC (*Merck*, Darmstadt, Germany), and 50% azo-PC) were dissolved in chloroform with a concentration of 10 nM each. From the solution 20 μL were dropcasted on the conductive side of the ITO substrate within the O-Ring area. The evaporation of the chloroform solvent leads to a stackwise lipid bilayer formation on the ITO substrate. After the chloroform solution evaporated, the chamber space within the O-ring was filled with pre-heated 250 μL of a sucrose solution with an concentration of 300 mM. The sugar solution increases the stability of the liposomes due to higher osmolarity. Subsequently, electroformation was performed with an electric field (5 Hz, 3 V) at 37°C for 120 min. This protocol has proven to deliver the highest yields of liposomes[56]. Afterwards the liposomes are stored in a fridge at 4°C and could be used for several days. For s-SNOM investigation the liposomes are dropcasted in the liquid cell and incubated for 30 min before conducting measurements.

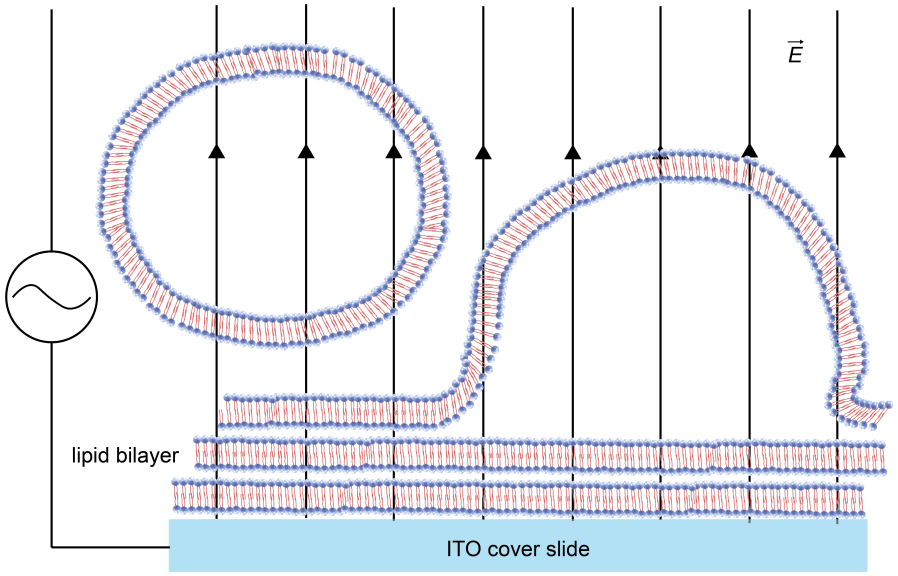

Figure 3.14: Liposome electroformation process. Stacked lipid bilayers, formed by drying a lipid solution, are rehydrated in a sucrose solution. Upon applying an alternating electric field, the lipid bilayers detach from the cover slide surface and form liposomes.

4

Near-field microscopic investigation of quasi-BIC metasurfaces

4.1 Introduction to quasi-BIC metasurfaces

The confinement of light within subwavelength volumes by nanostructures is not only utilized in s-SNOM for nanoscale imaging and spectroscopy but is a fundamental goal in photonics as it drastically enhances light-matter interactions. A pivotal platform technology in photonics for the confinement of light are optical metasurfaces comprising two-dimensional arrays of nanostructured elements with dimensions smaller than the wavelength of light. Metasurfaces excel in finely tuning the interaction of light with matter over a subwavelength thickness through the precise design of the subwavelength resonators[59–61]. The optical interaction is based on the scattering of light from the subwavelength resonators leading to structures resonantly interacting with light and being able to define phase, polarization, wavefront and spectrum of the light after the interaction with the metasurface with unprecedented accuracy[62]. This fact contrasts metasurfaces from classic optical lenses that are based on the refraction of propagating light and are much bulkier as well as challenging to miniaturise and

can contain less functionalities. The increased light-matter interactions possible with metasurfaces unlock unique applications in diverse fields such as lasing[63,64], nonlinear optics[65–67], structural color generation[68,69], quantum optics[70,71], ultrasensitive biosensing[72,73], compact and efficient spatial light modulators[74], enhanced chiral sensing[75–80] and photocatalysis[81,82].
In the beginning metasurfaces were based on plasmonic nanoantennas with strong subwavelength light confinement. However, these metasurfaces were limited in performance and efficiency through high ohmic losses. As a result optical metasurfaces based on dielectric materials such as silicon in the MIR-range and TiO_2 in the VIS-range exhibiting Mie-type resonances emerged as an alternative as they do not exhibit material losses in the respective ranges. In particular, all-dielectric metasurfaces supporting photonic bound states in the continuum (BICs) are a promising new metasurface platform for the precise engineering of strong light-matter interactions[61,78,83–85]. Due to the geometry of the subwavelength resonators, BICs are "dark states" that cannot couple to the far-field due to the suppression of radiative losses via destructive interference of the leaky modes. Therefore, BICs have an infinite quality factor (Q factor, defined as the resonance wavelength divided by the line width). Small perturbations to the resonators can transform these "dark" BIC modes into quasi-BIC states, resulting in very high but finite Q factors that are accessible from the far field[84]. For nanophotonic resonators in metasurfaces, the class of symmetry protected BICs is particularly advantageous as the breaking of the symmetry can be introduced in the manufacturing process through precisely engineered geometrical asymmetries in the resonator structures[83]. This concept gives rise to all-dielectric metasurfaces with high and easily controllable quality factors leading to high near-field enhancements[83]. Moreover, the spectral position of the metasurface resonances exhibits flexible tunability across a broad frequency spectrum, facilitated by the scaling of the resonator dimensions, while control over the Q factor's adjustability is achieved through the precise tuning of resonator asymmetry parameters[86].
However, to date, almost all studies on quasi-BIC metasurfaces rely on investigating quasi-BICs via far-field spectroscopy techniques[66]. While providing valuable insights, such approaches offer only limited information on the mode properties of metasurfaces. In comparison, investigations into the near-field characteristics of the collective quasi-BIC mode, important for a fundamental understanding of photonic modes and pivotal for numerous applications such as biosensing or catalysis[82], remain notably sparse. Crucial properties concerning the minimum array size for complete mode formation, the directionality of the coupling between unit cells, and the effect of the edge of a metasurface and defects on the mode formation are still not well understood.
The recent study by Dong *et al.*[87] represents a noteworthy step forward, as they succeeded in mapping the near-field distribution of an all-dielectric BIC metasurface by using electron energy loss spectroscopy (EELS) and cathodoluminescence (CL) based on a transmission electron microscope (TEM). In this study they showed that they could differentiate a "dark" true-BIC from a quasi-BIC through comparison of CL and EELS measurements. However, the practical applicability of EELS and CL for near-field mapping of individual resonators and arrays of resonators is limited due to the high cost and intricate operation procedures of TEM equipment, as well as the necessity to fabricate the metasurfaces on ultra-thin membranes with thicknesses of only around 30 nm. Furthermore, investigations based on EELS and CL cannot resolve the optical phase and are constrained in fully describing the out-of-plane electric field of such structures, consequently omitting crucial information integral to the complete characterization of collective mode properties.
In order to overcome these limitations, we leverage s-SNOM[11,33] as an alternative state-of-the-art method for the characterization of the near-field properties of photonic quasi-BIC

metasurfaces. This approach enables spatial resolution dictated solely by the tip radius[38], thus surpassing the limitations imposed by the diffraction limit. The demodulation and interferometric detection of the backscattered light allows the retrieval of both the optical amplitude and phase of the sample's near-field together with the correlated topography of the sample surface[11]. Notably, the method can be utilized for wavelengths ranging from the UV-VIS[17], near-infrared range[88], MIR range[89]and terahertz-range[90,91], since both the parabolic mirror used for focusing light onto the tip and the lightning rod effect that results in near-field confinement at the tip apex are wavelength independent[43]. The technique has been widely applied for the investigation of the near-field response of single[92–95] and arrays[88,89,96] of plasmonic and dielectric resonators. Moreover, a related technique called double near-field microscopy has already been applied in the terahertz range to investigate quasi-BIC mode properties, which shows the potential of this technique for optimizing terahertz metasurfaces[97,98]. In contrast to the limitations faced by EELS, s-SNOM does not require the metasurface to be fabricated on nanometer-thin membranes. Instead, it enables the non-destructive study of plasmonic, or dielectric samples fabricated in a configuration where it can be directly employed for on-chip applications.

In this chapter, the capability of s-SNOM imaging is augmented with an algorithmic image processing technique that extracts the experimentally recorded optical near-field phase of individual resonators, an observable which is in principle independent of the laser power used. Subsequently, the method compares the experimental data with the phase obtained from numerical simulations to assess the strength of the non-local quasi-BIC mode at the individual resonator level. Through this approach, we unravel the finite array effect of quasi-BIC mode formation. Notably, our investigations reveal that a minimum size of a 10 x 10-unit cell array is sufficient for the complete formation of the quasi-BIC mode, a number significantly smaller than what our far- field measurements on the same metasurface indicate.

Furthermore, we investigate the directional coupling effects in quasi-BIC resonators chains and show that the coupling strength between individual resonators is much stronger in the direction of electric field polarization. In addition, we experimentally verify that isolated single defects of missing resonator unit cells exert only minor effects on both the far-field response and the near-field enhancement. In contrast, we find that larger defects, exemplified by 3 x 3 missing unit cell configuration have a substantial impact on the far-field response and lead to a directional attenuation of surrounding resonator near-fields.

Moreover, from an experimental standpoint, especially important for applications such as biosensing or catalysis, it is crucial to understand how the quasi-BIC-mode decays towards the array edges, where extended periodicity in all in-plane directions is not given. Our near-field measurement could experimentally capture the decay, unveiling a noticeable quenching of the BIC mode up to 7-unit cells distant from the array border. Our findings underscore that there is a notable discrepancy between the observed far-field response and the now easily accessible near-field response of quasi-BIC metasurfaces. We believe that this study underscores the capabilities of s-SNOM for investigating optical metasurfaces and serves as a starting point for deepening our fundamental understanding of the quasi-BIC mode. Beyond the fundamental understanding our findings bear significant practical implications for optimizing the spatial footprint and increasing the active metasurface area to enhance the performance for applications such as catalysis[82], thermal emission[99] or lasing[100,101].

4.2 Experimental setup for the near-field investigation of quasi-BIC metasurfaces

To demonstrate the efficacy of our approach for accurately imaging and assessing the mode formation, we analyze a widely used BIC-driven metasurface geometry composed of pairs of tilted ellipses[102] fabricated on a CaF_2 substrate, which is lossless in the investigate MIR-range and does not noticeably distort the transmission measurements (Fig. 4.1a, b, c). Based on previous reports[86], we chose a tilting angle α of 20° which provides high far-field modulations while maintaining a comparably high Q factor of more than 80 in experiments (Fig. 4.1d). The spectral line width can be tuned by changing the tilting angle α and the spectral position is modified by uniformly scaling the in-plane dimensions of the unit cell. Based on this metasurface concept, we study the effects of finite array sizes (Fig. 4.1e), the directional coupling of the resonators (Fig. 4.1f), edge effects (Fig. 4.1g) and structural defects (Fig. 4.1h) in the near-field, facilitated by a transmission mode s-SNOM setup using a pseudo-heterodyne detection scheme (Fig. 4.1i, j)[36,94]. The investigated quasi-BIC mode is highly dispersive and shifts spectrally, when the angle of incident of the light is changed[44,103].

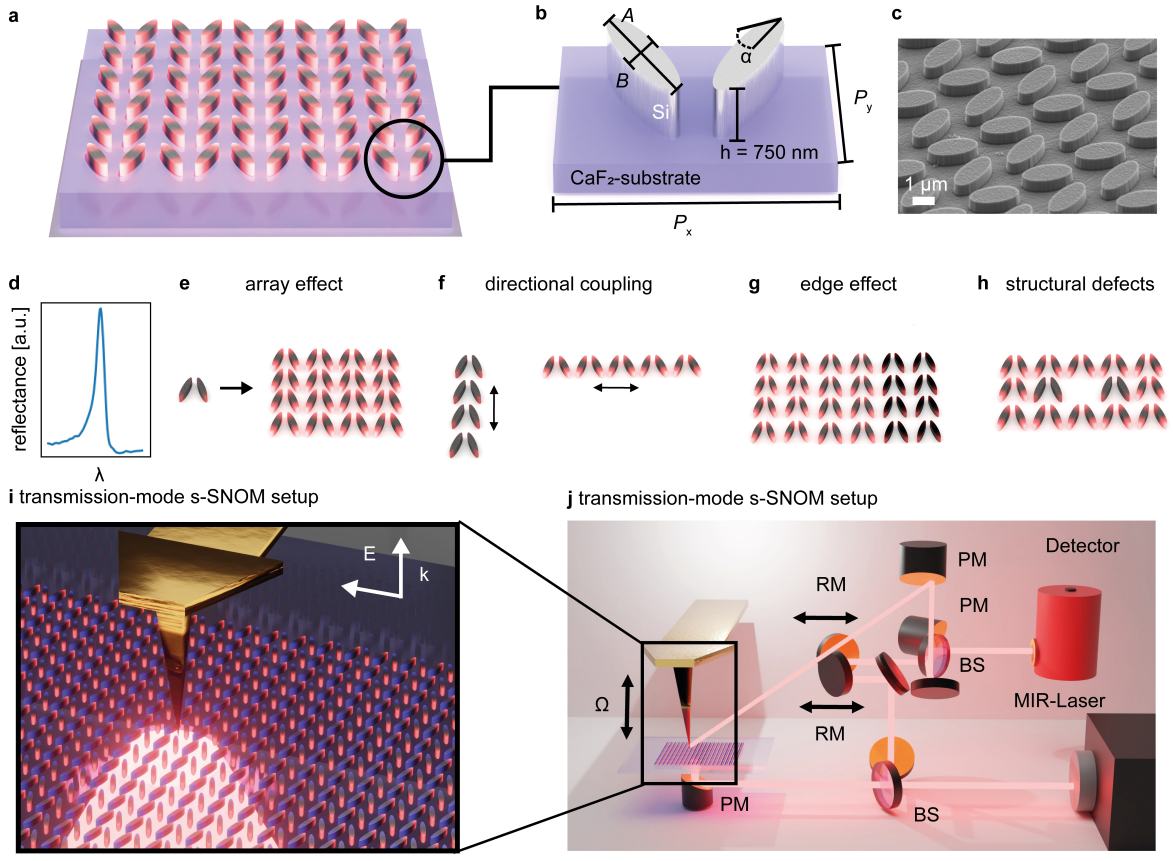

Figure 4.1: Quasi-BIC metasurface design and transmission s-SNOM setup for metasurface imaging. **(a)** Conceptual image of an all-dielectric quasi-BIC metasurface composed of pairs of tilted elliptical resonators. **(b)** A single unit cell showing a pair of tilted ellipses (α = 20°) made of silicon on a CaF_2 substrate. The structure is defined by the ellipses' long axis A and the short axis B and the pitch in x-direction P_x and in y-direction P_y. **(c)** SEM image of the fabricated metasurface. **(d)** Far-field reflection spectrum of a quasi-BIC metasurface resonance taken on **(c)**. Schematics showing an overview of the studied properties in quasi-BIC metasurfaces: **(e)** finite array size, **(f)** directional coupling, **(g)** edge effects and **(h)** structural defects. **(i, j)** Transmission mode s-SNOM working with a Mach-Zehnder interferometric beam path. The metasurface is illuminated from below with a parabolic mirror (PM) and with a polarization perpendicular to the ellipses' long axis.

To circumvent the resonance attenuation caused by this effect, the metasurface is excited with a normal-incident plane wave achieved through loosely focusing the laser beam with a parabolic mirror positioned below the sample. In principle, the s-SNOM technique should also work for quasi-BIC metasurfaces imaging in reflection with an angle of incident as long as the angular spread of the illumination is narrow[44]. In addition, the transmission mode configuration further minimizes tip-resonator coupling effects as the light polarization is perpendicular to the tip shaft[94]. Thus, the tip functions as a passive element which only scatters the metasurface near-fields with minimal perturbation to the quasi-BIC resonance. In order to achieve a high SNR and minimize unwanted background far-field signal, we analyzed the third order demodulated optical amplitude (s_3) and phase (φ_3) of the pseudo-heterodyne near-field signal. This demodulation order does not contain far-field background signal on the resonator as can be shown from the optical deproach curve signal[36] taken on the tip of a resonator, which does not show any far-field oscillations (Fig. 4.2e, f). In general, the recorded near-field signal is the weighted averaged of the resonator over the laser spectrum of the MIR laser, which, in our case, is around 10 cm^{-1} and can be flexibly tuned to the resonance peak position. If a higher spectral resolution is needed in future works for the study of BICs with higher Q factors a quantum cascade laser could be used with a spectral resolution of approximately 1 cm^{-1}. Notably, the recorded s-SNOM signal from the resonators closely mirrors the amplitude and phase of the axial electric field E_z on top of the resonator, as attested by the excellent agreement between the numerically simulated field $|E_z|$ and phase $\varphi(E_z)$ (Fig. 4.2a, b) and the recorded near-field optical amplitude (s_3) and phase images (φ_3) (Fig. 4.2c, d).[94] Particularly noteworthy is the characteristic quadrupole pattern in the experimental near-field phase, induced by the non-parallel opposing dipoles within resonator pairs that signifies the formation of a quasi-BIC mode.

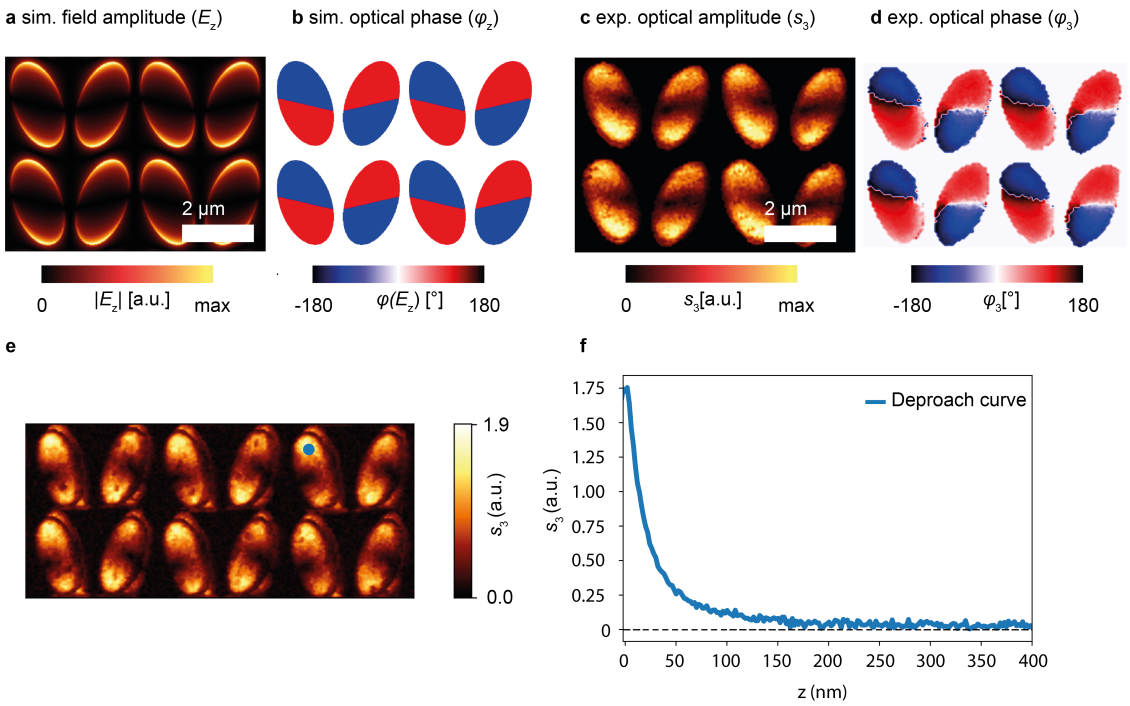

Figure 4.2: Numerical simulation and near-field measurement of the optical response of quasi-BIC resonators and an associated near-field deproach curve. **(a)** Numerically simulated optical near-field amplitude $|E_z|$ and **(b)** phase $\varphi(E_z)$ of the axial electric field of a quasi-BIC metasurface unit cell. **(c)** The corresponding experimentally measured demodulated (n = 3) optical near-field amplitude (s_3) and **(d)** near-field phase images (φ_3) of 30 × 30 array of resonators. **(e)** Optical amplitude image s_3 taken at the center of a quasi-BIC metasurface with the position of recorded near-field deporach curve marked by a blue point. **(f)** Deproach curve showing a steep drop off of the optical amplitude s_3 with increasing distance of the tip to the resonator.

4.3 Near-field image processing for single resonator quasi-BIC mode quantification

In order to quantify the collective quasi-BIC mode, it is important that the chosen approach remains independent of the excitation laser power. Thus, the laser-power dependent near-field amplitude s_3 is inadequate for the comparative analysis of the near-field signals across different structures and samples, as a potential normalization process of the optical amplitude for each measurement is error prone and time-consuming. To overcome this constraint, we introduce a method that is based on the experimentally measured near-field phase φ_3 as a more reliable observable for comparisons between measurements on different structures, since it should, in principle, remain invariant regardless of the power utilized. Therefore, we introduce a new FOM, which describes the behavior exhibited by the collective BIC mode and is named by us *BIC mode purity parameter B*. It is a measure of how closely the measured demodulated near-field phase resembles the ideal case of a quadrupole phase pattern, where for each unit cell, two opposing dipoles form in each individual resonator. This is expressed by the following equation, where N denotes the number of resonators, B_{sim} is a normalization factor extracted from the numerical simulations and F_{k} consist of surface integrals.

$$B = \frac{1}{NB_{\mathrm{sim}}} \sum_{\mathrm{k}=1}^{\mathrm{N}} [1 - F_{\mathrm{k}}] \in [0, 1] \tag{4.1}$$

The surface integrals can be expressed by the following equation:

$$F_{\mathrm{k}} = F_{\mathrm{k}}^{+} + F_{\mathrm{k}}^{-} = \frac{1}{\pi A_{\mathrm{k}}^{+}} \int_0^{A_{\mathrm{k}}^{+}} \mathrm{d}A' \left| \varphi_{\mathrm{k,exp}}(A') - \frac{\pi}{2} \right| + \frac{1}{\pi A_{\mathrm{k}}^{-}} \int_0^{A_{\mathrm{k}}^{-}} \mathrm{d}A' \left| \varphi_{\mathrm{k,exp}}(A') + \frac{\pi}{2} \right| \tag{4.2}$$

The two integrals calculate the difference between the measured near-field phase and the ideal phase pattern, where the phase on the top surface of the resonator is shifted by 180° compared to the bottom surface. A_{k}^{+} and A_{k}^{-} are the top and bottom surfaces of each resonator respectively. To take into account the results yielded by numerical simulations, which do not exactly follow this pattern, the score is divided by a normalization factor B_{sim}, which was obtained by comparing the simulations to the case of perfect opposing dipoles. For all cases, our structures yield around $B_{\mathrm{sim}} \approx 0.9$. If this score was applied to other structures with differing asymmetry, this normalization value would, of course, have to be adjusted. In the case of s-SNOM images, the recorded optical phase would be pixelated, which changes the above-mentioned integrals to summations and allows to redefine the equation. Considering an unit cell pitch of $P_{\mathrm{x}}P_{\mathrm{y}}$ and assuming the first resonator has a top surface with a near-field phase of +90° the above expression transforms to the following equation:

$$B = \frac{1}{NB_{\mathrm{sim}}} \sum_{\mathrm{k}=1}^{\mathrm{N}} \left[1 - \frac{2}{\pi P_{\mathrm{x}} P_{\mathrm{y}}} \sum_{\mathrm{x}=0}^{P_{\mathrm{x}}} \sum_{\mathrm{y}=0}^{P_{\mathrm{y}}/2} \left| \varphi_{\mathrm{k,exp}}(\mathrm{x}, \mathrm{y}) - (-1)^{\mathrm{k}-1} \frac{\pi}{2} \right| \right.$$
$$\left. - \frac{2}{\pi P_{\mathrm{x}} P_{\mathrm{y}}} \sum_{\mathrm{x}=0}^{P_{\mathrm{x}}} \sum_{\mathrm{y}=P_{\mathrm{y}}/2}^{P_{\mathrm{y}}} \left| \varphi_{\mathrm{k,exp}}(\mathrm{x}, \mathrm{y}) + (-1)^{\mathrm{k}-1} \frac{\pi}{2} \right| \right] \tag{4.3}$$

This expression can be directly applied for image processing purposes into external software such as Python or Matlab. In practice, this formula sums up the difference between experimental near-field phase and ideal case at each pixel, then sums all pixels up and calculates the average value. The sums need to remain separated, since the resonator is, as before, split into two halves, with one $(-1)^{(k-1)}$ and $(-1)^{(k)}$ capture the behavior of the alternating sign of the near-field phase between resonator pairs. In other words, if one resonator has a top surface of +90°, the other has, in an ideal case, a top surface of +90°. To account for phase offsets, which occur naturally during the measurements due to the interferometer drift, a phase delay can be chosen in such a way as to maximize the mode purity parameter B. This not only yields a higher sensitivity for the FOM, but also allows for adding the evaluated offset to experimental images of the near-field phase, making them appear visually closer to a quadrupole pattern. The error for the *mode purity parameter B* are determined by computing *B* for each individual resonator and calculating the standard deviation for *N* resonators in the following way:

$$\sigma = \sqrt{\frac{1}{N}\sum_{k=1}^{N}(B_k - B_{average})^2} \tag{4.4}$$

Given that s-SNOM is based on an AFM platform, it allows the correlative recording of both optical and topographical data, which makes it possible to isolate the optical phase of the resonators from the background. In our method, we first use the recorded topography Z (Fig. 4.3a, b) to extract the individual resonators. This involves choosing a threshold value $Z_{threshold}$ ($Z_{threshold} = 0.95 Z_{max}$ in our case) and setting all values below the threshold to 0 to separate the resonator surfaces from the surrounding topographic dataset, effectively isolating the resonators. This refined dataset can then be leveraged in combination with a *k-means* clustering algorithm[104], a widely employed method in image processing and data analysis across diverse research areas such as biology[105], in order to separate and identify each individual resonator (Fig. 4.3c, d) and generate a grid based on the unit cell dimensions of the metasurface (Fig. 4.3e). The execution of the unit cell clustering and subsequent grid generation was done in a straightforward way using Python. The modules used to achieve this are “sklearn.cluster” and “sklearn.preprocessing”. The ellipse fitting was conducted using the module “cv2”.

In the next step, we superimposed the grid onto the recorded near-field optical phase images (Fig. 4.3f). We then quantify how closely the measured phase of each resonator matches the numerically simulated near-field phase of the axial electric field $\varphi(E_z)$ by computing a surface integral of the difference between experimental recording and the numerical simulation over the entire resonator surface as outlined above. For the recorded pixelated image, this corresponds to subtracting the measured and numerically simulated near-field phase at each pixel and obtaining a map that shows how closely (φ_3) resembles the ideal phase of opposing dipoles (Fig. 4.3g, h). This computed score can then be averaged for each resonator pair, yielding a comprehensive map of the entire image revealing regions with a strong or weak quasi-BIC mode formation (Fig. 4.3i). We denote this FOM *BIC mode purity parameter* (*B*), which, by definition, ranges from 0 to 1 and describes the extent to which the near-field phase pattern mirrors the ideal quasi-BIC phase pattern derived from numerical simulations. In the upcoming sections, we will show that this parameter can provide additional critical information only obtained through near-field measurements on quasi-BIC mode properties.

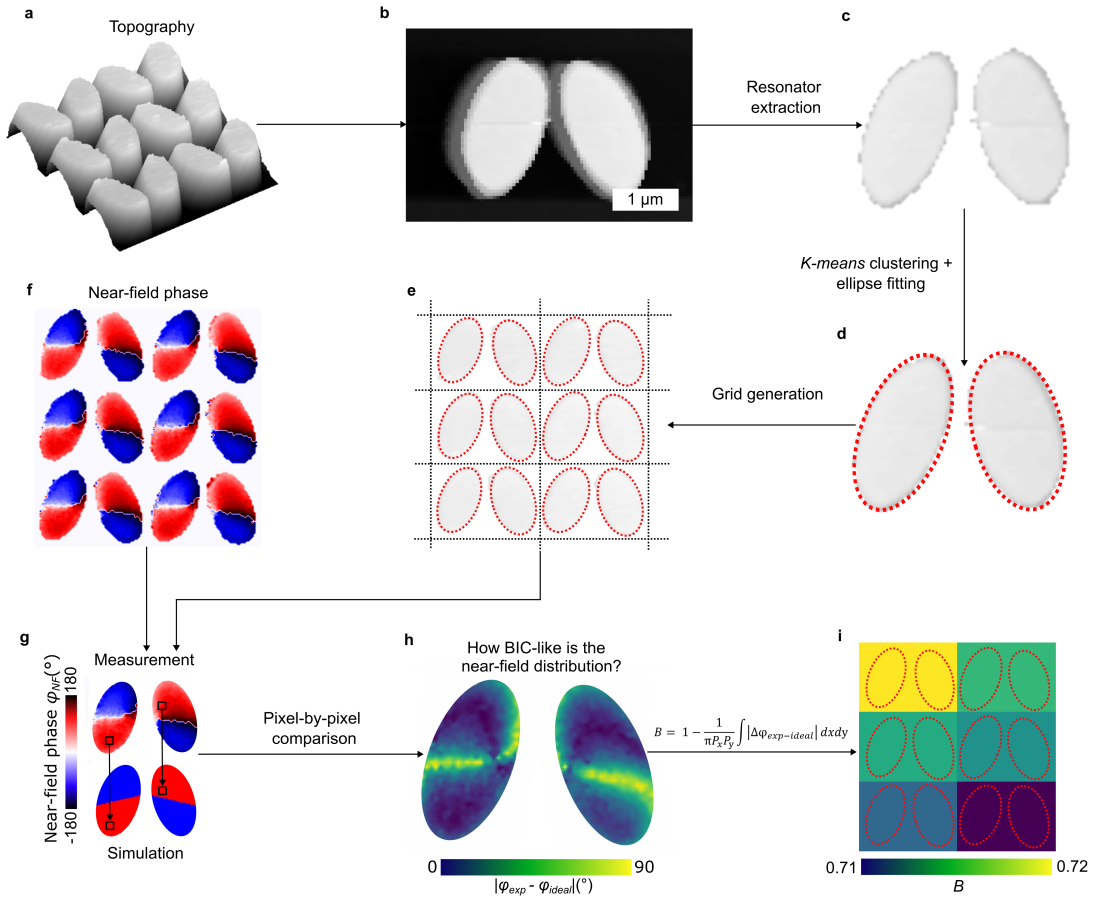

Figure 4.3: Image processing method for the determination of the *BIC mode purity parameter B*. **(a)** Recorded topography Zon a section of a 20 x 20 array of tilted ellipse resonators. **(b)** Topography of an individual unit cell. **(c)** Resonator pair extracted from **(b)** by setting an arbitrarily chosen threshold $Z_{\text{threshold}}$ for the height Z-value (here $Z_{\text{threshold}} = 0.95Z_{\text{max}}$). **(d)** Individual resonators are isolated by applying a clustering algorithm (*k-means*) and ellipses are fitted to each resonator. **(e)** A grid is generated based on the fitted ellipses in order to create a bounding box for each unit cell. **(f)** Correlated near-field optical phase image φ_3 recorded simultaneously to **(a)**. **(g)** Comparison between measured near-field phase φ_3 of an individual unit cell extracted via the procedure described in **(b-e)** and numerically simulated near-field phase. **(h)** Pixel-by-pixel subtraction of experimental data and simulation. **(i)** Calculation of the *BIC mode purity parameter B*, which can be described as an integral over the entire resonator surface, containing the difference of experimental and simulated near-field phase. The parameter A denotes the area of a unit cell.

4.4 Finding the minimal array size for the quasi-BIC mode formation

The first property we investigated with this newly introduced method of analysis is the impact of finite array sizes on the formation of the collective BIC mode. As fabricated metasurfaces are limited to finite array size, which perturbs the BIC mode and consequently lowers the achievable Q factor and field enhancement[66]. Although previous simulation and experimental far-field studies have been conducted on finite array size effects of quasi-mode formation[66,106–108], a critical gap exists in the experimental exploration of the near-field behaviours of finite quasi-BIC arrays essential for example for catalytic applications. For this study, we fabricated arrays of N x N-unit cells ranging from 1 x 1 to 30 x 30 (see optical microscopy images in Fig. 4.4a, b and SEM picture in Fig. 4.5a, b, c and d) and first measured each array with a far-field QCL-IR microscope (see chapter 3). The employed

microscope utilizes wide-field illumination, a method ideally suited for exciting quasi-BIC resonances in metasurfaces. This approach ensures uniform illumination across the entire metasurface, with minimal variation in excitation intensity and illumination angle. The maximum reflectance image and spectra of these arrays (Fig. 4.4c, d) display a continuous increase in peak reflectance with the expansion of the array size N. Furthermore, the quality factor of the quasi-BIC resonance deduced from the reflectance spectra (Fig. 4.4e) steadily increases with N reaching a quality factor of around 85 for a 30 x 30 array size. Noteworthy is the challenge in characterizing array field sizes smaller than 10 x 10-unit cells with standard far-field IR microscopes, as the signal cannot be reliably distinguished from background noise.

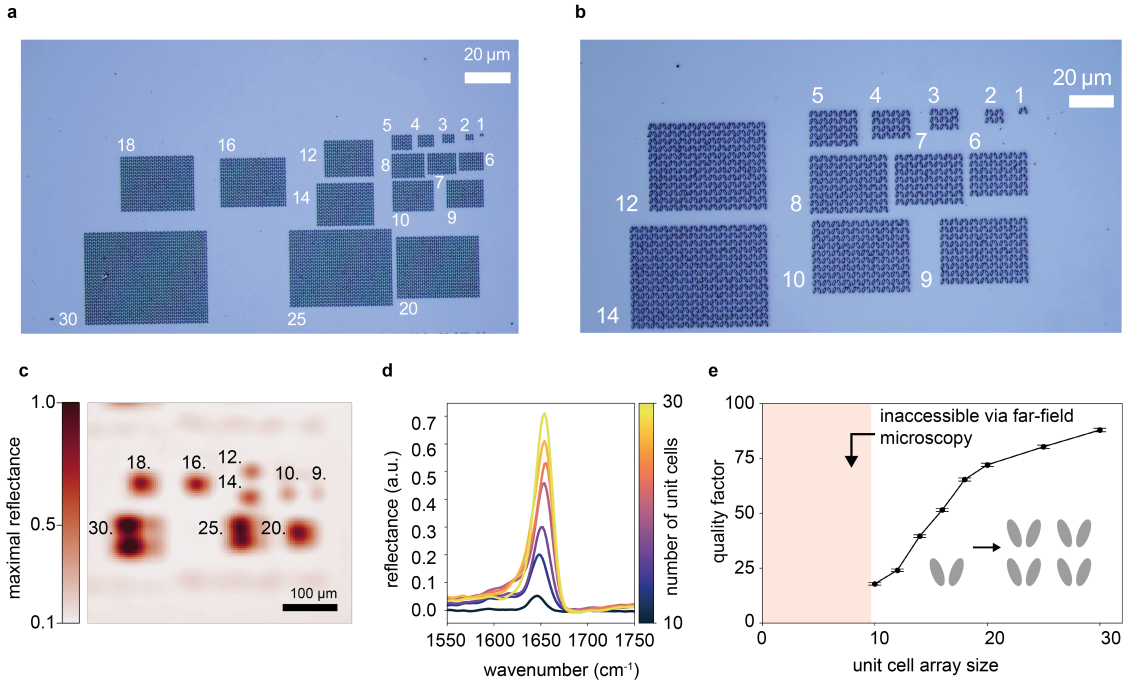

Figure 4.4: Far-field investigation of the finite array size effect in quasi-BIC metasurfaces. Optical microscopy overview image **(a)** and close-up image **(b)** of the finite array size effect sample. The associated array size number n x n is placed next to the different metasurfaces. **(c)** Peak reflectance image of different array sizes ranging from 8 to 30-unit cells. **(d)** Reflectance spectra of the different sized arrays. **(e)** Plot of the extracted quality factors from the spectra in **(d)**.

In contrast, the near-field images of the same arrays recorded at the center of each array (shown as red squares in Fig. 4.5a, b, c, d) and the derived *BIC mode purity B* (Fig. 4.5e) show different behavior of the collective quasi-BIC mode. The calculated *B*-Score equals $B = 0.18$ for a single unit cell and exhibits a rapid increase with each successive addition of unit cells to around $B = 0.55$ for a 5 x 5 array field. This increase underscores that every unit cell addition strengthens the quasi-BIC mode. Strikingly, after N > 10, the *B*-Score saturates between 0.65 and 0.75 and does not increase substantially even when the array size is increased. This trend shows that the quasi-BIC mode is already fully formed at an array size of approximately 10 x 10 resonators, a significantly smaller scale than implied by our far-field measurements. We attribute the mismatch between the observed full formation of the quasi-BIC mode on individual resonator level for N = 10 and the increase in far-field reflectance and quality factor with increasing N > 10 to a higher directionality of the transmitted or reflected light towards the microscopy objective[107–110]. The discrepancy between the ideal *B*-score of 1.0 and the experimentally observed saturated score of 0.65 to 0.75 can be caused by several factors, such as fabrication inhomogeneities[111] and minor asymmetries in bottom illumination of the metasurface by the bottom parabolic mirror[107]. Note, that the number of resonators

necessary for the full formation of the quasi-BIC mode is influenced by the Q factor of the resonances.

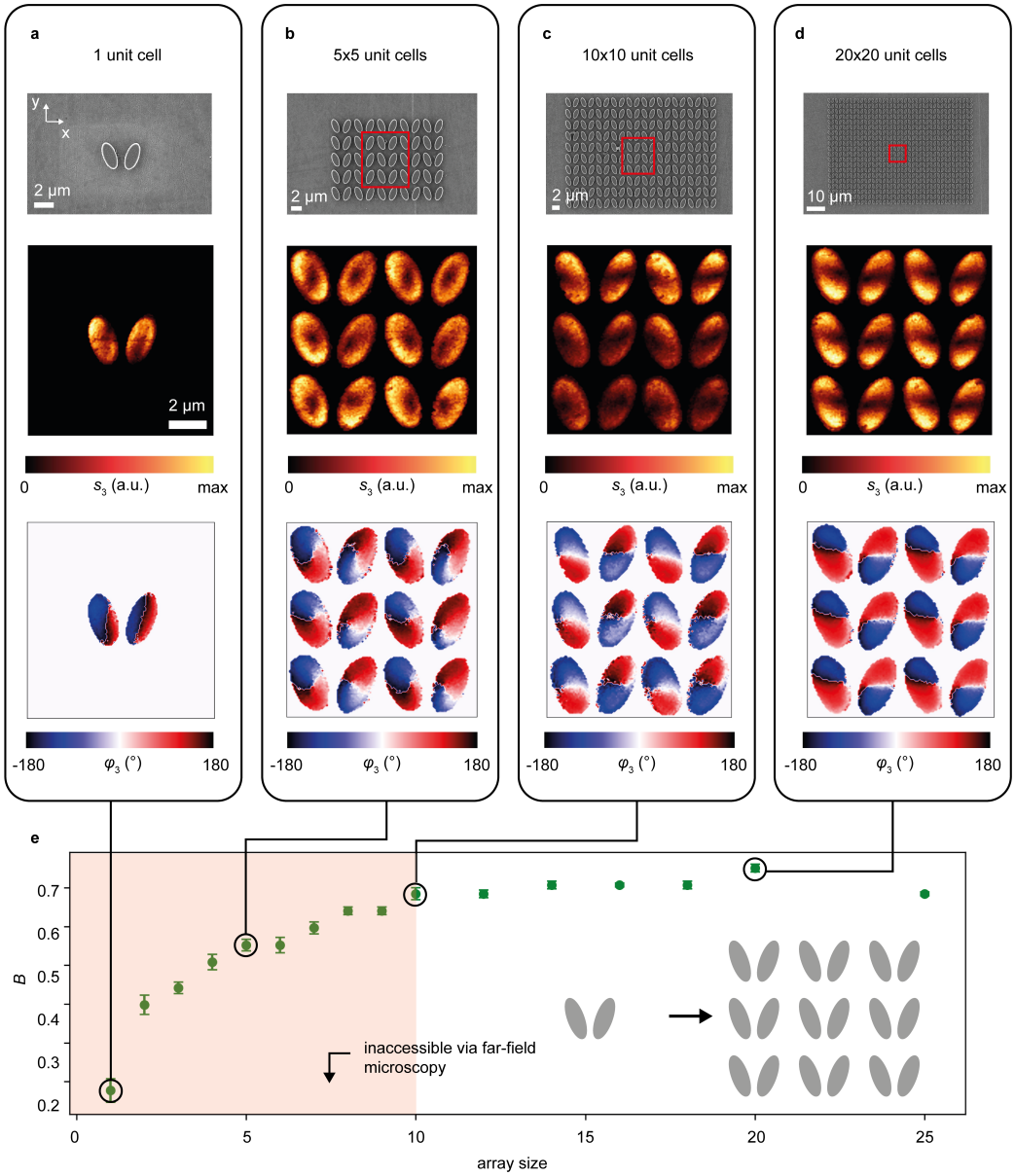

Figure 4.5: Near-field investigation of the finite array size effect in quasi-BIC metasurfaces. SEM, optical near-field amplitude (s_3) and phase images (φ_3) of different arrays with 1 **(a)**, 5 x 5 **(b)**, 10 x 10 **(c)** and 20 x 20 **(d)** unit cells recorded at the position of the red square in the SEM images. **(e)** Calculated *BIC mode purity parameter B* from the experimental near-field phase images. Error bars show the standard deviation of all B values obtained for each individual resonator in a phase image of the corresponding array size.

In order to explain the dependence of the mode formation on the radiative and non-radiative losses we use the theoretical framework proposed by K. L. Koshelev *et al.*[112] According to their model the total Q factor (Q_{tot}) can be decomposed into individual contributions by the following equation:

$$Q_{\text{tot}}^{-1} = Q_{\text{rad}}^{-1} + Q_{\text{surf}}^{-1} + Q_{\text{str}}^{-1} + Q_{\text{size}}^{-1} + Q_{\text{subs}}^{-1} + Q_{\text{abs}}^{-1} \tag{4.5}$$

including Q_{rad} for radiative coupling controlled by unit cell asymmetry, Q_{surf} for surface roughness, Q_{str} for structural disorder, Q_{size} for the finite array size, Q_{subs} for the substrate, and Q_{abs} for absorption within the resonator material as shown in the sketch in Fig. 4.6a. In

practical applications, all Q factors are finite, resulting in a reduction of the total Q factor due to each individual component.
In the context of our finite array size sweep study, we are only tuning one of these individual Q factors, namely Q_{size}. As the array size increases, we eventually converge to $Q_{\text{size}} \to \infty$, resulting in

$$Q_{\text{tot}}^{-1} = Q_{\text{rad}}^{-1} + Q_{\text{surf}}^{-1} + Q_{\text{str}}^{-1} + Q_{\text{subs}}^{-1} + Q_{\text{abs}}^{-1} \tag{4.6}$$

The other components, such as material choice affecting Q_{surf}, Q_{subs}, and Q_{abs}, or fabrication tolerances affecting Q_{surf}, and Q_{str}, remain unchanged by the array size sweep. Thus, the general concept of the array size study is applicable regardless of the specific combination of asymmetry, material choice, or fabrication tolerances.

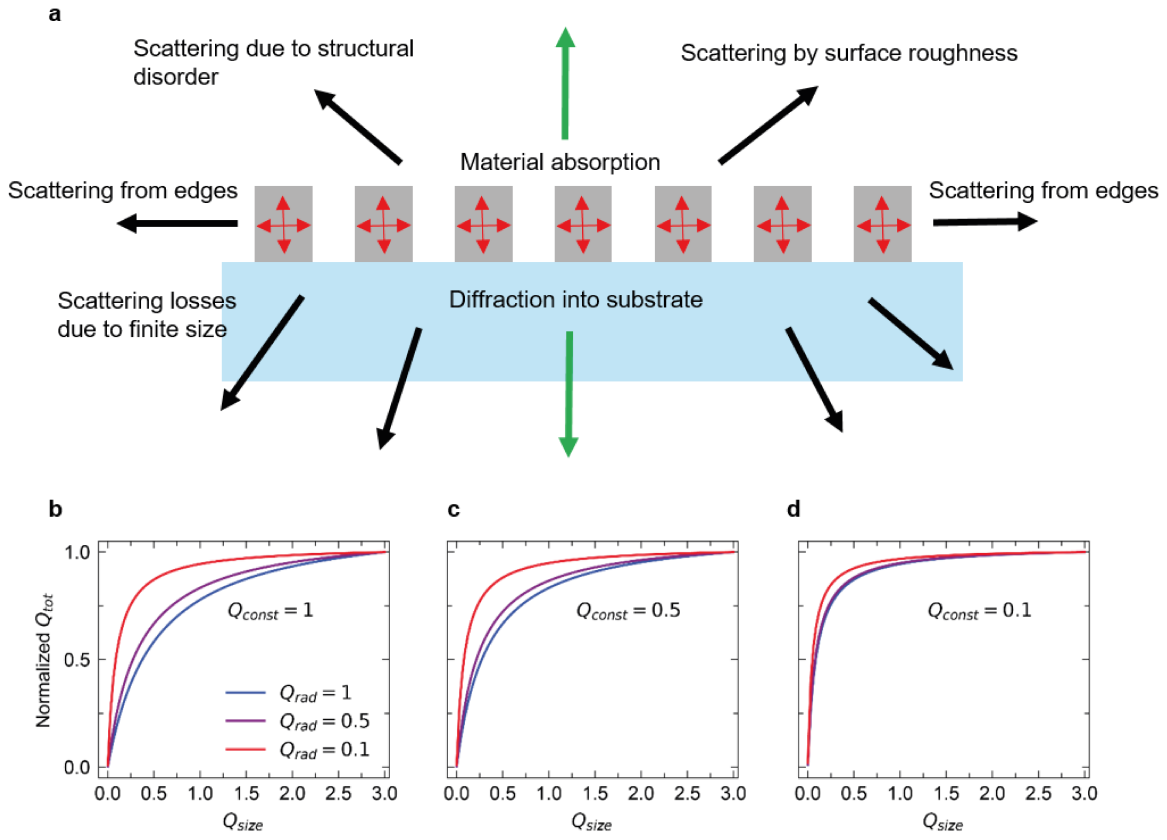

Figure 4.6: Analytical quasi-BIC array size consideration. **(a)** Sketch of different loss mechanism in quasi-BIC metasurfaces with influence on the Q factor. Analytical results for equations 4.5 using arbitrary values of Q_{rad} = 1, 0.5, and 0.1 and varied Q_{size} from 0 to 3 representing loss due to the finite array size. In **(b)** Q_{const} = 1, in **(c)** Q_{const} = 0.5, and in **(d)** Q_{const} = 0.1. For comparability, Q_{tot} is normalized to the highest value within the plotted range for each Q_{rad}. Notably Q_{rad} = 0.1 saturates first, even for small Q_{size} while Q_{rad} = 1 saturates only for high Q_{size}. This indicates that BIC metasurfaces with low Q-factors need smaller arrays than those with high Q-factors to negate the damping effect caused by the array size. Furthermore, if Q_{const} reduces from **(b)** to **(d)** by e.g. a change of the material or an increase in the surface roughness, Q_{tot} saturates for smaller Q_{size}.

Furthermore, we investigate how radiative losses like Q_{rad}, and material specific losses like Q_{abs} may change the number of unit cells needed to support the BIC mode. Fig. 4.6a shows analytical results based on equation 4.5. These results using arbitrary values, show Q_{size} varied from 0 to 3, considering three different Q_{rad} to represent different degrees of asymmetry, while keeping other losses caused by the chosen material system and fabrication technique combined in $Q_{\text{const}}^{-1} = Q_{\text{surf}}^{-1} + Q_{\text{str}}^{-1} + Q_{\text{subs}}^{-1} + Q_{\text{abs}}^{-1}$ fixed. This results in equation $Q_{\text{tot}}^{-1} = Q_{\text{rad}}^{-1} + Q_{\text{size}}^{-1} + Q_{\text{const}}^{-1}$. We find that lower Q_{rad} values lead to a faster saturation of

Q_{tot}. Similar effects should be observable in the near field. Changing the material and thus Q_{const} also effects the saturation behavior. When $Q_{constant}$ is decreased from 1 to 0.5 and 0.1 in Fig. 4.6b and c, respectively, the saturation behavior for Q_{tot} occurs at even smaller Q_{size} indicating that smaller arrays are needed if e.g. the material loss is high. Our method is ideally suited for investigating these effects, specifically the different influences of the intrinsic losses (governed by the choice of materials) and the radiative losses (determined by tuning of the asymmetry parameter) on the mode formation. Such investigations could open new opportunities for further reducing metasurface footprints and could also guide the development of new resonator geometries with improved properties. Importantly, the method could also be applicable for other array-based resonances[113], which are affected by finite size effects.

4.5 Resolving directional coupling effects in quasi-BIC metasurfaces

Our investigation of the finite array size effect on the near fields was predicated on the conventional quadratic arrangement of N x N-unit cells. Although this arrangement has until now been dominant in the literature[66,102,114,115], it is often based merely on intuition and convention. Here, we want to challenge this preconception and explore possibilities to further reduce the footprint of metasurfaces, while maintaining the quality of the quasi-BIC mode. For this purpose, we studied the quasi-BIC mode formation in metasurfaces with one long axis comprising 25-unit cells, and one short axis of N-unit cells, starting at N = 1. Thereby, we differentiate two main design cases with one case having the long axis in x-direction aligned along the polarization direction of the electric field (25 x N) and the other case having the long axis perpendicular to the x-direction and thus perpendicular to the polarization direction (N x 25). For this comparative analysis, we fabricated arrays based on unit cell dimension of 25 x N or N x 25 (Fig. 4.7a, b, c and d). A simple comparison of the 25 x 1 and 1 x 25 near-field distributions (Fig. 4.7a vs. Fig. 4.7c, phase images recorded at the position of the red square) immediately underscores a clear difference in the near-field behavior of the different design cases. Whereas the 25 x 1 array displays an emerging quasi-BIC phase pattern with B = 0.5, the 1 x 25 array does not exhibit the characteristic quadrupole phase pattern of two opposing dipoles and has a much lower score of B = 0.29. This discrepancy shows a preferred coupling direction for the 25 x N array case. The full comparison of measurements on arrays of either 25 x N, N x 25 and N x N-unit cells (Fig. 4.7e) further underlines this disparity in mode formation. The rectangular 25 x N arrays demonstrate a fully established quasi-BIC mode with a saturation score of B = 0.7 for N $\geq$ 2. In stark contrast, the second rectangular case of N x 25 shows a much slower increase of B, consistent with the collective mode behavior of the classic N x N array and attains a fully established quasi-BIC mode only for N = 10 (compare Fig. 4.5e). We attribute this strongly differing mode formation to a difference in the strength of the directional coupling of the resonator chains. The net dipole moments of the unit cells along the polarization direction can constructively interact, facilitating the formation of the BIC mode even with a singular chain of resonators in the 25 x 1 design case. Conversely, columns of unit cells perpendicular to the polarization cannot constructively interact, thereby necessitating an array size (N = 10) for quasi-BIC formation. The analogous mode formation characteristics observed between the N x N configuration and the N x 25 arrangement highlight the predominant influence of coupling along the polarization direction, while the perpendicular coupling demonstrates minimal impact on mode formation. This

trend is further corroborated by far-field measurements on the same metasurfaces (Fig. 4.7f), where 25 x N arrays achieve their maximum quality factor at N = 9, considerably earlier than the N x 25 arrays, which require N = 25 to obtain a comparable quality factor. These findings suggest that a rectangular array design featuring a substantial number of unit cells aligned along the polarization axis can exhibit a similar quasi-BIC mode quality compared to conventional square metasurfaces, albeit with considerably reduced footprint. Moreover, this directional coupling concept provides a compelling explanation for design principles governing radial BIC geometries, where lines of BIC unit cells are arranged in a circular pattern for compactness and polarization invariance[65]. This is a clear demonstration that the method allows to understand fundamental mode properties, unlocking further reductions of metasurface footprint by challenging established principles such as commonly used square metasurface designs for quasi-BIC resonators.

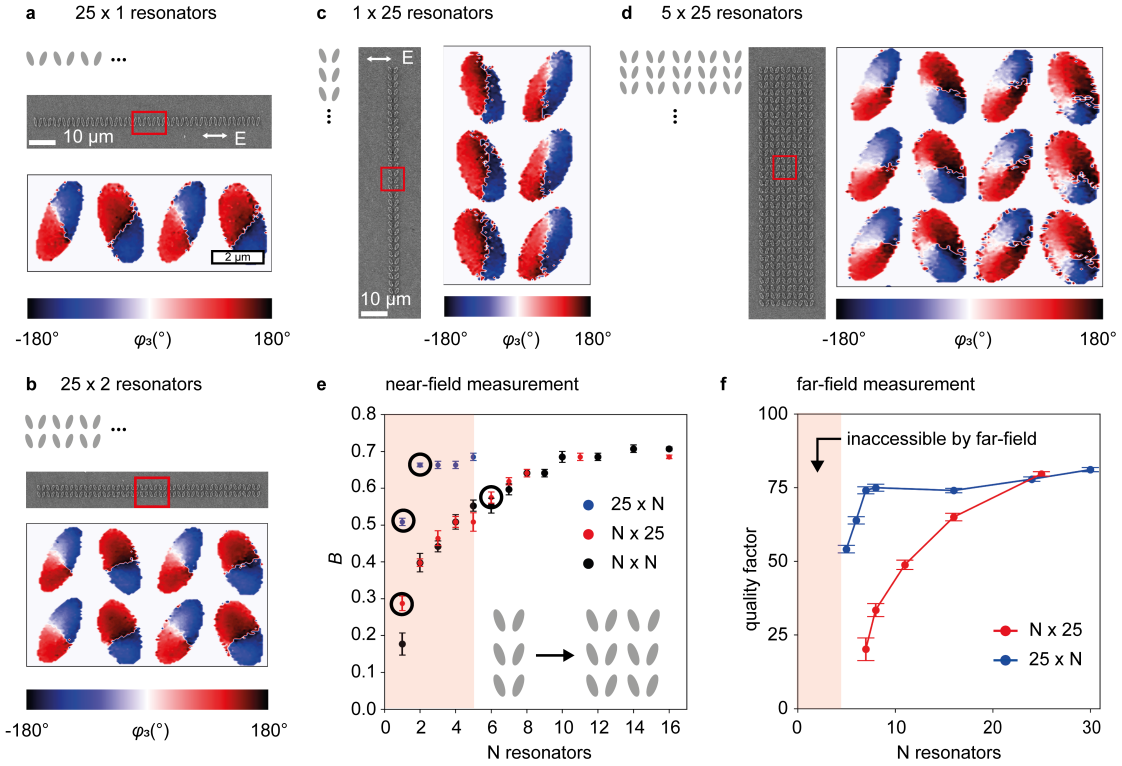

Figure 4.7: Investigation of directional coupling effects in quasi-BIC metasurfaces. **(a)** SEM and optical near-field phase images (φ_3) recorded at the position marked by the red square of **(a)** horizontal chain of 25 x 1-unit cells and **(b)** of 25 x 2-unit cells. SEM and near-field phase images of **(c)** a vertical chain of 1 x 25-unit cells and **(d)** 5 x 25-unit cells. **(e)** Extracted *BIC mode purity parameter B* from near-field phase images. **(f)** Extracted quality factors from far-field reflectance spectra of different numbers of columns and rows. The red squares marks the region, where far-field measurements are not able to differentiate the signal from background noise. Error bars show the standard deviation of all *B* values obtained for each individual resonator in a phase image of the corresponding array size.

4.6 Quantifying the near-field effects of defects in quasi-BIC metasurfaces

Besides the quenching of the quasi-BIC mode imposed by the finite array size, another attenuating effect on the quasi-BIC can be caused by lattice defects within the array. Despite their commonplace occurrence during the fabrication process, the impact of these irregularities on

neighboring unit cells remains largely unexplored. Leveraging the s-SNOM technique, we can now directly quantify the influence of such irregularities on the mode formation. For simplicity, vacancies in the form of missing unit cells were chosen as perturbations of the metasurface.

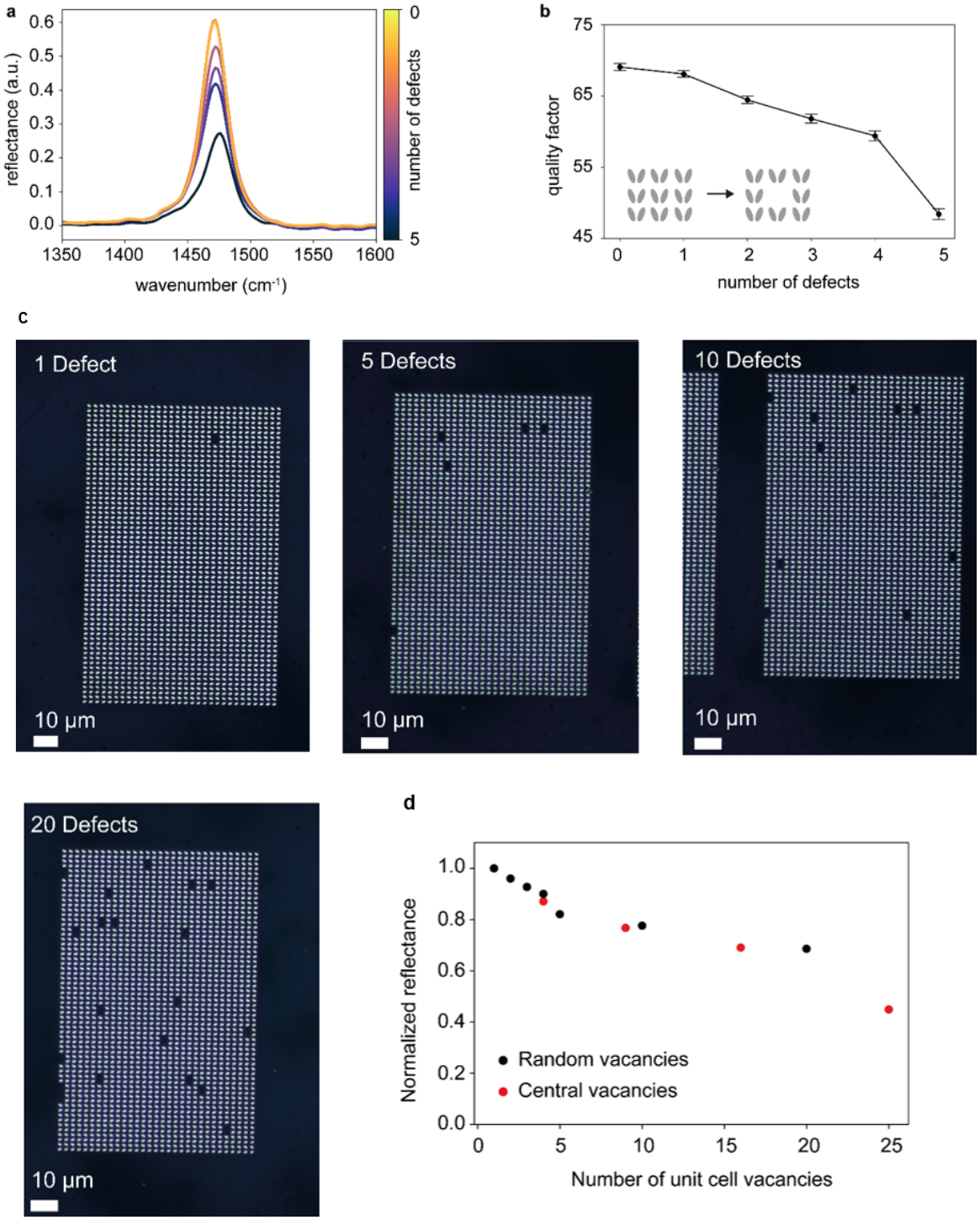

Figure 4.8: Far-field investigation of vacancy defects in quasi-BIC metasurfaces. (a) Reflectance spectra of 30 x 30-unit cell array with a central defect ranging in size from 0 to 5 x 5-unit cells. **(b)** Q factors extracted from the spectra shown in **(a)**. **(c)** 30 x 30 unit cell metasurfaces with $\alpha = 20^{\circ}$ tilting angle and with an increasing number of randomly distributed single unit cell vacancy defects. A seed ensures that arrays containing more defects also include all the defects in the same location as present in arrays with fewer defects. **(d)** Comparison of randomly distributed vacancy defects and central vacancy defects as shown in **(a)**. All spectra are normalized to the single defect case.

Various sizes of vacancies were fabricated, ranging from single-(1 x 1) up to multi-vacancies (5 x 5) in the center of a 30 x 30-unit cell metasurface array (Fig. 4.9a, d) on a different sample with slightly different tilted ellipse geometry resulting in slightly differences of Q factor and resonance position compared to samples investigated in the previous sections (Fig. 4.5 and 4.7). The resulting far-field reflectance spectra and extracted quality factors measured on these structures reveal that a solitary unit cell defect induces only marginal alterations in the far-field response (Fig. 4.8a, b), yielding a quality factor of Q = 68 compared to Q = 69 for the same structure without defects. However, the introduction of a 2 x 2-unit cell vacancy already substantially lowers the quality factor and peak reflectance of the metasurface to below Q = 65. Importantly, a similar trend in loss of peak reflectance can be measured, if the unit cell vacancy defects are randomly distributed in a 30 x 30-unit cell, as has been done for the metasurfaces in Fig. 4.8c and can be seen for the comparison of the normalized peak reflectance values for metasurfaces with random and central defects displayed in Fig. 4.8d. This behavior is also seen in the near-field images of the same structure (Fig. 4.9b, c).
In these specific measurements the near-field optical amplitude (s_3) can be directly compared for each resonator, because the optical amplitude of all resonators are recorded in the same measurement with negligible laser power fluctuation and signal drift. Importantly, the *BIC mode purity B* of the metasurface with a single unit cell defect does not decrease around the vacancy, and the near-field amplitude s_3 only shows a minimal decrease for the unit cells adjacent to the defect parallel to the polarization axis. Conversely, in the case of a 3 x 3-unit cell defect (Fig. 4.9e, f), both s_3 and B exhibit a substantial decrease at the periphery of the defect and along the polarization axis (to the right and left of the defect). In contrast, the unit cells neighboring the defect perpendicular to the polarization axis show a smaller decrease in s_3 and B. A vacancy defect disturbs the resonator coupling in both directions, but since the vertical coupling is much weaker than the horizontal coupling, the mode strength above and below the defect remains strong despite missing vertical neighbors.

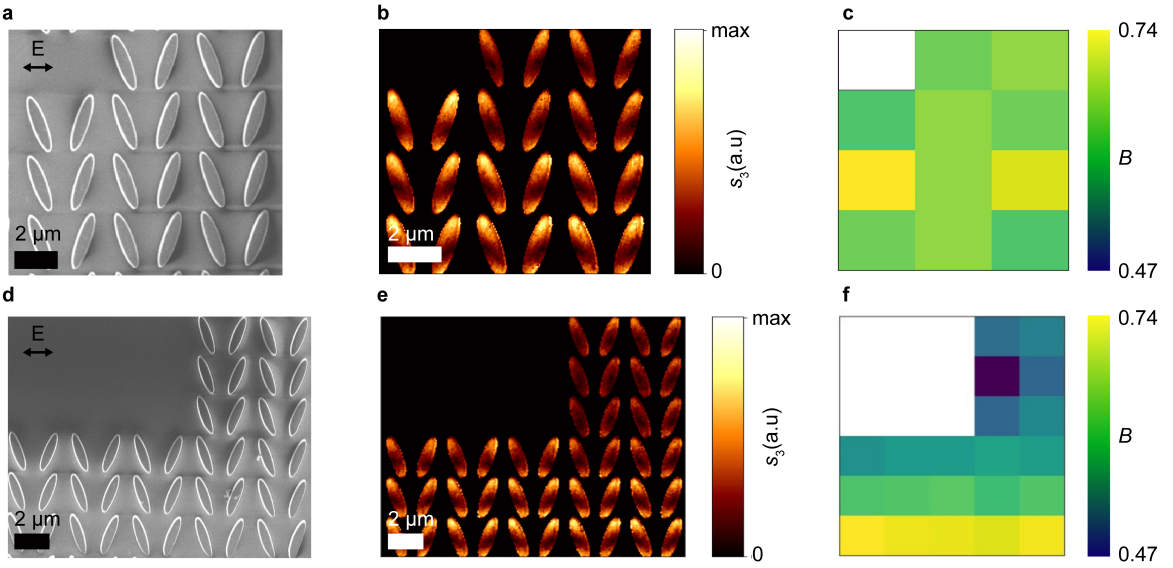

Figure 4.9: Near-field investigation of vacancy defects in quasi-BIC metasurfaces. (a) SEM, **(b)** optical near-field amplitude (s_3) and **(c)** calculated *BIC mode purity B* score of a 30 × 30-unit cell array with a central defect of 1 missing resonator pair. **(d)** SEM, **(e)** optical near-field amplitude (s_3) and **(f)** *BIC mode purity B* score of an array with 3 × 3 missing unit cell defect.

These measurements underscore the pivotal role played by unit cell neighbors horizontally aligned with the polarization axis in establishing the collective quasi-BIC mode, in contrast to their vertically aligned counterparts. Ultimately, these measurements show the tolerance of the quasi-BIC metasurfaces against single missing unit cell defects, both from a near- and a far-field perspective, which are the most common vacancies occurring during fabrication processes. However, their performance is significantly compromised in the presence of larger defects, particularly those exceeding the size of 2 x 2-unit cells. Note, that if a vacancy defect is located in close proximity to the edge of the metasurface, the defect collective quasi-BIC mode is further attenuated through overlapping defect and edge effects (Fig. 4.10). Therefore, the ellipses within 5–6-unit cells of the edge may exhibit an even lower mode purity as they would be quenched both by the edge effect and the vacancy. Similar superposition would take place, if the density of vacancy defects is simply increased in a single metasurface causing a superposition of the quenching effect of multiple defects on the neighboring resonators. In general, the presented defect studies demonstrate the value of our s-SNOM based method for the quality control of optical metasurfaces and other nanofabricated photonic structures, especially in comparison to current state-of-the-art methods such as SEM or AFM. A key advantage of s-SNOM is that it can assess the optical mode quality of the structure at the same time as recording a topographic map of the resonator fields, enabling the optics-based evaluation of fabrication discrepancies.

4.7 Near-field behavior of edge states of quasi-BIC metasurfaces

In addition to attenuation imposed by the finite array size, edge effects are another crucial factor when determining metasurface dimensions for concrete use cases. While 10 x 10-unit cells are sufficient to fully create a quasi-BIC mode, high Q factors and strong field-enhancements are only present in the very center of the metasurface. However, many technologically relevant applications, such as molecular sensing, require larger areas, where the quasi-BIC mode is fully developed, to enable the averaging of spectral signals for improved SNR[116,117].

Our s-SNOM method helps to decipher the negative effect of the edges and their penetration depth within the metasurface. To this end, we conducted scans along the polarization direction at the edge of a 30 x 30 array. The recorded optical near-field amplitude and the extracted amplitude at the top edge of the resonators (Fig. 4.10a, b) reveal that the optical amplitude begins to decrease when approaching the seven outermost unit cells at the edge of the array. Specifically, the optical amplitude undergoes a pronounced decline upon reaching the third resonator pair from the edge, culminating in near-complete attenuation upon reaching the final unit cell at the periphery. These findings agree well with EELS measurements of the edge effect conducted by Dong *et al.*[87] The near-field phase and the derived mode purity B (Fig. 4.10c, d) show a similar trend, reaching a steady-state between 5 and 6 neighbors away from the edge, complementing the near-field amplitude measurements. Moreover, we conducted measurements at the corner of a metasurface (Figure 4.11), where we find again a pronounced susceptibility of the mode at the lateral edge, in contrast to the near-fields at the upper edge, which exhibit much higher robustness of the collective mode. This observation underlines that the horizontal coupling direction plays a dominant role, similarly to what has been observed previously in Fig. 4.7.

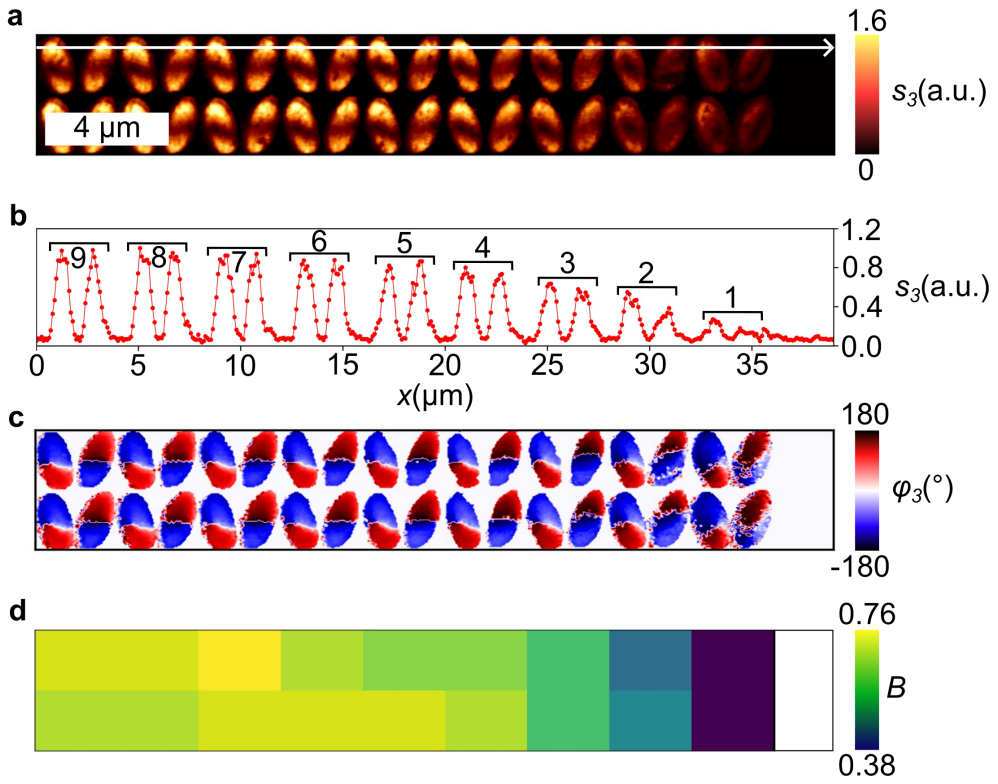

Figure 4.10: Resolving edge effects in quasi-BIC metasurfaces with near-field microscopy. (a) Optical near-field amplitude (s_3) of the horizontal edge section of a 30 x 30-unit cell array. **(b)** The extracted near-field amplitude signal (s_3) from the white line in **(a)** with the number of unit cells marked by the number above the plotted optical amplitude of the resonators. **(c)** Optical near-field phase (φ_3) and **(d)** the extracted mode purity B for each resonator pair of the same edge as in **(a)**.

This fact supports a rectangular metasurface geometry with many unit cells aligned along the polarization axis to achieve an increase of overall active near-field area. Such a design would overall decrease the area of the metasurface susceptible to attenuating edge effects. Furthermore, these findings indicate that, when performing sensing applications or enhancing emitters for example through the Purcell-effect[118], the last six neighbors at the lateral edge of the metasurface provide a significantly reduced light-matter coupling compared to the unit cells at the center. In the future, the methods introduced here could be used to decipher the influence of parameters such as resonator geometry or material on edge effects and guide the design of new metasurfaces to reduce their potential negative on impact on the near-field enhancement.

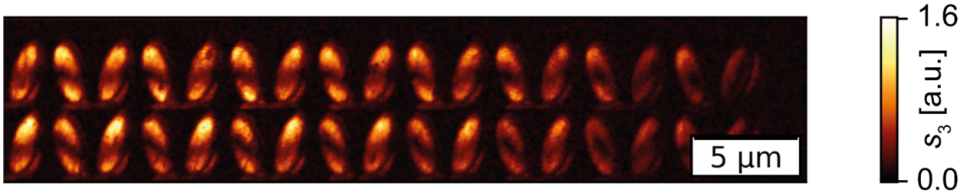

Figure 4.11: Near-field attenuation at a quasi-BIC metasurface corner. Optical amplitude scan s_3 recorded on the corner of a metasurface. The scan shows a decrease of the near-field in horizontal direction along the polarization axis of the electric field but no decrease in near-field intensity along the vertical direction.

4.8 Discussion

We have demonstrated that transmission-mode s-SNOM in combination with correlative image processing is a versatile technique to characterize photonic metasurfaces by quantifying mode properties such as the finite size effect, directional coupling, edge state effects and vacancy effects on quasi-BIC metasurfaces on the individual resonator level. We showed that the quasi-BIC mode is already established at an array size of 10 x 10-unit cells an array size much smaller than expected from far-field measurements. This fact suggests that applications, which are solely based on the near-field of the metasurface, such as catalysis or nanoscale heating, can be performed with arrays of much smaller size than commonly assumed. We further demonstrate that commonly used square metasurface arrays are, in fact, not necessarily optimal for realizing high-Q resonances in compact nanophotonic devices. As we have shown experimentally for rectangular arrays consisting of tilted ellipses, rectangular metasurfaces with a large number of unit cells aligned along the polarization axis can deliver much smaller footprints while maintaining high mode quality and reducing the length of metasurface boundaries susceptible to edge effects. We believe our results will help to produce metasurfaces with higher active areas and smaller footprints to boost applications such as biosensing and non-linear optics.
This concept can be applied in a straightforward manner to the mapping of the chiral response of chiral BIC metasurfaces[90], as has already been demonstrated previously for plasmonic metasurfaces[119], or to compare the mode properties of dielectric and plasmonic BIC metasurfaces. Moreover, our method enables a direct comparison of different BIC metasurface resonator designs with respect to near-field enhancement, finite array effect, material, and defect and edge response to determine an optimal resonator design that significantly improves upon existing designs across all these metrics, making it highly beneficial at the application level for metasurface based energy conversion[82] and sensing[116]. Furthermore, we believe that our general image processing methodology for assessing mode properties from near-field microscopy data can be directly applied to a multitude of nanophotonic systems ranging from plasmonic resonators[94] and polaritons in 2D materials[120] to the study of topologically structured light such as finite barrier bound states[121], optical vortices and optical skyrmions in thin films systems[122]. Ultimately, the method might even be of us for industrial applications in quality control of optical metalenses or photonic on the chip applications. In the same direction goes the next chapter of this thesis, which describes the investigation of a solid state biological sample in the form of different dental materials. It showcases the ability to analyse the micro- and nanoscale properties of the material with different far-field and near-field infrared microscopic techniques, which serves as an inspiration for dental material scientist to use these techniques for optimizing these medical relevant materials to improve the quality of life of patients.

5

Infrared microscopy of the micro- and nanoscopic properties of dental materials

The content of this chapter is published in the scientific journal Acta Biomaterialia (M. Beddoe, T. Gölz et al., Acta Biomater. ***168****, 309 (2023), see ref. [50]). As the foundation of the chapter, the peer-reviewed publication is used and text elements such as words, sentences, full passages, as well as graphic content and figures, are drawn directly from the publication in accordance with the Elsevier publication guidelines that allows the reprinting of own contributions in theses and in accordance with the terms of the CC-BY Creative Commons Attribution 4.0 International license http://creativecommons.org/licenses/by/4.0/.*

5.1 Introduction to dental materials

Oral diseases represent a significant public health problem worldwide, placing an enormous burden on the healthcare system[123]. The phase-down of amalgam restorations required by the Minamata Convention[124] has not yet been compensated for by an inexpensive and effective restorative material. Higher in cost but with the benefit of unbeatable aesthetics, resin-based composites are the most popular type of restoration today[125]. Modern light-cured resin-based composites (RBCs) offer a wide variation in the chemical composition of each component, their distribution, interaction, and morphology, allowing fine-tuning toward improved bioactivity[126] and mechanical performance[127], lower shrinkage[128], and improved polishability and aesthetics[129]. In general, RBCs are made from a mixture of microparticles embedded in a polymer matrix (see chapter 3) as displayed in Fig. 5.1. Most fillings perform well over time, however, fracture and secondary caries are the most common cause of failure in composite fillings, with the incidence of fractures increasing significantly[130,131]. In addition,

a number of risk factors for the longevity of a restoration have been identified in a recent review that are either related to the patient, particularly those associated with lifestyle and health choices (e.g. risk of caries, parafunctional habits, number of check-ups per year, socioeconomic status), the dentist (experience and the fact that changing the dentist is often associated with a restoration replacement) and the tooth/restoration condition (such as endodontic treatment, tooth type, and number of restored surfaces)[131]. The same review found no influence of the way a restorative material was cured, e.g. the type of polymerization unit or exposure time on secondary caries formation and thus longevity of a restoration[131]. The clinical longevity of a restoration not only depends on the properties of the restorative material, but also to a large extent on the adhesive system that ensures the bond between tooth and composite and minimizes the risk of secondary decay or restoration failure.

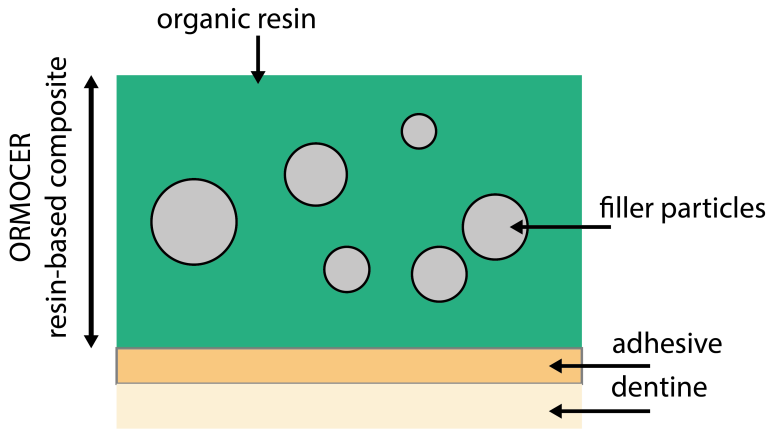

Figure 5.1: Illustration of the dental material system. It is composed of an ORMOCER resin-based composite filler, which is important for the structural integrity of the dental filling, and an adhesive that bonds the composite filling to the dental surface.

In addition, the adhesives prevent microleakage, which take place when bacteria or fluids penetrate between the filling and the tooth. Adhesives are composed of an etchant, primer and the actual adhesive (see chapter 3). The purpose of the etchant is to create micropores and remove the thin layer formed during tooth preparation. On the other hand, the primer prepares the dentin surface for bonding with the adhesive system converting the hydrophilic dentin into a more hydrophobic surface ready for bonding with the hydrophobic adhesives. Finally, the adhesive itself is made of hydrophobic resin monomers, such as Bis-GMA that are compatible with the RBC. The importance of adhesives for the longevity of a dental restoration led to special attention being paid to the development of adhesives systems, which are designed for different application methods (e.g. etch&rinse, self-etch, different number of application steps) and, in addition to the purely mechanical interlocking of older systems, aim to actively enter into a chemical bond with the hard tooth substance. Moreover, the collagen degradation by host-derived proteinases[132] and hydrolysis of the bond[133] are crucial for the longevity of a restoration.
The effect of these interactions is often tested indirectly, in macroscopic or microscopic bond strength tests[134], but with little power to elucidate bond mechanisms or aging behavior. Therefore, the search for modern investigation methods that can accurately resolve changes in the micro and nano range is becoming increasingly important. One of the leading analytical techniques for investigating the chemical composition of materials and their interaction with biological structures is IR spectroscopy[12]. This technique makes it possible to identify the chemical components of multi-material systems based on their characteristic absorption signatures. In addition, infrared spectroscopy is inherently fast, non-invasive, and non-

destructive, since only low energy photons interact with the sample and no time consuming and perturbative labeling with dyes or radionucleotides is required. Infrared spectroscopy has also been adopted in the field of dental medicine and material research[135,136] to detect early forms of fluorosis[137] and carious processes[138], to investigate the polymerization kinetics of adhesive polymers[139], and to study novel nanoparticles in dental fillings and their effect on bacterial growth[140]. However, spectroscopic studies on dental materials have, so far, mainly relied on traditional IR measurements carried out on bulk materials with low intensity globar IR light sources. In such experiments, the investigated dental materials are studied in isolation from their dental environment and the interaction of resins or composite materials with the environment cannot be studied in sufficient detail. Moreover, significant sample contamination is expected, when the sample is extracted from the tooth section, obscuring the desired dental material information. Furthermore, these studies lack access to spatially resolved molecular information of the heterogeneous samples commonly found in modern high-tech dental materials, as the acquired bulk spectra only show an averaged spectrum over all molecular compounds in the sample masking spatial chemical heterogeneities of the sample. Finally, globar light sources have a low intensity, which makes it difficult to detect trace amounts of molecules that may yield important indications about toxic compounds or material failure processes.

These challenges have been addressed through rapid advances in infrared optics. For example, the advent of commercially available MIR-Laser sources[18,45,47] has drastically improved the signal-to-noise ratio of IR spectra and images. Furthermore, the generation of MCT and microbolometer-based focal plane array detectors in combination with, e.g., reflective Cassegrain objectives as well as refractive objectives for laser-based systems have led to the development of spectral imaging infrared microscopes. These microscopes map heterogeneous chemical information with a spatial resolution down to the micrometer range and already constitute a significant advancement of spatial resolution over classical IR-spectroscopy[141–143]. Still, they cannot resolve spectral information on the nanoscale due to the optical diffraction limit. However, through the combination of powerful laser sources and AFM systems, a fundamentally different kind of infrared imaging and spectroscopy technology was invented, that makes it possible to overcome this limit[27,33]. One such infrared microscope is the s-SNOM. As the microscope's near field can image and spectroscopically investigate the infrared response of the sample surface with a resolution of about 20 nm, achieving a subdiffraction resolution two orders of magnitude below the diffraction limit of MIR light[38]. This conceptual advance gives access to nanoscale infrared spectroscopic information about the structure and chemistry of materials, which is essential to understand and optimize modern-day high-end materials[144]. Already, FTIR-imaging microscopes and s-SNOM are starting to be applied to dental material research. For example, a FTIR-microscope was used to map and evaluate the formation of a biomimetic interface between the natural tooth and the adhesive and to evaluate the bonding of adhesive to a caries-affected dentin[145,146]. On the other hand, s-SNOM was used to map chemical heterogeneities of apatite nanocrystals close to tubulin structures in the dentin[147] and AFM-IR a method similar to s-SNOM was used to study mineralization and remineralization processes of human dentin[148].

In the context of the increasing number of studies conducted with IR-imaging technologies in dental material research, it is worthwhile to discuss the different strengths and weaknesses of the techniques. In this work, we provide a detailed comparison and overview of three major state-of the art IR imaging methods for the study of dental materials. Specifically, we compare the quality of IR-images and spectra of dental filling materials and adhesives from a far-field FTIR-microscope and a QCL-IR microscope as well as a s-SNOM. These three microscopy methods are exemplary for the possibilities of modern-day commercial IR

imaging, as they span a wide range of IR sources and optics. Still, it has to be mentioned that there are countless other technologies in the field of IR-spectroscopy such as AFM-IR[149] or optical photothermal infrared spectroscopy[150] and this study can only evaluate a part of this technological landscape.
In this comparative study, all measurements were performed on the same dental sample with two similar class I cavities prepared in a human third molar and restored with a low shrinkage bulk-fill resin-based composite bonded with two different adhesives (Fig 5.2 and chapter 3 for further details of the dental fillings). We choose the specific low-shrinkage composite to focus on the specific chemical interaction and to not have any damage effects from shrinkage on the bond. Furthermore, the interesting Si-O-Si bond characteristics present in both the ORMOCER matrix and the fillers have been a compelling target for nanoscale IR-microscopy study.

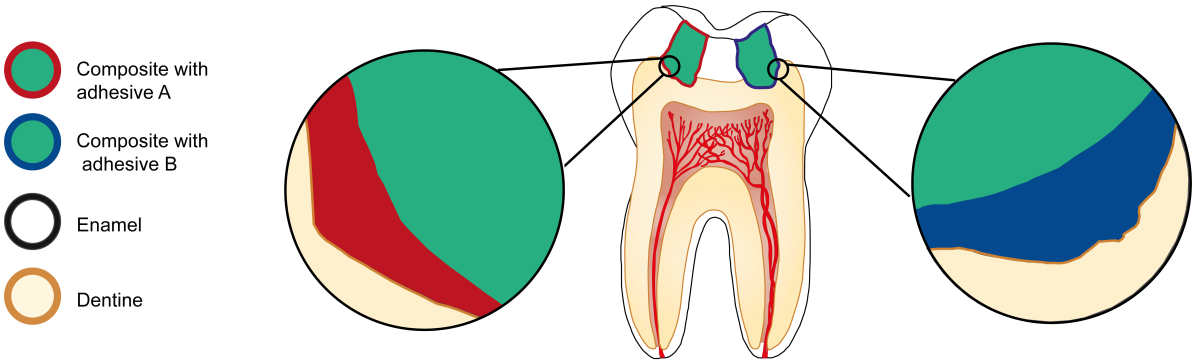

Figure 5.2: Schematic illustration of the investigated dental sample with two kinds of composite adhesive fillings. Sketch of the tooth cross section with two different fillings, both with the same composite, but one containing a commercial adhesive A and the other an experimental adhesive B. The two zoomed in images next to the tooth cross section show the investigated interface between dentin, adhesive and composite.

5.2 Imaging FTIR-spectroscopy for chemical differentiation

Previous FTIR spectroscopic investigations on bulk samples have identified a rich structure of different vibrational peaks originating from the tooth material and the dental fillings and established connections to biological and chemical processes[135,136]. The central advantage of imaging IR spectroscopy in general is that it can map the chemical composition of a sample based on characteristic IR absorption signatures. The main molecular vibrations of the dental samples investigated in this study are illustrated in Fig. 5.3a and can be correlated with the main molecular components of the dental filling. One major vibrational absorption band is associated with the C-O-C stretch at around 1150 cm^{-1} originating from the aliphatic ether groups in monomer building blocks of the adhesive. Further important vibrational bands are the C=O stretching of the ester group in the methacrylate groups of the polymer chains[16] around 1715 to 1735 cm^{-1} and the Si-O stretching in the composite[135]. The Si-O stretch vibration creates a strong absorption feature from around 900 to 1100 cm^{-1} and can be linked to the Si-O bonds in the glass filler particles in the composite as well as the silica nanoparticles and the Si-O bonds in the polymer chains in the ORMOCER matrix[135]. A final important vibration is the C-H stretching mode found around 2900 to 3000 cm^{-1}, originating from the hydrocarbon compounds found, e.g., in the polymers[135].

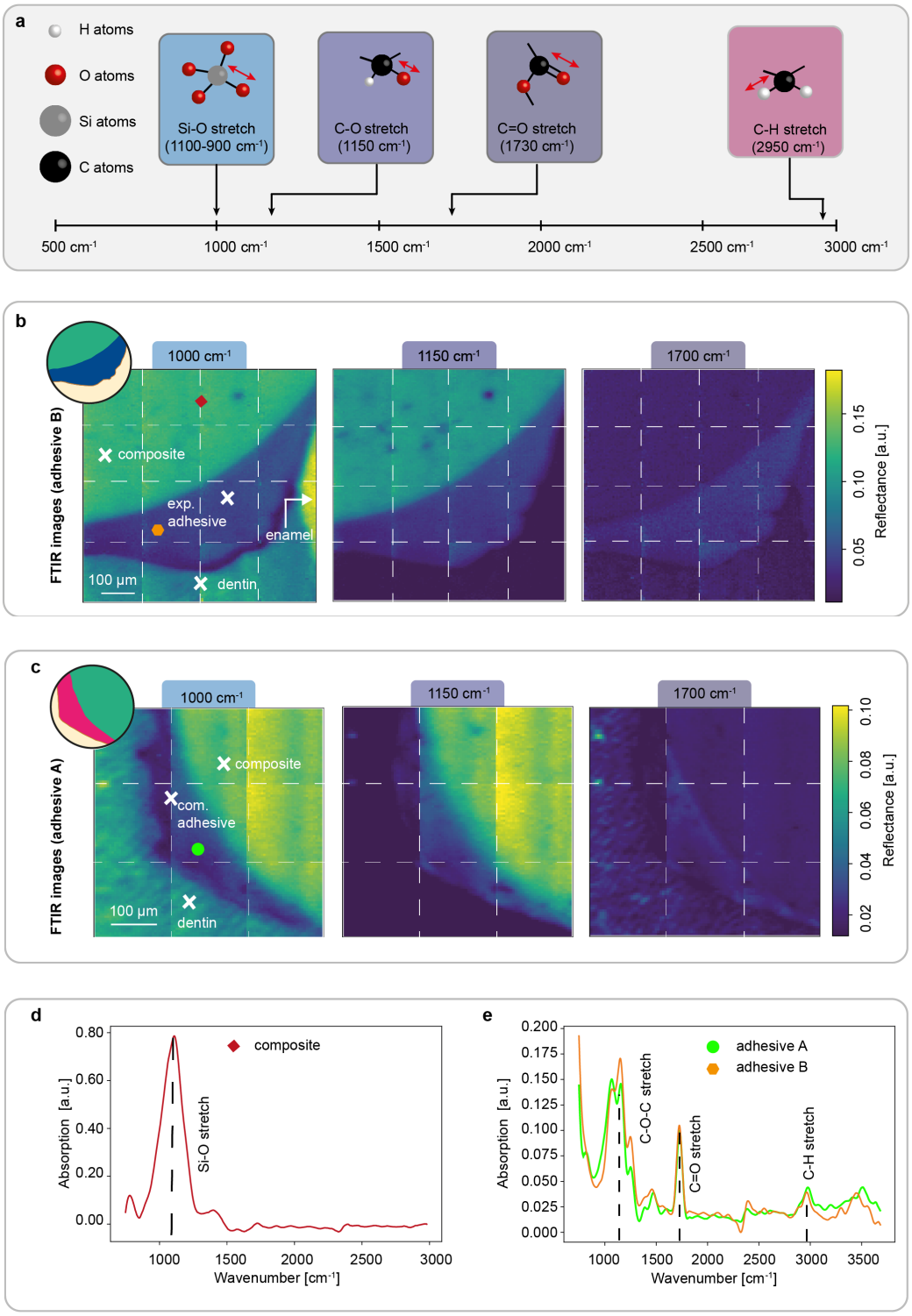

Figure 5.3: Spectroscopic investigations of dental fillings featuring different adhesives using FTIR imaging spectroscopy. (a) Depiction of the relevant molecular resonances with corresponding wavenumbers. These resonances are directly correlated with the materials contained in the composite and adhesive. **(b)** Recorded reflectance images of the experimental adhesive B at 1000 cm^{-1}, 1150 cm^{-1} and 1700 cm^{-1} with labels for the different parts of the tooth cross section and white crosses and arrows which indicate the areas of the different parts of the dental section. The small inset on the left shows the approximate location of the imaged area in relation to the whole tooth cross section and relates to Fig. 5.2. The complete image is composed of 4 × 4 single images acquired sequentially and stitched together as highlighted through the white dashed lines. The red rhomb and the orange polygon indicate the location where the red and orange FTIR spectra in **(d)** and **(e)** were acquired. The different materials can be best separated at a wavenumber of 1000 cm^{-1}. **(c)** FTIR reflectance images of the commercial adhesive A composed of 3 × 3 single images at the same wavenumbers as in **(b)**. The green circle shows the location at which the green spectrum in **(e)** was recorded. **(d)** The plotted spectrum of the composite area of the tooth cross section with a clear Si-O stretching vibration. **(e)** Spectra of both the adhesive A and B with strong carbonyl and C-O stretching and C-H stretching vibrations.

Importantly, this mode can only be spectroscopically detected by the FTIR-microscope (see chapter 3 for details of the microscope), because the other imaging devices compared in this study utilize laser light sources that cover a smaller spectral range. Based on the first three characteristic wavenumbers, the difference in chemical composition of the dental fillings can be mapped with the FTIR-microscope.
Fig. 5.3b and c show the recorded reflectance maps for the adhesives A and B, respectively, at wavenumbers of 1000 cm^{-1}, 1150 cm^{-1} and 1700 cm^{-1}. The small inset on the left shows the rough location of the reflectance maps in context of the tooth cross section and relates to Fig. 5.2. The field of view (FOV) of the FTIR-microscope is too small to map the whole area of interest. Therefore, the acquisition and stitching of multiple images is necessary (see chapter 3). The borders of the individual images are denoted by white dotted lines. This specific area of the dental sample was chosen as it represents one of the most complex areas of the restoration with enamel, dentin, the adhesive and restorative composite all being present in one image, which makes it interesting for the study of the complex chemistry of the different materials with the IR-microscope. At 1000 cm^{-1}, the enamel and the dentin as well as the composite region show the highest reflectance and can be well separated. The contrast can be explained by the correlation between the reflectance and absorption, meaning materials with a strong absorption show a high reflectance close to their absorption peak. Both enamel and dentin are mainly composed of apatite minerals, which contain many phosphate groups and exhibit a strong P-O-stretching resonance at around 1000 cm^{-1} as displayed in Fig. 5.4 for the FTIR spectra of enamel and dentin[136]. Also, the composite has a strong Si-O stretch resonance around 1000 cm^{-1} due to the silica contained in the ORMOCER matrix and filler particles in the composite. The stronger reflectance of the enamel compared to the dentin can be explained by the degree of mineralization and the higher density of apatite crystals in the enamel compared to the dentin of the tooth[151].

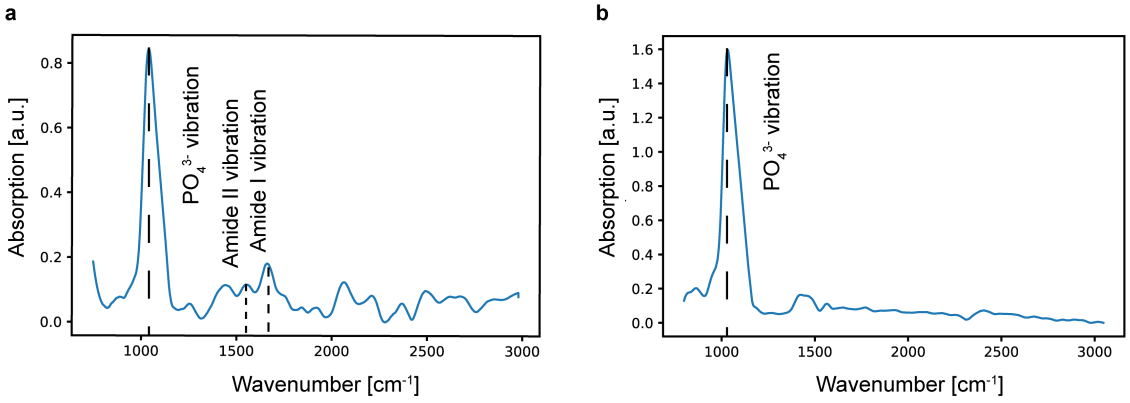

Figure 5.4: FTIR spectroscopy of the dentin and enamel dental region. (a) FTIR microscope absorption spectrum of dentin. The most intense vibration of the dentin spectrum is the asymmetric vibrations of the P-O bond of the PO_4^{3-} group of the hydroxyapatite[138]. Amide II and Amide I peaks can also be identified. **(b)** FTIR microscope absorption spectrum of enamel. The characteristic peak around 1060 cm^{-1} is ascribed to the asymmetric vibrations of the P-O bond of the PO_4^{3-} building block of the hydroxyapatite crystal[147].

In contrast, the adhesive does not have any strong resonance in this spectral region, which explains the comparative lower reflectance. The reflectance values start to invert with the second map at 1150 cm^{-1}, where the composite and the adhesive show a high reflectance because both materials have a significant amount of ether groups with resonances in this spectral position. Finally, in the last map recorded at 1700 cm^{-1}, the adhesive shows the highest reflectance because the adhesive is based on a methacrylate polymer with a high

density of ester groups with an IR-resonance in this region. Notably, the enamel and the dentin can only be separated in the first map at 1000 cm^{-1}, which can be explained by their very low reflectance at the other wavenumbers. Because the imaging FTIR microscope records the full IR reflectance spectrum at every pixel of the mapped sample, precise chemical characterization and localization can be performed at any pixel of the image.
Three exemplary positions, for which the absorption spectrum have been plotted (see small symbols in Fig. 5.3b and c for the exact position), have been picked. The absorption was calculated from the recorded reflectance values with the Kramers-Kronig relations[22]. One of the positions is in the composite region and, as expected, the spectrum (Fig. 5.3d) is dominated by the strong Si-O vibration, at around 1080 cm^{-1}[135]. The two weak side peaks at approximately 1270 cm^{-1} and 780 cm^{-1} can be assigned to the methyl groups found in the silicon organic compounds in the ORMOCER matrix of the composite. The peak at 1270 cm^{-1} corresponds to the Si-CH_3 symmetric bending mode and the peak at 780 cm^{-1} to the respective Si-CH_3 rocking mode[38]. The other two investigated positions correspond to the regions of adhesives A and B. Their absorption spectra are very similar and show the typical IR-resonances of a methacrylate-based polymer (Fig. 5.3e). As already discussed, the peak around 1150 cm^{-1} originates from the C-O-C stretching mode, while the peaks at around 1260 cm^{-1} and 1370 cm^{-1} are a result of different C-O stretching vibrations and CH_3-bending modes from the methacrylate polymer building blocks of the adhesive[16,135,152]. The absorption maximum at 1730 cm^{-1} is caused by the C=O stretching of ester groups[16,135]. Furthermore, the C-H stretching mode at 2900 cm^{-1} and the O-H stretching mode at 3400 cm^{-1}[16] can be clearly identified. Another vibrational band in the FTIR spectra is located at 1550 cm^{-1}, which relates to the aromatic C=C vibrations of the bis-GMA building block and is often used in relation with the aliphatic C=C vibration from the methacrylate located around 1600 cm^{-1} (see Fig. 5.5 for a close up of the specific area in Fig. 5.3e)[153].

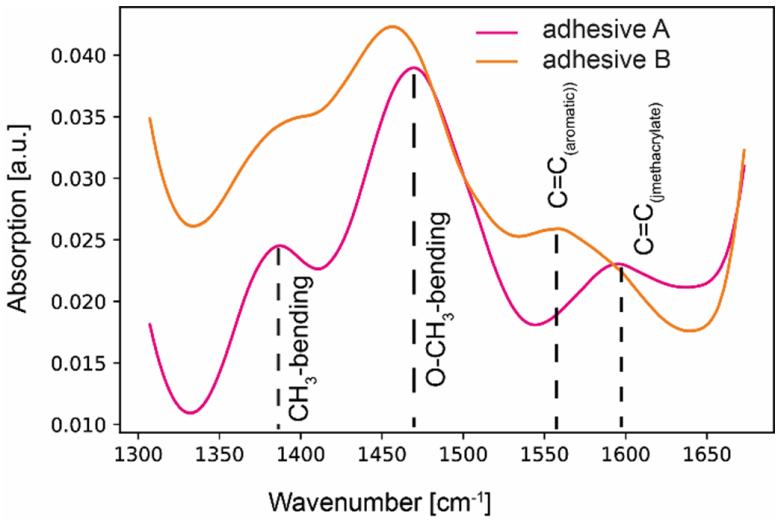

Figure 5.5: Close-up of the FTIR spectra of the adhesive A and B shown in Fig. 5.3e. The experimental adhesive B spectrum shows a resonance at a wavenumber of around 1560 cm^{-1}. The resonance typically correlates with an unsaturated aromatic double bond originating in the case of the adhesive A from the bis-GMA building block of the adhesive polymer.

Importantly, the bis-GMA building block is the only polymer building block with an aromatic structure and it is only contained in the experimental adhesive B. This shows that the FTIR microscope is sensitive enough to distinguish very similar polymers based on unique building blocks. Furthermore, through monitoring the change in the signal intensity ratio of both peaks the degree of polymerization can be evaluated. The aromatic C=C vibrations stays constant

as the aromatic building block does not take part in the polymerization reaction, whereas the aliphatic C=C vibration of the methacrylate decreases throughout the polymerization process[153]. By monitoring the spatial intensity ratio of these peaks, crucial information about the polymerization degree in certain areas of the adhesive could be obtained through the use of FTIR microscopy in future studies. In general, the reflectance images and the FTIR-spectra from the FTIR-microscope show that it is easily possible to differentiate chemically heterogeneous samples on the microscale and acquire a understanding of the molecular composition of the sample by plotting the spatially resolved FTIR-spectra. This workflow is especially helpful for characterizing samples with an unknown molecular composition on the microscale, due to the ease with which different materials can first be contrasted by mapping them and then be identified in their composition by FTIR spectra.

5.3 QCL-IR microscopy and porosity evaluation

By combining the high power of laser-based light sources and improvements in imaging performance mediated by high-resolution microbolometer detectors and high-NA MIR refractive objectives, additional insights such as porosity evaluation and statistical evaluation of the spectral quality can be obtained from dental samples through QCL-IR microscopy. In contrast to the imaging FTIR approach presented above, the QCL-IR microscope (see chapter 3 for details of the microscope) provides a much larger field of view of 650 μm x 650 μm, circumventing the need to combine multiple reflectance maps taken at different positions and therefore avoiding stitching artefacts. These reflectance maps are plotted from the corresponding hyperspectral data cubes recorded by rapidly tuning the high-brilliance external cavity quantum cascade laser (EC-QCL) source through the whole range from 950 to 1800 cm^{-1}. Noteworthy are improvements in accelerating the measurements by a factor of up to 170 compared to commonly used FTIR microscopes recently reported with a QCL-IR microscope[154].
The reflectance maps at 1000 cm^{-1} of the adhesives A and B (Fig. 5.6a and b with the inset showing the approximate location of the map in the overall tooth section) is consistent with the reflectance contrast shown at the above FTIR maps. Importantly, the maps in Fig. 5.6 resolve the dental fillings with a higher resolution compared to the FTIR images. For example, it is possible to identify small regions of inhomogeneous reflectance in the composite and dentin region of the adhesive A sample. In comparison, these inhomogeneities are only hinted at in the FTIR-maps. The areas with different reflectance contrast can be further investigated by plotting the whole absorption spectrum at specific spatial points (indicated by the small rhombs in Fig. 5.6a and b) and analyzing the chemical composition through identifying the characteristic fingerprints in these spectra (Fig. 5.6c). Like in the FTIR spectra for the adhesives A and B, the main vibrations such as the C-O stretching and C=O stretching vibration peak are clearly visible. However, unlike the FTIR-microscope data shown previously, the large amount of high-resolution spectral data available from the acquired reflectance images opens perspectives for the statistical evaluation of the optical response. To demonstrate this capability, we evaluate the standard deviation of all the spectra within a 20 × 20-pixel area around the specified points, which is indicated as the semi-transparent area around the averaged spectra shown in Fig. 5.6c. In general, the standard deviation is low compared to the peak intensity, showing the high quality of the signal-to-noise characteristics of the spectra. Interestingly, certain peaks show a higher standard deviation compared to other peaks, which could indicate a difference in polymer composition in the averaged area and different polymerization outcome of the cured polymers.

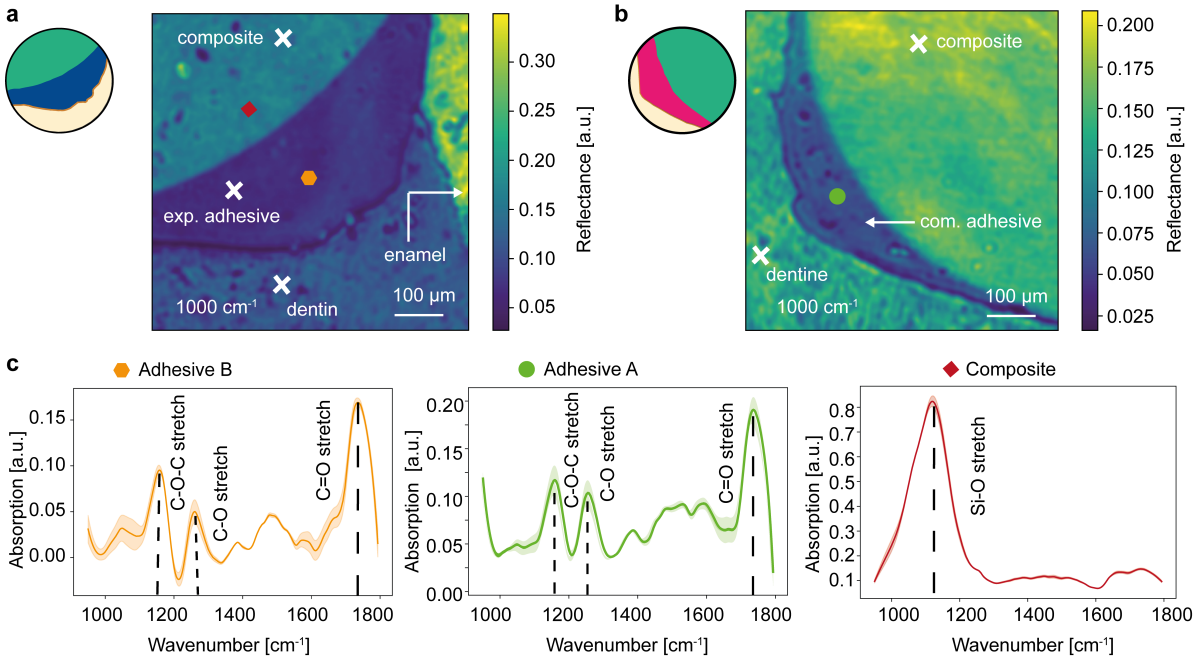

Figure 5.6: QCL-IR microscopy for chemical mapping. **(a)** MIR reflectance image at 1000 cm^{-1} of the experimental adhesive B filling. The red rhomb and the orange polygon indicate the location where the red and orange spectra in **(c)** were recorded. **(b)** Corresponding MIR-image for the commercial filling with the green circle indicating the location where the green spectra of the adhesive A shown in **(c)** were acquired. The different materials of the tooth section are labeled and assigned to the specific area by the white crosses or white arrows and can be easily differentiated based on the recorded reflectance values. **(c)** Absorption spectra obtained from the reflectance spectra on the adhesive B (orange), adhesive A (green) and composite (red) with resonances assigned to functional groups found in the materials. The semitransparent area around the spectra indicated the standard deviation.

Additionally, the high-resolution reflectance images from the QCL-IR-microscope allow to rapidly calculate and evaluate the adhesive porosity as another interesting parameter in dental material research. Normally, the porosity determination would be performed with microscale computer tomography and thus require additional equipment and measurement time. The workflow necessary to calculate the porosity of the different adhesives is based on an algorithm and is shown in Fig. 5.7a. The algorithm processes two different reflectance images for each sample shown on the left side of the flow chart. The reflectance image at 1000 cm^{-1} is used to identify the total adhesive area (A) in the recorded image, as the image at this wavenumber shows a strong contrast between the different dental areas. On the other hand, the reflectance images at 1710 cm^{-1} reveal the precise locations of pores as dark spots contrasted from the whole dental area. The reflectance of the adhesive is very high at this wavelength and therefore inhomogeneities in the area can be easily detected. The total adhesive area and the total pore area are detected from the reflectance images using the Hoshen-Kopelman-algorithm[155,156] as illustrated in Fig. 5.7b. The algorithm converts regions with different reflectance into clusters with an index of a size of 5 × 5 pixels. The clusters are determined by the difference of the reflectance between neighboring pixels. Two neighboring pixels belong to the same cluster, if the difference of their reflectance is smaller than a minimum threshold value *a*. The threshold values were chosen such that the pores, respectively the area of the adhesives can be easily identified by the algorithm. As the reflectance values vary significantly between the different samples the same threshold *a* could not be used between different samples and wavenumbers. However, to ensure the comparability of the porosity between the different samples, a relative threshold a_{rel} was

defined as the average reflectance of the adhesive area of the sample minus the average reflectance of the pores area of the sample divided by the defined threshold value *a*. This value a_{rel} was kept constant for both the adhesive A and B for the specific image processing wavenumbers. The relative threshold for the adhesive area detection at 1000 cm^{-1} is 2.39 and the relative threshold for the pore detection is 3.6. The algorithm extracts the adhesive area (A) as a cluster of similar reflectance values, as shown in the lower middle image of the flow chart. The cluster of the pores in the adhesive and composite is extracted from the image at 1710 cm^{-1} (upper middle image in Fig. 5.7a).

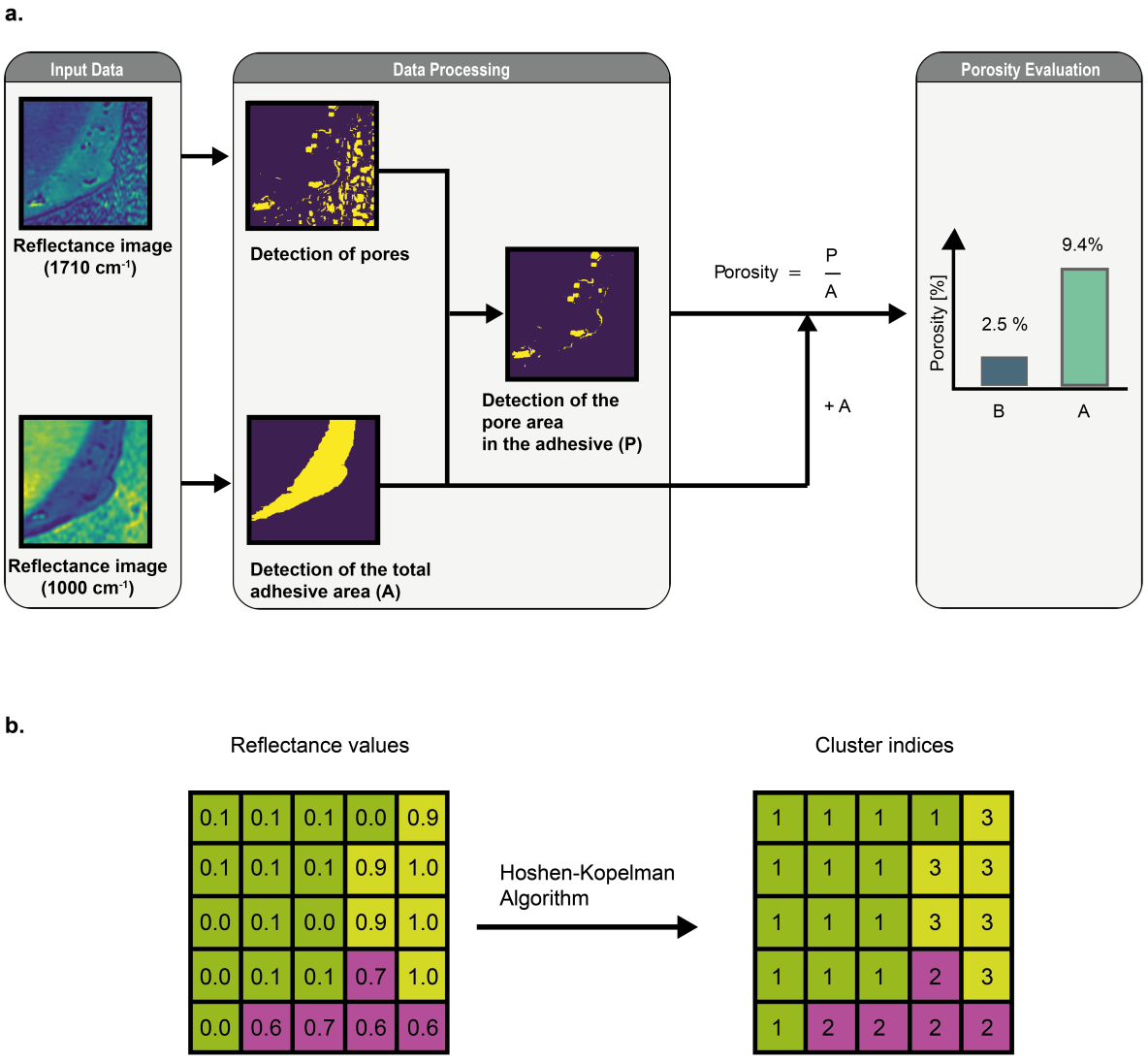

Figure 5.7: Data processing of QCL-IR images for the quantification of the adhesive porosity with the Hoshen-Kopelman-algorithm. **(a)** Scheme for calculating the porosity of the commercial adhesives A from reflectance images at 1000 cm^{-1} and 1710 cm^{-1}. The reflectance image at 1000 cm^{-1} shows high contrast between the different material components of the tooth filling and is used to extract the area A of the adhesive with a clustering algorithm. The reflectance image at 1710 cm^{-1} is used to detect the pores in the image, since it shows strong pore contrast and higher spatial resolution. By combining the whole detected pore area with the adhesive area (A), the adhesive area with pores (P) can be extracted. Then, both areas (A) and (P) are used to calculate the porosity of the adhesive. The porosity of the commercial adhesive A is 4 times higher than the porosity of the experimental adhesive B. **(b)** Clustering of reflectance data points based on the Hoshen-Kopelman-algorithm and a minimum threshold value of a = 0.2. As exemplified on an array with reflectance values similar to the values recorded by the QCL-IR microscope (left) and the corresponding identified clusters by Hoshen-Kopelman-algorithm (right).

Importantly, the identified pores from the composite and the adhesive cannot be differentiated by the algorithm at this wavenumber because the contrast between the composite and the adhesive is low. Therefore, it is necessary to combine the adhesive cluster map and the pore map to extract another map of the pores only located in the adhesive (P) without the pores of the composite. The map of the pores in the adhesive is shown by the last map in the data processing flowchart. In the end, the porosity is calculated by dividing the pore area in the adhesive (P) by the total adhesive area (A). Strikingly, we find a significant difference in porosity between the experimental adhesive B (2.5%) and the commercial adhesive A (9.4%). The results are encouraging as the experimental adhesive with 7% inorganic fillers (see chapter 3 for exact composition) mixed into the organic matrix showed smooth processing under laboratory conditions, especially as the mixing process of both components is a source for inducing porosity. In general, the porosity can have important implications for the stability of dental fillings and can be used as a design parameter for the development of adhesives.

5.4 Nanoscale spectral characterization of dental materials with s-SNOM

The study of dental material with nanoscale resolution through the use of s-SNOM offers an exciting perspective both for material science and dentistry, because modern composites are complex nanotechnological materials[157]. The technique was already used to study the dentin tubuli in a section of a tooth and showed that it could identify microscale hydroxyapatite structures[147]. In this study, the microscope is used to image and spectroscopically explore the dental composite and the interface between the composite and the experimental adhesive B, focusing on interesting chemical heterogeneities in these areas. We particularly choose this area because it gives a challenging but also interesting interface as both the composite matrix and the adhesive are methacrylate based and not easily distinguishable. In addition, scans on the composite were performed to study the interface between the filler particles and composite matrix where possible biodegradation processes can take place.
The scan is started by positioning the AFM-tip above a location of interest with the help of an optical overview microscope. The optical microscopy image in Fig. 5.8a shows the tip placement at the interface between the composite (colored in green) and the adhesive B (colored in blue). Because of its technological versatility, s-SNOM can operate in multiple modes to analyze the dental materials. In every optical imaging mode, a correlated topography image is recorded with the AFM like the one shown in Fig. 5.8b. The topographic data can be used to distinguish between the adhesive (smooth and flat section in the right upper corner) and the composite section even after the grinding process of the dental section. In addition, the topography gives information about the quality of the grinding and polishing process of the dental material. Another important function of the topographic information is that it can be correlated with the recorded optical signals to verify if the signals truly originate from the optical material contrast and does not originate from topographic artefacts. A better differentiation between dissimilar material sections in the dental filling is possible with the parallel recorded optical imaging modes such as white light imaging (see chapter 3). The dark clusters visible in the white light image (Fig. 5.8c) with a low optical amplitude show the dense glass filler (84.0 wt.% Ba-Al-Si-glass and SiO_2) embedded in the ORMOCER matrix.

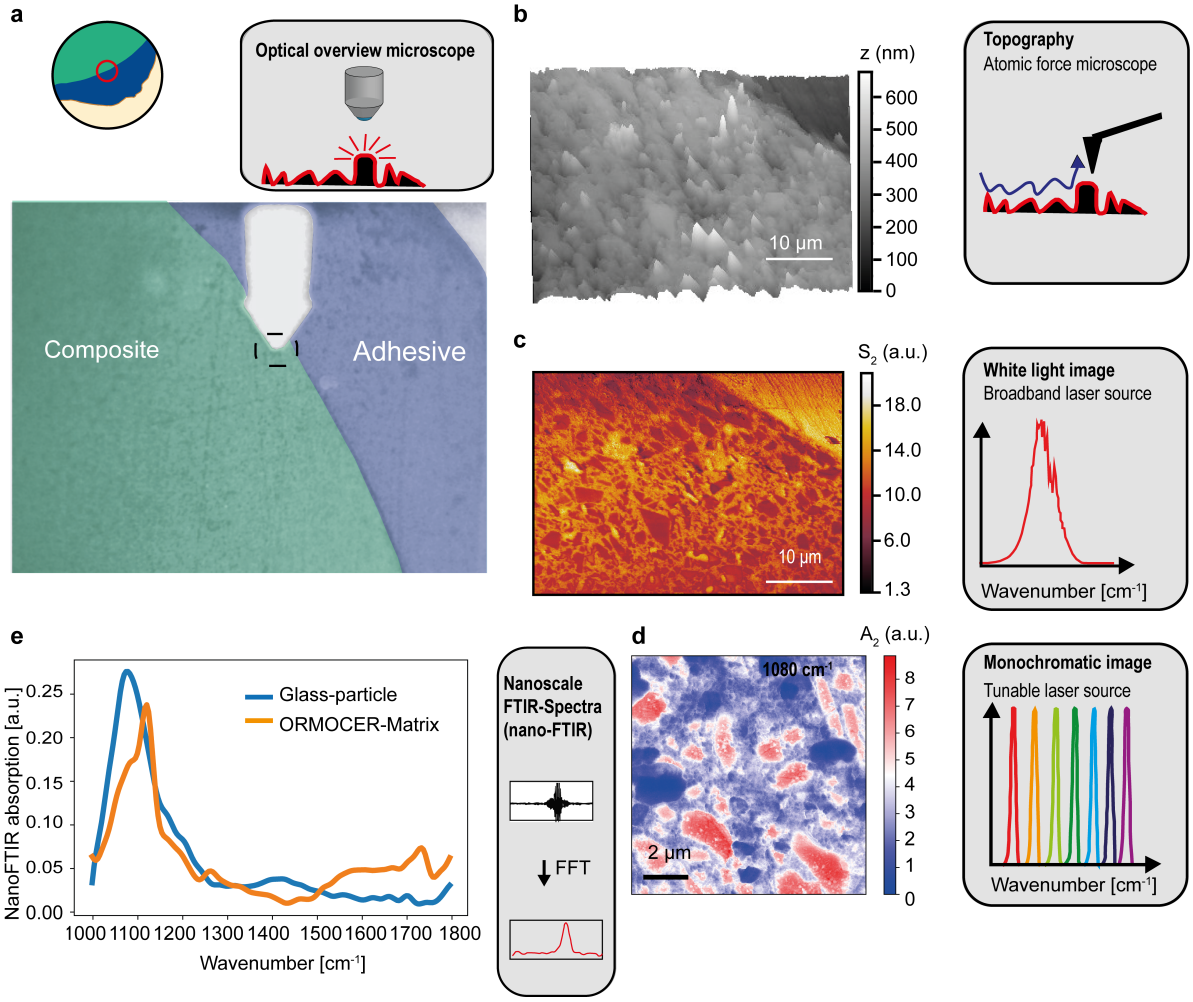

Figure 5.8: Correlated s-SNOM data from a dental sample. (a) Overview image of the optical microscope used to place the AFM cantilever in contact with the surface at the composite (green) and experimental adhesive B (blue) boundary. The red circle in the inset indicates the investigated area of the tooth section. **(b)** 3D AFM topography (z height) map of the composite-adhesive interface showing a clear topographic difference between the flat adhesive and the rough composite section. **(c)** White light image plotted from the second demodulated optical amplitude s_2 correlated to the AFM-image shown in **(b)**. The white light image displays a heterogeneous optical response, which makes it easy to distinguish adhesive, composite, and clusters inside the composite. **(d)** Monochromatic absorption images of the composite area at the second demodulation (A_2) at a wavelength of 1080 cm^{-1}. The filler particles and the surrounding ORMOCER can be separated by their optical response. **(e)** Nano-FTIR absorption spectra from the second demodulation recorded on a glass particle (blue) and on the ORMOCER matrix (orange).

Additionally, the interface between the adhesive and the composite can be distinguished because the adhesive exhibits a high and a more uniform scattering signal in contrast to the ORMOCER matrix in the composite. Importantly, the white light imaging mode does not convey any specific chemical information, as it is based on the integrated backscattering intensity and thus only shows optical contrast and no chemical contrast (see chapter 3). In contrast, the pseudo heterodyne imaging works in the case of this study with a 10 cm^{-1} narrow wavelength range and can probe specific chemical resonances. The pseudo heterodyne image at 1080 cm^{-1} (Fig. 5.8d) shows cluster particle in the composite matrix imaged based on their Si-O stretch resonance. At this wavelength both the ORMOCER matrix and the glass particles show a Si-O resonance. However due to the material density and resonance intensity of the phononic Si-O stretch of the glass particles, the ORMOCER matrix can still be distinguished from the filler material in the image. For attaining chemical information about a certain

area after a white light scan is conducted, a nano-FTIR spectrum can be recorded. Based on the white light map, specific points, or lines of points at a particular position of the map can be investigated. By comparing two nano-FTIR spectra taken at different positions, one being on a glass particle and the second being on the ORMOCER matrix (Fig. 5.8e blue and orange spectrum), the materials can be clearly distinguished, and the material content can be analyzed. The spectrum of the filler particle shows only one broad peak at about 1080 cm^{-1} originating from the strong Si-O-stretching mode. On the other hand, the ORMOCER matrix shows a richer spectrum. The strongest vibrational mode is the Si-O stretching at 1120 cm^{-1} originating from the Si-O stretch in the silicon polymer. The shoulder at around 1080 cm^{-1} coincides exactly with the recorded Si-O resonances measured on the glass particles.

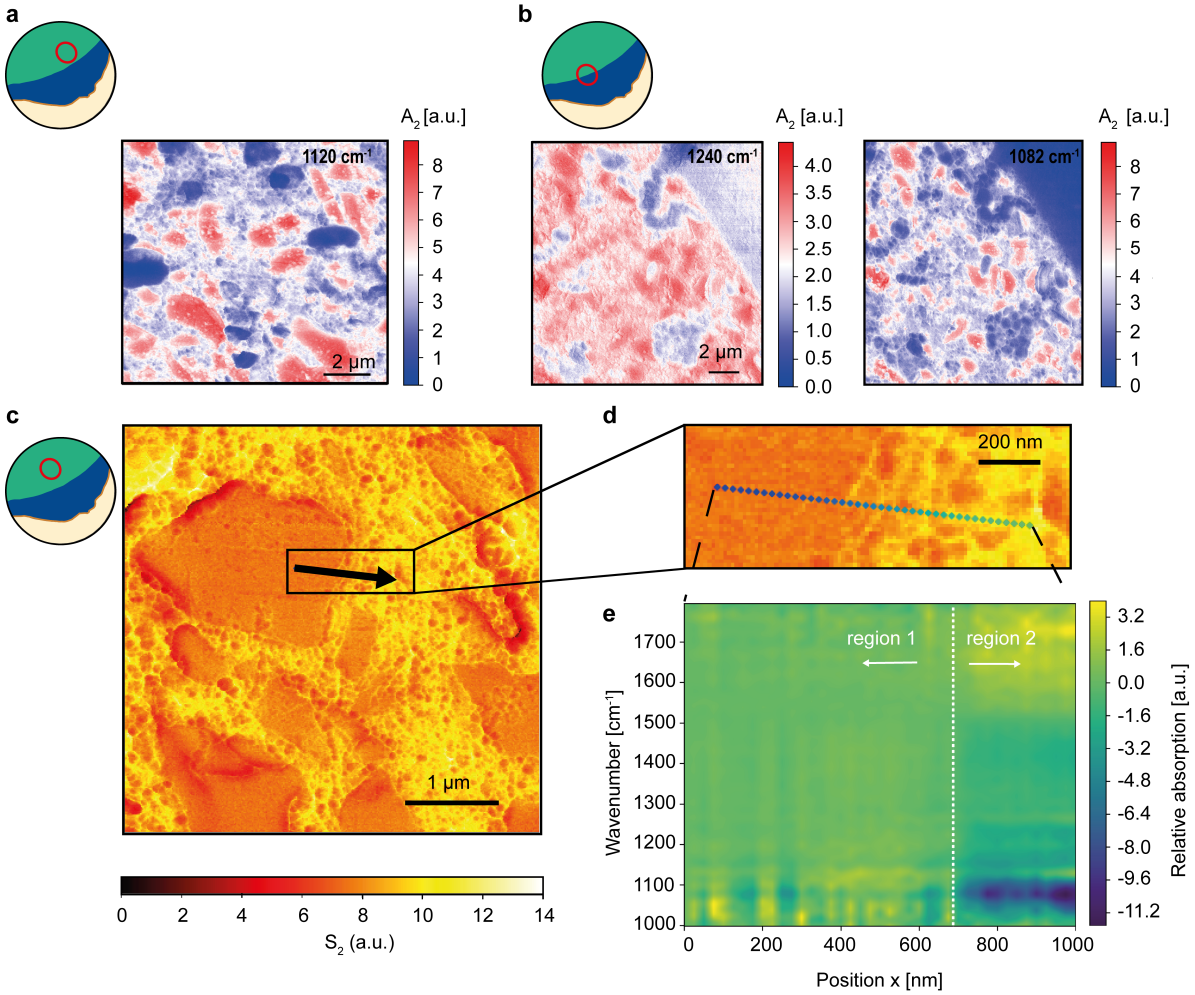

Figure 5.9: Nanoscale resolved chemical specific mapping of dental fillings and hyperspectral investigation of a cluster-ORMOCER interface. (a) Monochromatic absorption images of the second demodulation (A_2) showing the composite at 1120 cm^{-1} and **(b)** the composite-adhesive interface at 1240 cm^{-1} and 1082 cm^{-1} (right) with red circles in the insets showing the approximate region where the scans were conducted on the overall dental section. The strongly differing infrared absorption of different materials makes it possible to visualize the heterogeneity of the composite filling and adhesive-composite interface. **(c)** White light image of the composite matrix with several clusters. The arrow shows the position and direction of a 1 μm long spectroscopic line scan. **(d)** Shows a close up of the overview white light scan with the exact position of each of the nano-FTIR spectra recorded during the line scan. **(e)** Relative difference nano-FTIR absorption density plot, whereby the relative near-field absorption signal of the second demodulation between wavenumbers of 1000 cm^{-1} to 1800 cm^{-1} is defined as the difference in absorption between the first spectrum (position x = 0 nm) taken on the middle of the glass particle and the following spectra at position x. In the density plot, two distinct regions can be identified. The first region is defined by a very strong signal around 1080 cm^{-1}, which correlates with the glass particle location. The second region has a weaker absorption signal at 1080 cm^{-1} and correlates with the beginning of the ORMOCER matrix.

Thus, it seems likely that this shoulder originates from nanosized silica inclusions also contained in the ORMOCER matrix, which are too small to be visualized by white light imaging. The peaks around 1250 cm^{-1} and 1730 cm^{-1} are due to the Si-CH_3 and C=O stretching and the carbonyl stretch from the organic part of the ORMOCER matrix respectively.
This short overview of different s-SNOM modes based on the investigated dental material shows the broad applicability of this method for visualizing and identifying dental material components. Especially the pseudo heterodyne imaging mode is useful to investigate heterogeneities in dental fillings, as it allows a direct and fast visualization. Through the imaging of the cluster resonance at 1080 cm^{-1} (Fig. 5.8d) and at the ORMOCER resonance at 1120 cm^{-1} (Fig. 5.9a), maps of the cluster distribution and cluster size can be easily obtained. These images can be used in the future to study possible aggregation processes or the distribution of clusters for different composite formulations. Another interesting finding of this imaging mode is the possibility to image the intrusion of the adhesive into the composite matrix and the morphology of cluster particles at the interface as shown at Fig. 5.9b, when imaging the interface at the cluster resonance of 1080 cm^{-1} and at the resonance of the C-O stretch of the adhesive at 1240 cm^{-1}. The optical maps show a clear contrast between the adhesive B and the composite area. The intrusion can be identified through the small blue islands in the composite layer, which is especially visible when imaged at 1240 cm^{-1}[135]. This method could be used to optimize the interfaces between dental materials, as the interface between the materials can be investigated with a high chemical contrast compared to state-of the art techniques such as scanning electron microscopy. In turn this information could help to improve binding properties and interface compatibility of dental materials.
Another way to study such crucial interfaces is a hyperspectral nano-FTIR linescan. Such a linescan was performed at the interface between a glass particle and the surrounding ORMOCER matrix. As already shown by the spectra in Fig. 5.8e the two different materials have only slight spectroscopic differences as they have quite similar Si-O bonds and only differ through a polymer peak and a shift of the Si-O resonance position. The white light scan of the region of interest is shown in Fig. 5.9c. The arrow added to the white light scan shows the rough positions and direction, at which the linescan was performed. The close up of the area of the linescan is shown in Fig. 5.9d, whereby the colored dots show all the positions of each recorded nano-FTIR spectra. The linescan consists of 40 single nano-FTIR spectra at steps of 25 nm over a total distance of 1000 nm. In Fig. 5.9e, the relative nano-FTIR absorption change between the first spectrum and the following spectra is plotted against the distance away from the starting position (x = 0 nm) of the linescan. From the nanoscale spectroscopic mapping, the glass particle (1st region) and the ORMOCER matrix (2nd region) can be clearly separated from each other. The glass particle region ranging from 0 nm to about 650 nm has a strong Si-O stretch resonance at 1080 cm^{-1} which decreases when the ORMOCER matrix region is probed at about 650 nm as the response of the ORMOCER matrix is much weaker. In addition, the relative intensity change shows a clear increase in intensity at the frequency of 1730 cm^{-1}. This signal increase can be explained through the probing of the carbonyl resonance of the beginning composite matrix. These results show that, using a hyperspectral linescan, the chemical nature of interface heterogeneities can be studied with a very high resolution of a few tens of nanometers. These interface studies are particularly interesting for dental materials showing material failures, as achieving a deeper understanding of the failure process based on chemical anomalies may, in the future, lead to improvements of the materials used.

5.5 Discussion

Our comparative study shows that multiscale infrared spectroscopy is a powerful method to understand the complex multi-material systems associated with dental fillings. The acquired spectral data sets provide a unique opportunity to directly compare different state-of-the-art IR microscopy techniques on a dental sample and show the advantages and disadvantages of each individual method and clarifies which spectroscopic and imaging questions they are best suited to answer.
The FTIR-microscope possesses a broad spectral range (700 – 4500 cm^{-1} limited by the detector). This ability, which makes it possible to detect most vibrational peaks, can even be used to identify all C-H and O-H stretching vibrations at higher wavenumbers. These resonances cannot be detected with the QCL-IR microscopes or the s-SNOM, as it is out of the tuning range of the IR lasers used in this study. The whole spectroscopic response of the sample in each pixel of the FOV can be mapped and is obtained in the form of hyperspectral data cubes. However, the low intensity globar light source, which is also used in traditional FTIR-spectrometers, leads to low SNR and causes long integration times of around three hours for a high-quality spectroscopic map of the whole dental filling. Furthermore, the FOV of 170 × 170 µm is too small to map the whole dental filling, which requires stitching together of single maps to visualize the entire area and can lead to stitching artefacts. In addition, the resolution of the FTIR-microscope is relatively low due to the low resolution of the FPA detector. This makes it difficult to identify the position of the interface between adhesive and composite from the reflectance maps at 1000 cm^{-1} and the pores at 1710 cm^{-1}.
In contrast, laser-based QCL-IR microscopy is ideal for mapping the dental fillings and for advanced image analysis, because it benefits from a better FPA detector and achieves a higher resolution than FTIR-microscope. The FOV is large enough to image the adhesive, part of the dentin/enamel and part of the composite. An additional advantage is the fast acquisition time for the hyperspectral data cube of the dental sample. It takes anywhere from 1 to 15 min, depending on how much data is averaged to achieve precise results. The high-quality reflectance images can then be utilized to rapidly calculate the porosity of adhesives. The example of the algorithmic porosity detection is just one of many possible uses of high-resolution infrared reflectance maps of the tooth sample. We envision that similar to current trends in label-free automated digital pathology[154], dental material and tissue can soon be rapidly classified and assessed with the help of artificial intelligence trained on many high-resolution images obtained from QCL-IR microscopes. A disadvantage of QCL-IR microscopy is the current limited spectral range of the quantum cascade laser system from 950 to 1800 cm^{-1}. Important vibrations above 1800 cm^{-1} such as the C-H stretching vibration located around 3000 cm^{-1} or the cyanide stretching vibration located at 2200 cm^{-1} cannot be detected. This limit makes it more difficult to map and detect certain chemical groups and processes which are connected to these functional groups.
As opposed to far-field microscopes such as the FTIR- and QCL-IR microscopes, which are not able to resolve structures below a few micrometers in size, s-SNOM is perfectly suited to investigate the nanostructure of the samples surface and to decipher chemical heterogeneities on the nanoscale essential for modern day high-tech composite materials. Its resolution is in principle only limited by the radius of the tip, which is in the case of this study around 40 nm. Another advantage of the s-SNOM is that it records topographical maps and optical maps simultaneously. This capability comes with the price of a very small scan area of at the most 100 × 100 μm. Additionally, as opposed to the maps obtained by the other two microscopes, the optical map is not a full hyperspectral data cube. The map shows either the IR-absorption of the sample at a very narrow wavelength with the pseudo-heterodyne detection mode or an

averaged backscattering intensity of the broadband laser spectrum in the white light mapping mode, which does not carry specific chemical information. The acquisition of FTIR spectra is, of course, possible in the nano-FTIR mode, but already a single point spectrum has an acquisition time of about 2 min thus, making it difficult and time-consuming to attain a full well-resolved and high signal to noise spectral data cube of a large scan area. However, by first attaining a white light map of the sample and then investigating optically interesting areas with nano-FTIR point spectra or a hyperspectral linescan, it is possible to attain nanoscale chemical information in several minutes. Finally, the nano-FTIR mode is limited at the moment by the wavelength range of the nano-FTIR laser of 800 cm^{-1} with five different central tuning points ranging from 600 cm^{-1} to 2000 cm^{-1}. This limits the nano-FTIR investigation to a comparatively small range of wavenumbers for a single spectrum. However, if only a single specific resonance is imaged using the pseudo-heterodyne imaging mode, it is possible to obtain images of several micrometer sized areas in a few minutes.
Similar results to pseudo heterodyne imaging can also be attained by using the AFM-IR imaging technology, which is based on photothermal expansion as opposed to scattering[148]. Furthermore, a similar study has been conducted in which the authors monitor the degree of conversion and the local polymer strain of similar adhesive polymers with synchrotron-based FT-IR wide-angle imaging with spatial oversampling[158]. This IR-imaging and spectroscopy method has the advantage of a wide spectral range from 4000 cm^{-1} to 800 cm^{-1}, a better SNR compared to the classic FTIR microscope systems and high resolution with an effective pixel size of 0.54 μm × 0.54 μm at the sample plane over the whole MIR range and a fast acquisition time of 5 min per FOV. This study nicely demonstrates amount of material related information, which can be extracted from hyperspectral maps of dental materials but is limited in applicability to classic material science laboratories as it is based on an advanced synchrotron light source, which is normally not easily accessible for fast material optimization studies. Finally, Raman based imaging and spectroscopy methods should also be thought of, when thinking of methods to analyse complex dental material as the interesting results of for example C-F Raman spectroscopy show when analyzing the fluorosis of dental samples[159]. This comparison shows that there is no jack of all trades but that, the right imaging solution needs to be chosen and carefully evaluated depending on the required information.

In conclusion, we conducted a comparative study of three state-of-the-art IR microscopy techniques on the same dental sample. Our results reveal that all the microscopes can visualize the different functional areas on the dental sample based on the recorded IR-images and characterize their chemical content with IR-spectra. The FTIR-microscope is perfectly suited to identify the most relevant molecular components of the adhesive and composite in the dental fillings by their absorption spectra. Furthermore, it can visualize different materials in the dental section. The images from QCL-IR microscopy show a higher resolution and can be used for more sophisticated image processing such as the rapid algorithmic determination of the porosity of the adhesive. A better understanding of the nanocomposition of the dental filling can be obtained with s-SNOM, which can visualize the nanostructures found in the composite as well as the interface between the adhesive and the composite. We envision that the use of spectroscopic IR microscopy will lead to better insights of the micro- and nanostructure of dental materials and, as a result, in materials with lower failure rates, potentially lower cost, better biocompatibility and a more positive patient experience. Furthermore, we hope that the comparative study helps dental material scientist to better understand the techniques and to adopt these techniques in their work flow.
Importantly, the study was limited to dried biological samples as the operation of the AFM in liquid is difficult. Furthermore, the alignment of infrared optics in water is very difficult due

to the strong water absorption in the infrared range. However, it would be of great use to study processes and samples in-liquid because most of the processes and samples in biology, biochemistry and pure chemistry such as cells, proteins or catalysts are associated with a liquid environment. In the next chapter a study is presented, which shows a method that enables hour long stable measurements of soft matter samples in liquid.

6

Transient infrared nanoscopy of single photoswitchable lipid vesicles in water

6.1 Introduction to photoswitchable lipid particles

Lipid-based nanocarriers, such as liposomes and lipid nanoparticles (LNPs), have emerged as a leading platform technology in nanomedicine[160,161]. Their key advantage lies in the ability to encapsulate hydrophobic drugs or molecular nanoagents for targeted delivery. Unilamellar vesicles, the most basic form of nanocarriers, have already found their way into clinical applications[162]. In addition, LNPs represent arguably the most advanced nanocarrier technology and have played a crucial role for the successful in-vivo administration of mRNA-based vaccines[163]. Enhancing the performance of liposomal nanocarriers, including both liposomes and LNPs, depends on optimizing strategies to control site-specific release mechanisms and upon an external trigger[164]. Light is ideally suited for this task due to its contactless nature and ease of focus. Photoswitchable molecules integrated into or forming part of the lipid membrane can facilitate liposome release. Recently, Chander *et al.* made significant progress towards this goal by using the azobenzene-based photoswitchable-phosphatidylcholines azo-PC[55], and red-Azo-PC[165], in lipid nanoparticle formulations, enabling controlled drug release upon irradiation at specific wavelengths[166]. Their work demonstrates the feasibility

of integrating photolipids into clinically approved lipid formulations, showing large promise for future development.

Imaging and spectroscopy techniques in the MIR spectral range are an ideal toolkit for investigating the chemical composition of different organic and inorganic samples[12] due to the wavelength-specific absorption of infrared light by the chemical material's bonds, often referred to as the "spectroscopic fingerprint". In the case of photoswitchable lipid membranes, MIR spectroscopy is particularly useful for analyzing the isomerization of the membrane-embedded photolipids in a label-free and non-destructive manner without interfering with the switching process itself[13,167]. However, conducting MIR imaging and spectroscopy on a single lipid vesicle requires a methodology that simultaneously provides sufficient nanoscale spatial resolution and high temporal resolution to resolve the photoswitching dynamics. s-SNOM[11,33] is ideally suited for this task due to it's spatial resolutions down to 20 nm[38]. The method has been highly successful for studying dried single biological macromolecules[15] and dried lipid monolayers[168], and has already been extended to observe living biological entities in their native environment[48].

A critical gap in optimizing photolipid-nanocarriers has been the lack of effective tools for studying membrane photoisomerization at the single liposome level. Previous studies have shown that azobenzenes quench fluorescence and dye molecules further interfere with the isomerization process[169], which renders fluorescence-based methods less favorable. While atomic force microscopy AFM[170], interferometric scattering microscopy[171] and TEM[172] allow for investigating liposome shape and size with sufficient resolution, they do not provide any chemical insights into the isomerization process. Nanophotonic based sensing approaches show great promise for spectroscopically tracking complex dynamics, but lack the simultaneous flexibility to image the system[73,173–175].

Here, we demonstrate the use of in-situ nanoscopy to image and spectroscopically analyze, individual photoswitchable lipid vesicles with sizes down to 176 nm in aqueous environments. In contrast to previous investigations on naturally progressing biological systems[48], we present the first in-situ s-SNOM study on actively induced dynamic processes by reversibly changing the morphology of a vesicle through repeated ultraviolet/blue light illumination and tracking its spectral response at 30 ms temporal resolution. We demonstrate not only the possibility to detect and distinguish two photoisomeric states of the lipid molecules on the single lipid vesicle level based on subtle changes in their near-field MIR spectra, but also monitor the photoinduced transformations of the lipids in their aqueous environment in real time.

6.2 In-situ near-field infrared spectroscopy of a photoswitchable lipid vesicle

In our experiments, the MIR near field of an irradiated metallic s-SNOM tip probes a water-suspended lipid vesicle through a 10 nm thick SiN membrane, where the vesicle remains adsorbed by Van-der-Waals-forces for extended periods of time (Fig. 6.1a). The advantage of using the membrane is that it prevents sample evaporation while also protecting the tip from contamination by the solution (for experimental details, see chapter 3). Furthermore, the SiN membrane-based in-situ technique enables hours long mechanically stable s-SNOM measurements, without the need to realign optics even when changing samples[48]. The MIR laser beam is tightly focused by a paraboloid mirror onto the tip to generate a highly concentrated near field under the apex (Fig. 6.1a, red area). The optical near field penetrates

through the SiN layer and probes more than 100 nm into the underlying liquid compartment[48]. Back-scattered coherent MIR light is detected in a Michelson interferometer setup, which allows for the extraction of both the MIR amplitude s_2 and phase φ_2 (Fig. 6.1b and chapter 3). The reversible photoisomerization is induced by light from either of two LEDs emitting at 365 nm and 465 nm, respectively, which are aligned to illuminate the whole SiN membrane area homogeneously without generating enhanced near fields (Fig. 6.1a, blue area, Fig. 6.1b). The vesicles under investigation are composed of a 50:50 % mixture of 1,2-Dioleoyl-sn-glycero-3-phosphocholine (DOPC) and azo-PC (see Fig. 6.1c and chapter 3 for details on sample preparation)[55]. We choose this ratio as it presents a good compromise between vesicle stability that decrease when the azo-PC content is increased and visible deformation behavior due to photoswitching that is more significant with increasing azo-PC content. The switching wavelengths were chosen from the azo-PC UV-VIS spectra (Fig. 6.1d). Illumination of the lipid vesicles with a wavelength of 365 nm triggers the isomerization of the azobenzene moiety from *trans* to *cis*, while, conversely, illumination at 465 nm switches the molecules to the thermodynamically more stable *trans*-state.

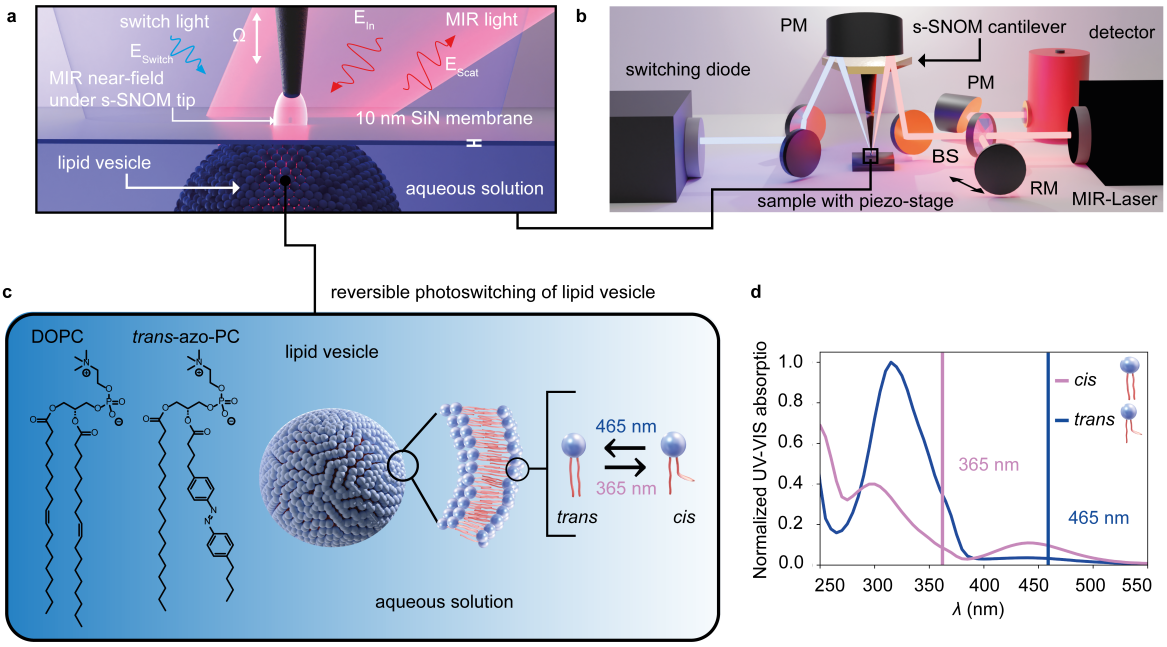

Figure 6.1: In-situ s-SNOM setup and infrared spectroscopy of photoactive lipid vesicles. (a) Operating principle of the membrane-based in-situ s-SNOM method. An s-SNOM tip with its associated near field scans in tapping mode at a tapping frequency Ω above a 10 nm thin SiN membrane, which separates the tip from lipid vesicles suspended in an aqueous medium. The tip and membrane are illuminated by two different light sources: a MIR beam (E_{in}) for near-field spectroscopy and imaging and a UV-VIS source (E_{switch}) to switch the lipid vesicles between their different photoisomeric states. **(b)** S-SNOM setup with the MIR beam and the UV light focused onto the s-SNOM tip and sample by a parabolic mirror (PM). The focused MIR beam creates an enhanced near field that interacts with the sample underneath. The MIR light backscattered from the tip (E_{Scat}) containing the spectroscopic information of the liquid sample is collimated and interferes with a reference beam that is reflected by a movable reference mirror (RM). The resulting signal is recorded by a fast response infrared detector (see chapter 3). **(c)** Molecular structure of the DOPC and *trans*-azo-PC lipids constituting the lipid vesicle in a ratio 50:50 and sketch of the light-induced conformational change. **(d)** UV-VIS spectrum of both lipid isomers with switching wavelengths labeled by the blue and violet vertical lines.

The photoswitching of azo-PC lipids has been analysed by MIR spectroscopy[13,167], as we confirm for our samples using ATR-FTIR spectra of dried azo-PC films (Fig. 6.2). The carbonyl band at 1743 cm^{-1} remains unaffected by the photoswitching[55,167], whereas clear differences in spectral intensity between the *cis*/*trans*-isomers are evident from the resonances

at 1606 cm^{-1}, 1495 cm^{-1} and 1463 cm^{-1}, which can be assigned to the ring breathing mode of the *trans*-azo-group and CH_2-backbone modes found in the azo-PC lipids[13]. All studied resonances feature increased absorption in the *trans*-conformation[13]. In contrast, the DOPC lipid ATR-FTIR spectrum does not change in intensity with different illumination wavelength and does not show a band at around 1600 cm^{-1} (Fig. 6.2).

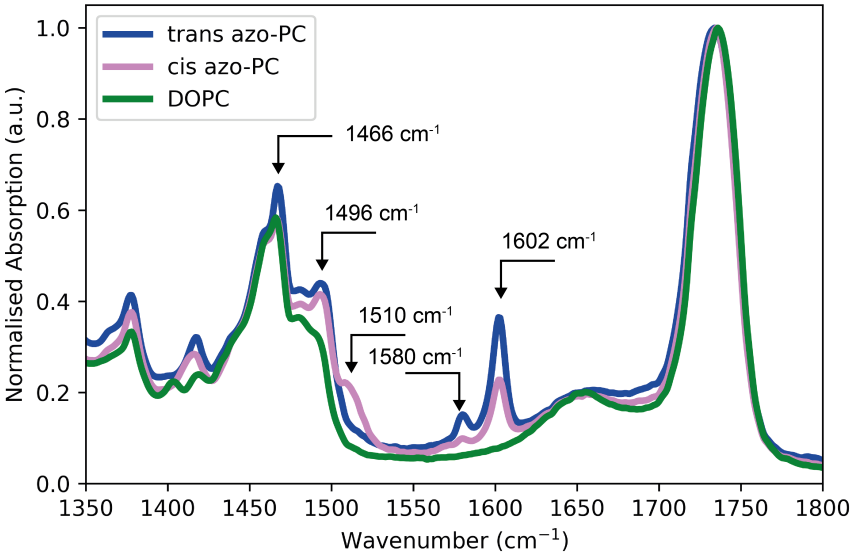

Figure 6.2: ATR-FTIR spectra of lipid vesicle compounds. Normalised ATR-FTIR spectra of pure DOPC (green) and pure azo-PC in the *trans*-(blue) and *cis*-state (violet) measured on dried samples. The data of each spectrum are normalised to the corresponding carbonyl resonance at around 1735 cm^{-1} to compare the peak intensities between the different spectra. The photoswitching between the *cis*/*trans*-state was performed by illuminating the dried sample on the ATR-crystal with 365 nm (*trans* to *cis*) and 465 nm light (*cis* to *trans*).

The in-situ s-SNOM technique enables MIR spectroscopy on individual lipid vesicles in an aqueous environment at length scales impossible to reach by standard far-field spectroscopy approaches. Since the most interesting lipid resonance at 1606 cm^{-1} would be masked by a strong H_2O vibration at 1650 cm^{-1}, we suspended all vesicles in this work in D_2O, a common practice in FTIR spectroscopy of organic materials[48,176] (see Fig. 6.3b, c for comparison of near-field spectra of vesicles in H_2O and D_2O). We first present a spectrally averaged MIR near-field amplitude image (Fig. 6.3d, "white-light image" s_2, see chapter 2 and 3) to identify and target a membrane-fixed vesicle in aqueous solution for further spectroscopic measurements. We subsequently recorded nano-FTIR phase spectra φ_2 at the vesicle's center (Fig. 6.3d location of the red cross and 6.3e), where the highest scattered white-light signal is observed and therefore a high SNR of the recorded spectra is expected. In both photoisomerization states, these spectra show the characteristic resonances of the lipid system, such as the carbonyl peak, the CH_2-backbone modes[13,167], and a resonance at 1606 cm^{-1} (see Fig. 6.3a for a detailed assignment to the molecular bonds of DOPC and azo-PC). Notably, the resonance at 1606 cm^{-1} decreases in intensity after illumination at 365 nm, indicative for *trans*-to-*cis* isomerization. In addition, the CH_2-backbone modes at 1463 and 1495 cm^{-1} also decrease in intensity. These differences are consistent with our measurements of ensemble averaged far-field ATR-FTIR spectra (Fig. 6.2) and with reports in literature[13,167]. Importantly, the carbonyl signal at 1742 cm^{-1} of the nano-FTIR spectrum with illumination at 365 nm does not change in intensity compared to the nano-FTIR spectrum at 465 nm as expected from the reference ATR-FTIR spectrum. This fact underlines that there was no fluctuation in the

laser power, change in optical alignment on the tip or detector responsivity in between the recording of the two spectra leading to intensity changes. Therefore, the spectra demonstrate our capability to analyze the chemical composition and distinguish between photoisomers of a nanoscale lipid vesicle by their associated nano-FTIR spectra. Note that the spectroscopic signal of a lipid vesicle in H_2O outside the 1650 cm^{-1} H_2O band (Fig. 6.3c) is of similar good quality and therefore should allow future studies in H_2O suspension.

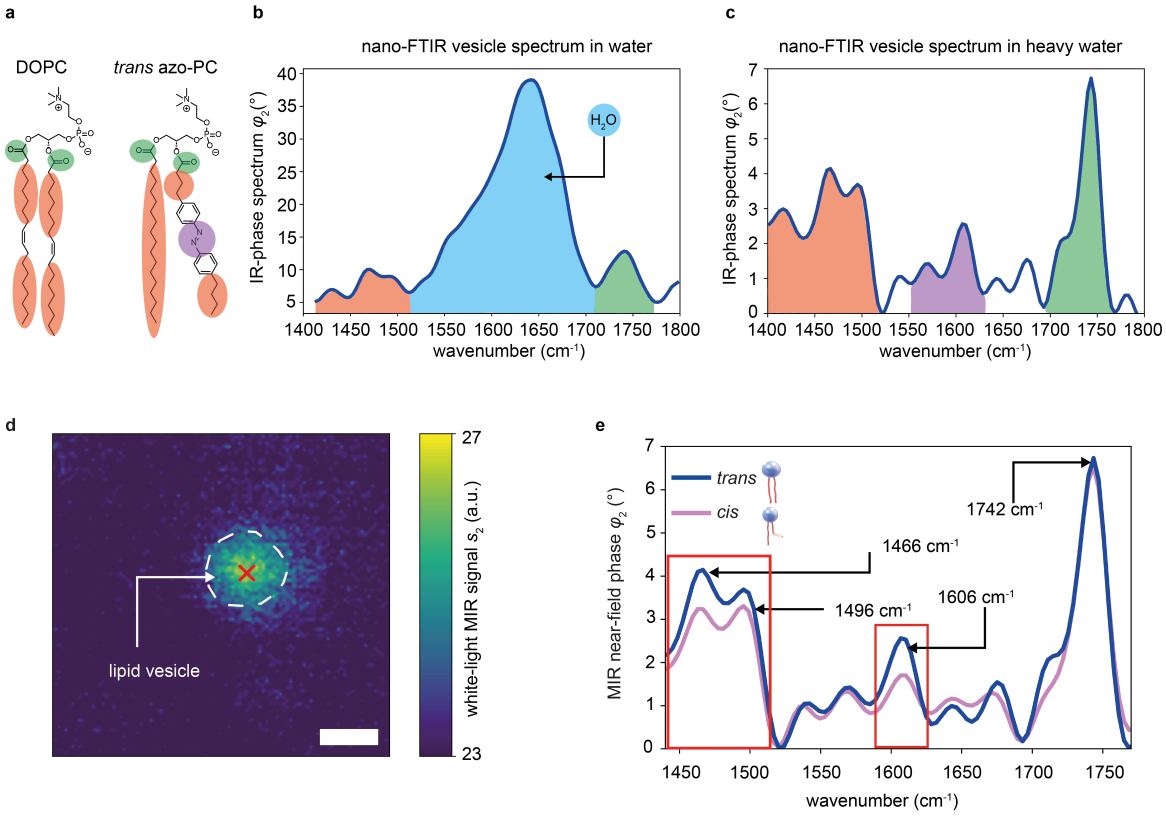

Figure 6.3: Nano-FTIR spectroscopy of a photoswitchable lipid vesicle. (a) Molecular sketches of DOPC and *trans*-azo-PC composing the lipid vesicles with bonds highlighted in specific colours to assign them to the resonances in the nano-FTIR phase spectra **(b, c)**. Experimentally determined nano-FTIR phase spectra (φ_2) of a lipid vesicle suspended in H_2O **(b)** and D_2O **(c)**. **(d)** Spectrally averaged MIR amplitude image (s_2, white-light image) of a lipid vesicle in *trans*-state in D_2O, scale bar 500 nm. **(e)** MIR near-field phase spectra (φ_2) of a *trans*- (blue) and *cis*-state (violet) lipid vesicle **(e)** recorded at the position of the red cross. Red boxes highlight two lipid vibrational MIR bands that respond strongly to the switching light.

6.3 Resonance specific near-field imaging of lipid vesicle

Based on the nano-FTIR spectra recorded on the lipid vesicle, we chose the intense carbonyl resonance to record resonance-specific MIR images. A larger area scan (15 μm x 15 μm) demonstrates the side-by-side coexistence of numerous vesicles of varying sizes, simultaneously measured in both amplitude s_2 (Fig. 6.4a) and phase φ_2 (Fig. 6.4b). Individual vesicles can be clearly identified and localized, as exemplified by close-up views of four differently sized vesicles, indicated as colored boxes (Fig. 6.4c). The vesicles typically exhibit near-uniform phase $\varphi_2 > 25^\circ$ throughout their inside (shown in red), surrounded by a fringe of around 100 nm width (shown in white). We extract quantitative phase profiles along the lines indicated in Fig. 6.4c and determine each vesicle's apparent full width at half maximum

(FWHM, Fig. 6.4d). Despite only being 176 nm in width, the smallest analysed lipid vesicle is still well resolved (albeit with reduced phase signal), which is consistent with the spatial resolution of our setup on the order of 100 to 150 nm[48]. Importantly, this result demonstrates the capability of our method to characterize nanoscale objects even in water, at length scales way beyond the reach of standard fluorescence and phase contrast microscopy.

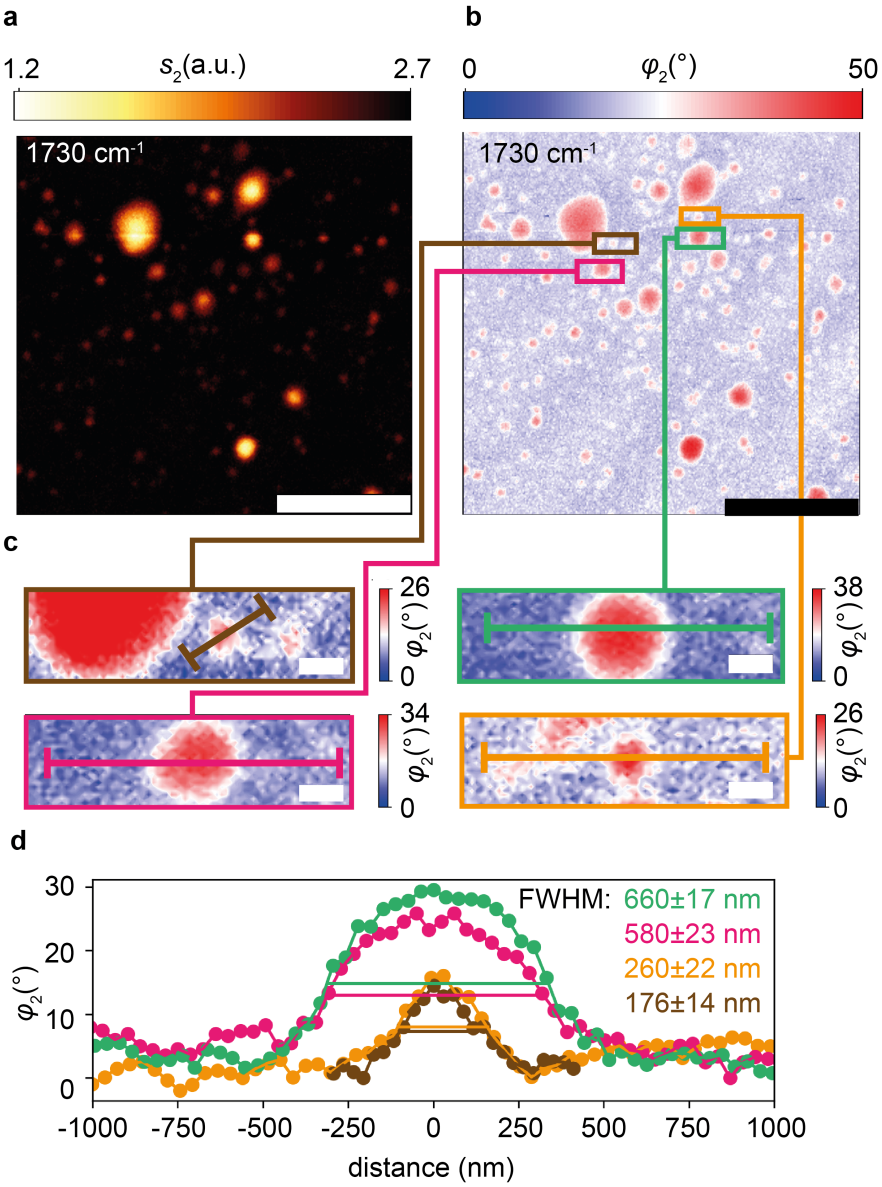

Figure 6.4: Chemically specific MIR near-field imaging of nanoscale lipid vesicles. S-SNOM optical amplitude (s_2) **(a)** and phase images (φ_2) **(b)** of several lipid vesicles suspended in D_2O measured at 1730 cm^{-1} at the carbonyl resonance (see Fig. 6.3e), scale bars 5 μm, acquisition duration 12 min. **(c)** Enlarged phase images (φ_2) of four differently sized lipid vesicles, scale bars 300 nm. **(d)** Extracted profiles along lines drawn in **(c)**, showing full widths at half maxima (FWHM) of 660±17 nm, 580 nm±23, 260±22 nm, and 176±14 nm determined by fitting a Gaussian function to the extracted profile, the error bars being the square root of the diagonal elements in the obtained covariance matrix.

The uniform phase within and amongst differently sized vesicles (Fig. 6.4b) indicates that they undergo a deformation and flattening when adhering to the SiN membrane, as sketched in Fig. 6.1a. This interpretation of the measured, uniform signal is in accordance with previous subsurface s-SNOM studies, which showed that the near-field sensing reaches to around 100 nm depth, whereas objects beyond 200 nm below the tip remain virtually invisible[40,49].

To corroborate this flattening behavior, we compare phase profiles of the 660 nm FWHM vesicle and the largest vesicle (next to the brown box in Fig. 6.4b) with an analytical model for the phase signal of a non-deformable polymeric sphere hanging from a single adhesion point on the SiN membrane. We find that the theoretical profiles have a different form and are narrower than the experimental profiles (Fig. 6.5a, b), supporting our hypothesis of vesicle flattening. This observation demonstrates our optical methods ability to study details of nanoscale adhesion of soft matter systems in aqueous environments. Independent further information about the vesicles can be gained by examining the simultaneously acquired mechanical images or vesicle "footprints"[48], which show a displacement of the SiN membrane upwards by about 1 nm for the green-boxed vesicle location and up to 2 nm for the largest vesicle (Fig. 6.5c, d). This observation clearly shows that even nanoscale soft-matter objects can be detected via distinct deformations of the SiN membrane, in agreement with previous studies[48,176], and should be applicable to characterize even more complex lipid systems.

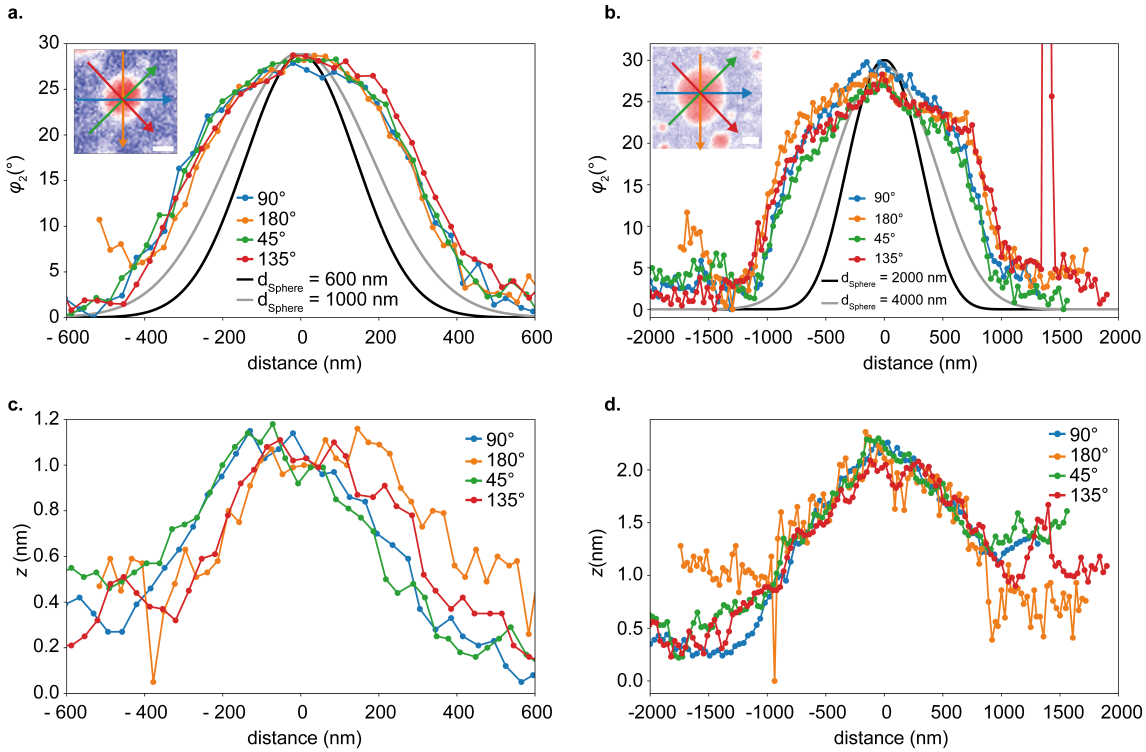

Figure 6.5: Correlated optical phase and topography response of single lipid vesicles. (a, b) Profiles of the green-boxed vesicle and the largest vesicle (next to the brown box) in the phase image shown in Fig. 6.4b, extracted along the arrows indicated in the inset (scale bars 300 nm and 1 μm, respectively). **(c, d)** Correlative topography profiles from the simultaneously measured topographic images (not shown). The theoretical curves in **(a, b)** result from analytically predicting the phase profiles of differently sized, undeformed spheres (d_{Sphere} = 600 nm, 1000 nm, 2000 nm and 4000 nm, material PMMA, tip radius = 60 nm and tapping amplitude a = 80 nm) which are assumed to adhere at one point on the lower surface of a 10 nm SiN membrane (for details see previous literature[48]).

6.4 Near-field imaging resolves reversible photoswitching of a single lipid vesicle

An approximately 500 nm wide vesicle was selected to map photoswitching-induced morphological changes by recording MIR images at 1603 cm^{-1} (Fig. 6.6a, b). Each pair of images was acquired during intervals of approximately 2 min, with illumination periods of at least 1 min for inducing the photoswitching between each step. The time series commences with a round vesicle in the *trans*-state (Fig. 6.6a, b), followed by a blue/UV light illumination sequence to switch the photolipids multiple times between *trans* and *cis*. During the photoisomerization steps, reversible changes of the vesicle shape, directionality of deformation and size were observed. These size expansions of the vesicle when switching from *trans* to *cis* are in good agreement with previous reports, where it was shown that vesicles undergo transformations into less symmetric shapes following *trans*-to-*cis* isomerization[55], and that the area per photolipid molecule increases by about 20%[177] to 25%[178] for *cis* photolipids due to a higher packing density of *trans*-azo-PC in a lipid membrane. For the *cis* isomer, the conformational change of one lipid tail (see Fig. 6.1c) would increase the chain volume, with the lipids assuming a slightly inverted wedge shape. This change in packing density is reflected in the morphological change of the vesicles, which requires a rearrangement of the lipid molecules.

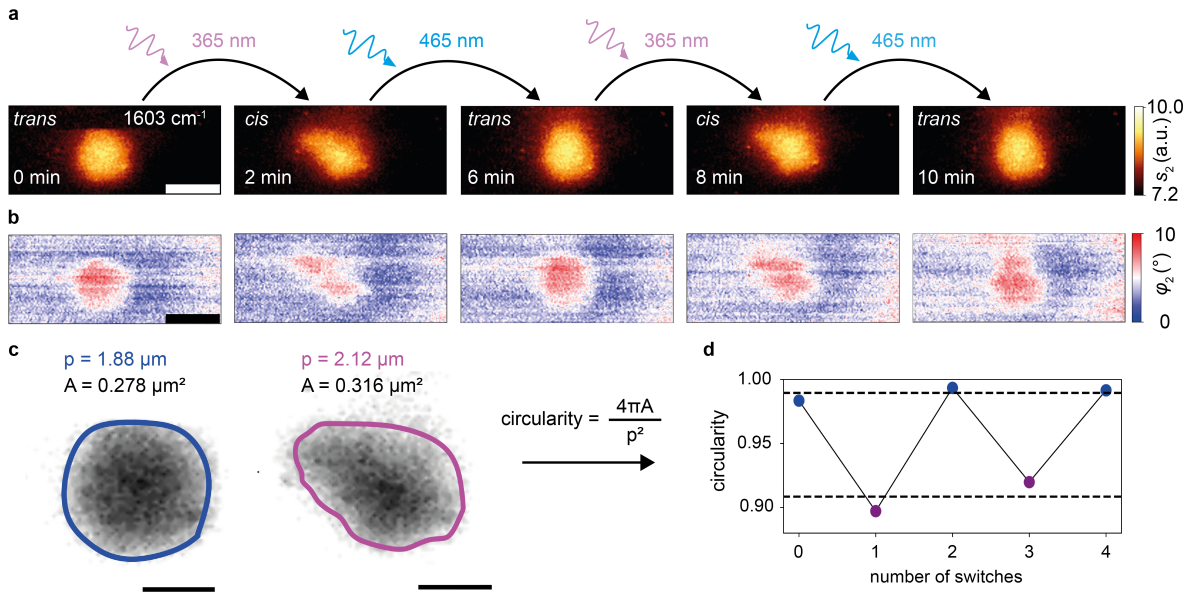

Figure 6.6: Near-field imaging of the reversible photoswitching of a 500 nm diameter lipid vesicle. **(a)** Monochromatic MIR amplitude (s_2) and **(b)** phase images (φ_2) at 1603 cm^{-1} of a lipid vesicle in D_2O being reversibly photoswitched between the *trans*-state and *cis*-state, scale bars 500 nm. **(c)** Illustrated extraction of a "circularity" value for a lipid vesicle defined as $4\pi A/p^2$, with circumference p and area A, where the boundary criterion was s_2 = 7.8 a.u, scale bar 300 nm. **(d)** Reversible change in circularity between the *trans*- (blue) and *cis*-state (violet) of the lipid vesicle over two switching cycles.

To confirm that we can monitor reversible photoswitching over long times and investigate a different lipid configuration in the form of a supported membrane patch adhering to the SiN membrane, we conducted a similar photoswitching time series (Fig. 6.7). The results again highlight reversible area changes due to photoswitching over four cycles within one hour, confirming the high stability and reproducibility of the s-SNOM measurements and the good reversibility of the switching process.

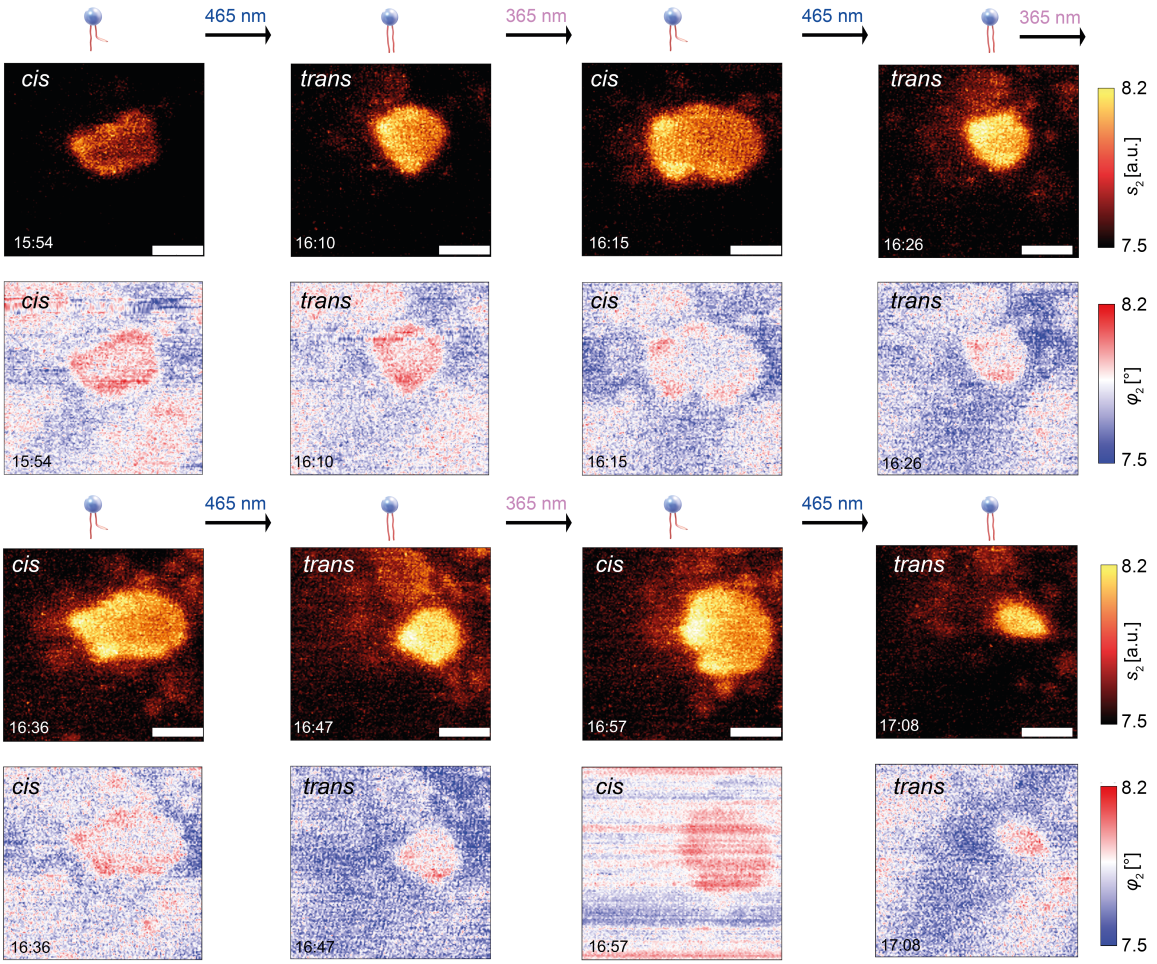

Figure 6.7: Reversible photoswitching of a lipid patch. Optical amplitude (s_2) and phase (φ_2) image series of a lipid patch being reversible photoswitched between the *cis* and *trans*-state showing a reversible expansion (*cis*-state) and contraction (*trans*-state) over a 1 h measurement time, scale bar of 1 µm for all images.

Furthermore, the time-series images (Fig. 6.6a, b), were used to extract both the vesicle's area A and its "circularity" as a FOM for the asymmetry between both states as defined in Fig. 6.6c. Circularity is a commonly employed shape factor in image analysis[179,180], that numerically describes the comparability of the vesicle to a perfect circle. The vesicle resembles a perfect circle at a value of one and deviates from the ideal circle shape with a lower value. We delineate the vesicle's boundary by setting a threshold value of s_2 = 7.8 a.u. This value was chosen to encompass the area where the optical amplitude is above $\frac{1}{e}$ of its maximum value at the particle center (after background subtraction). The changes between both photoisomerization states are significant and well reproduced (Fig. 6.6d), amounting to an increase of 10% in area and a decrease of 8% in circularity for the *trans*-to-*cis* transition. One possible explanation for the change in circularity is that the 50% mixture of azo-PC and DOPC used in our samples displays lower bending rigidities (which quantifies the energy needed to change the membrane curvature[181]) in the *cis* compared to the *trans*-state, which aids vesicle deformation and explains the observed change in morphology[182]. Additionally, the photostationary state (PSS) i.e. the *trans*-to-*cis*-ratio reached by the photoisomerization process, may not be quantitative, meaning that not all azo-PC lipids assume a 100% *trans*- or *cis*-conformation due to photoisomerization. The PSS is influenced by many experimental parameters, including the solvent, temperature, and the illumination conditions. For pure azo-PC vesicles in water, it was shown by small angle X-ray scattering that the fraction of *cis*-lipids

in the blue adapted state (after 465 nm illumination) is still about 30%, while a considerable fraction of about 27% of the photolipids remain in a *trans*-state after UV illumination[183]. Furthermore, *trans*-lipids are prone to form H-aggregates, which may lead to phase separation and demixing of *trans*-lipids into different domains on the vesicle membrane leading to the observed expansion[184]. Our method opens the door to studying such complex photoinduced deformation effects on a multitude of other nanoscale systems such as photoswitchable metal-organic frameworks[185] and nanoparticles[186].

6.5 MIR near-field signal tracking of the switching dynamics of a single lipid vesicle

Resolving fast photoswitching dynamics of single lipid vesicles requires nanoscopy methods that effectively track rapid structural and chemical changes. However, standard s-SNOM imaging is limited by slow mechanical scanning speeds even for comparatively low per-pixel signal integration times t_p, resulting in long imaging durations, for example, 50 s for a sub-μm lipid particle in water (Fig. 6.6a, b), where 150 pixel by 100 pixel were acquired using t_p = 3.3 ms.

We address this inherent limitation of scanning probe methods by implementing a transient MIR nanoscopy method applicable to both aqueous and dry samples. The method continuously records the near-field s-SNOM signals s_2 and φ_2 at a set integration time. A specific wavelength is selected to achieve the maximum spectral response to photoswitching, and the tapping tip is placed on the center of a selected vesicle and remains stationary during the recording. A suitable vesicle is first identified by recording an MIR image at 1603 cm^{-1} (Fig. 6.8a, b). Subsequently, we confirm the vesicle's photoresponsivity by imaging the morphological distortion of the vesicle due to photoswitching. We then place the tip onto the center of the vesicle (red and black crosses in Fig. 6.8a, b) to prevent signal distortion due to movement of the vesicle. The s-SNOM signals are recorded at this defined position at 1603 cm^{-1} and a time resolution of t_p = 500 ms (Fig. 6.8c, d). The signal acquisition was started after illuminating the sample for over 1 min at 465 nm, followed by switching once every minute between 365 nm and 465 nm (violet and blue part of the signal trace in Fig. 6.8c, d). When the vesicle is switched to the *cis*-state, both amplitude and phase traces show clearly monotonic decreases, consistent with the recorded ATR-FTIR and nano-FTIR spectra (see Fig. 6.3). Likewise, both signals increase monotonically when the vesicle is switched back. Upon exposure to 365 nm light, the optical amplitude decreases by about 10%, from 1.16 to 1.07 (normalized to the average signal of D_2O), while the phase decreases by about 1.6°. Notably, after an initial slow change, the signals in Fig. 6.8c, d exhibit drastically accelerated changes that last only down to 1 s in some cases and appear delayed after about 11 s in both amplitude and phase.

This overall sigmoidal behavior indicates that interesting cooperative effects between the lipid molecules might come into play during membrane photoswitching. Non-exponential and delayed-onset transitions have been observed for pure azo-PC vesicles by ensemble-averaged UV absorption measurements in liquid suspension[177,184]. During photoisomerization, abrupt changes of the lipid conformation along with a change of intermolecular interactions between *trans*- and *cis*-azobenzene embedded in a DOPC environment affect the isomerization dynamics[187]. Stronger lipid-lipid interactions of azo-PC are present in the *trans*-state, where the molecules form H-aggregates[184,188] and are packed more densely[177,189]. At the onset of UV illumination, the *trans*-*cis* ratio changes towards a *cis*-rich environment.

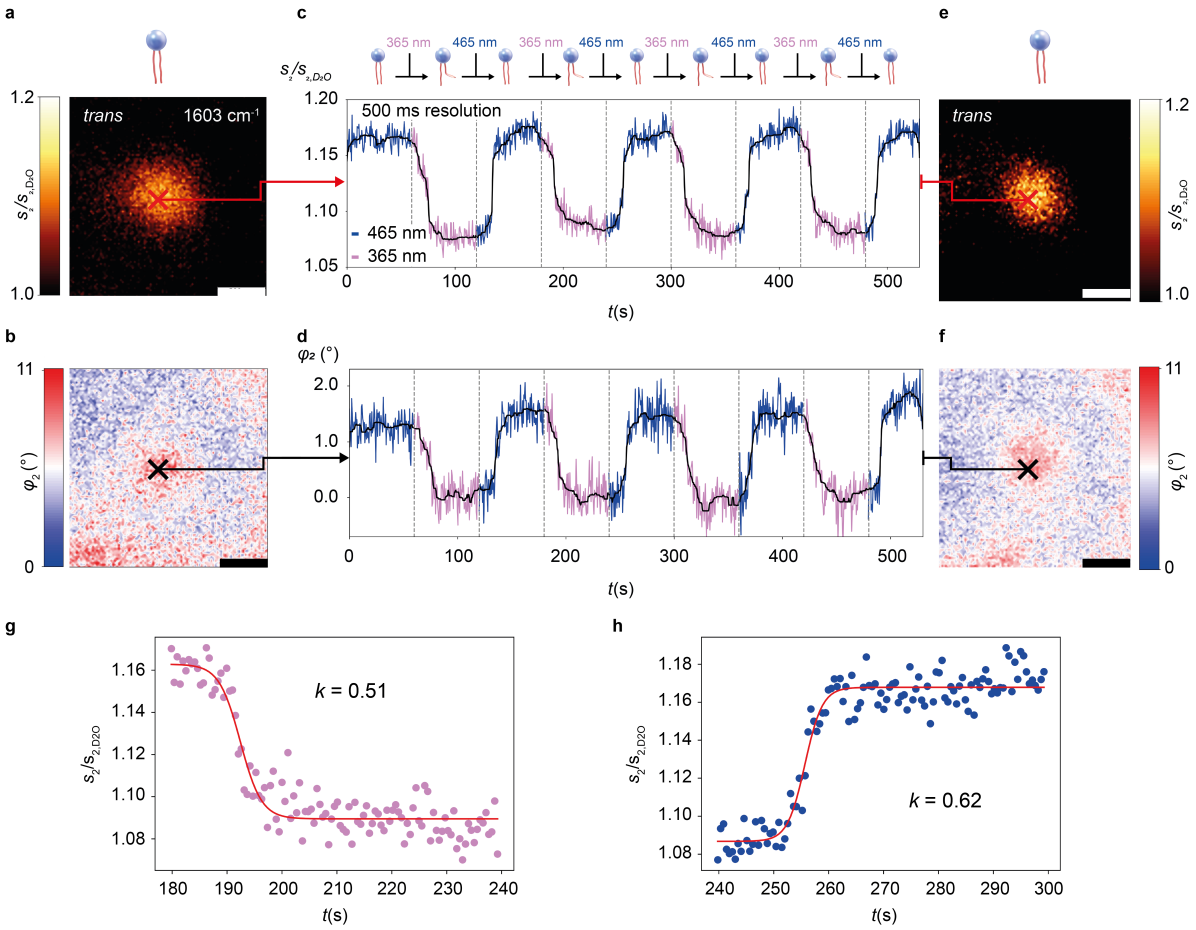

Figure 6.8: Resolving the photoswitching dynamics of a single nanoscale lipid vesicle by millisecond MIR near-field signal traces. (a) Optical near-field amplitude image normalized to the surrounding D_2O (s_2 /s_{2,D_2O}) and **(b)** near-field phase image (φ_2) recorded at 1603 cm^{-1} with 2 min acquisition time, directly before starting the MIR signal trace acquisition at the position of the cross, scale bars 500 nm. The recorded amplitude (s_2 /s_{2,D_2O}) in **(c)** together with the phase (φ_2) in **(d)** reveal the photoswitching dynamics at a temporal resolution of 500 ms. The symbols above in combination with the dashed vertical lines indicate when the illumination wavelength was switched to the value written above. The blue and violet coloring of the signal traces mark the switching light's wavelength at each point. The black curves are moving averages of the measured points. **(e)** Optical amplitude and **(f)** phase images taken directly after acquiring the near-field traces show that the vesicle remained stable in both position and signal strength, even after seven consecutive switching transitions, scale bars 500 nm. **(g, h)** Exemplary sigmoidal fit of the transient time trace for investigating the photoswitching dynamic in *trans*-to-*cis* and *cis*-to-*trans* direction. The extracted growth parameters k determines the steepness of the switching behaviour describing how fast the system responds. The average k-value for the *trans*-to-*cis* switching is 0.4±0.1, whereas the k-value for the *cis*-to-*trans* switching is 0.8±0.4, indicating that the *cis*-to *trans*-switching occurs faster. The fitting was performed with a sigmoidal function of the following form $f(x) = \frac{L}{1+e^{-k(x-x_0)}} + C$.

Therefore, the photoisomerization is slower in the beginning, where a lipid conformation change is sterically hindered in the dense membrane assembly. In the extreme case of self-assembled monolayers, it has been shown that steric hindrance can even prevent the *trans*-to-*cis* isomerization altogether[190]. As the membrane is shifted towards a *cis*-rich state, more space is made available, which facilitates the overall switching of the azobenzenes.
In general, *cis*-to-*trans* isomerization is faster, as lipids are switched to their thermodynamically favorable state, although switching rates are strongly dependent on the illumination conditions and light intensity[177]. This fact is supported by the extracted growth parameters k through a sigmoidal fit of the time traces (Fig. 6.8g, h), which indicate a higher switching speed in the *cis*-to-*trans*-direction in comparison to the *trans*-to-*cis*-direction. The abrupt

change of the isomerization curve observed in both directions (Fig. 6.8c, d) has not been observed in absorption measurements of vesicle solutions. Furthermore, a delay was also observed for the onset of *cis*-to-*trans* isomerization, which likely originates from membrane reorganization taking place as the photolipids reduce their lipid footprint accompanied by an overall reduction of the bilayer fluidity[182] and vesicle deformation (Fig. 6.6).

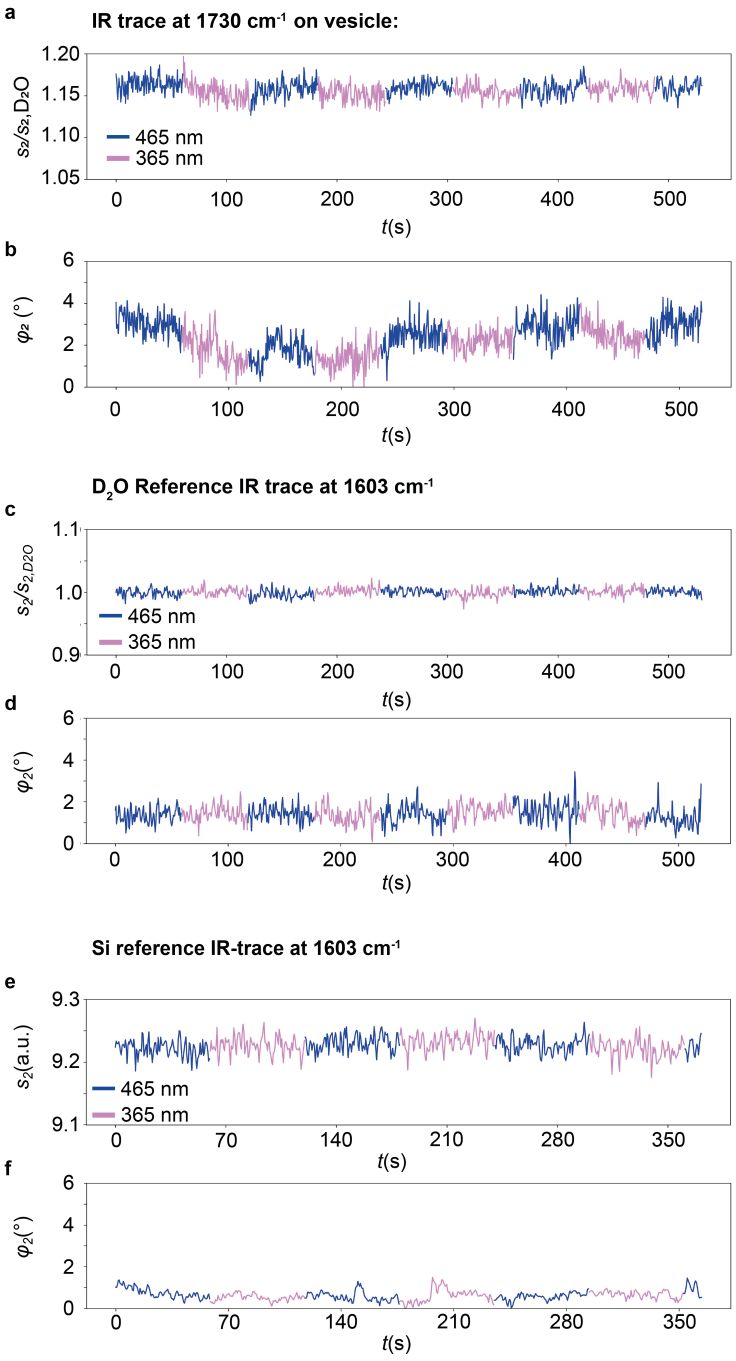

Figure 6.9: Reference near-field signal traces. Near-field signal trace of the optical amplitude normalised to the D_2O signal (s_2 /s_{2,D_2O}) **(a)** and of the optical phase (φ_2) **(b)** recorded at 1730 cm^{-1} on the vesicle shown in Fig. 6.8. Near-field optical amplitude (**c**) and phase (**d**), recorded at 1603 cm^{-1} on D_2O next to the vesicle shown in Fig. 6.8. Near-field optical amplitude **(e)** and phase **(f)** signal trace recorded at 1603 cm^{-1} on a clean Si surface. The blue and violet colouring of the trace specifies the wavelength of the switching light of 465 nm and 365 nm used at the specific time of the trace.

However, the finding is consistent with the dynamics observed by time-resolved monitoring of supported photolipid bilayer isomerization by single particle plasmonic sensing[191]. This supports our understanding that nanoscopy on a single vesicle level, where real-time information is obtained from a localized membrane area under homogeneous illumination, provides further insight to otherwise hidden details of photoisomerization dynamics of photolipids in a bilayer assembly. Remarkably, this back-and-forth switching could be continuously monitored over an 8 min duration, encompassing four complete switching cycles. After recording the time trace, we recorded another MIR image (Fig. 6.8e, f) to verify that the vesicle has not shifted in position relative to the tip, thus eliminating the possibility of signal fluctuations due to vesicle displacement during the switching process.
For comparison, we recorded a second transient signal trace at 1730 cm^{-1} (Fig. 6.9a, b), probing the carbonyl resonance that should remain unaffected by the photoswitching-induced molecular changes observed in Fig. 6.2. We measured only relatively small amplitude and phase signal changes, verifying that at 1603 cm^{-1} we did probe the molecular switching. We attributed the recorded decrease in amplitude and phase from the *trans*- to the *cis*-state to a reduced lipid density in the *cis*-state[184]. Moreover, we recorded a signal trace on D_2O next to the vesicle (Fig. 6.9c, d) and on a clean silicon surface (Fig. 6.9e, f). Both traces exhibited stable amplitude and phase signals, confirming that the measured switching signals are not due to mechanical or optical artifacts induced by the switching light.
To explore the temporal resolution limits of our in-situ tracking of dynamic processes, we repeated photoswitching experiments at different integration times of the Ps-Het signal trace t_p ranging from 30 ms to 500 ms (Fig. 6.10). The signal-to-noise characteristics allowed to detect a photoswitching signature at a temporal resolution as short as 30 ms with a statistical significance limit of 3.72σ (see Fig. 6.10c). Notably, by increasing the integration time to 100 ms the SNR jumps to 5.5σ, showing the great potential for the technique to also be applied to dried samples such as for example the investigation of photoactive proteins at the single-molecule level[176]. Since these experiments do not need to be conducted in aqueous environment, even higher SNR as shown here could be expected. In addition, this method could be extended to a multi-color Ps-Het approach[36]. In this case multiple wavelength are measured at the same time allowing to record the transient dynamics at several wavelengths simultaneously providing richer chemical information about the underlying dynamic process.

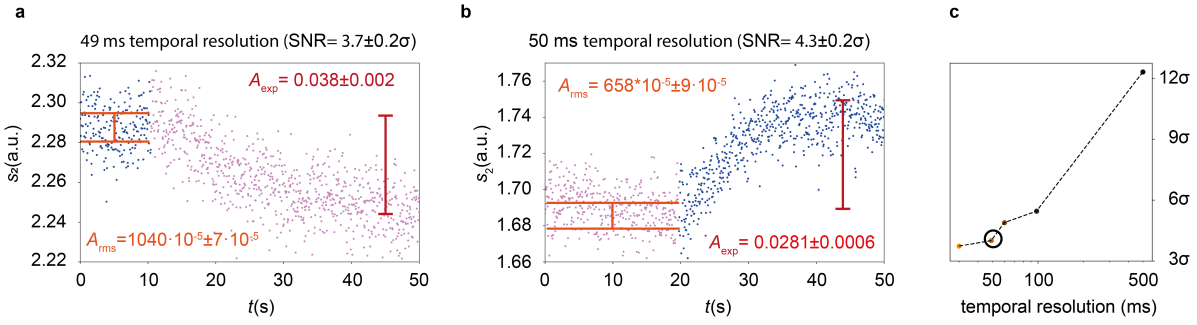

Figure 6.10: Temporal resolution limit of the in-situ photoswitching detection. Exemplary near-field time traces of the optical amplitude s_2 recorded with 49 ms temporal resolution of the **(a)** *trans*-to-*cis*-switching process and **(b)** *cis*-to-*trans*-switching process. The recorded experimental signal values (A_{exp}) are marked by the red bars and the root mean-square of the noise of the steady-state signal (A_{rms}) before the switching perturbation is marked by the orange bars. Based on these values the signal-to-noise values for the photoswitching process have been determined. (**c**) The associated signal-to-noise metrics in relationship to time traces with different temporal resolutions of the photoswitching dynamics. For all the recorded time-traces the commonly accepted threshold value of 3σ is exceeded showing that the dynamic photoswitching process can be resolved with 30 ms temporal resolution.

6.6 Discussion

By combining near-field microscopy with ultrathin membranes and fast signal acquisition methods, we have demonstrated the label-free imaging and spectroscopic detection of actively triggered photoswitching processes in lipid nanovesicles as small as 176 nm in their native aqueous environment. Specifically, we utilized our method to resolve reversible photoinduced shape changes in the vesicles over multiple switching cycles. This capability enables future studies of shape effects in photorelease processes for a wide range of nanocarriers. Furthermore, leveraging the inherent spectral and therefore chemical sensitivity of MIR nanoscopy, even at the single lipid vesicle level, we could differentiate two main photoisomeric states of the photoswitchable vesicles based on nano-FTIR spectra. The chemical specificity of this method holds great potential for investigating other complex lipid systems on the nanoscale, such as the chemical composition of domains in lipid vesicles[184] or dynamics of lipid nanoparticles loaded with therapeutic compounds like mRNA. Here, one could consider first forming a supported bilayer on the SiN membrane and then studying the fusion process of the lipid nanoparticle with the bilayer, mimicking a cellular environment and circumventing the problem of the vesicles adhering on the membrane and changing their dynamics.
Additional information about the geometry of the vesicles was obtained by comparing measured phase profiles of a single vesicle with an analytical model for a nondeformable sphere, suggesting a distinct flattening of the vesicles when adhering to the membrane. The vesicles were also identifiable in the correlative mechanical images, where we attribute the upward displacement of the membrane to van-der-Waals-forces exerted by the vesicle. A potential solution to removing unwanted topographical artefacts caused by surface roughness is to use image reconstruction algorithms to correct optical images via the simultaneously measured topography[192], as well as improving fabrication methods.
Importantly, we implemented a transient MIR nanoscopy technique to extract the switching dynamics of a single lipid vesicle with millisecond time resolution. It is significant to note that we conducted the experiments on vesicular systems in liquid, which exhibit rather weak backscattering. One way to increase the scattering signals and with it the time resolution by as much as an order of magnitude would be the use of broader tips (albeit leading to reduced spatial resolution)[43]. With other, more strongly scattering objects, the time resolution would potentially improve to the μs range. This could be particularly interesting for electrically modulated solid-state materials[193], and would require higher phase modulation frequencies offered by photo-elastic or acousto-optic modulators[194,195]. Moreover, improvements in MIR laser stability and power, in addition to optimizing collection optics, could increase the SNR and lead to shorter acquisition times.
It is important to acknowledge the short coming of the membrane based liquid s-SNOM method and contrast it to competing methods, which also enable liquid s-SNOM. For one, the resolution of the membrane-based method is around 100 nm using 10 nm SiN membranes. In comparison, there are several approaches that measure s-SNOM or AFM-IR directly in liquid achieving resolutions only limited by the apex of the tip and enabling the recording of the full topographic information of the sample[196–198]. However, these approach all employ an ATR-based transmission illumination of the tip, which is difficult and time consuming to align. Moreover, we believe that our method enables more robust and longer duration experiments as the tip and the optical alignment is protected from the liquid environment. This protection allows more complex nanoscopy studies of e.g. living cell[48] or in the case of this manuscript dynamic photoswitching. To increase the resolution limit with a membrane method a straightforward approach would be to deploy a thinner membrane layer, which is still mechanical stable enough for water to adhere to it and perform a tapping AFM move-

ment. For example, liquid s-SNOM studies have been conducted with ultra-thin graphene capping layer[199–201] and oxide capping layers such as TiO_2 and Al_2O_3[202], which enable higher resolution imaging in liquid. Elevating this idea, it has been demonstrated that a liquid virus sample can be wrapped in a graphene sheet and investigated with s-SNOM enabling true nanosale imaging and topography recording with a capping layer[203]. These capping layers have the additional benefit of having no phonon resonance in the MIR compared to SiN, which exhibit a strong resonance in the range of 800 to 1150 cm^{-1} masking important molecular infrared resonances[48]. Ultimately, it is also the ease of availability and usage that makes complex studies with many consecutive experiments possible. Here, the wide and cheap commercial availability of the SiN membranes help to match these requirements as opposed to other capping layers, which need to be self-fabricated for every experiment.
In applications requiring super-resolution imaging, using finer tips in our s-SNOM measurements (ideally down to about 30 nm) in combination with thinner membranes could significantly improve both the optical and the mechanical spatial resolution. This would also reduce the near-field probing depth to 30 nm as the near-field probing depth is highly dependent on the tip. The small probing depth[48] would be ideally suited to image the adhering portion of a vesicle's membrane with improved contrast. Additionally, this approach could be key to detecting inhomogeneities like lipid rafts and other nanostructures[43].
Note that in principle, our method is not limited to either relatively slow imaging (Fig. 6.6a, b) or fast one-pixel tracing (Fig. 6.8c, d), but could combine both for a truly spatio-temporal assessment in real time. When extended to perform rapidly repeated, short line scans across a vesicle's edge, our method could capture abrupt spectroscopic changes inside and simultaneously morphological expansions to the outside of a vesicle in a correlative manner[48].
As a future prospect, the stable membrane-based in-situ s-SNOM technique demonstrated in this work can be integrated with state-of-the-art microfluidics and environmental controls. This integration holds great promise for the nanoscale investigation of dynamic biochemical processes actively triggered by changes in temperature, pH, osmolality, or the injection of chemical compounds. Additionally, the method is compatible with correlated measurements such as fluorescence and Raman imaging, as well as for THz-nanoscopy, for which higher tapping amplitudes (>200 nm) are mechanically possible can be used to obtain optimal results. Finally, we believe that the accuracy and versatility of our method opens up unprecedented avenues for future studies of even more complex lipid-associated phenomena and a multitude of other highly relevant systems, ranging from dynamic metal-organic-frameworks in chemistry[185,204], the assembly of Alzheimer-associated peptides in medicine[205], to the electronic modulation of 2D materials in physics[193].

7

Conclusion and Outlook

In this thesis we utilized s-SNOM as an advanced superresolution infrared nanoscopy method accompanied by several far-field microscopy techniques to investigate diverse phenomena and samples ranging from the fundamental study of photonic modes in optical metasurfaces to dental materials in human third molars and photoswitchable lipid vesicles. Furthermore, this work addressed two major limitations of s-SNOM: the difficulty of investigating liquid samples and the temporal resolution constraints for studying dynamic processes in soft matter samples. The new concepts introduced in this work will enable the deciphering of complex metasurface properties, the investigation of dental material samples and the exploration of complex materials in their native environment with in-situ s-SNOM. Further interesting studies that could be conducted on quasi-BIC metasurfaces are for example a comparison of gold and dielectric resonators, the comparison of different resonator structures and the mapping of the chirality of chiral resonator fields.

Quasi-BIC mode formation investigated by near-field microscopy. The difficulty to investigate the near-field of photonic metasurfaces has held back the fundamental and practical understanding of the properties of photonic metasurfaces. At the moment, photonic mode formations are mostly investigated by means of the far-field response or with numerical simulations. By introducing a transmission-mode s-SNOM based concept in combination with an image processing method and applying it for the investigation of the near-field of quasi-BIC metasurfaces, it is possible to analyze properties of photonic metasurfaces on the single resonator level. It was possible to visualize and quantify the finite array effect, the directional coupling of the resonators, the effect of defects and edges on metasurfaces. The attained insights will help to optimize the design of metasurfaces to lower the footprint and increase their active area to boost applications such as catalysis, biosensing or on-chip lasing. Ultimately, the introduced concept can be applied to a range of nanophotonic materials ranging from all-optical skyrmions, waveguides and nanoantennas as long as the optical phase response can be simulated. In addition, the concept could be applied in industry in the emerging field of metalens technology for failure analysis and metrology.

Infrared imaging and spectroscopy of dental materials. Modern dental materials are complex nanoscale multicomponent materials to satisfy the complex requirements profiles faced in real world patient settings. In order to optimize the materials, it is vital to understand

the chemical composition of the complex material mix. By applying a multiscale approach of different far-field and near-field infrared microscopy and spectroscopy techniques a proof-of-concept was demonstrated to locally decipher the chemical nature of a dental filling from the micro to the nanoscale. The study showed that the different components of the dental filling could be identified and mapped. In addition, by utilizing an image processing algorithm the porosity of adhesives could be investigated based on the infrared reflectivity of the hyperspectral images. The introduced concepts will be a stepping stone for further studies in dental material research and medicine. For example, it would be interesting to study degradation of dental material due to factors such as pH, temperature, salivary enzymes or bacteria on the nanoscale to better understand the failure points of a dental filling. Moreover, there have been barely any study that uses near-field optics to investigate the interfaces of the tooth material with the adhesive and the interfaces of the composite, filler particles and adhesives with each other. Furthermore, near-field optics could be deployed to address the important question of shrinkage stress. s-SNOM could provide a spatial map of stress-affected areas particularly around filler particles and resolve microcracks. Finally, far-field and near-field infrared microspectrocopy could give insight on the light-curing process and could resolve regions of suboptimal curing, cross-linking density and premature degradation.

Transient in-situ nanoscopy of photoswitchable lipids. The limitation of s-SNOM to dried samples has hindered the broad adoption of the nanoscopy method to life science, chemistry and the study of dynamic processes. In the final project of this thesis an ultra-thin membrane based in-situ s-SNOM method is introduced that enables complex nanoscopy measurements of liquid samples over hours. The work shows for the first time an actively induced dynamic process of a soft matter sample that is investigated with s-SNOM. In addition, it shows that nanoscale spectroscopy of soft matter samples in liquid can be performed gaining insights about the chemistry of the sample. Furthermore, a transient s-SNOM method was demonstrated that allows the millisecond resolved tracking of the infrared response of a sample in aqueous environment. This method will unlock a new realm of samples and phenomena previously impossible to be investigated by infrared nanoscopy such as complex lipid associated phenomena such as drug loaded vesicles or lipid domain formation. Furthermore, it is now possible to investigate the time dynamics of many materials down to the millisecond regime important for host-guest materials or structural changes in biomolecules. From here on it would be very interesting to develop a pump-probe liquid s-SNOM method, which already exists for dried solid-states samples. This setup helps to investigated the temporal dynamics of soft matter samples with even more information. Another avenue of research could be to develop a gas phase in-situ s-SNOM cell on the basis of the SiN membrane technology. The cell would enable the study of for example gas phase crystal growth processes on the nanoscale. In essence, the field of in-situ s-SNOM is just emerging, with many studies routinely conducted in related fields, such as in-situ TEM, SEM, and AFM, now possible but not yet performed in s-SNOM.

In conclusion, this thesis unequivocally establishes s-SNOM as a transformative and indispensable tool across diverse fields, including nanophotonics, dental material research, and biophysics. By demonstrating the capability to acquire critical nanoscale information, s-SNOM enables the optimization of material properties and paves the way for future innovations and scientific breakthroughs. The profound insights garnered from near-field measurements not only enhance the properties of these materials but also drive advancements in their respective fields.

References

[1] L. A. Robertson, 'Antoni van leeuwenhoek 1723-2023: a review to commemorate van leeuwenhoek's death, 300 years ago : for submission to antonie van leeuwenhoek journal of microbiology', Antonie van Leeuwenhoek **116**, 919–935 (2023) (cited on page 1).

[2] M. Susser and Z. Stein, 'Germ theory, infection, and bacteriology', in *Eras in epidemiology*, edited by M. Susser and Z. Stein (Oxford University Press, 2009), pp. 107–122 (cited on page 1).

[3] A. Leitner, 'The life and work of joseph fraunhofer (1787–1826)', American Journal of Physics **43**, 59–68 (1975) (cited on page 1).

[4] E. HECHT, *Optik* (DE GRUYTER OLDENBOURG, [S.l.], 2023) (cited on pages 1, 6).

[5] L. E. Franken, K. Grünewald, E. J. Boekema, and M. C. A. Stuart, 'A technical introduction to transmission electron microscopy for soft-matter: imaging, possibilities, choices, and technical developments', Small (Weinheim an der Bergstrasse, Germany) **16**, e1906198 (2020) (cited on page 2).

[6] E. Betzig, G. H. Patterson, R. Sougrat, O. W. Lindwasser, S. Olenych, J. S. Bonifacino, M. W. Davidson, J. Lippincott-Schwartz, and H. F. Hess, 'Imaging intracellular fluorescent proteins at nanometer resolution', Science (New York, N.Y.) **313**, 1642–1645 (2006) (cited on page 2).

[7] M. J. Rust, M. Bates, and X. Zhuang, 'Sub-diffraction-limit imaging by stochastic optical reconstruction microscopy (storm)', Nature methods **3**, 793–795 (2006) (cited on page 2).

[8] L. Schermelleh, A. Ferrand, T. Huser, C. Eggeling, M. Sauer, O. Biehlmaier, and G. P. C. Drummen, 'Super-resolution microscopy demystified', Nature cell biology **21**, 72–84 (2019) (cited on page 2).

[9] S. Wäldchen, J. Lehmann, T. Klein, S. van de Linde, and M. Sauer, 'Light-induced cell damage in live-cell super-resolution microscopy', Scientific reports **5**, 15348 (2015) (cited on page 2).

[10] L. Yin, W. Wang, S. Wang, F. Zhang, S. Zhang, and N. Tao, 'How does fluorescent labeling affect the binding kinetics of proteins with intact cells?', Biosensors & bioelectronics **66**, 412–416 (2015) (cited on page 2).

[11] X. Chen, D. Hu, R. Mescall, G. You, D. N. Basov, Q. Dai, and M. Liu, 'Modern scattering-type scanning near-field optical microscopy for advanced material research', Advanced materials (Deerfield Beach, Fla.) **31**, e1804774 (2019) (cited on pages 2, 24, 26, 50, 51, 86).

[12] B. H. Stuart, *Infrared spectroscopy: fundamentals and applications* (Wiley, 2004) (cited on pages 2, 5–7, 11, 14, 15, 68, 86).

[13] F. Crea, A. Vorkas, A. Redlich, R. Cruz, C. Shi, D. Trauner, A. Lange, R. Schlesinger, and J. Heberle, 'Photoactivation of a mechanosensitive channel', Frontiers in molecular biosciences **9**, 905306 (2022) (cited on pages 7, 86–88).

[14] A. Krüger, A. Bürkle, K. Hauser, and A. Mangerich, 'Real-time monitoring of parp1-dependent parylation by atr-ftir spectroscopy', Nature communications **11**, 2174 (2020) (cited on page 7).

[15] I. Amenabar, S. Poly, W. Nuansing, E. H. Hubrich, A. A. Govyadinov, F. Huth, R. Krutokhvostov, L. Zhang, M. Knez, J. Heberle, A. M. Bittner, and R. Hillenbrand, 'Structural analysis and mapping of individual protein complexes by infrared nanospectroscopy', Nature communications **4**, 2890 (2013) (cited on pages 7, 86).

[16] A. Almusa, A. H. S. Delgado, P. Ashley, and A. M. Young, 'Determination of dental adhesive composition throughout solvent drying and polymerization using atr-ftir spectroscopy', Polymers **13**, 10.3390/polym13223886 (2021) (cited on pages 7, 70, 73).

[17] K. J. Kaltenecker, E. Krauss, L. Casses, M. Geisler, B. Hecht, N. A. Mortensen, P. U. Jepsen, and N. Stenger, 'Mono-crystalline gold platelets: a high-quality platform for surface plasmon polaritons', Nanophotonics **9**, 509–522 (2020) (cited on pages 7, 51).

[18] S. Amarie and F. Keilmann, 'Broadband-infrared assessment of phonon resonance in scattering-type near-field microscopy', Physical Review B **83**, 10.1103/PhysRevB.83.045404 (2011) (cited on pages 7, 37, 69).

[19] G. L. Hansen, J. L. Schmit, and T. N. Casselman, 'Energy gap versus alloy composition and temperature in hg1− x cd x te', Journal of Applied Physics **53**, 7099–7101 (1982) (cited on page 7).

[20] F. Huth, 'Nano-ftir-nanoscale infrared near-field spectroscopy', PhD thesis (Universidad Del Pais Vasco, 2015) (cited on pages 9–11).

[21] B. Schrader, ed., *Infrared and raman spectroscopy: methods and applications* (VCH, Weinheim et al., 1995) (cited on pages 11, 12).

[22] P. R. Griffiths and J. A. de Haseth, *Fourier transform infrared spectrometry* (Wiley, 2007) (cited on pages 12, 13, 73).

[23] F. J. Harris, 'On the use of windows for harmonic analysis with the discrete fourier transform', Proceedings of the IEEE **66**, 51–83 (1978) (cited on page 12).

[24] P. Larkin, *Ir and raman spectroscopy: principles and spectral interpretation* (Elsevier, Oxford, 2011) (cited on page 16).

[25] L. Novotny and B. Hecht, *Principles of nano-optics*, Second edition (Cambridge University Press, Cambridge, 2012) (cited on pages 17, 19–22).

[26] A. Hartschuh, 'Tip-enhanced near-field optical microscopy', Angewandte Chemie (International ed. in English) **47**, 8178–8191 (2008) (cited on pages 17, 18).

[27] B. Knoll and F. Keilmann, 'Electromagnetic fields in the cutoff regime of tapered metallic waveguides', Optics Communications **162**, 177–181 (1999) (cited on pages 22, 69).

[28] A. Mancini, 'Surface phonon polaritons in silicon carbide nanostructures revealed by near-field imaging and spectroscopy', PhD thesis (Ludwig-Maximilians-Universität München, 2023) (cited on page 22).

[29] A. J. Huber, F. Keilmann, J. Wittborn, J. Aizpurua, and R. Hillenbrand, 'Terahertz near-field nanoscopy of mobile carriers in single semiconductor nanodevices', Nano letters **8**, 3766–3770 (2008) (cited on pages 22, 23).

[30] S. Berweger, J. M. Atkin, R. L. Olmon, and M. B. Raschke, 'Light on the tip of a needle: plasmonic nanofocusing for spectroscopy on the nanoscale', The journal of physical chemistry letters **3**, 945–952 (2012) (cited on page 23).

[31] F. Huth, A. Chuvilin, M. Schnell, I. Amenabar, R. Krutokhvostov, S. Lopatin, and R. Hillenbrand, 'Resonant antenna probes for tip-enhanced infrared near-field microscopy', Nano letters **13**, 1065–1072 (2013) (cited on page 23).

[32] A. Cvitkovic, N. Ocelic, and R. Hillenbrand, 'Analytical model for quantitative prediction of material contrasts in scattering-type near-field optical microscopy', Optics express **15**, 8550–8565 (2007) (cited on pages 24, 25).

[33] F. Keilmann and R. Hillenbrand, 'Near-field microscopy by elastic light scattering from a tip', Philosophical transactions. Series A, Mathematical, physical, and engineering sciences **362**, 787–805 (2004) (cited on pages 24, 50, 69, 86).

[34] L. Mester, A. A. Govyadinov, and R. Hillenbrand, 'High-fidelity nano-ftir spectroscopy by on-pixel normalization of signal harmonics', Nanophotonics **11**, 377–390 (2022) (cited on page 25).

[35] N. Ocelic, A. Huber, and R. Hillenbrand, 'Pseudoheterodyne detection for background-free near-field spectroscopy', Applied Physics Letters **89**, 10.1063/1.2348781 (2006) (cited on page 26).

[36] E. Vicentini, W. Nuansing, I. Niehues, I. Amenabar, A. M. Bittner, R. Hillenbrand, and M. Schnell, 'Pseudo-heterodyne interferometry for multicolor near-field imaging', Optics express **31**, 22308–22322 (2023) (cited on pages 26–28, 40, 52, 53, 97).

[37] F. Huth, M. Schnell, J. Wittborn, N. Ocelic, and R. Hillenbrand, 'Infrared-spectroscopic nanoimaging with a thermal source', Nature materials **10**, 352–356 (2011) (cited on pages 29, 40).

[38] F. Huth, A. Govyadinov, S. Amarie, W. Nuansing, F. Keilmann, and R. Hillenbrand, 'Nano-ftir absorption spectroscopy of molecular fingerprints at 20 nm spatial resolution', Nano letters **12**, 3973–3978 (2012) (cited on pages 29, 30, 51, 69, 73, 86).

[39] I. Amenabar, S. Poly, M. Goikoetxea, W. Nuansing, P. Lasch, and R. Hillenbrand, 'Hyperspectral infrared nanoimaging of organic samples based on fourier transform infrared nanospectroscopy', Nature communications **8**, 14402 (2017) (cited on page 29).

[40] L. Mester, A. A. Govyadinov, S. Chen, M. Goikoetxea, and R. Hillenbrand, 'Subsurface chemical nanoidentification by nano-ftir spectroscopy', Nature communications **11**, 3359 (2020) (cited on pages 30, 31, 90).

[41] T. Taubner, F. Keilmann, and R. Hillenbrand, 'Nanoscale-resolved subsurface imaging by scattering-type near-field optical microscopy', Optics express **13**, 8893–8899 (2005) (cited on page 30).

[42] A. A. Govyadinov, S. Mastel, F. Golmar, A. Chuvilin, P. S. Carney, and R. Hillenbrand, 'Recovery of permittivity and depth from near-field data as a step toward infrared nanotomography', ACS nano **8**, 6911–6921 (2014) (cited on page 30).

[43]C. Maissen, S. Chen, E. Nikulina, A. Govyadinov, and R. Hillenbrand, 'Probes for ultrasensitive thz nanoscopy', ACS Photonics **6**, 1279–1288 (2019) (cited on pages 31, 51, 98, 99).

[44]L. M. Berger, M. Barkey, S. A. Maier, and A. Tittl, 'Metallic and all–dielectric metasurfaces sustaining displacement–mediated bound states in the continuum', Advanced Optical Materials, 10.1002/adom.202301269 (2023) (cited on pages 33, 52, 53).

[45]Y. Yao, A. J. Hoffman, and C. F. Gmachl, 'Mid-infrared quantum cascade lasers', Nature Photonics **6**, 432–439 (2012) (cited on pages 34, 69).

[46]T. Steinle, F. Mörz, A. Steinmann, and H. Giessen, 'Ultra-stable high average power femtosecond laser system tunable from 1.33 to 20 µm', Optics letters **41**, 4863–4866 (2016) (cited on page 36).

[47]F. Mörz, R. Semenyshyn, T. Steinle, F. Neubrech, U. Zschieschang, H. Klauk, A. Steinmann, and H. Giessen, 'Nearly diffraction limited ftir mapping using an ultrastable broadband femtosecond laser tunable from 133 to 8 µm', Optics Express **25**, 32355 (2017) (cited on pages 36, 69).

[48]K. J. Kaltenecker, T. Gölz, E. Bau, and F. Keilmann, 'Infrared-spectroscopic, dynamic near-field microscopy of living cells and nanoparticles in water', Scientific reports **11**, 21860 (2021) (cited on pages 42, 86–88, 90, 91, 98, 99).

[49]E. Baù, T. Gölz, M. Benoit, A. Tittl, and F. Keilmann, 'Nanoscale mechanical manipulation of ultrathin sin membranes enabling infrared near-field microscopy of liquid-immersed samples', Small (Weinheim an der Bergstrasse, Germany), e2402568 (2024) (cited on pages 43, 90).

[50]M. Beddoe, T. Gölz, M. Barkey, E. Bau, M. Godejohann, S. A. Maier, F. Keilmann, M. Moldovan, D. Prodan, N. Ilie, and A. Tittl, 'Probing the micro- and nanoscopic properties of dental materials using infrared spectroscopy: a proof-of-principle study', Acta biomaterialia **168**, 309–322 (2023) (cited on pages 44, 46, 67).

[51]N. Ilie, N. Erich Serfözö, D. Prodan, J. Diegelmann, and M. Moldovan, 'Synthesis and performance of experimental resin-based dental adhesives reinforced with functionalized graphene and hydroxyapatite fillers', Materials & Design **221**, 110985 (2022) (cited on page 45).

[52]H. Wolter, W. Storch, and H. Ott, 'New inorganic/organic copolymers (ormocer ® s) for dental applications', MRS Proceedings **346**, 10.1557/PROC-346-143 (1994) (cited on page 45).

[53]P. Bottenberg, M. Alaerts, and F. Keulemans, 'A prospective randomised clinical trial of one bis-gma-based and two ormocer-based composite restorative systems in class ii cavities: three-year results', Journal of dentistry **35**, 163–171 (2007) (cited on page 45).

[54]N. Moszner, A. Gianasmidis, S. Klapdohr, U. K. Fischer, and V. Rheinberger, 'Sol-gel materials 2. light-curing dental composites based on ormocers of cross-linking alkoxysilane methacrylates and further nano-components', Dental materials : official publication of the Academy of Dental Materials **24**, 851–856 (2008) (cited on page 45).

[55]C. Pernpeintner, J. A. Frank, P. Urban, C. R. Roeske, S. D. Pritzl, D. Trauner, and T. Lohmüller, 'Light-controlled membrane mechanics and shape transitions of photoswitchable lipid vesicles', Langmuir : the ACS journal of surfaces and colloids **33**, 4083–4089 (2017) (cited on pages 46, 85, 87, 92).

[56]P. Urban, 'Optical control of lipid interaction in photolipid membranes', PhD thesis (Ludwig-Maximilians-Universität München, 2021) (cited on page 46).

[57]M. Angelova and D. S. Dimitrov, 'A mechanism of liposome electroformation', in *Trends in colloid and interface science ii*, Vol. 76, edited by V. Degiorgio, Progress in Colloid & Polymer Science (Steinkopff, Darmstadt, 1988), pp. 59–67 (cited on page 46).

[58]T. Gölz, E. Baù, A. Aigner, A. Mancini, M. Barkey, F. Keilmann, S. A. Maier, and A. Tittl, 'Revealing mode formation in quasi-bound states in the continuum metasurfaces via near-field optical microscopy', Advanced materials (Deerfield Beach, Fla.) **36**, e2405978 (2024) (cited on page 49).

[59]C.-W. Qiu, T. Zhang, G. Hu, and Y. Kivshar, 'Quo vadis, metasurfaces?', Nano letters **21**, 5461–5474 (2021) (cited on page 49).

[60]H.-T. Chen, A. J. Taylor, and N. Yu, 'A review of metasurfaces: physics and applications', Reports on progress in physics. Physical Society (Great Britain) **79**, 076401 (2016) (cited on page 49).

[61]A. V. Kildishev, A. Boltasseva, and V. M. Shalaev, 'Planar photonics with metasurfaces', Science (New York, N.Y.) **339**, 1232009 (2013) (cited on pages 49, 50).

[62]D. Neshev and I. Aharonovich, 'Optical metasurfaces: new generation building blocks for multi-functional optics', Light, science & applications **7**, 58 (2018) (cited on page 49).

[63] A. Kodigala, T. Lepetit, Q. Gu, B. Bahari, Y. Fainman, and B. Kanté, 'Lasing action from photonic bound states in continuum', Nature **541**, 196–199 (2017) (cited on page 50).

[64] M.-S. Hwang, H.-C. Lee, K.-H. Kim, K.-Y. Jeong, S.-H. Kwon, K. Koshelev, Y. Kivshar, and H.-G. Park, 'Ultralow-threshold laser using super-bound states in the continuum', Nature communications **12**, 4135 (2021) (cited on page 50).

[65] L. Kühner, L. Sortino, R. Berté, J. Wang, H. Ren, S. A. Maier, Y. Kivshar, and A. Tittl, 'Radial bound states in the continuum for polarization-invariant nanophotonics', Nature communications **13**, 4992 (2022) (cited on pages 50, 61).

[66] Z. Liu, Y. Xu, Y. Lin, J. Xiang, T. Feng, Q. Cao, J. Li, S. Lan, and J. Liu, 'High-q quasibound states in the continuum for nonlinear metasurfaces', Physical review letters **123**, 253901 (2019) (cited on pages 50, 56, 60).

[67] K. Koshelev, Y. Tang, K. Li, D.-Y. Choi, G. Li, and Y. Kivshar, 'Nonlinear metasurfaces governed by bound states in the continuum', ACS Photonics **6**, 1639–1644 (2019) (cited on page 50).

[68] L. V. Poulikakos, M. Lawrence, D. R. Barton, S. S. Jeffrey, and J. A. Dionne, 'Guided-mode-resonant dielectric metasurfaces for colorimetric imaging of material anisotropy in fibrous biological tissue', ACS Photonics **7**, 3216–3227 (2020) (cited on page 50).

[69] Z. Haddadin, S. Khan, and L. V. Poulikakos, 'Cutting corners to suppress high-order modes in mie resonator arrays', ACS Photonics **11**, 187–195 (2024) (cited on page 50).

[70] A. S. Solntsev, G. S. Agarwal, and Y. S. Kivshar, 'Metasurfaces for quantum photonics', Nature Photonics **15**, 327–336 (2021) (cited on page 50).

[71] L. Sortino, A. Gale, L. Kühner, C. Li, J. Biechteler, F. J. Wendisch, M. Kianinia, H. Ren, M. Toth, S. A. Maier, I. Aharonovich, and A. Tittl, 'Optically addressable spin defects coupled to bound states in the continuum metasurfaces', Nature communications **15**, 2008 (2024) (cited on page 50).

[72] F. Yesilkoy, E. R. Arvelo, Y. Jahani, M. Liu, A. Tittl, V. Cevher, Y. Kivshar, and H. Altug, 'Ultrasensitive hyperspectral imaging and biodetection enabled by dielectric metasurfaces', Nature Photonics **13**, 390–396 (2019) (cited on page 50).

[73] O. Limaj, D. Etezadi, N. J. Wittenberg, D. Rodrigo, D. Yoo, S.-H. Oh, and H. Altug, 'Infrared plasmonic biosensor for real-time and label-free monitoring of lipid membranes', Nano letters **16**, 1502–1508 (2016) (cited on pages 50, 86).

[74] X. Sun, J. Sun, Z. Wang, L. Wang, F. Qiu, and L. Wen, 'Manipulating dual bound states in the continuum for efficient spatial light modulator', Nano letters **22**, 9982–9989 (2022) (cited on page 50).

[75] J. García-Guirado, M. Svedendahl, J. Puigdollers, and R. Quidant, 'Enhanced chiral sensing with dielectric nanoresonators', Nano letters **20**, 585–591 (2020) (cited on page 50).

[76] M. L. Solomon, A. A. E. Saleh, L. V. Poulikakos, J. M. Abendroth, L. F. Tadesse, and J. A. Dionne, 'Nanophotonic platforms for chiral sensing and separation', Accounts of chemical research **53**, 588–598 (2020) (cited on page 50).

[77] J. García-Guirado, M. Svedendahl, J. Puigdollers, and R. Quidant, 'Enantiomer-selective molecular sensing using racemic nanoplasmonic arrays', Nano letters **18**, 6279–6285 (2018) (cited on page 50).

[78] C. Xu, Z. Ren, H. Zhou, J. Zhou, C. P. Ho, N. Wang, and C. Lee, 'Expanding chiral metamaterials for retrieving fingerprints via vibrational circular dichroism', Light, science & applications **12**, 154 (2023) (cited on page 50).

[79] Z. Wang, J. Sun, J. Li, L. Wang, Z. Li, X. Zheng, and L. Wen, 'Customizing 2.5d out-of-plane architectures for robust plasmonic bound-states-in-the-continuum metasurfaces', Advanced science (Weinheim, Baden-Wurttemberg, Germany) **10**, e2206236 (2023) (cited on page 50).

[80] L. Kühner, F. J. Wendisch, A. A. Antonov, J. Bürger, L. Hüttenhofer, L. de S Menezes, S. A. Maier, M. V. Gorkunov, Y. Kivshar, and A. Tittl, 'Unlocking the out-of-plane dimension for photonic bound states in the continuum to achieve maximum optical chirality', Light, science & applications **12**, 250 (2023) (cited on page 50).

[81] H. Hu, T. Weber, O. Bienek, A. Wester, L. Hüttenhofer, I. D. Sharp, S. A. Maier, A. Tittl, and E. Cortés, 'Catalytic metasurfaces empowered by bound states in the continuum', ACS nano **16**, 13057–13068 (2022) (cited on page 50).

[82] E. Cortés, F. J. Wendisch, L. Sortino, A. Mancini, S. Ezendam, S. Saris, L. de S Menezes, A. Tittl, H. Ren, and S. A. Maier, 'Optical metasurfaces for energy conversion', Chemical reviews **122**, 15082–15176 (2022) (cited on pages 50, 51, 66).

[83]K. Koshelev, S. Lepeshov, M. Liu, A. Bogdanov, and Y. Kivshar, 'Asymmetric metasurfaces with high-q resonances governed by bound states in the continuum', Physical review letters **121**, 193903 (2018) (cited on page 50).

[84]C. W. Hsu, B. Zhen, A. D. Stone, J. D. Joannopoulos, and M. Soljačić, 'Bound states in the continuum', Nature Reviews Materials **1**, 10.1038/natrevmats.2016.48 (2016) (cited on page 50).

[85]S. Joseph, S. Pandey, S. Sarkar, and J. Joseph, 'Bound states in the continuum in resonant nanostructures: an overview of engineered materials for tailored applications', Nanophotonics **10**, 4175–4207 (2021) (cited on page 50).

[86]A. Aigner, T. Weber, A. Wester, S. A. Maier, and A. Tittl, 'Continuous spectral and coupling-strength encoding with dual-gradient metasurfaces', Nature nanotechnology, 10.1038/s41565-024-01767-2 (2024) (cited on pages 50, 52).

[87]Z. Dong, Z. Mahfoud, R. Paniagua-Domínguez, H. Wang, A. I. Fernández-Domínguez, S. Gorelik, S. T. Ha, F. Tjiptoharsono, A. I. Kuznetsov, M. Bosman, and J. K. W. Yang, 'Nanoscale mapping of optically inaccessible bound-states-in-the-continuum', Light, science & applications **11**, 20 (2022) (cited on pages 50, 64).

[88]R. Deshpande, V. A. Zenin, F. Ding, N. A. Mortensen, and S. I. Bozhevolnyi, 'Direct characterization of near-field coupling in gap plasmon-based metasurfaces', Nano letters **18**, 6265–6270 (2018) (cited on page 51).

[89]R. Büchner, T. Weber, L. Kühner, S. A. Maier, and A. Tittl, 'Tip coupling and array effects of gold nanoantennas in near-field microscopy', ACS Photonics **8**, 3486–3494 (2021) (cited on page 51).

[90]S. Chen, P. L. Leng, A. Konečná, E. Modin, M. Gutierrez-Amigo, E. Vicentini, B. Martín-García, M. Barra-Burillo, I. Niehues, C. Maciel Escudero, X. Y. Xie, L. E. Hueso, E. Artacho, J. Aizpurua, I. Errea, M. G. Vergniory, A. Chuvilin, F. X. Xiu, and R. Hillenbrand, 'Real-space observation of ultraconfined in-plane anisotropic acoustic terahertz plasmon polaritons', Nature materials **22**, 860–866 (2023) (cited on pages 51, 66).

[91]X. Guo, K. Bertling, B. C. Donose, M. Brünig, A. Cernescu, A. A. Govyadinov, and A. D. Rakić, 'Terahertz nanoscopy: advances, challenges, and the road ahead', Applied Physics Reviews **11**, 10.1063/5.0189061 (2024) (cited on page 51).

[92]M. Schnell, A. García-Etxarri, A. J. Huber, K. Crozier, J. Aizpurua, and R. Hillenbrand, 'Controlling the near-field oscillations of loaded plasmonic nanoantennas', Nature Photonics **3**, 287–291 (2009) (cited on page 51).

[93]T. Neuman, P. Alonso–González, A. Garcia–Etxarri, M. Schnell, R. Hillenbrand, and J. Aizpurua, 'Mapping the near fields of plasmonic nanoantennas by scattering–type scanning near–field optical microscopy', Laser & Photonics Reviews **9**, 637–649 (2015) (cited on page 51).

[94]M. Schnell, A. Garcia-Etxarri, A. J. Huber, K. B. Crozier, A. Borisov, J. Aizpurua, and R. Hillenbrand, 'Amplitude- and phase-resolved near-field mapping of infrared antenna modes by transmission-mode scattering-type near-field microscopy', The Journal of Physical Chemistry C **114**, 7341–7345 (2010) (cited on pages 51–53, 66).

[95]V. A. Zenin, A. B. Evlyukhin, S. M. Novikov, Y. Yang, R. Malureanu, A. V. Lavrinenko, B. N. Chichkov, and S. I. Bozhevolnyi, 'Direct amplitude-phase near-field observation of higher-order anapole states', Nano letters **17**, 7152–7159 (2017) (cited on page 51).

[96]J. d'Archangel, E. Tucker, E. Kinzel, E. A. Muller, H. A. Bechtel, M. C. Martin, M. B. Raschke, and G. Boreman, 'Near- and far-field spectroscopic imaging investigation of resonant square-loop infrared metasurfaces', Optics express **21**, 17150–17160 (2013) (cited on page 51).

[97]N. J. J. van Hoof, D. R. Abujetas, S. E. T. ter Huurne, F. Verdelli, G. C. A. Timmermans, J. A. Sánchez-Gil, and J. G. Rivas, 'Unveiling the symmetry protection of bound states in the continuum with terahertz near-field imaging', ACS Photonics **8**, 3010–3016 (2021) (cited on page 51).

[98]S. ter Huurne, D. R. Abujetas, N. van Hoof, J. A. Sanchez–Gil, and J. Gómez Rivas, 'Direct observation of lateral field confinement in symmetry–protected thz bound states in the continuum', Advanced Optical Materials **11**, 10.1002/adom.202202403 (2023) (cited on page 51).

[99]S. Yang, M. He, C. Hong, J. Nordlander, J.-P. Maria, J. D. Caldwell, and J. C. Ndukaife, 'Single-peak and narrow-band mid-infrared thermal emitters driven by mirror-coupled plasmonic quasi-bic metasurfaces', Optica **11**, 305 (2024) (cited on page 51).

[100]S. T. Ha, Y. H. Fu, N. K. Emani, Z. Pan, R. M. Bakker, R. Paniagua-Domínguez, and A. I. Kuznetsov, 'Directional lasing in resonant semiconductor nanoantenna arrays', Nature nanotechnology **13**, 1042–1047 (2018) (cited on page 51).

[101] M.-S. Hwang, K.-Y. Jeong, J.-P. So, K.-H. Kim, and H.-G. Park, 'Nanophotonic nonlinear and laser devices exploiting bound states in the continuum', Communications Physics **5**, 10.1038/s42005-022-00884-5 (2022) (cited on page 51).

[102] A. Tittl, A. Leitis, M. Liu, F. Yesilkoy, D.-Y. Choi, D. N. Neshev, Y. S. Kivshar, and H. Altug, 'Imaging-based molecular barcoding with pixelated dielectric metasurfaces', Science (New York, N.Y.) **360**, 1105–1109 (2018) (cited on pages 52, 60).

[103] A. Leitis, A. Tittl, M. Liu, B. H. Lee, M. B. Gu, Y. S. Kivshar, and H. Altug, 'Angle-multiplexed all-dielectric metasurfaces for broadband molecular fingerprint retrieval', Science advances **5**, eaaw2871 (2019) (cited on page 52).

[104] S. Jafar–Zanjani, M. M. Salary, D. Huynh, E. Elhamifar, and H. Mosallaei, 'Tco–based active dielectric metasurfaces design by conditional generative adversarial networks', Advanced Theory and Simulations **4**, 10.1002/adts.202000196 (2021) (cited on page 55).

[105] N. Nidheesh, K. A. Abdul Nazeer, and P. M. Ameer, 'An enhanced deterministic k-means clustering algorithm for cancer subtype prediction from gene expression data', Computers in biology and medicine **91**, 213–221 (2017) (cited on page 55).

[106] E. N. Bulgakov and A. F. Sadreev, 'High- q resonant modes in a finite array of dielectric particles', Physical Review A **99**, 10.1103/PhysRevA.99.033851 (2019) (cited on page 56).

[107] N. Ustimenko, C. Rockstuhl, and A. B. Evlyukhin, 'Resonances in finite-size all-dielectric metasurfaces for light trapping and propagation control', Physical Review B **109**, 10.1103/PhysRevB.109.115436 (2024) (cited on pages 56, 57).

[108] E. N. Bulgakov and D. N. Maksimov, 'Light enhancement by quasi-bound states in the continuum in dielectric arrays', Optics express **25**, 14134–14147 (2017) (cited on pages 56, 57).

[109] M. S. Mikhailovskii, M. A. Poleva, N. S. Solodovchenko, M. S. Sidorenko, Z. F. Sadrieva, M. I. Petrov, A. A. Bogdanov, and R. S. Savelev, 'Engineering of high- q states via collective mode coupling in chains of mie resonators', ACS Photonics **11**, 1657–1663 (2024) (cited on page 57).

[110] Z. F. Sadrieva, M. A. Belyakov, M. A. Balezin, P. V. Kapitanova, E. A. Nenasheva, A. F. Sadreev, and A. A. Bogdanov, 'Experimental observation of a symmetry-protected bound state in the continuum in a chain of dielectric disks', Physical Review A **99**, 10.1103/PhysRevA.99.053804 (2019) (cited on page 57).

[111] J. Kühne, J. Wang, T. Weber, L. Kühner, S. A. Maier, and A. Tittl, 'Fabrication robustness in bic metasurfaces', Nanophotonics **10**, 4305–4312 (2021) (cited on page 57).

[112] K. L. Koshelev, Z. F. Sadrieva, A. A. Shcherbakov, Y. Kivshar, and A. A. Bogdanov, 'Bound states in the continuum in photonic structures', Physics-Uspekhi **66**, 494–517 (2023) (cited on page 58).

[113] V. G. Kravets, A. V. Kabashin, W. L. Barnes, and A. N. Grigorenko, 'Plasmonic surface lattice resonances: a review of properties and applications', Chemical reviews **118**, 5912–5951 (2018) (cited on page 60).

[114] J.-.-H. Yang, Z.-.-T. Huang, D. N. Maksimov, P. S. Pankin, I. V. Timofeev, K.-.-B. Hong, H. Li, J.-.-W. Chen, C.-.-Y. Hsu, Y.-.-Y. Liu, T.-.-C. Lu, T.-.-R. Lin, C.-.-S. Yang, and K.-.-P. Chen, 'Low–threshold bound state in the continuum lasers in hybrid lattice resonance metasurfaces', Laser & Photonics Reviews **15**, 10.1002/lpor.202100118 (2021) (cited on page 60).

[115] A. Aigner, A. Tittl, J. Wang, T. Weber, Y. Kivshar, S. A. Maier, and H. Ren, 'Plasmonic bound states in the continuum to tailor light-matter coupling', Science advances **8**, eadd4816 (2022) (cited on page 60).

[116] J. Wang, S. A. Maier, and A. Tittl, 'Trends in nanophotonics–enabled optofluidic biosensors', Advanced Optical Materials **10**, 10.1002/adom.202102366 (2022) (cited on pages 64, 66).

[117] H. Altug, S.-H. Oh, S. A. Maier, and J. Homola, 'Advances and applications of nanophotonic biosensors', Nature nanotechnology **17**, 5–16 (2022) (cited on page 64).

[118] E. Csányi, Y. Liu, S. D. Rezaei, H. Y. L. Lee, F. Tjiptoharsono, Z. Mahfoud, S. Gorelik, X. Zhao, L. J. Lim, Di Zhu, J. Wu, K. E. J. Goh, W. Gao, Z.-.-K. Tan, G. Leggett, C.-.-W. Qiu, and Z. Dong, 'Engineering and controlling perovskite emissions via optical quasi–bound–states–in–the–continuum', Advanced Functional Materials **34**, 10.1002/adfm.202309539 (2024) (cited on page 65).

[119] A. B. Khanikaev, N. Arju, Z. Fan, D. Purtseladze, F. Lu, J. Lee, P. Sarriugarte, M. Schnell, R. Hillenbrand, M. A. Belkin, and G. Shvets, 'Experimental demonstration of the microscopic origin of circular dichroism in two-dimensional metamaterials', Nature communications **7**, 12045 (2016) (cited on page 66).

[120]J. Duan, G. Álvarez-Pérez, A. I. F. Tresguerres-Mata, J. Taboada-Gutiérrez, K. V. Voronin, A. Bylinkin, B. Chang, S. Xiao, S. Liu, J. H. Edgar, J. I. Martín, V. S. Volkov, R. Hillenbrand, J. Martín-Sánchez, A. Y. Nikitin, and P. Alonso-González, 'Planar refraction and lensing of highly confined polaritons in anisotropic media', Nature communications **12**, 4325 (2021) (cited on page 66).

[121]S. Liu, Q. Han, W. Luo, W. Lei, J. Zhao, J. Wang, Y. Jiang, and M. B. Raschke, 'Recent progress of innovative infrared avalanche photodetectors', Infrared Physics & Technology, 105114 (2024) (cited on page 66).

[122]S. Tsesses, E. Ostrovsky, K. Cohen, B. Gjonaj, N. H. Lindner, and G. Bartal, 'Optical skyrmion lattice in evanescent electromagnetic fields', Science (New York, N.Y.) **361**, 993–996 (2018) (cited on page 66).

[123]F. N. Hugo, N. J. Kassebaum, W. Marcenes, and E. Bernabé, 'Role of dentistry in global health: challenges and research priorities', Journal of dental research **100**, 681–685 (2021) (cited on page 67).

[124]M. A. Coulter, 'Minamata convention on mercury', International Legal Materials **55**, 582–616 (2016) (cited on page 67).

[125]H. V. Worthington, S. Khangura, K. Seal, M. Mierzwinski-Urban, A. Veitz-Keenan, P. Sahrmann, P. R. Schmidlin, D. Davis, Z. Iheozor-Ejiofor, and M. G. Rasines Alcaraz, 'Direct composite resin fillings versus amalgam fillings for permanent posterior teeth', The Cochrane database of systematic reviews **8**, CD005620 (2021) (cited on page 67).

[126]Y. Fujimoto, M. Iwasa, R. Murayama, M. Miyazaki, A. Nagafuji, and T. Nakatsuka, 'Detection of ions released from s-prg fillers and their modulation effect', Dental materials journal **29**, 392–397 (2010) (cited on page 67).

[127]N. Ilie, T. J. Hilton, S. D. Heintze, R. Hickel, D. C. Watts, N. Silikas, J. W. Stansbury, M. Cadenaro, and J. L. Ferracane, 'Academy of dental materials guidance-resin composites: part i-mechanical properties', Dental materials : official publication of the Academy of Dental Materials **33**, 880–894 (2017) (cited on page 67).

[128]H. Al Sunbul, N. Silikas, and D. C. Watts, 'Polymerization shrinkage kinetics and shrinkage-stress in dental resin-composites', Dental materials : official publication of the Academy of Dental Materials **32**, 998–1006 (2016) (cited on page 67).

[129]E. H. Ismail and R. D. Paravina, 'Color adjustment potential of resin composites: optical illusion or physical reality, a comprehensive overview', Journal of esthetic and restorative dentistry : official publication of the American Academy of Esthetic Dentistry ... [et al.] **34**, 42–54 (2022) (cited on page 67).

[130]N. Alvanforoush, J. Palamara, R. H. Wong, and M. F. Burrow, 'Comparison between published clinical success of direct resin composite restorations in vital posterior teeth in 1995-2005 and 2006-2016 periods', Australian dental journal **62**, 132–145 (2017) (cited on page 67).

[131]F. F. Demarco, M. S. Cenci, A. F. Montagner, V. P. de Lima, M. B. Correa, R. R. Moraes, and N. J. M. Opdam, 'Longevity of composite restorations is definitely not only about materials', Dental materials : official publication of the Academy of Dental Materials **39**, 1–12 (2023) (cited on pages 67, 68).

[132]D. H. Pashley, F. R. Tay, C. Yiu, M. Hashimoto, L. Breschi, R. M. Carvalho, and S. Ito, 'Collagen degradation by host-derived enzymes during aging', Journal of dental research **83**, 216–221 (2004) (cited on page 68).

[133]M. Hashimoto, H. Ohno, M. Kaga, K. Endo, H. Sano, and H. Oguchi, 'In vivo degradation of resin-dentin bonds in humans over 1 to 3 years', Journal of dental research **79**, 1385–1391 (2000) (cited on page 68).

[134]F. Beck and N. Ilie, 'Riboflavin and its effect on dentin bond strength: considerations for clinical applicability-an in vitro study', Bioengineering (Basel, Switzerland) **9**, 10.3390/bioengineering9010034 (2022) (cited on page 68).

[135]A. S. Khan, H. Khalid, Z. Sarfraz, M. Khan, J. Iqbal, N. Muhammad, M. A. Fareed, and I. U. Rehman, 'Vibrational spectroscopy of selective dental restorative materials', Applied Spectroscopy Reviews **52**, 507–540 (2017) (cited on pages 69, 70, 73, 80).

[136]C. d. C. A. Lopes, P. H. J. O. Limirio, V. R. Novais, and P. Dechichi, 'Fourier transform infrared spectroscopy (ftir) application chemical characterization of enamel, dentin and bone', Applied Spectroscopy Reviews **53**, 747–769 (2018) (cited on pages 69, 70, 72).

[137]P. Seredin, D. Goloshchapov, Y. Ippolitov, and J. Vongsvivut, 'Development of a new approach to diagnosis of the early fluorosis forms by means of ftir and raman microspectroscopy', Scientific reports **10**, 20891 (2020) (cited on page 69).

[138]U. S. Almhöjd, J. G. Norén, A. Arvidsson, Å. Nilsson, and P. Lingström, 'Analysis of carious dentine using ftir and tof-sims', Oral health and dental management **13**, 735–744 (2014) (cited on pages 69, 72).

[139] A. H. Delgado and A. M. Young, 'Modelling atr-ftir spectra of dental bonding systems to investigate composition and polymerisation kinetics', Materials (Basel, Switzerland) **14**, 10.3390/ma14040760 (2021) (cited on page 69).

[140] A. Mansoor, M. T. Khan, M. Mehmood, Z. Khurshid, M. I. Ali, and A. Jamal, 'Synthesis and characterization of titanium oxide nanoparticles with a novel biogenic process for dental application', Nanomaterials (Basel, Switzerland) **12**, 10.3390/nano12071078 (2022) (cited on page 69).

[141] P. Alonso-Gonzalez, M. Schnell, P. Sarriugarte, H. Sobhani, C. Wu, N. Arju, A. Khanikaev, F. Golmar, P. Albella, L. Arzubiaga, F. Casanova, L. E. Hueso, P. Nordlander, G. Shvets, and R. Hillenbrand, 'Real-space mapping of fano interference in plasmonic metamolecules', Nano letters **11**, 3922–3926 (2011) (cited on page 69).

[142] S. Primpke, M. Godejohann, and G. Gerdts, 'Rapid identification and quantification of microplastics in the environment by quantum cascade laser-based hyperspectral infrared chemical imaging', Environmental science & technology **54**, 15893–15903 (2020) (cited on page 69).

[143] B. Bird and J. Rowlette, 'High definition infrared chemical imaging of colorectal tissue using a spero qcl microscope', The Analyst **142**, 1381–1386 (2017) (cited on page 69).

[144] C. Westermeier, A. Cernescu, S. Amarie, C. Liewald, F. Keilmann, and B. Nickel, 'Sub-micron phase coexistence in small-molecule organic thin films revealed by infrared nano-imaging', Nature communications **5**, 4101 (2014) (cited on page 69).

[145] P. Seredin, D. Goloshchapov, Y. Ippolitov, and J. Vongsvivut, 'Engineering of a biomimetic interface between a native dental tissue and restorative composite and its study using synchrotron ftir microscopic mapping', International journal of molecular sciences **22**, 10.3390/ijms22126510 (2021) (cited on page 69).

[146] P. Spencer, Y. Wang, J. L. Katz, and A. Misra, 'Physicochemical interactions at the dentin/adhesive interface using ftir chemical imaging', Journal of biomedical optics **10**, 031104 (2005) (cited on page 69).

[147] S. Amarie, P. Zaslansky, Y. Kajihara, E. Griesshaber, W. W. Schmahl, and F. Keilmann, 'Nano-ftir chemical mapping of minerals in biological materials', Beilstein journal of nanotechnology **3**, 312–323 (2012) (cited on pages 69, 72, 77).

[148] G. Sereda, A. VanLaecken, and J. A. Turner, 'Monitoring demineralization and remineralization of human dentin by characterization of its structure with resonance-enhanced afm-ir chemical mapping, nanoindentation, and sem', Dental materials : official publication of the Academy of Dental Materials **35**, 617–626 (2019) (cited on pages 69, 82).

[149] A. Dazzi and C. B. Prater, 'Afm-ir: technology and applications in nanoscale infrared spectroscopy and chemical imaging', Chemical reviews **117**, 5146–5173 (2017) (cited on page 70).

[150] N. E. Olson, Y. Xiao, Z. Lei, and A. P. Ault, 'Simultaneous optical photothermal infrared (o-ptir) and raman spectroscopy of submicrometer atmospheric particles', Analytical chemistry **92**, 9932–9939 (2020) (cited on page 70).

[151] S. Hayashi-Sakai, M. Sakamoto, T. Hayashi, T. Kondo, K. Sugita, J. Sakai, J. Shimomura-Kuroki, M. Ike, Y. Nikkuni, and H. Nishiyama, 'Evaluation of permanent and primary enamel and dentin mineral density using micro-computed tomography', Oral radiology **35**, 29–34 (2019) (cited on page 72).

[152] A. M. Young, S. A. Rafeeka, and J. A. Howlett, 'Ftir investigation of monomer polymerisation and polyacid neutralisation kinetics and mechanisms in various aesthetic dental restorative materials', Biomaterials **25**, 823–833 (2004) (cited on page 73).

[153] R. H. Halvorson, R. L. Erickson, and C. L. Davidson, 'The effect of filler and silane content on conversion of resin-based composite', Dental materials : official publication of the Academy of Dental Materials **19**, 327–333 (2003) (cited on pages 73, 74).

[154] F. Großerueschkamp, H. Jütte, K. Gerwert, and A. Tannapfel, 'Advances in digital pathology: from artificial intelligence to label-free imaging', Visceral medicine **37**, 482–490 (2021) (cited on pages 74, 81).

[155] S. Frijters, T. Krüger, and J. Harting, 'Parallelised hoshen–kopelman algorithm for lattice-boltzmann simulations', Computer Physics Communications **189**, 92–98 (2015) (cited on page 75).

[156] M. Kotwica, P. Gronek, and K. Malarz, 'Efficient space virtualization for the hoshen–kopelman algorithm', International Journal of Modern Physics C **30**, 1950055 (2019) (cited on page 75).

[157] G. C. Padovani, V. P. Feitosa, S. Sauro, F. R. Tay, G. Durán, A. J. Paula, and N. Durán, 'Advances in dental materials through nanotechnology: facts, perspectives and toxicological aspects', Trends in biotechnology **33**, 621–636 (2015) (cited on page 77).

[158]S. Sirovica, J. H. Solheim, M. W. A. Skoda, C. J. Hirschmugl, E. C. Mattson, E. Aboualizadeh, Y. Guo, X. Chen, A. Kohler, D. L. Romanyk, S. M. Rosendahl, S. Morsch, R. A. Martin, and O. Addison, 'Origin of micro-scale heterogeneity in polymerisation of photo-activated resin composites', Nature communications **11**, 1849 (2020) (cited on page 82).

[159]F. Menaa, B. Menaa, and O. Sharts, 'Development of carbon-fluorine spectroscopy for pharmaceutical and biomedical applications', Faraday discussions **149**, 269–78, discussion 333–56 (2011) (cited on page 82).

[160]T. M. Allen and P. R. Cullis, 'Liposomal drug delivery systems: from concept to clinical applications', Advanced drug delivery reviews **65**, 36–48 (2013) (cited on page 85).

[161]H. Nsairat, D. Khater, U. Sayed, F. Odeh, A. Al Bawab, and W. Alshaer, 'Liposomes: structure, composition, types, and clinical applications', Heliyon **8**, e09394 (2022) (cited on page 85).

[162]N. Lamichhane, T. S. Udayakumar, W. D. D'Souza, C. B. Simone, S. R. Raghavan, J. Polf, and J. Mahmood, 'Liposomes: clinical applications and potential for image-guided drug delivery', Molecules (Basel, Switzerland) **23**, 10.3390/molecules23020288 (2018) (cited on page 85).

[163]K. Swetha, N. G. Kotla, L. Tunki, A. Jayaraj, S. K. Bhargava, H. Hu, S. R. Bonam, and R. Kurapati, 'Recent advances in the lipid nanoparticle-mediated delivery of mrna vaccines', Vaccines **11**, 10.3390/vaccines11030658 (2023) (cited on page 85).

[164]L. Sercombe, T. Veerati, F. Moheimani, S. Y. Wu, A. K. Sood, and S. Hua, 'Advances and challenges of liposome assisted drug delivery', Frontiers in pharmacology **6**, 286 (2015) (cited on page 85).

[165]S. D. Pritzl, D. B. Konrad, M. F. Ober, A. F. Richter, J. A. Frank, B. Nickel, D. Trauner, and T. Lohmüller, 'Optical membrane control with red light enabled by red-shifted photolipids', Langmuir : the ACS journal of surfaces and colloids **38**, 385–393 (2022) (cited on page 85).

[166]N. Chander, J. Morstein, J. S. Bolten, A. Shemet, P. R. Cullis, D. Trauner, and D. Witzigmann, 'Optimized photoactivatable lipid nanoparticles enable red light triggered drug release', Small (Weinheim an der Bergstrasse, Germany) **17**, e2008198 (2021) (cited on page 85).

[167]F. Baserga, A. Vorkas, F. Crea, L. Schubert, J.-L. Chen, A. Redlich, M. La Greca, J. Storm, S. Oldemeyer, K. Hoffmann, R. Schlesinger, and J. Heberle, 'Membrane protein activity induces specific molecular changes in nanodiscs monitored by ftir difference spectroscopy', Frontiers in molecular biosciences **9**, 915328 (2022) (cited on pages 86–88).

[168]A. Cernescu, M. Szuwarzyński, U. Kwolek, P. Wydro, M. Kepczynski, S. Zapotoczny, M. Nowakowska, and L. Quaroni, 'Label-free infrared spectroscopy and imaging of single phospholipid bilayers with nanoscale resolution', Analytical chemistry **90**, 10179–10186 (2018) (cited on page 86).

[169]M. Autret, M. Le Plouzennec, C. Moinet, and G. Simonneaux, 'Intramolecular fluorescence quenching in azobenzene-substituted porphyrins', Journal of the Chemical Society, Chemical Communications, 1169 (1994) (cited on page 86).

[170]N. Hartrampf, S. M. Leitao, N. Winter, H. Toombs-Ruane, J. A. Frank, P. Schwille, D. Trauner, and H. G. Franquelim, 'Structural diversity of photoswitchable sphingolipids for optodynamic control of lipid microdomains', Biophysical journal **122**, 2325–2341 (2023) (cited on page 86).

[171]A. Stollmann, J. Garcia-Guirado, J.-S. Hong, H. Im, H. Lee, J. O. Arroyo, and R. Quidant, 'Molecular fingerprinting of biological nanoparticles with a label-free optofluidic platform', ArXiv (2023) (cited on page 86).

[172]V. Bello, G. Mattei, P. Mazzoldi, N. Vivenza, P. Gasco, J. M. Idee, C. Robic, and E. Borsella, 'Transmission electron microscopy of lipid vesicles for drug delivery: comparison between positive and negative staining', Microscopy and microanalysis : the official journal of Microscopy Society of America, Microbeam Analysis Society, Microscopical Society of Canada **16**, 456–461 (2010) (cited on page 86).

[173]D. Rodrigo, A. Tittl, N. Ait-Bouziad, A. John-Herpin, O. Limaj, C. Kelly, D. Yoo, N. J. Wittenberg, S.-H. Oh, H. A. Lashuel, and H. Altug, 'Resolving molecule-specific information in dynamic lipid membrane processes with multi-resonant infrared metasurfaces', Nature communications **9**, 2160 (2018) (cited on page 86).

[174]N. J. Wittenberg, H. Im, X. Xu, B. Wootla, J. Watzlawik, A. E. Warrington, M. Rodriguez, and S.-H. Oh, 'High-affinity binding of remyelinating natural autoantibodies to myelin-mimicking lipid bilayers revealed by nanohole surface plasmon resonance', Analytical chemistry **84**, 6031–6039 (2012) (cited on page 86).

[175]R. Quidant, 'Plasmon nano-optics: designing novel nano-tools for biology and medicine', in *Plasmonics*, Vol. 167, edited by S. Enoch and N. Bonod, Springer Series in Optical Sciences (Springer Berlin Heidelberg, Berlin, Heidelberg, 2012), pp. 201–222 (cited on page 86).

[176]V. A. Lorenz-Fonfria, 'Infrared difference spectroscopy of proteins: from bands to bonds', Chemical reviews **120**, 3466–3576 (2020) (cited on pages 88, 91, 97).

[177]S. D. Pritzl, P. Urban, A. Prasselsperger, D. B. Konrad, J. A. Frank, D. Trauner, and T. Lohmüller, 'Photolipid bilayer permeability is controlled by transient pore formation', Langmuir : the ACS journal of surfaces and colloids **36**, 13509–13515 (2020) (cited on pages 92, 94, 95).

[178]M. Aleksanyan, A. Grafmüller, F. Crea, V. N. Georgiev, N. Yandrapalli, S. Block, J. Heberle, and R. Dimova, 'Photomanipulation of minimal synthetic cells: area increase, softening, and interleaflet coupling of membrane models doped with azobenzene–lipid photoswitches', Advanced Science **10**, 10.1002/advs.202304336 (2023) (cited on page 92).

[179]Y. Takashimizu and M. Iiyoshi, 'New parameter of roundness r: circularity corrected by aspect ratio', Progress in Earth and Planetary Science **3**, 10.1186/s40645-015-0078-x (2016) (cited on page 93).

[180]N. Ritter and J. Cooper, 'New resolution independent measures of circularity', Journal of Mathematical Imaging and Vision **35**, 117–127 (2009) (cited on page 93).

[181]H. A. Faizi, S. L. Frey, J. Steinkühler, R. Dimova, and P. M. Vlahovska, 'Bending rigidity of charged lipid bilayer membranes', Soft matter **15**, 6006–6013 (2019) (cited on page 93).

[182]P. Urban, S. D. Pritzl, M. F. Ober, C. F. Dirscherl, C. Pernpeintner, D. B. Konrad, J. A. Frank, D. Trauner, B. Nickel, and T. Lohmueller, 'A lipid photoswitch controls fluidity in supported bilayer membranes', Langmuir : the ACS journal of surfaces and colloids **36**, 2629–2634 (2020) (cited on pages 93, 96).

[183]M. F. Ober, A. Müller-Deku, A. Baptist, B. Ajanović, H. Amenitsch, O. Thorn-Seshold, and B. Nickel, 'Saxs measurements of azobenzene lipid vesicles reveal buffer-dependent photoswitching and quantitative z→e isomerisation by x-rays', Nanophotonics **11**, 2361–2368 (2022) (cited on page 94).

[184]P. Urban, S. D. Pritzl, D. B. Konrad, J. A. Frank, C. Pernpeintner, C. R. Roeske, D. Trauner, and T. Lohmüller, 'Light-controlled lipid interaction and membrane organization in photolipid bilayer vesicles', Langmuir : the ACS journal of surfaces and colloids **34**, 13368–13374 (2018) (cited on pages 94, 97, 98).

[185]A. M. Rice, C. R. Martin, V. A. Galitskiy, A. A. Berseneva, G. A. Leith, and N. B. Shustova, 'Photophysics modulation in photoswitchable metal-organic frameworks', Chemical reviews **120**, 8790–8813 (2020) (cited on pages 94, 99).

[186]R. Tong, H. D. Hemmati, R. Langer, and D. S. Kohane, 'Photoswitchable nanoparticles for triggered tissue penetration and drug delivery', Journal of the American Chemical Society **134**, 8848–8855 (2012) (cited on page 94).

[187]S. Osella, G. Granucci, M. Persico, and S. Knippenberg, 'Dual photoisomerization mechanism of azobenzene embedded in a lipid membrane', Journal of materials chemistry. B **11**, 2518–2529 (2023) (cited on page 94).

[188]J. M. Kuiper and J. B. F. N. Engberts, 'H-aggregation of azobenzene-substituted amphiphiles in vesicular membranes', Langmuir : the ACS journal of surfaces and colloids **20**, 1152–1160 (2004) (cited on page 94).

[189]J. M. Kuiper, M. C. A. Stuart, and J. B. F. N. Engberts, 'Photochemically induced disturbance of the alkyl chain packing in vesicular membranes', Langmuir : the ACS journal of surfaces and colloids **24**, 426–432 (2008) (cited on page 94).

[190]D. T. Valley, M. Onstott, S. Malyk, and A. V. Benderskii, 'Steric hindrance of photoswitching in self-assembled monolayers of azobenzene and alkane thiols', Langmuir : the ACS journal of surfaces and colloids **29**, 11623–11631 (2013) (cited on page 95).

[191]J. Zhang, F. Schuknecht, L. Habermann, A. Pattis, J. Heine, S. D. Pritzl, D. Trauner, and T. Lohmüller, 'Label–free time–resolved monitoring of photolipid bilayer isomerization by plasmonic sensing', Advanced Optical Materials **12**, 10.1002/adom.202302266 (2024) (cited on page 97).

[192]A. Mancini, L. Nan, R. Berté, E. Cortés, H. Ren, and S. A. Maier, 'Multiplication of the orbital angular momentum of phonon polaritons via sublinear dispersion', Nature Photonics **18**, 677–684 (2024) (cited on page 98).

[193]Z. Fei, A. S. Rodin, G. O. Andreev, W. Bao, A. S. McLeod, M. Wagner, L. M. Zhang, Z. Zhao, M. Thiemens, G. Dominguez, M. M. Fogler, A. H. Castro Neto, C. N. Lau, F. Keilmann, and D. N. Basov, 'Gate-tuning of graphene plasmons revealed by infrared nano-imaging', Nature **487**, 82–85 (2012) (cited on pages 98, 99).

[194]R. Hillenbrand, B. Knoll, and F. Keilmann, 'Pure optical contrast in scattering-type scanning near-field microscopy', Journal of microscopy **202**, 77–83 (2001) (cited on page 98).

[195]E. Pfitzner, *Surface and tip-enhanced infrared spectroscopy in life science*, 2019 (cited on page 98).

[196]D. Virmani, A. Bylinkin, I. Dolado, E. Janzen, J. H. Edgar, and R. Hillenbrand, 'Amplitude- and phase-resolved infrared nanoimaging and nanospectroscopy of polaritons in a liquid environment', Nano letters **21**, 1360–1367 (2021) (cited on page 98).

[197]B. T. O'Callahan, K.-D. Park, I. V. Novikova, T. Jian, C.-L. Chen, E. A. Muller, P. Z. El-Khoury, M. B. Raschke, and A. S. Lea, 'In liquid infrared scattering scanning near-field optical microscopy for chemical and biological nanoimaging', Nano letters **20**, 4497–4504 (2020) (cited on page 98).

[198]E. Pfitzner and J. Heberle, 'Infrared scattering-type scanning near-field optical microscopy of biomembranes in water', The journal of physical chemistry letters **11**, 8183–8188 (2020) (cited on page 98).

[199]Y.-H. Lu, J. M. Larson, A. Baskin, X. Zhao, P. D. Ashby, D. Prendergast, H. A. Bechtel, R. Kostecki, and M. Salmeron, 'Infrared nanospectroscopy at the graphene-electrolyte interface', Nano letters **19**, 5388–5393 (2019) (cited on page 99).

[200]L. M. Meireles, I. D. Barcelos, G. A. Ferrari, P. A. A. de A Neves, R. O. Freitas, and R. G. Lacerda, 'Synchrotron infrared nanospectroscopy on a graphene chip', Lab on a chip **19**, 3678–3684 (2019) (cited on page 99).

[201]X. Zhao, D. Li, Y.-H. Lu, B. Rad, C. Yan, H. A. Bechtel, P. D. Ashby, and M. B. Salmeron, 'In vitro investigation of protein assembly by combined microscopy and infrared spectroscopy at the nanometer scale', Proceedings of the National Academy of Sciences of the United States of America **119**, e2200019119 (2022) (cited on page 99).

[202]Y.-H. Lu, C. Morales, X. Zhao, M. A. van Spronsen, A. Baskin, D. Prendergast, P. Yang, H. A. Bechtel, E. S. Barnard, D. F. Ogletree, V. Altoe, L. Soriano, A. M. Schwartzberg, and M. Salmeron, 'Ultrathin free-standing oxide membranes for electron and photon spectroscopy studies of solid-gas and solid-liquid interfaces', Nano letters **20**, 6364–6371 (2020) (cited on page 99).

[203]O. Khatib, J. D. Wood, A. S. McLeod, M. D. Goldflam, M. Wagner, G. L. Damhorst, J. C. Koepke, G. P. Doidge, A. Rangarajan, R. Bashir, E. Pop, J. W. Lyding, M. H. Thiemens, F. Keilmann, and D. N. Basov, 'Graphene-based platform for infrared near-field nanospectroscopy of water and biological materials in an aqueous environment', ACS nano **9**, 7968–7975 (2015) (cited on page 99).

[204]A. F. Möslein, M. Gutiérrez, B. Cohen, and J.-C. Tan, 'Near-field infrared nanospectroscopy reveals guest confinement in metal-organic framework single crystals', Nano letters **20**, 7446–7454 (2020) (cited on page 99).

[205]A. Perálvarez-Marín, A. Barth, and A. Gräslund, 'Time-resolved infrared spectroscopy of ph-induced aggregation of the alzheimer abeta(1-28) peptide', Journal of molecular biology **379**, 589–596 (2008) (cited on page 99).

Acknowledgments

Producing and publishing scientific work is always accompanied by a lot of stress and doubt. Therefore, it is only possible through great teamwork, which I was fortunate to experience during the years of my PhD journey.

First and foremost, I would like to express my deepest gratitude to **Prof. Andreas Tittl**, who hosted me throughout the second phase of my PhD and whose input from the grand project ideas to the minute detail of crafting beautiful figures greatly improved the success of my PhD projects. Moreover, I am deeply grateful for his calm and trusting manner even during heated debates.

Furthermore, I am greatly thankful to **Dr. Korbinian Kaltenecker**, who supervised my work at attocube and taught me all the technical knowledge to perform cutting-edge near-field microscopy. In addition, I am very thankful for all the fun moments we had during our measurement sessions, development and customer meetings.

I would like to thank **Dr. Fritz Keilmann** for introducing me to near-field microscopy and for his intense commitment to pushing the field further. I will always cherish the memories of our Alptip hikes.

At the same time, I would like to thank **Prof. Stefan Maier** for supervising me during my first year of my PhD and for kick starting my PhD with attocube and managing the lab in a pragmatic manner during the pandemic.

I would like to thank my PhD committee, especially **Prof. Dr. Achim Hartschuh**, **Prof. Dr. Joachim Rädler**, **Prof. Dr. Jan von Delft** and **Prof. Dr. Alexander Urban**

I am deeply grateful to **Enrico Baù** for managing with me the near-field microscopy lab and establishing with me through hard work near-field microscopy as a part of the Functional Nanophotonics group. Furthermore, I am thankful for all the fun time we had at conferences, in the lab and at the office.

In addition, I would especially like to thank **Andreas Aigner** and **Andrea Mancini** for all their hard work and scientific support making the publications in this thesis possible.

I would like to thank **Dr. Theo Lohmüller**, **Jinhua Zhang** and **Prof. Nicoleta Ilie** for the great collaborations.

Another big thanks goes to my office mates over the years in the 1st and 4th floor, **Michael Hirler**, **Connor Heimig**, **Dr. Wenzheng Lu** and **Dr. Anil Pal** . It was great fun sharing my daily struggles with you.

Moreover, I would like to thank the whole Chair in Hybrid Nanosystems and especially the Functional Nanophotonics group for the great working atmosphere with many cakes, celebrations and group trips.

I would like to thank my family and friends for the immense support during the whole journey especially **Thomas Pickl**, who could understand my troubles and helped me to overcome them.

Last but not least, I am greatly thankful to my **Simone**, who endured me during all the highs and lows of my PhD and gave me the motivation to continue with my work.